Single-Photon Gates Mediated by Single-Blockade-Sized Rydberg Medium

Master's Thesis in Physics
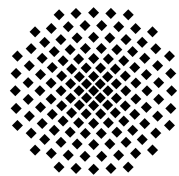
submitted by

Christian Zimmer

on

May 4, 2016.

This thesis has been carried out at the

5th Institute of Physics
University of Stuttgart

under the supervision of

Prof. Dr. Tilman Pfau and
Prof. Dr. Gert Denninger.

Ehrenwörtliche Erklärung

Hiermit erkläre ich, diese Arbeit selbstständig verfasst und nur die als Quellen angegebenen Hilfsmittel verwendet zu haben, wobei alle wörtlich oder sinngemäß aus anderen Werken übernommenen Aussagen als solche gekennzeichnet sind. Die vorliegende Arbeit war weder vollständig noch teilweise Gegenstand eines anderen Prüfungsverfahrens. Weiterhin stimmt das elektronische Exemplar dieser Arbeit mit der gedruckten Version überein.

Stuttgart, den 4. Mai 2016

Christian Zimmer

Zusammenfassung

Ziel dieser Masterarbeit war es in erster Linie, den bestehenden Aufbau des Rydberg-Quantenoptik (RQO) Experiments dahingehend zu modifizieren, dass es letztendlich möglich ist, kohärente quantenmechanische Schaltelemente auf Einzelphotonen-Ebene zu realisieren. Darauf aufbauend, sollten im Rahmen dieser Arbeit auch erste Anwendungen im umgestalteten Aufbau umgesetzt und eingehend studiert werden.

Alle Experimente, die im RQO-Experiment durchgeführt werden, basieren im Wesentlichen auf Phänomenen der Rydberg-Physik, einem speziellen Gebiet der Quantenoptik. Rydberg-Atome sind dadurch gekennzeichnet, dass ein oder mehrere der in der Hülle am weitesten außenliegenden Elektronen mithilfe quantenoptischer Methoden in energetisch hochangeregte Zustände mit großer Hauptquantenzahl n versetzt werden. Im vorliegenden Experimentaufbau wird dazu die Wechselwirkung zwischen Licht und Materie ausgenutzt. Mittels 2-Photonen Raman-Anregung wird das Elektron zunächst auf ein Zwischenniveau $|e\rangle$ versetzt, um von dort aus direkt auf das finale Rydbergniveau $|r\rangle$ angeregt zu werden.

Bei den angeregten Atomen handelt es sich jedoch keineswegs um isolierte Atome. Vielmehr sind sie Teil einer ultrakalten Wolke bestehend aus ^{87}Rb-Atomen, die im Zentrum eines attraktiven optischen Dipolpotentials bei einer Temperatur von nur wenigen Mikrokelvin eingeschlossen sind.

Innerhalb dieses Teilchenensembles ist es auf folgende Art und Weise möglich, die besonderen Eigenschaften der Rydberg-Atome auszunutzen, um letzten Endes die Propagationseigenschaften einzelner Photonen mithilfe nur eines vorangehenden Photons zu beeinflussen:

Aufgrund des sehr hochangeregten Elektrons besitzt das Rydbergatom eine außerordentlich hohe Polarisierbarkeit, welche wiederum große dipolare Wechselwirkungen induziert. Das damit verbundene Wechselwirkungspotentials hat Einfluss auf alle benachbarten Atome innerhalb des so genannten Blockadevolumens, welches sich über Größenordnungen von mehr als $10\,\mu\mathrm{m}$ ausdehnen kann. Alle Atome, die sich in diesem Bereich aufhalten, erfahren Energieniveau-Verschiebungen, die weitere Rydberg-Anregungen verhindern [1], [2]. Aufgrund der einzelnen Rydberganregung erhält die Wolke in diesem Bereich eine Art *Einzelquanten-Charakter* [3].

Innerhalb der Atomwolke bleibt die Rydberganregung jedoch nicht auf ein einzelnes Atom beschränkt, sondern verteilt sich auf *kohärente* Art und Weise kollektiv auf alle blockierten Atome [4].

Mithilfe weiterer Laseranregung kann die Rydberganregung wieder in ein Photon zurückverwandelt werden [5], sodass die Rydberg-Rydberg Wechselwirkung effektiv als Vermittler einer Wechselwirkung zwischen einzelnen Photonen auftritt [6], [7], beziehungsweise es ermöglicht, das Propagationsverhalten nachfolgender Photonen mithilfe des Anregungsphotons zu kontrollieren [8].

Alle dieser Arbeit vorausgegangenen, im bisherigen Experimentaufbau durchgeführten Experimente, erforderten stets lange Wechselwirkungszeiten zwischen Licht und Atomen, was durch Kombination aus langgestrecktem Rydberg-Medium sowie hohen optischen Dichten erreicht wurde.

Um nun jedoch innerhalb dieses Rydberg-Systems Anwendungen auf *Einzelphotonen*-Ebene zu realisieren, die vor allen Dingen auch *kohärenten* Charakter besitzen, muss der blockierte

Bereich auf alle Atome des Ensembles ausgedehnt werden [9].

Genau an dieser Stelle setzten die im Rahmen dieser Masterarbeit durchgeführten Tätigkeiten an. Durch Umgestaltung des optischen Dipolpotentials in Form einer Potentialvertiefung, die durch einen zusätzlichen Laserstrahl erzeugt wird, konnte die Ausdehnung der Wolke erfolgreich auf den Bereich des Blockaderadius reduziert werden. Dabei können noch immer ausreichend hohe optische Dichten gewährleistet werden.

Im Anschluss daran konnten erste Schaltelemente mithilfe dieses umgeformten Rydberg-Mediums realisiert werden. Um an zuletzt durchgeführte Messungen im vorangegangenen Dipolfallenpotential anzuschließen, lag der Fokus dabei zunächst auf der Umsetzung des kohärenten Einzelphotonen-Transistors.

Schließlich konnte am Ende dieser Arbeit noch eine weitere Anwendung, der so genannte Einzelphotonen-Absorber, eingehend untersucht werden. Zum einen wurde dessen Mechanismus mithilfe einer Monte-Carlo-Simulation erforscht, indem der Einfluss charakteristischer physikalischer Parameter auf das Absorber-Endresultat studiert wurde. Parallel dazu wurden nach experimenteller Implementierung auch Messungen durchgeführt, die schließlich mit den Simulationsergebnissen verglichen werden konnten.

Contents

Introduction

Shaping the world according to their own preferences has always been one of mankind's greatest interests. Especially in science, physical laws are exploited for redesigning nature and creating artificial states of matter.

In the course of time human's ability for manipulating their environment refined towards increasingly small scales. Ultimately, the discovery and exploration of the surprising world of quantum mechanics, allowed expanding creative power to the tiniest constituents of matter. Especially initiated by Max Planck's quantum hypothesis in 1900 [10] and Albert Einstein's postulation of a quantized world in 1905 [11], the business of investigating atoms and photons began to develop rapidly.

In full compliance with our intrinsic character of being keen on shaping the world by using tools that are provided by nature itself, the field of quantum optics arose particular interest. The astonishing phenomenon of interaction between light and matter on the quantized level turned out to offer plenty of possibilities whose vital importance immediately becomes clear when considering several Nobel Prizes within the last two decades [12]–[15]. However, related achievements are by no means only restricted to science. In fact, gained knowledge as well facilitated incredible technological developments, one need only think of the laser and its applications.

Besides allowing for the modification of the properties of single atoms, light-matter interaction also enables adjusting the optical response of the system and thereby changing the propagation behaviour of individual photons. However, all these phenomena will of course not be of great value if their range of influence is restricted to the size of effects caused by single particles. To extend interaction ranges one might therefore enhance atom-light coupling for example by placing individual atoms into a cavity or by confining the light to small areas using waveguides. A much less elaborate approach, though, is to directly exploit inter-atomic interactions:

By means of optical photons it is possible to excite a single electron which is bound to an atom's nucleus to principal quantum numbers n that are very high-lying in energy, so called Rydberg-states. The resulting Rydberg atom whose appearance highly reminds of an hydrogen atom exhibits a number of peculiar exaggerated properties:

Due to a significant enhancement of their dimension which scales as n^2, Rydberg atoms generally feature large polarizabilities which in turn introduce strong interactions. Building on these dipolar Rydberg interactions, light-matter interaction ranges can be extended to orders that largely exceed the size of neutral atoms as well as the optical wavelength [16]. As a result only one single Rydberg atom can prevent the excitation of other atoms within a range of more than $10\,\mu\mathrm{m}$ which could experimentally finally be demonstrated by Urban et al. in 2009 [1]. This is referred to as the Rydberg blockade effect.

If Rydberg atoms are not isolated but are excited within an ultracold cloud of atoms these strong Rydberg interactions can be exploited to control the properties of neighbouring ground state atoms [16]. The blockade effect which even gets enhanced with increasing density [4], [17] inherently prevents all others to get excited to Rydberg levels as well [2]. In this way the cloud will thus suddenly exhibit single-quantum character[3].

Beyond that, inside the cloud the Rydberg excitation will by no means stay localized at

one atom but will rather be collectively and *coherently* shared between thousands of blockaded atoms as experimentally shown by Heidemann et al. [4]. Sufficiently small trapping areas of the ensemble would therefore make it possible to attribute both single-quantum character and the aspect of coherent single-photon storage to the *whole* ensemble [9] yielding a promising quantum mechanical many-particle system.

By exploiting well-understood excitation techniques such as electromagnetically induced transparency (EIT) [18] the coherent Rydberg excitation can be converted back to photons. In this way the strong and long-range Rydberg-Rydberg interaction are mapped onto photons [5]. This process gives rise to a remarkable effect that has been a long-standing goal in quantum optics: Rydberg excitations can be used as a mediator to effectively realize photon-photon interactions [6], [7]. Beyond that, the resulting attraction or repulsion between *single* photons is highly controllable [8] due to the tunability of the Rydberg dipole interaction [19].

Furthermore, Rydberg excitations generally exhibit very long radiative life times scaling as n^3 [19], which under certain conditions can even reach orders of microseconds [20]. Consequently, this quantum mechanical system provides for remarkably long coherence times.

Finally, the combination of all these effects of course opens up a huge variety of possible applications.

The Rydberg blockade effect itself can for example be exploited for the robust creation of entangled states between two atoms [21] which could be extended to tens of atoms [22]. In connection with the effective photon-photon interactions and their inherent single-quantum character it is even possible to employ Rydberg media for the generation of artificial non-classical states of light [7], [16].

Moreover, due to the single-quantum character Rydberg media can also directly be used as a single-photon source [3] representing an important precondition for the realization of quantum gates. In fact, the combination of long coherence, long-range interactions and the resulting dipole blockade makes these systems ideally suited for quantum information processing.

After several proposals have shown that Rydberg excitations in ultracold gases are promising candidates for the realization of scalable quantum logic gates [16], [23], [24], not long afterwards experimentally successful implementations could repeatedly be demonstrated [3], [25].

Not least the potential for simulating quantum many-body physics [8], [26] finally indicates the outstanding role Rydberg physics plays to understand and shape the world of quantum mechanics.

This Thesis

In the first instance, this thesis is intended for providing the basis for the realization of *coherent* gates on the single-photon level within the existing Rydberg Quantum Optics (RQO) experiment.

Hitherto, all experiments performed in this setup required long interaction times which have been achieved by the combination of a long Rydberg medium and high optical depths. Recent reports and proposals which have also partly been mentioned above, though, show that a reliable incorporation of coherence inherently demands for cloud dimensions that are smaller than the Rydberg blockade effect.

To this end, the first goal of this thesis was to modify the existing setup, namely by reducing the trapping volume of the ultracold cloud of ^{87}Rb-atoms. This can be accomplished

by altering the optical dipole potential which was formerly generated by two crossed laser beams yielding the required elongation of the cloud. For the purpose of this adjustment a dimple was introduced to the existing configuration which makes it possible to significantly reduce the longitudinal length.

The first part of this thesis comprises all, oftentimes very technically oriented tasks that have been performed in this context. To begin with, the first chapter presents the theoretical concepts of the most important physical techniques that have thereby been employed. This is followed by a calculation of the dipole potential and the design of all required optical parts.

In compliance with the course of events, the next two chapters describe the two approaches that have been made in order to realize the dimpled potential. They only differ in the light source that is intended to provide the dimple laser beam. Subsequent to a comprehensive characterization of the first source it is then discussed why this approach has finally not been pursued further.

The first part of this thesis is closed by the characterization of the final dimpled dipole trap resulting from the second approach.

Based on these practical achievements the next goal of this thesis was the realization of single-photon gates mediated by the reshaped Rydberg medium that now exhibits sizes in the order of a single blockade.

Continuing measurements that have been performed last in the former trap configuration, activities have first been focussed on the implementation of a *coherent* all-optical single-photon transistor. This is presented in chapter one of the second part, directly followed by reporting on the realization of yet another photon gate, the single-photon absorber. In the scope of this thesis this gate was studied experimentally as well as by means of a Monte-Carlo simulation.

Part I

A Dimpled Optical Dipole Trap

Chapter 1

Theoretical Basics

This chapter lays the theoretical foundation of the physical phenomena which are the base for tasks that have been performed during this thesis. For this purpose the descriptions are restricted only to the vital aspects that are necessary to understand why actions have been taken in their particular way.

The chapter starts with a detailed treatment of the theory of the optical dipole force which represents the underlying principle of optical dipole traps that nowadays are a common tool of experiments in the context of quantum optics.

However, there is a variety of different methods for realizing such a trap. In the particular experiment which has been worked on in this thesis the trap is established by means of Gaussian beams. Therefore, the next section of this chapter outlines how they are formed, what their basic characteristics are and how they can be applied for the trapping of atoms.

Further minor and oftentimes more technical theoretical concepts such as fundamentals of scanning Fabry-Pérot cavities and their necessity in the context of this work will be described separately where appropriate. Theoretical concepts of the actual physical investigations which have been made possible by the new setup and which are presented in part II are as well not part of this chapter but will rather be described there if required.

1.1 Theory of the Optical Dipole Force

Light can be used to apply forces on single atoms. This effect relies on the interaction of light and matter where the electric field $\vec{E}$ can induce a dipole moment of $-e\vec{r} = \epsilon_0 \chi_{atom} \vec{E}$ on an atom with polarizability $\epsilon_0 \chi_{atom}$. This process is described by the corresponding Hamiltonian

$$H(t) = e\vec{r} \cdot \vec{E} \tag{1.1}$$

Movement of this dipole within the electric field $\vec{E}$ leads to an interaction energy of

$$U = -\int_0^E \varepsilon_0 \chi_{atom} E' dE' = -\frac{\varepsilon_0}{2} \chi_{atom} E^2 = \frac{e}{2} \vec{r} \vec{E} \tag{1.2}$$

where E denotes the amplitude of the electric field. The acting force results from the energy gradient and is given by

$$F_z = -\frac{\partial U}{\partial z} = \varepsilon_0 \chi_{atom} E \frac{\partial E}{\partial z} \tag{1.3}$$

Here, without loss of generality, the z-direction is chosen to be the predominant axis, such that the radiation can be modelled as a linearly polarized electric field $\vec{E} = E_0 \cos(\omega t - kz)\hat{e}_x$ propagating along the z-axis with angular frequency ω. This, in turn, results in the bipartite force

$$F_z = -ex \left[\frac{\partial E_0}{\partial z} \cos(\omega t - kz) + k E_0 \sin(\omega t - kz) \right] \tag{1.4}$$

In order too understand the meaning of the both parts, one has to consider the expression of the dipole moment $-eD_x$ in terms of the Bloch vector $\vec{R} = u\hat{e}_1 + v\hat{e}_2 + w\hat{e}_3$. Its elements u and v are defined in terms of the so called coherences, the off-diagonal elements of the density matrix $\hat{\rho} = |\Psi\rangle \langle\Psi|$ (with $|\Psi\rangle$ representing the quantum mechanical wavefunction) according to

$$\begin{aligned} u &= \rho_{12} \exp(-i\delta t) + \rho_{21} \exp(i\delta t) \\ v &= -i(\rho_{12} \exp(-i\delta t) - \rho_{21} \exp(i\delta t)) \end{aligned} \tag{1.5}$$

Here $\delta = \omega - \omega_0$ denotes the detuning of the radiation from the resonant transition between the atomic energy levels. In the simplified case considered here, the two-level system is fully described by a density matrix which comprises only four elements. The third coefficient w is given by the population difference $\rho_{11} - \rho_{22}$ of both contributing levels [27].

The Bloch vector indicates the position on the Bloch sphere of the state that describes the quantum mechanical system. The Bloch sphere, in turn, geometrically represents the pure state space of the system.

Dipole and Scattering Force

Using u and v the electric dipole moment can be written as

$$-ex(t) = -eX_{12}(u\cos(\omega t) - v\sin(\omega t)) \tag{1.6}$$

with $X_{12} = \langle 1| x |2\rangle$. Put into equally (1.4), this finally leads to the time-averaged force

$$\overline{F}_z = -\frac{eX_{12}}{2} \left[u\frac{\partial E_0}{\partial z} - vE_0 k \right] = F_{dipole} + F_{scatt} \tag{1.7}$$

Obviously, the first part of the force is expressed in terms of the component u which is in-phase with the electric field represents the dipole force and the second one is responsible for scattering [27].

Expressions for the coefficients of the Bloch vector can now be derived by solving the optical Bloch equation which in this case describes the interaction of radiation with the two-level atom.

At time scales much longer than the lifetime $\tau = \Gamma^{-1}$ of the upper level the corresponding steady-state solution reduces to

$$u = \frac{\Omega\delta}{\delta^2 + \Omega^2/2 + \Gamma^2/4} \qquad \text{and} \qquad v = \frac{\Omega\Gamma/2}{\delta^2 + \Omega^2/2 + \Gamma^2/4} \qquad (1.8)$$

where $\Omega = eX_{12}E_0/\hbar$ denotes the Rabi frequency which induces a power-broadening of the linewidth Γ by a factor of $\sqrt{1 + 2\Omega^2/\Gamma^2}$. This finally results in the following expressions for the dipole and scattering force [27]

$$F_{dipole} = -\frac{\hbar\delta}{2} \frac{\Omega}{\delta^2 + \Omega^2/2 + \Gamma^2/4} \frac{\partial\Omega}{\partial z}$$
$$F_{scatt} = k\frac{\hbar\delta}{2} \frac{\Gamma}{\delta} \frac{\Omega^2/2}{\delta^2 + \Omega^2/2 + \Gamma^2/4} \qquad (1.9)$$

A more convenient quantity representing scattering is the scattering rate R_{scatt} which is connected to the scattering force via the photon momentum $\hbar k$ according to

$$F_{scatt} = \hbar k \cdot R_{scatt} \qquad (1.10)$$

Dipole Potential and Scattering Rate for Large Detuning δ

Apparently, the dipole force generally vanishes on resonance $\delta = 0$. Thus, large detunings are required in order to apply strong forces on the atom.

For detunings much larger than both the linewidth ($|\delta| \gg \Gamma$) and the intensity in terms of the Rabi frequency ($|\delta| \gg \Omega$) the dipole force becomes equal to the derivative of the light shift which results from the so called alternating current (AC) Stark effect:

$$F_{dipole}\left(|\delta| \gg \Gamma, |\delta| \gg \Omega\right) \quad \longrightarrow \quad -\frac{\partial}{\partial z}\left(\frac{\hbar\Omega^2}{4\delta}\right) \qquad (1.11)$$

Hence, in this case the AC Stark shift can be interpreted as a dipole potential U_{dipole} which the atom moves in and thereby experiences the force

$$\vec{F}_{dipole} = -\nabla U_{dipole} \qquad (1.12)$$

By additionally using the saturation intensity $I_{sat} = \frac{\pi}{3}\frac{hc}{\lambda^3\tau}$ with the speed of light c and the wavelength λ corresponding to the atomic transition, in the regime of large detunings the dipole potential can finally be expressed as

$$U_{dipole} = \hbar\frac{\Gamma}{8}\frac{\Gamma}{\delta}\frac{I}{I_{sat}} \qquad (1.13)$$

From this expression one can easily extract the character of the potential that governs the movement of the atom: For blue detuning, that means $\delta > 0$, the potential is maximized at the highest intensity, however, for red detuning ($\delta < 0$) it grows with decreasing intensity. Thus, in the first case the atom is repelled from the light field whereas in the second case the interaction becomes attractive for higher intensities.

Moreover, in the limit of large frequency detuning $|\delta| \gg \Gamma$ the scattering rate becomes

$$R_{scatt} \quad \longrightarrow \quad \frac{\Gamma}{8}\frac{\Gamma^2}{\delta^2}\frac{I}{I_{sat}} \quad = \quad \frac{1}{\hbar}\frac{\Gamma}{\delta}U_{dipole} \qquad (1.14)$$

which scales as I/δ^2 whereas the dipole potential is proportional to I/δ [28]. Consequently, by choosing a sufficiently large detuning the scattering rate can be reduced while the dipole trap can be kept reasonably deep.

Optical Dipole Trap (ODT)

As already discussed above, in the case of red detuning the atom can be confined in the focus of a laser beam where the intensity is known to be maximized. Additionally, if $|\delta| \gg \Gamma$ one can simultaneously minimize scattering and still obtain a reasonably deep dipole potential. These two effects can be exploited in a so called dipole trap where an atom is trapped in the region of highest intensity of a light field. The basic physical principle of dipole traps in far-detuned light fields can solely be described using the two relations for the dipole potential and the scattering rate given by (1.13) and (1.14) respectively.

Generally, there are mainly two requirements which have to be taken into account for the design of such a trap:

- The potential depth must be sufficiently large in order to ensure reliable confinement at low temperatures.

- Values for the frequency detuning should be chosen such that scattering is reduced as much as possible to avoid heating of the atoms.

The temperature of the atoms which can still be confined is determined by the trap depth. As the dipole force is derived from a potential, it shows a conservative character, which means that the total energy stays constant during motion. Therefore, in order to remove kinetic energy from the atoms for loading the trap, some mechanism of energy dissipation is required such as spontaneous emission which is made use of in magneto-optical traps is required.

1.2   Theory of Gaussian beams

In the experiment described in this thesis, optical dipole traps are realized by the means of tightly focussed laser beams propagating along well-defined directions through a cloud of atoms. These laser beams can be modelled sufficiently well by Gaussian beams. A Gaussian beam is an electromagnetic field that propagates in free isotropic space and comprises both transverse magnetic and electric components. Therefore, it is also referred to as a transverse electromagnetic mode or shortly TEM_{mn}. The indices m and n denote the Gaussian modes which in turn indicate their particular waveform.

1.2.1   Mathematical Description

Mathematically, Gaussian beamsin terms of Hermite-Gaussian modes[1] are obtained as one solution of the Helmholtz equation in paraxial approximation. As the name "Gaussian beam" suggests this kind of light refers to radiation whose field amplitude is characterized by Gaussian functions. The TEM_{00} mode, also known as fundamental mode, is the lowest order mode whose amplitude obeys a pure Gaussian function. The amplitudes of all higher Gaussian or TEM_{mn} modes are additionally modulated by Hermite polynomials $H_j(x)$ with indices $j = m$ and n [29].

Lasers are typically intended for emitting TEM_{00} modes which are the types of beams that can be focussed best into a concentrated spot. This is why the following brief description of Gaussian beams is restricted to these kinds of modes.

---

[1]   Hermite-Gaussian modes are described in carthesian coordinates. Another important class of solution comprises the so called Laguerre-Gaussian modes which are obtained after the transition to cylindrical coordinates $\{x,y\} \rightarrow \{r,\varphi\}$.

Electric Field

Assuming propagation in z-direction and further supposed the radially symmetric electric field $\vec{E}(r,z)$ is polarized in x-direction, the beam is well defined by the following expression

$$\vec{E}(r,z) = E_0 \cdot \hat{\vec{e}}_x \cdot \frac{w_0}{w(z)} \cdot \exp\left(-\left(\frac{r}{w(z)}\right)^2\right) \cdot \exp\left(-ik\frac{r^2}{2R(z)}\right) \cdot \exp\left(-i\left(kz - \psi(z)\right)\right) \quad (1.15)$$

where $E_0 = E(0,0)$ denotes the electric field amplitude at the origin [30].

The corresponding magnetic field $\vec{H}(r,z)$ in turn is proportional to the electric component, so that it is described by an identical equation. The parameters that appear in (1.15) and characterize the beam are illustrated in figure 1.1 and are described next.
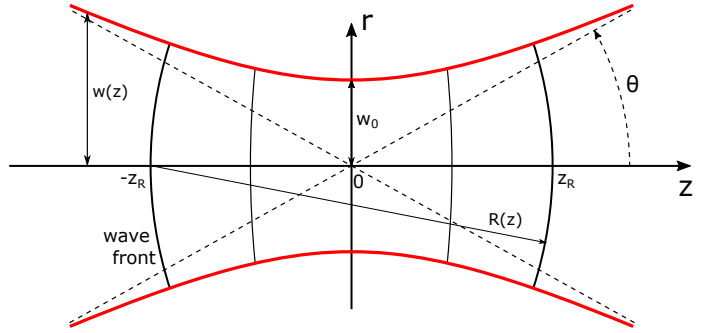
FIGURE 1.1: *Gaussian beam profile including the beam width $w(z)$, its waist w_0, the Rayleigh range z_R, the wavefront curvature $R(z)$ and the divergence θ.*

Beam Waist and Rayleigh Range

The profiles of both the electric and magnetic field components can be described by solely one parameter, the so called waist w_0. This quantity is defined as the radial distance from the focal position on the axis of propagation where the electric field amplitude drops to $1/e$. The evolution of the radial $1/e$-width $w(z)$ of the beam relative to its focus with $w(z=0) = w_0$ is then given by this single parameter according to

$$w(z) = w_0 \cdot \sqrt{1 + \left(\frac{z}{z_R}\right)^2} \qquad \text{where} \qquad z_R = \frac{\pi w_0^2}{\lambda} \qquad (1.16)$$

denotes the so called Rayleigh range. This is the distance from the focal position where the width has increased to $w(z_R) = \sqrt{2}w_0$ or, respectively, the intensity to $I(r = 0, z = z_R) = I_0/2$ (with $I_0 = I(r = 0, z = 0)$). The region $|z| \leq z_R$ is also known as the depth of focus or confocal parameter [30].

Beam Curvature

Another parameter characterizing a Gaussian beam is the parameter $R(z)$ which characterizes the curvature of the wavefronts. The spatial evolution of this radius of curvature is given by

$$R(z) = z\left[1 + \left(\frac{z_R}{z}\right)^2\right] \qquad (1.17)$$

[30]. At the focal position the radius becomes infinity which implies plane wavefronts. However, in contrast to homogeneous plane waves, the radial intensity profile of Gaussian beams is not constant but rather obeys a Gaussian function which spreads during propagation along z so that the beam diverges and the wavefronts bend for $z \neq 0$.

Divergence

As illustrated in figure 1.1, the radial envelope approaches a straight line for large z yielding a cone-like shape. Thus, the diverging behaviour can be quantified by the corresponding opening angle of the cone, called divergence of the beam θ. By using equation (1.16), θ can be expressed by the Gaussian beam parameters w_0 and z_R according to

$$\theta = \arctan\left(\frac{w(z)}{z}\right) = \arctan\left(w_0\sqrt{\frac{1}{z^2} + \frac{1}{z_R^2}}\right) \xrightarrow{z \to \infty} \arctan\left(\frac{w_0}{z_R}\right) \tag{1.18}$$

Gouy Phase

The last parameter which is required to fully describe a well-defined Gaussian beam is the Gouy phase

$$\psi(z) = \arctan\left(\frac{z}{z_R}\right) \tag{1.19}$$

From equation (1.15) one can easily see, that the Gouy phase leads to a change of the beam's periodicity in z-direction. Equivalently, this can also be interpreted as a modification of the apparent wavelength of the beam which finally results in a changing phase velocity [31].

Practically, the Gouy phase is not very important especially when using fundamental TEM_{00} modes where its influence can typically not be observed. However, it can become relevant for higher-order Gaussian modes.

Beam Intensity

The intensity I of a Gaussian beam can be calculated according to the relation $I = \frac{1}{2}\Re(E \times H^*)$. Using expression (1.16) for the Gaussian width $w(z)$ the intensity can be written as

$$\begin{aligned}
I(r,z) &= I_0 \left(\frac{w_0}{w(z)}\right)^2 \exp\left(-\frac{2r^2}{w(z)^2}\right) \\
&= I_0 \frac{1}{1 + (z/z_R)^2} \exp\left(-\frac{2(r/w_0)^2}{1 + (z/z_R)^2}\right)
\end{aligned} \tag{1.20}$$

The power which is enclosed by an aperture of radius r at the focus is then given by

$$P(r) = \int_0^r I(r',0)dr' = P_{tot}\left[1 - \exp\left(-\frac{2r^2}{w_0^2}\right)\right] \qquad \text{where} \qquad P_{tot} = \frac{\pi}{2}w_0^2 I_0 \tag{1.21}$$

represents the total power of the laser beam [30].

1.2.2 Application in Optical Dipole Traps

Gaussian beams are a common tool for establishing dipole traps by means of single laser beams. By substituting equation (1.20) into equation (1.13) the dipole potential will then depend on the spatial coordinates (r,z) in the following way:

$$U(r,z) = -\frac{U_0}{1 + (z/z_R)^2} \exp\left(-\frac{2(r/w_0)^2}{1 + (z/z_R)^2}\right) \tag{1.22}$$

assuming the beam to be red detuned with respect to the utilized atomic transition. All Gaussian beam parameters which do not appear here, have been merged in the trap depth $U_0 = |U(0,0)|$ at the focal position with $U_0 = const. > 0$.

Multilevel Atoms

In the case of alkali atoms and Gaussian laser beams with a distinct polarization that is specified by the ellipticity[2] ϵ, U_0 can be calculated according to [28], [32], [33]

$$U_0 = \hbar \frac{\Gamma}{8} \cdot \frac{\Gamma}{3} \left[\left(\frac{1}{\delta_1} + \frac{2}{\delta_2} \right) - g_F m_F \sqrt{1 - \epsilon^2} \left(\frac{1}{\delta_1} - \frac{1}{\delta_2} \right) \right] \cdot \frac{I_0}{I_{sat}} \tag{1.23}$$

δ_1 and δ_2 represent the frequency detuning of the laser with respect to the characteristic D_1 and D_2 lines of alkali atoms which belong to the $(5^2S_{1/2} \rightarrow 5^2P_{1/2})$ and $(5^2S_{1/2} \rightarrow 5^2P_{3/2})$ transition respectively [34]). The second term in (1.23) accounts for the optical Zeeman splitting where m_F denotes the Zeeman sublevel whose shift is characterized by the corresponding Landé g-factor g_F.

For the derivation of this expression for the trap depth U_0, all energy levels have to be taken into account which could principally contribute to the excitation of the atom. Especially, this means to consider the full number of Zeeman sublevels of both the D_1 as well as the D_2 line as possible excited energy levels[3]. This is also the reason why the D_2 line becomes double-weighted in equation (1.23):

Each transition that obeys the selection rules for the specific used light polarization is weighted by its corresponding Clebsch-Gordan-coefficient. The Clebsch-Gordan-coefficients, also known as transition coefficients, arise from the coupling of different angular momenta and basically account for the coupling strength between the involved ground and excited state depending on their angular momenta and the particular laser polarization.

The resulting total energy shift which is equal to the dipole potential and experienced by the atom in the far-detuned light field can then be obtained by summing up the contributions of all pairs of ground and excited states. This finally leads to the expression given by equation (1.23)[4].

Harmonic Approximation

In case of small thermal energy $k_B T$ of the atoms in the trap, the potential can be approximated sufficiently well by an harmonic oscillator, that means by a Taylor series expansion which is truncated after the second order that corresponds to the r^2-dependence. For small axial and radial distances from the focus (such that $z^4 \ll z_R^4$ and $r^4 \ll w_0^4$ respectively) the dipole potential will then simplify to [35], [36]

$$U(r,z) \approx -U_0 \left[1 - 2 \left(\frac{r}{w_0} \right)^2 - \left(\frac{z}{z_R} \right)^2 \right] \tag{1.24}$$

Using this equation (1.24) one can easily derive radial and axial trapping frequencies ω_r and ω_z which, in principal, are equivalent to the harmonic oscillator frequencies that result

---

[2] The ellipticity ϵ is defined as $\vec{\epsilon} = \left(\sqrt{1 + \epsilon} \, \hat{\vec{e}}_x + i \sqrt{1 - \epsilon} \, \hat{\vec{e}}_y \right) / \sqrt{2}$ in terms of the components of the electric field polarization vector [32].

[3] Contributions of other excited states are sufficiently small, so that they can be neglected here. Furthermore, in order to simplify the calculation the hyperfine structure of the excited states are assumed to be unresolved which is justified for detunings much larger than the hyperfine splitting ($|\delta| \gg \Delta_{HFS}$).

[4] For a more detailed treatment, see [28].

from the general solution of the equation of motion. These frequencies that are commonly used in order to characterize optical dipole traps are given by

$$\omega_r = \sqrt{\frac{4U_0}{mw_0^2}} \quad \text{and} \quad \omega_z = \sqrt{\frac{2U_0}{mz_R^2}} \tag{1.25}$$

In the case of Gaussian beams with elliptic instead of round radial cross section which exhibits two different waists $w_{0,x}$ and $w_{0,y}$, w_0^2 has to be replaced by $w_{0,x} \cdot w_{0,y}$.

Choice of Beam Parameters

Basically, optical dipole trapping at defined detuning δ and with a certain potential depth U_0, that means $I_0 = const.$, can be realized by setting either one of two interdependent beam parameters. By either choosing the beam waist w_0 or the total power P_{tot} of the beam, the desired trapping potential can be established. Referring to equation (1.20), both quantities depend on each other according to the following relationship[5]

$$I_0 = \frac{2P_{tot}}{\pi w_0^2} \tag{1.26}$$

Indeed, changing these quantities while keeping the ratio P_{tot}/w_0^2 constant does not influence the absolute trap depth U_0, however, according to (1.20) it will have an effect on the intensity distribution and, thus, also on the potential profile. For example, an increase of both the waist and the total powerresults in a more narrow but steeper trap with the same minimal value. This has to be kept in mind for designing the trap.

Alternatively, instead of setting the frequency to a well-defined value and varying the waist of the beam, one can keep the latter quantity constant and use the frequency as a degree of freedom. This becomes important, for instance, for choosing an appropriate light source where one is interested in the effect of changes in δ on the total power of the beam such that absolute trap depth stays constant. From equation (1.13) it can be deduced that U_0 scales as I_0/δ for given Γ and the constraint of large detunings. Accordingly, using Gaussian beams the trapping potential in the focus is proportional to $P_{tot}/(\delta \cdot w_0^2)$ which implies that the power in the beam has to be increased for larger detunings (and vice versa) in order to maintain U_0 if all other beam parameters remain unchanged.

However, referring to equation (1.14) the scattering rate scales as I/δ^2 or, respectively, as P_{tot}/δ^2. Consequently, a reduction of the detuning will negatively affect the scattering rate, namely by heating and enhanced loss of atoms, even if the power is decreased by the same factor. Again, this aspect has to be considered when choosing a laser with appropriate beam characteristics for establishing a desired optical dipole trap.

---

[5] Again, in the case of elliptical Gaussian beam profiles, w_0^2 has to be replaced by $(w_{0,x}w_{0,y})$.

Chapter 2

Design

After having introduced the most important theoretical concepts related to practical tasks and their applications which are described in part II, the first step towards the realization of the dimpled optical dipole trap is to thoroughly design of all required parts which is described in this chapter.

However, before presenting related calculations and planning tasks, first of all a general overview of the existing experiment setup is given based on which practical work during this thesis has been performed.

This will directly be followed by simulations of the optical dipole potential both for the existing crossed trap configuration as a reference as well as for the effect of the additional dimple beam.

Next, design and development concerning the optical setup and here especially the way of introducing the dimple laser beam to the experiment are described. The latter task necessitated a modification of the existing imaging light path. Therefore, the optical performance also regarding aspects such as aberrations induced by the new configuration was investigated in a systematic and elaborate way. A discussion of obtained results closes this chapter.

2.1   Experiment Setup

The whole sequence of the experiment which has been worked on and which in this thesis is referred to as the "RQO[6]-experiment" starts with the preparation of the atoms into an state which is appropriate for subsequent measurements in terms of both internal and external features of the atoms.

Therefore, ^{87}Rb atoms which are released from a dispenser are first loaded from the background gas into a magneto-optical trap (MOT) for laser cooling by pairs of counter-propagating laser beams red-detuned from the transition $(5^2S_{1/2}, F = 2) \rightarrow (5^2P_{3/2}, F = 3)$. An additional repumper which excites the transition $(5^2S_{1/2}, F = 1) \rightarrow (5^2P_{3/2}, F = 2)$ is used to close the cooling cycle. A detail of the ^{87}Rb level scheme which includes all levels and transitions mentioned throughout the thesis is shown in figure 2.1.

Subsequent to the initial state preparation, the atoms are loaded into an optical dipole trap yielding an atomic cloud of about 2.5×10^4 ^{87}Rb atoms. In the ODT they are optically pumped into the $(5^2S_{1/2}, F = 2, m_F = 2)$ state in order to enhance the optical depth (OD) of the cloud for later experiments. Additionally, in the ODT evaporative cooling is performed. This is a common technique to reach sub-recoil temperatures by removing the most energetic atoms of the energy distribution. Subsequent re-thermalization of the remaining atoms by

---

[6]   The acronym RQO stands for Rydberg Quantum Optics and describes the focus of physical investigation carried out in this experimental setup.
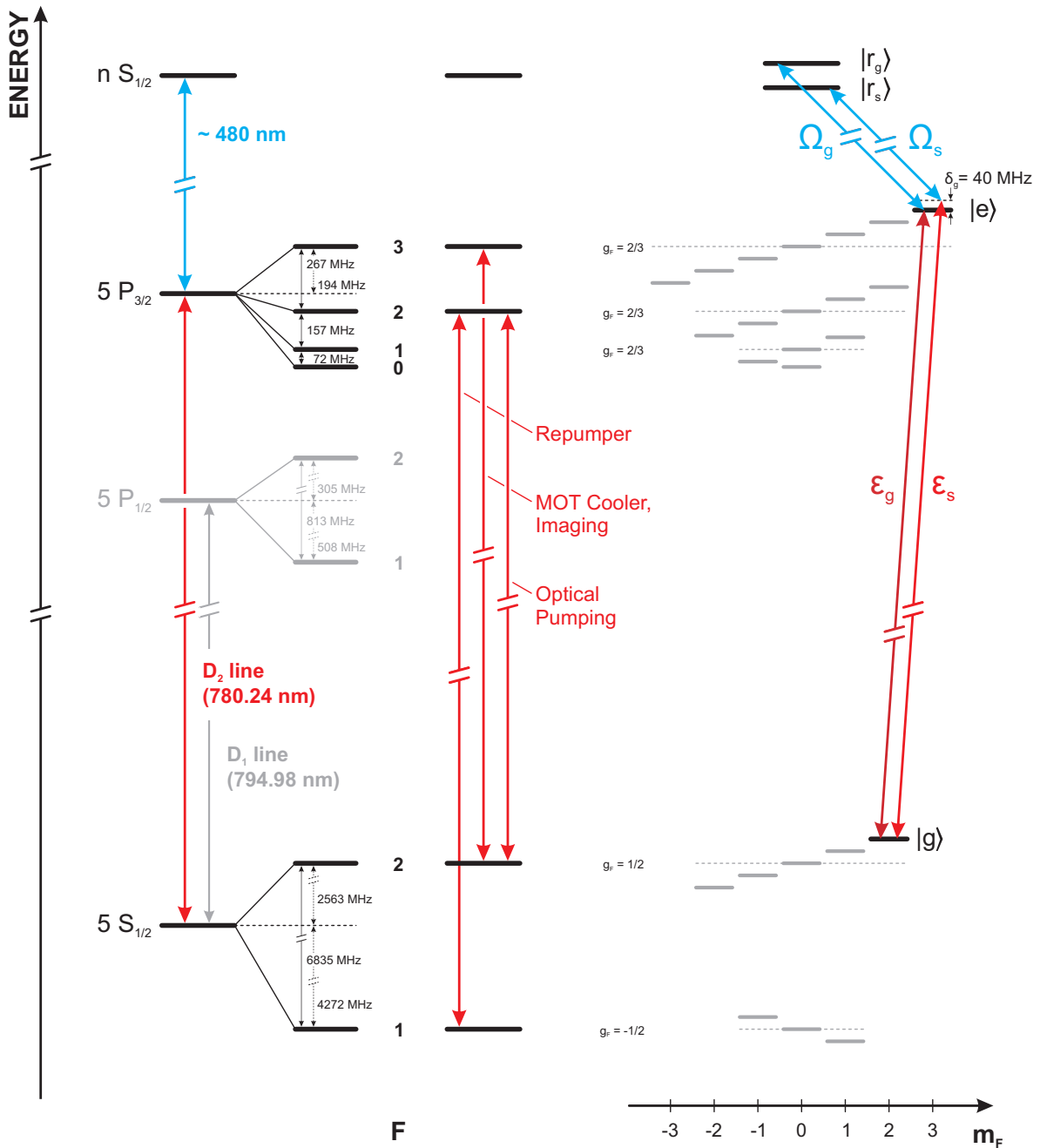
FIGURE 2.1: **Left:** *Detail of the Energy Level Structure of* ^{87}Rb *including all states and sub-states as well as two crucial transitions (red and blue) used for Rydberg quantum optics in ultracold gases. Splittings are not true to scale. [37], [38]*
Middle: *Diagram of three important transitions, denoted by the experiment steps which they are employed for.*
Right: *Excitation scheme of the single-photon gates presented in part II. Transitions identified with $\mathcal{E}$ belong to the probe laser field, those with Ω to the control field. Zeeman splittings depends o then applied magnetic field intensity, corresponding g-factors are given [37].*

elastic collisions yields a reduction of the average kinetic energy and, thus, of the temperature of the atomic ensemble. The final temperature of this ensemble was measured to be $T = 40\,\mu K$ in the former setup and from EIT spectra a total optical depth of $OD = 25$ was extracted.

In order to avoid unwanted disturbance due to level shifts induced by the Stark effect the ODT is normally turned off for measurements.

Experiment Control

All above-mentioned steps take place at the same place, that is within the evacuated experiment chamber on an optical table which in the following will be referred to as the "experiment table". The settings of most devices and components that are required for the experiment such as AOM voltages, currents for magnetic field coils, shutters or triggers as well as their exact relative timings are centrally programmed at the computer control so that devices and settings can be remotely accessed and modified. From the computer the sequence is transferred to and executed by an *ADwin-Pro II* system which comprises 32 digital and 16 analog channels and is especially designed for performing high-speed tasks with a time resolution of $20\,\mu s$.

However, as the experiment schedule requires an even faster control of shutters or AOMs, additionally a FPGA-based pulse generator is used which is also triggered by the ADwin. This allows to create and apply pulses to the experiment at time steps of only $2\,ns$.

The corresponding time schedule which is centrally prepared at the computer control defines all timings by assigning each device to a digital or analog channel and each setting to a variable.

Existing Optical Dipole Trap

The most important part of the experiment concerning this thesis is the optical dipole trap. As depicted in sketch 2.2, up to now the ODT is realized by means of a single laser beam at a wavelength of $1070\,nm$ which passes twice through the cloud at an angle of $31.4\,°$. This crossed beam configuration yields an elongated "cigar-shaped" cloud with a length of $80\,\mu m$ in longitudinal y-direction and a radial diameter of $50\,\mu m$ in both the x- and z-direction. At the centre of the trap the beam features a waist of $33\,\mu m$ and a final optical power of $0.5\,W$ after several ramps of evaporative cooling.

By means of the script presented in section 2.2.2 it can be calculated that a beam with these properties establishes an optical dipole trap with a depth of $U_0 = 74.3\,\mu K$. Further characteristics are listed in table 2.1 in the context of designing and calculating the required dimpled trap configuration.

Laser Setup

Apart from the chamber and its surroundings, the most important devices for performing measurements on the ultracold cloud of atoms are the lasers sources. All of them together with required optics are placed on a separate optical table, referred to as the "laser table". The emitted laser beams are then transferred to the experiment via optical fibres.

Figure 2.1 shows all transitions which are required in order to prepare the ultracold cloud of atoms (shown in the middle) and subsequently modify the atoms during experiments. The utilized atomic species ^{87}Rb provides for an easy level structure for performing experiments dedicated to Rydberg Quantum Optics.

All preparatory steps can be performed by transitions between sublevels that belong to the characteristic D_2-line at $780.24\,nm$. Thereby, each of the excitation beams features a certain
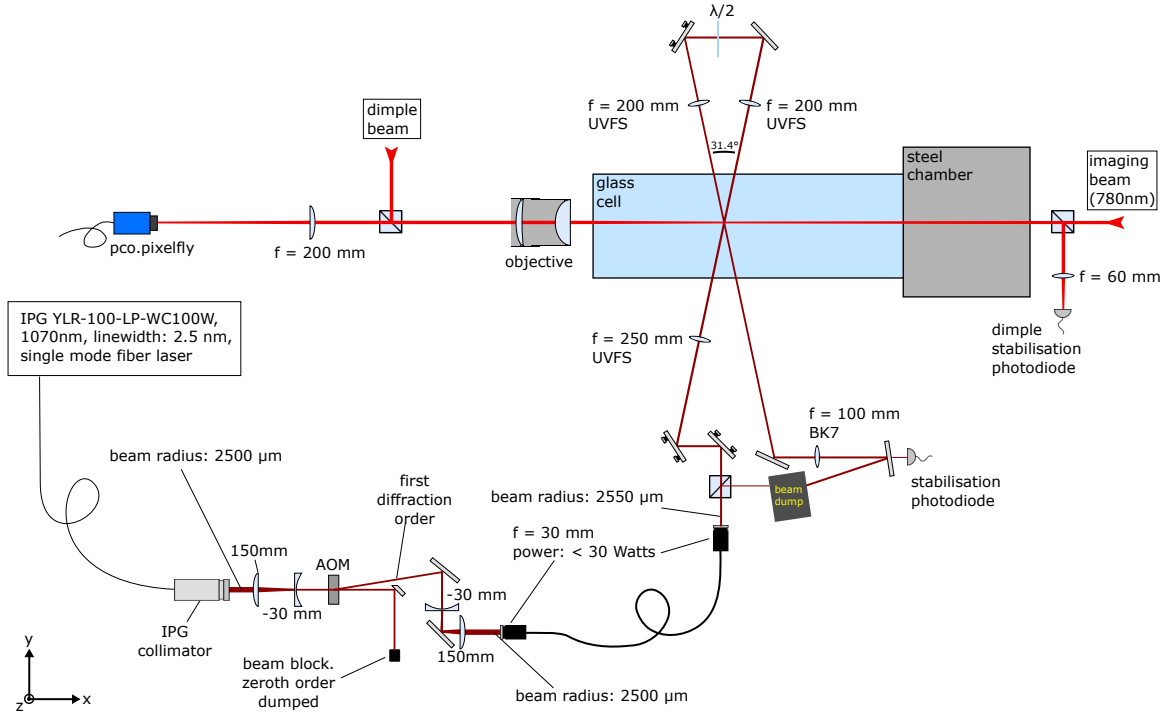
FIGURE 2.2: *Overview of the optical dipole trap setup.* *The schematic shows all optical components used for generating the crossed ODT (laser beam marked in dark red). Additionally, it comprises the final dimple beam path (light red) as well as the horizontal absorption imaging setup.*
The coordinate system defined here is used throughout the whole thesis.

detuning depending on its particular purpose, such as red-detuning for the cooling in the MOT. For carrying out absorption imaging the same transition is employed, however, here the excitation performed resonantly.

During experiments the atoms in the trap are modified by means of a pair of so called "probe" which are indicated by $\mathcal{E}$ and another pair of "control" (Ω) laser beams with each being pulsed with certain pulse lengths. The probes drives a transition between the ground state $|g\rangle$ and the excited intermediate state $|e\rangle$ that as well belongs to the D_2-line, though with special detunings. The (much stronger) control lasers at about $480\,\text{nm}$ couple the intermediate state to highly excited Rydberg states with principal quantum numbers that can be modified by tuning the laser frequency so that they can be adapted to the particular experimental purpose. The meaning of the indices g and s is not important for the present. It will only be used in the context of the transistor application presented in chapter 5.

Each pair of laser beams, that means both the probes and the controls, is counter-propagating and passes through the cloud in the way shown in figure 2.3. The schematic on the left also shows the optical access for single-photon detection by means of single photon counting modules (SPCMs).

All probe and control laser beams are tightly focussed onto the cloud of atoms. At the focal position in the centre of the cloud both probes feature a waist ($1/e^2$-radius) of $w_{0,probe} = 5\,\mu\text{m}$.
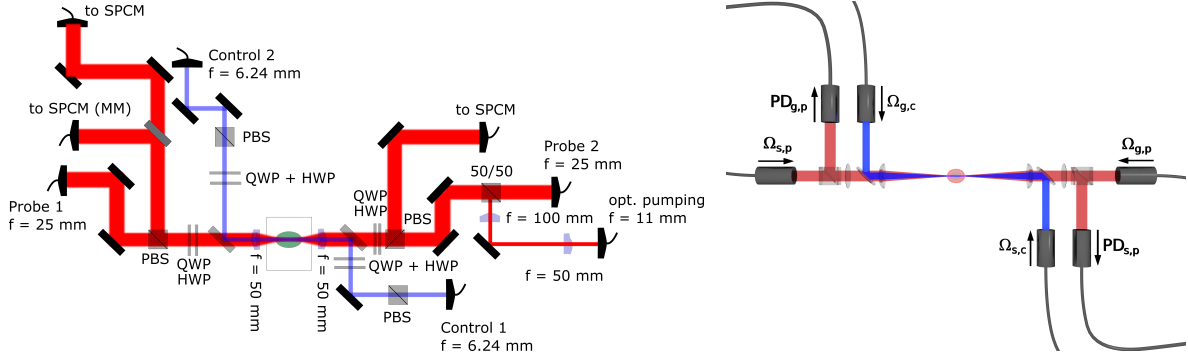
FIGURE 2.3: *Schematic overview of the laser setup required for applications presented in part II. All laser beams marked in red belong to the probe (p) light field at* 780 nm *which excites the atoms from the ground state* $|g\rangle$ *to the intermediate state* $|e\rangle$ *(compare figure 2.1). The blue ones represent the control (c) laser at* 480 nm *which couples* $|e\rangle$ *to the final Rydberg state* $|r\rangle$.

Further Important Parts

At this point, also other experiment parts should be briefly mentioned which will play a role within the thesis.

The experiment setup comprises an electric field control which allows further, also space-resolved, manipulation of the atoms by applying arbitrary fields. More details on its capabilities and the exact technical configuration can be found in [39].

Another important part which has been employed frequently and whose setup was modified during practical work on this thesis is the imaging system for monitoring the atomic cloud. Imaging is performed both in vertical and in horizontal direction which means picturing either the x-y- or the y-z-plane respectively by means of absorption imaging.

More detailed information on the experimental setup will be given where appropriate.

2.2 Dimpled Dipole Potential

Aiming at the realization of the particularly smaller shape of the ultracold gas of atoms, the existing crossed ODT has to be modified. The easiest way to achieve this is by introducing a third Gaussian beam into the setup which produces a dimple in the dipole potential. This is why the corresponding laser beam which is also shown in figure 2.2 and which induces this modification is called "dimple beam" and the resulting trap is referred to as the "dimpled ODT". In order to reduce the cloud size to the order of the Rydberg blockade radius, which is on the range of few micrometers, by means of a dimpled ODT the responsible beam has to fulfill certain demands.

Especially, the narrow dimple in the optical dipole potential can only be produced by tightly focussing the Gaussian beam onto the centre of the cloud. In contrast to the existing ODT where the same beam is mirrored and passes the cloud once more under a defined angle resulting in the crossed configuration, the dimple beam will cross the cloud only once.

2.2.1   Requirements

At a given temperature of the atoms the size of the confinement of the cloud is governed by the dipole potential. Since the configuration of the crossed dipole trap produces radial confinement which is already sufficiently narrow, the additional dimple solely has to deepen the potential in longitudinal direction and keep the radial component unchanged. Furthermore, the most important experimental aspect demanding for an unchanged radial dipole potential is the fact that the cross section of the probe laser beam with a width of $w_{0,probe} = 5\,\mu m$ and which propagates in longitudinal direction should still fully penetrate the cloud.

This requirement of confining the potential in only one dimension can solely be satisfied by maens of a Gaussian beam that features an elliptical instead of round cross section. This means that it will not only possesses one single waist in radial direction but rather two different ones in y- and z-direction[7]. In case of the dimple beam the radial direction[8] of the Gaussian beam is equal to the plane defined by the y- and z-axis since it has to propagate either along the x-axis or z-axis in order to modify the potential in the desired way. Here the x-axis was chosen for the sake of experimental feasibility.

As it becomes apparent from equation (1.22), the optical dipole potential for focussed Gaussian beams becomes exponentially narrower for smaller waists w_0. Thus, in order to modify the dipole potential only in y-direction and keep it otherwise unchanged, the responsible beam profile has to be squeezed as well along this axis resulting in a vertically elongated beam profile. According to (1.26), I_0 and U_0 respectively scale as $1/(w_{0,y}w_{0,z})$ for constant laser output power, hence the trap depth grows for smaller waists.

Furthermore, the dimple laser beam should extend the crossed ODT's potential in such a way that trapping of as many atoms as possible is guaranteed which is crucial for maintaining the high optical depth. Experiments which have been conducted in the crossed ODT show that high optical densities are an essential ingredient for the creation of large optical nonlinearities mediated by the atomic cloud so that it is advisable to maximize the OD in the new configuration as well.

At the same time, however, the demands on the light source especially concerning laser power and the optical setup for focussing the beam to a tiny spot, should preferably be kept low. Only then, there is a chance to use simple laser diodes (LD) instead of expensive diode laser systems as a dimple laser source.

Considering these aspects, the dimple was designed to at least double the trap depth.

2.2.2   *MATHEMATICA* Simulation

Estimations on the features of the required light source for the dimple as well as calculations about the resulting dipole trap have been obtained from analytical simulations that were performed by means of the software *MATHEMATICA* in the following way.

Structure

The *MATHEMATICA* script is built up as follows: After defining all required parameters of a Gaussian beam in carthesian coordinates its intensity profile is calculated. The reason for choosing carthesian instead of cylindrical coordinates is the fact, that the dimple laser is

---

[7]   These coordinates comply with the coordinate system which is shown in figure 2.2 and used throughout the whole thesis.

[8]   Radial direction always means perpendicular to the longitudinal or axial direction of propagation.

supposed to exhibit an elliptical radial beam profile. The coordinate system was defined to be similar to the one shown in 2.2 such that y is the longitudinal direction along which the cloud is elongated in the crossed ODT. The z-axis is the vertical direction and x is the dimple beam's direction of propagation. Thus, the y- and z-axis represent its radial direction.

Subsequently, using expression (1.20) for the intensity $I(r,z)$ the complete trapping potential $U(r,z)$ of the ODT also including the dimple is evaluated as a function of the position and various parameters, such as the angles of incidence of all contributing beams, their power and wavelengths as well as their beam waists. The value for the potential depth U_0 is estimated according to equation (1.23) with the assumption of zero magnetic field. Additionally, an expression for the scattering rate is derived in terms of the same parameters. In the next step the trapping frequencies for all three spatial dimensions are retrieved from a harmonic oscillator approximation as described in section 1.2.2.

Finally, after setting all parameters to the experimental values, plots of the potential as well as resulting numbers for the trapping frequencies and scattering rates are generated.

Method

Appropriate parameters for the dimple laser beam could now be determined by iteratively varying them and compare the resulting trapping features. For this purpose, mainly three characteristics of the Gaussian beam were taken into account: its wavelength and thus the detuning, the required power and finally the beam waists.

In doing so, the wavelength and power were given top priority. This is because once the waist is set such that the desired spatial confinement is achieved, there are only these two left for further adjustment. Moreover, the power and wavelength are principally the only features of interest for choosing an appropriate laser diode.

As discussed in the last passage of the previous chapter the required laser power can be reduced for smaller detunings at constant beam waists. However, this in turn conflicts with a higher scattering rate, so that a compromise has to be made between reasonable demands for optical power and still acceptable scattering rates.

Since the simulation results for the crossed ODT agree pretty well with the experiment, the estimations for the dimple trap are assumed to deliver reliable values as well.

Results

Based on the outcome of these analytical investigations, beam waists of about $10\,\mu\text{m}$ in horizontal (that means along the y-axis) and $40\,\mu\text{m}$ in vertical z-direction were assumed to be appropriate for the realization of a trapping potential that finally yields the desired cloud size. Provided that a single-mode fibre with a typical core diameter of less than $5\,\mu\text{m}$ is used this beam profile can be easily generated by using the optical setup which will be presented in section 2.3.

After having assembled the whole optical setup for the dimple and having conducted a first experimental beam characterization, including precise measurements of both the wavelength λ and the waists of the dimple beam at the focal position, the exact shape of the resulting potential was ultimately simulated again.

Figure 2.4 exemplarily shows such a dimpled ODT potential generated by the Gaussian beam with waists of $w_{0,y} = 12.33\,\mu\text{m}$ in horizontal, $w_{0,z} = 43.6\,\mu\text{m}$ in vertical direction and

$\lambda = 823.6\,\text{nm}$ measured for the laser diode[9] which was used for the first approach of realizing the dimpled trap. The power in the beam at the focus was measured to be $P_{tot} = 90\,\text{mW}$. The procedure and according setup for measuring these parameters will be described in detail in section 3.5.2.
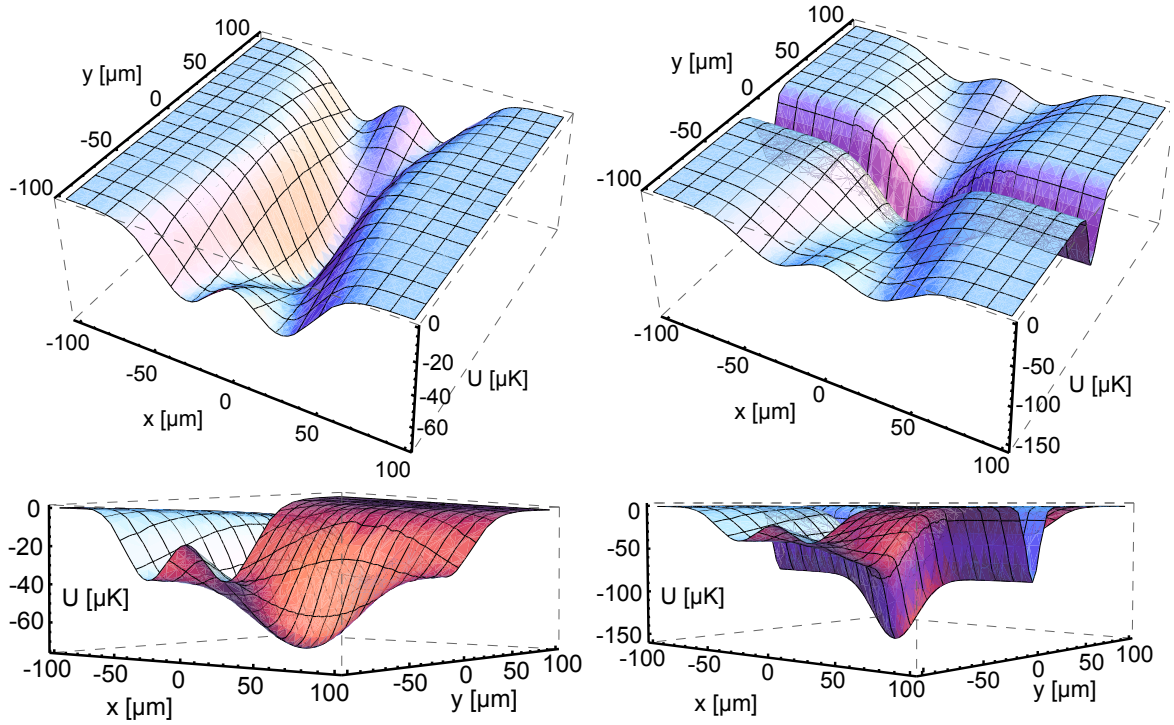
FIGURE 2.4: *Plots of simulated optical dipole potential.* *Top views (top) and side views (bottom) of the potential U are shown for both the crossed (left) and the dimpled (right) optical dipole trap configuration. The evaluation has been performed using MATHEMATICA and is based on optical power values provided by the light source used in the first approach for realizing the dimple. Values for the potential are given in units of temperature. The origin of the coordinate system has been placed in the minimum of the trapping potential.*

Table 2.1 lists values for the resulting characteristics of the ODT both for the case with and without dimple. Obviously, the target of doubling the trap depth can be reached. Furthermore, the trapping frequency in y-direction can be increased considerably while keeping the remaining directions almost unchanged. Furthermore, the scattering rates will not be enhanced too much.

Thus, the laser diode used in the first approach principally seems to be appropriate for providing the required beam and generating the desired potential.

Estimations of the actual cloud size in the trap depend on the temperature T of the atoms and can be retrieved from the simulation results. In an easy model, if scattering is neglected and the trapping potential is approximated harmonically around the centre as described in section 1.2.2, the distance which the atoms can escape from the centre only depends on their

---

[9] In fact, according to its data sheet, this *Thorlabs* diode of type L830P200 features a specified centre wavelength of $\lambda_{LD} = 824\,\text{nm}$ and a deviation of $\Delta\lambda_{LD} = \pm 6\,\text{nm}$. The maximum output power is specified to be $P_{opt,LD} = 200\,\text{mW}$ for a cw[10] operation at a current of $I_{LD} = 210\,\text{mA}$ and an operating voltage of $V_{op} = 2.1\,\text{V}$ [40].

Configuration	ω_x [Hz]	ω_y [Hz]	ω_z [Hz]	U_0 [μK]	R_{scatt} [s^{-1}]
Crossed ODT	$2\pi \cdot$ 774.4	$2\pi \cdot$ 217.7	$2\pi \cdot$ 804.4	74.3	0.58
Dimpled ODT	$2\pi \cdot$ 774.8	$2\pi \cdot$ 2303.6	$2\pi \cdot$ 1033.3	156.7	4.58

TABLE 2.1: *Simulation results of characteristic trapping parameters. For each the crossed and the dimpled ODT configuration all three trapping frequencies $\omega_{\{x,y,z\}}$, the trap depth U_0 in units of temperature and the scattering rate R_{scatt} in the centre are listed as obtained from the MATHEMATICA simulation. The calculation for the dimpled ODT is based on light at $\lambda = 823.6$ nm with total optical power of $P_{tot} = 90$ mW.*

kinetic energy E_{kin} which is then assumed to be equal to the thermal energy $E_{therm} = k_B T$. Translated to the picture of the energy landscape, the radius of the cloud σ is equal to the horizontal distance which the atoms can move up the wall of the potential. This is where the atom's kinetic energy intersects the trapping potential which is mathematically expressed by

$$U_{ODT}(r)|_{r=\sigma} = E_{kin} \tag{2.1}$$

where $U_{ODT} = \frac{m}{2}\omega^2 r^2$. In this simplified model the radius of the cloud σ_i along direction i can then be calculated according to

$$\sigma_i = \frac{\sqrt{\frac{2k_B T}{m}}}{\omega_i} \tag{2.2}$$

where k_B denotes the Boltzmann constant and m the atomic mass [41].

Assuming a typical temperature of $T = 40$ μK and using the trapping frequencies given in table 2.1 and an atomic mass of $m_{87Rb} = 1.44 \cdot 10^{-25}$ kg, after evaporative cooling the ultracold cloud of atoms is expected to exhibit dimensions as listed in table 2.2.

Configuration	σ_x [μm]	σ_y [μm]	σ_z [μm]
Crossed ODT	18.0	64.0	17.3
Dimpled ODT	18.0	6.0	13.5

TABLE 2.2: *Calculated dimension of atomic cloud trapped in ODT. For each the crossed and the dimpled ODT configuration radii $\sigma_{\{x,y,z\}}$ into all three spatial directions have been calculated according to (2.2). The resulting values given in table 2.1 and an ensemble temperature of $T = 40$ μK have been used for the calculation which is based on a harmonic approximation of the dipole potential.*

Even though the calculated radii for the crossed ODT are of the correct order, their exact values slightly deviate from the measured values which is most likely owing to the simplified model which the calculation is based on. Therefore, they should only be consulted for rough estimations of the cloud sizes. However, from these values it could be inferred as well that the desired trap modification should be achievable by means of the laser diode and the above mentioned beam properties.

2.3 Optical Setup for the Dimple Beam

As described in detail in the next two chapter 3 and 4 about the implementation of the dimpled ODT, two different light sources have been tested, one after another for establishing the final trap. Reasons for not proceeding with the laser diode used in the first approach will be discussed there. Independent of the source, the optical setup for the dimple beam basically consists of the same three segments which are set up in different places and described next.

In order to save space on the experiment table and to have easy access, it was originally planned to set up the first segment, namely the laser source including all optics which is only needed for the purpose of switching and stabilizing the beam, on a dedicated laser table. However, due to the small size of the laser diode housing this was only done in the final realization whereas in the first approach the source and corresponding optics was mounted in one corner of the experiment table.

Anyway, subsequently a single-mode fibre, the second segment, was always employed for transfer of the light from the laser site to the experiment table or, respectively, to the remaining optical parts that are required for the final adjustment of the beam which represents the third segment. A convenient and important side effect of the single-mode fibre is its property to filter the modes of the beam, such that only the fundamental mode will be transmitted.

2.3.1 Pre-Fibre Setup

First of all, the laser beam leaving the source has to be modified in such a way that, in the next step, it can be efficiently coupled into a polarization maintaining single-mode fibre. Furthermore, additional devices are required especially to allow for the option of switching the light on or off as fast as possible via the experiment control without turning off the light source. This can easily be achieved by sending the light through an acousto-optic modulator[11] (AOM) which is also used for an active intensity stabilization of the laser beam (described and characterized in section 3.4).

Of course the collimation lens and other required lenses for the setup in front of the fibre have to be selected according to the output profile of the light source. However, the remaining segments of the whole optical setup, namely the fibre and the optics behind it, do not have to be changed if another light source is used.

2.3.2 Fibre

Coupling of the light into the fibre should generally be carried out in a polarization maintaining way. Only this ensures that polarization does not rotate while the light is guided through the fibre. Polarization stability is essential for reliably performing experiments. To guarantee this, the fibre has to be isolated against thermal contacts since thermal drifts induce elongations of the fibre which possibly lead to a rotation of the light polarization[12].

---

[11] Type: *Gooch & Housego*, AOM 3080-122

[12] This is due to the fact that the light's phase velocity depends on its direction of polarization, either being horizontally or vertically polarized. Even after polarization maintaining coupling, which basically aims at modifying the light such that it is polarized along only one of the fibre's axis, there might be a slight component along the other axis yielding a fibre output that depends on the length of the fibre. A more detailed description of this effect can be found in the context of the final dimple realization in section 4.1.3 which also presents the technique used to minimize it.

In the first approach the dimple beam initially was to be characterized before being introduced into the experiment. Instead of on the actual experiment table this was planned to be done in the framework of a test setup on a separate breadboard. The fibre used for this purpose should be an already available one from *OZ Optics*[13]. Before being finally integrated into the setup the fibre was polished on both ends in order to optimize light transmission performance.

2.3.3 Post-Fibre Setup

The task of the last segment is to modify the beam leaving the fibre[14] once more, such that it can finally be employed in the experiment inside the glass chamber. All required optical components shall be mounted on the experiment table. Their planned arrangement is schematically illustrated in figure 2.5.

FIGURE 2.5: *Schematic of the optical setup required for the dimple beam on the experiment table after fibre transmission (x-y-plane). After getting elliptically shaped (see text for description of curvature orientation) the beam is shifted to the final experiment height of* 125 mm *above the table. By means of a polarizing beamsplitter the beam is introduced to the experiment chamber via the same optical path that is used for horizontal absorption imaging. The objective focusses the collimated beam onto the cloud. (The wave plate (HWP) behind the out-coupler will become important in the context of polarization maintaining fibre coupling.)*

Subsequent to the fibre, the collimated beam passes a telescope consisting of cylindrically shaped lenses with the inherent property of refracting the light is only along one direction. This is necessary in order to finally obtain the elliptical beam profile. As explained before, for the desired modification of the confinement of the atomic cloud in horizontal y-direction the dimple beam's focus has to be horizontally squeezed as well. This implies that the beam's waists has to be horizontally larger than in vertical direction before striking the final focussing lens. This is because the larger the waist the narrower foci can be achieved. In order to meet this demand

---

[13] Type: *OZ Optics*, PMJ-3A3A-850-5/125-3A-3-1

[14] Via a *Thorlabs* aspheric out-coupler lens of type A110TM-B with $f = 6.24$ mm and $NA = 0.40$ for the first approach and C230TMD-B ($f = 4.51$ mm, $NA = 0.55$) for the final realization.

by means of the cylindrical telescope it has to be kept in mind that the periscope which is placed between the telescope and the focussing optics will swap the horizontal and vertical beam dimensions. Thus, as the telescope is designed to magnify the beam waist instead of reducing it, the telescope's constituent lenses have to be curved vertically. The required waist ratio resulting from the *MATHEMATICA* simulation is obtained by choosing a magnification factor of four.

Generally, the most important selection criterion for appropriate lenses is aberration. In order to minimize this effect, particularly spherical aberration in case of monochromatic beams, it is advisable to use focal lengths $|f|$ as large as experimentally feasible[15].

To comply with this while keeping the setup as compact as possible, lenses with $f = -50\,\mathrm{mm}$ and $f = 200\,\mathrm{mm}$ shall be used.

For the sake of stability, the fibre out-coupler as well as the cylindrical telescope are mounted as low as possible, namely on posts such that the beam height is $50\,\mathrm{mm}$. Afterwards the periscope consisting of two mirrors tilted by $45\,^\circ$ is used to elevate the beam to a height of $125\,\mathrm{mm}$ which is required for the experiment.

Finally, by using a polarizing beamsplitter (PBS) cube , the dimple beam is introduced to the experiment via the same optical path that is already used for the horizontal imaging. This step forces the beam to be s-polarized[16], which means vertical polarization for the orientation of the PBS here, because only then maximum reflection of the beam can be achieved.

2.3.4 Combined Optical Setup for Imaging and Dimple Beam

The experiment setup allows for monitoring the shape of the MOT and the cloud in the ODT in both the horizontal and vertical direction by performing the absorption imaging technique [42]. Therefore, light at a wavelength of $780.247\,\mathrm{nm}$ which is resonant with the transition from the ground to the intermediate state as shown in the level structure in 2.1 is sent through the cloud and detected on the opposite side.

If this optical detection setup shall now be additionally employed to insert the dimple beam into the experiment the performance of either application might be impaired. Since the dimple beam features another wavelength than the imaging, chromatic aberration could be induced by the optical device that is used for both purposes, focussing the dimple beam and collimating the imaging light coming from the experiment. This has to be kept in mind later on for the experimental alignment of the dimple. If the optical components are optimized for imaging, the focus of the dimple beam can be expected to be located slightly behind the center of the atomic cloud. This necessitates to compromise about maximized imaging resolution and best dimple performance.

For experiments which have been performed chronologically before this thesis has been started, the detection setup of the imaging optics solely consisted of one single plano-convex lens with $f = 100\,\mathrm{mm}$ placed directly behind the chamber as illustrated in figure 2.6.

Instead of changing the position of this lens other optical components in the dimple light path such as the position of the out-coupler or the telescope lenses could be adjusted to

---

[15] Additionally, when using lenses with only one curved surface, spherical aberration can easily be reduced by always placing the lens into the beam such that its curved side faces the more collimated beam. Then the beam will be diffracted twice which minimizes optical defects.

[16] This is due to this particular beamsplitter which separates s- and p-polarization by reflecting the s-component. Originally it is designed to be used for beam transmission so that the extinction ratio in this direction is enhanced by a factor of 1000 compared to reflection path.

FIGURE 2.6: *Schematic of the former optical setup for horizontal absorption imaging. While integrating the dimple beam into the experiment the previously used spherical $f = 100$ mm lens was replaced by the objective and a polarizing beamsplitter was inserted which allows for using the optical path for both the dimple beam and imaging (compare figure 2.5).*

circumvent chromatic aberration. This would imply that the dimple beam is not perfectly collimated but rather slightly diverging when striking the final focussing lens which might enable that the foci of the imaging as well as the one of the dimple beam will coincide exactly at the centre of the cloud. However, the disadvantage of this method is that an uncollimated beam results in a smaller Rayleigh range z_R or depth of focus respectively. As the width $w(z)$ of a Gaussian beam depends on z_R (according to equation (1.16)) this might, in turn, lead to a modification of the dimpled ODT in z-direction which is not desired here.

Modification of Focussing Optics

Additionally, it has already been proposed in an earlier thesis to replace the single lens by an objective consisting of two lenses [39]. As discussed there, this objective was designed to enable high-resolution imaging which could provide the opportunity for Rydberg state tomography. Furthermore, the objective is infinity-corrected which means that it will collimate an incoming focussed beam or, vice versa, focus a collimated one. This finally allows the image-forming optics, that is responsible for focussing the collimated beam into a detection device such as the *pco.pixelfly* CCD-camera in the present setup, to be selected separately. Such an high-resolution imaging setup suits various applications independent of the particular experimental in-vacuum system [43]–[45].

The lenses which constitute this objective have already been assembled in the required configuration, though, it has never been employed in the experiment yet.

Now, that the optical setup near the experiment anyway has to be modified in order to realize the dimpled ODT, it makes sense to simultaneously integrate the objective.

As a convenient side effect, the use of the objective might also defuse the aberration issues mentioned before since it was also designed with the aim of inducing a minimum of image defects [43]. To which extent this can be achieved in the particular experimental implementation within this thesis will be analyzed in section 2.4.3.

Setup of the Objective

As schematically illustrated in figure 2.7, the objective comprises two lenses, namely one aspheric lens[17] with numerical aperture $NA = 0.240$, focal length $f = 100$ mm and thickness $d_1 = 10.0$ mm and one meniscus lens[18] with $f = 300$ mm and $d_2 = 5.1$ mm).

The first lens was chosen to be aspherically shaped in order to minimize aberrations induced by the glass wall of the experiment chamber [43]. The second lens is then used to reduce

---

[17] Type: *Thorlabs*, AL50100-B
[18] Type: *Thorlabs*, LE1985-B
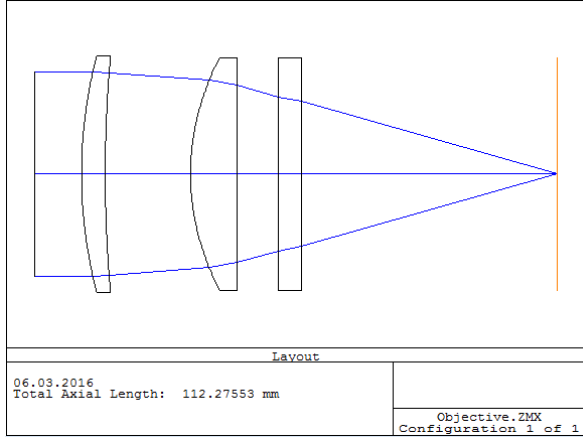
FIGURE 2.7: *Schematic of the lens configuration of the objective.* By means of Zemax the lens configuration of the objective was optimized for focussing the collimated dimple beam onto the cloud of atoms at a distance of $54.9\,\mathrm{mm}$ behind the glass wall of the experiment chamber which is represented by the flat plate between lenses and focus. The drawing shows the optimized configuration for the final dimple wavelength of $855.2\,\mathrm{nm}$.

the effective focal length of the objective. In the following analysis of the objective for the purpose of the combined use for the dimple beam and imaging, the positions of the "inner" surface (which means facing the experiment) of the lenses relative to the "outer" surface of the corresponding precedent one are indicated by the parameters x_i:

- x_0 is the distance of the inner side of the glass chamber with respect to the focal position of the particular beam which ideally should coincide with the centre of the atomic cloud.

- x_1 represents the position of the plane surface of the aspheric lens relative to the outer side of the chamber.

- Finally, x_2 identifies the distance between the inner surface of the meniscus lens and the convex side of the aspheric one.

The optical axis of the whole assembly corresponds to the x-direction.

Resolution of the Objective

The most important property of the objective that determines its diffraction-limited resolution is the numerical numerical aperture NA of its constituent parts. According to the Abbe diffraction limit the resolution of the objective in terms of the smallest resolvable distance R in a medium with refractive index n is given by

$$R = \frac{\lambda}{2NA} = \frac{\lambda}{2n\sin\left(\frac{D}{2f}\right)} \tag{2.3}$$

where $NA = n \cdot \sin\theta_{NA}$ is the numerical aperture of the front lens [46], [47]. In case of lenses the numerical aperture NA or respectively the angle of aperture θ_{NA} is given by $\theta_{NA} = D/(2f)$ where f denotes the lenses' focal length and D is their diameter. In a system comprising several lenses D and f are the characteristics of the first lens which is struck by the light. For the objective considered here, the lenses were chosen to exhibit diameters of $2''$ in order to provide for maximized aperture.

However, it should be pointed out that in the existing experiment setup the amount of light captured by the objective is not necessarily limited by the lens diameters. In fact, light coming from the experiment or, respectively, propagating towards the atoms is clipped at the front edge of the electric field control setup which is shown in figure 2.8.

26

Thus, when using lenses with large diameter of $D = 2''$ the resolution is in fact limited by this clipping effect. Since the vertical distance between the edges is $h = 20\,\mathrm{mm}$ and the atomic cloud is horizontally located at a distance of $l = 35\,\mathrm{mm}$ relative to the front of the field control, the aperture angle amounts to $\theta_{NA} = \arctan\left(h/(2l)\right) = 15.95\,^\circ$. For absorption imaging with $\lambda_{imag} = 780.284\,\mathrm{nm}$ this yields a resolution of $R = 1.42\,\mu\mathrm{m}$. This value is considerably smaller than the Rydberg blockade radius making the objective usable for monitoring single Rydberg atoms.
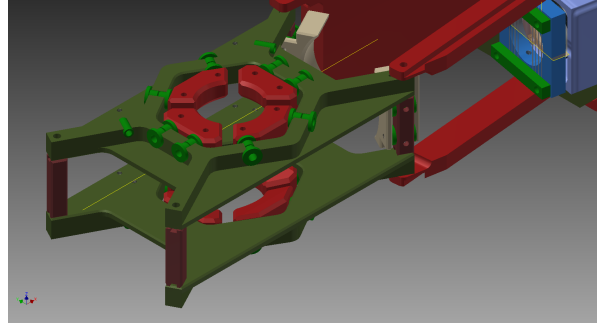
**FIGURE 2.8: Autodesk Inventor *drawing of electric field control setup.* ** *The aperture angle of the imaging light beam arriving at the objective is limited by the setup due to clipping at its front edge (on the left in the illustration).*

2.4 *Zemax* Analysis of Optical Setup

When the objective was designed it was characterized and optimized for performing high-resolution imaging. However, now that it is no longer dedicated to solely this purpose, it shall be redesigned in such a way as to enable both resolution at highest possible resolution and proper alignment of the dimple beam so that the focal positions coincide at the centre of the atomic cloud. This redesign including necessary calculations has been carried out by means of the optical design software *Zemax*. This software was afterwards also used in order to characterize and systematically analyze the optical performance of the objective for both wavelengths as described next.

The results of this analysis are also intended to provide numbers for the case that the objective or its position and alignment will be modified again at any time in the future.

2.4.1 *Zemax* - Scope of Operation

Among other functions, *Zemax* is designed to optimize specific lens configurations in terms of aberration using light at wavelengths that are defined by the user. This optimization is computed by varying the relative lens positions.

Additionally, *Zemax* delivers various technical properties of the resulting optical system such as the effective focal length or the refraction limit of the lens configuration in terms of the radius of the Airy disk [48] a parameter that quantifies the Rayleigh criterion [49]. Furthermore, it also calculates parameters which characterize the optical performance. Therefore, either the final root mean square (RMS) spot radius or the RMS wavefront can be defined as the preferred parameter for optimization.

2.4.2 Optimization Method

For analyzing the objective, the RMS spot radius was used as appraisal criterion (called "Default Merit Function" in *Zemax*[19]) next to minimizing aberration. In doing so, it was paid

---

[19] *Zemax*: Button "MFE" → Flag "Tools" → Section "Optimization Function and Reference" → Settings: "RMS", "Spot Radius", "Centroid"

special attention to a final setup being only limited by refraction, that means possessing a spot radius r_{RMS} smaller than the Airy disk radius r_{Airy}.

As mentioned, *Zemax* mainly uses the relative position of the lenses during the optimization procedure by means of the "Damped Least Squares" algorithm. However, the user has the choice to set these distances either variable or fixed so that they will either be used for optimization or not. All free parameters are then varied until the optimization criterion is satisfied at its best.

2.4.3   Results

In the proposal for the objective an additional glass plate with a thickness of $d_0 = 5.0$ mm is used to represent the wall of the glass chamber [39] in order to account for its inherent property of causing spherical aberration. In order to properly characterize and analyze the complete optical setup this glass plate is used again here.

In the chronological course of events of this thesis, the final dimple beam wavelength of $\lambda = 855.2$ nm was not considered for first *Zemax* calculations. This is because at that time it was planned to employ the *Thorlabs* laser diode as the dimple light source, so that *Zemax* investigations were carried out by only accounting for the imaging and the laser diode's wavelengths of $\lambda_{imag} = 780.284$ nm and $\lambda_{LD} = 823.6$ nm. For the final realization of the dimpled ODT using the *Toptica* diode laser system, the *Zemax* analysis has been performed in the same way again, but then for $\lambda_{dODT} = 855.2$ nm. For this reason, the following discussion comprises all three wavelengths. With the previous knowledge of the final implementation, the proposed optical configuration is of course optimized for $\lambda_{dODT} = 855.2$ nm.

For all calculations an aperture value of 44.075 mm has been chosen for an aperture of type "Entrance Pupil Diameter"[20]. This value corresponds to the aperture angle which has been evaluated above.

> *Strictly speaking the use of this aperture angle is only correct for the objective's purpose of detecting imaging light, where it is employed to capture the light coming from the experiment. Only this light beam, which strikes the objective at the front, is the one which is clipped. However, for all applications where the objective is used to modify light that is incident at its back side such as for the dimple beam, the aperture value should in fact be set to the respective value of the incoming beam for the purpose of analyzing the objective. As these beams are propagating towards the experiment they cannot be clipped at the field control before transmission of the objective.*
>
> *Though, the results of the following* Zemax *analysis reveal that the effect of the aperture value on the beam parameters is in fact very small so that they can be neglected for further calculations. Therefore, the assumption of equal aperture values seems to be justified for all applications of the objective.*

In the following analysis several aspects are investigated, not only chromatic aberration for example, but also characteristics such as the effective focal length or how sensitive the optical performance is regarding alignment errors. Finally, based on these results, the optimized positioning of the lenses which is best suited for both purposes is worked out as a revision of the assembly formerly recommended in [39].

---

[20] *Zemax*: Button "Gen" → Tab "Aperture" → Settings: "Aperture Type"="Entrance Pupil Diameter", "Aperture Value"=44.075

Rayleigh Range

First of all the Rayleigh range z_R is calculated for the imaging light at $\lambda_{imag} = 780\,\text{nm}$ in order to obtain a reference which the resulting values of the chromatic aberration can later be compared to. In the case of the objective, this characteristic quantity of a Gaussian beam can also be used to evaluate how the resolution changes along the optical axis around the focus.

Therefore, an expression for the relationship between the resolution R and the Rayleigh range z_R has to be derived starting from the expression $z_R = \pi w_0^2/\lambda$ which by using equations (1.16) and (1.18) yields $z_R = \pi/\lambda \cdot z_R^2 \cdot \tan^2\theta$ Solving this relation for z_R results in $z_R = \frac{\lambda}{\pi \tan^2\theta}$. Supposed the Gaussian beam stretches out over the complete objective aperture angle θ_{NA}, θ_{NA} and the beam divergence θ can be equalized. Furthermore, pursuant to equation (2.3), θ_{NA} is connected to the resolution R via $\theta_{NA} = \arcsin\left(\frac{\lambda}{2nR}\right)$. Finally this yields the following expression for the Rayleigh range in terms of the resolution:

$$z_R = \frac{\lambda}{\pi \tan^2\left(\arcsin\left(\frac{\lambda}{2nR}\right)\right)} \tag{2.4}$$

Using the resolution $R = 1.420\,\mu\text{m}$ calculated above, the Rayleigh range for imaging by means of the objective amounts to $z_R = 3.041\,\mu\text{m}$ and respectively the corresponding depth of focus is $2z_R = 6.082\,\mu\text{m}$.

This is a rough estimation for the precision which the positioning of the optical components building up the objective is required to comply with. Only if the focal position is within this range, high resolution can be guaranteed.

Chromatic Aberration

Next, for investigating the setup concerning chromatic aberration, the lens configuration is optimized separately for the different wavelengths.

For the two dimple beam wavelengths the distance between the inner surface of the glass chamber and the cloud is set fixed to $x_0^{(fixed)} = 54.9\,\text{mm}$ because their focal position should be exactly at the centre $x = 0$ of the cloud whose position cannot be shifted easily. The two remaining distances x_1 and x_2 are used as variables. Running the optimization yields values listed in table 2.3.

Wavelength	$x_0^{(fixed)}$ [mm]	$x_1^{(opt)}$ [mm]	$x_2^{(opt)}$ [mm]	r_{RMS}	r_{Airy}
λ_{LD}	*54.9*	**8.879**	**17.924**	$1.268\,\mu\text{m}$	$1.833\,\mu\text{m}$
λ_{dODT}	*54.9*	**8.933**	**18.343**	$1.256\,\mu\text{m}$	$1.909\,\mu\text{m}$

TABLE 2.3: ***Zemax optimization results for investigation of chromatic aberration.*** *The objective's lens configuration was optimized for both dimple beam wavelengths. In addition to the optimized relative distances $x_{1/2}^{(opt)}$ between the components the resulting RMS- and Airy disk radii r_{RMS} and r_{Airy} are listed in the last two columns.*
Whereas values of fixed variables (denoted by (fixed)) are italicized, those ones resulting from optimization (opt) are bold.

Now, for both λ_{LD} and λ_{dODT} chromatic aberration can be calculated separately with respect to the imaging light in the following way: First, x_1 and x_2 were fixed to the optimal values obtained for the dimple beam wavelength which the imaging shall be compared to. The

lens configuration is then optimized for the imaging wavelength $\lambda_{imag} = 780.284\,\text{nm}$ by using x_0 as the only variable. After executing the algorithm, the difference between the optimal value $x_0^{(opt,780)}$ and the fixed value of $x_0^{(fixed)} = 54.9\,\text{mm}$ for the dimple beam is used to quantify chromatic aberration in terms of $\Delta x^{(\lambda)} \equiv \left| x_0^{(fixed)} - x_0^{(opt,\lambda)} \right|$. This approach is justified for the case of optimizing the objective for the dimple beam at either $823.6\,\text{nm}$ or $855.2\,\text{nm}$ and using exactly this configuration additionally for detection of the imaging light. The resulting values for chromatic aberration are listed in 2.4.

Case	$x_0^{(opt,780)}$ [mm]	$x_1^{(fixed)}$ [mm]	$x_2^{(fixed)}$ [mm]	$\Delta x^{(\lambda)}$
λ_{imag} vs. λ_{LD}	**54.778**	*8.879*	*17.924*	$122\,\mu\text{m}$
λ_{imag} vs. λ_{dODT}	**54.694**	*8.933*	*18.343*	$206\,\mu\text{m}$

TABLE 2.4: *Zemax optimization results for investigation of chromatic aberration. Chromatic aberration induced by the dual-used objective is quantified in terms of the deviation of the focal positions of the imaging and respective dimple beam yielding $\Delta x^{(\lambda)}$. In both cases, which only differ in the dimple beam wavelength, the lenses have therefore been fixed to the optimized values for the use with the dimple beam (see 2.4). The only variable used for subsequent optimization (opt) of imaging (λ_{imag}) is the distance x_0 between the experiment chamber and the focus.*

Changes in the imaging performance can now be analyzed by comparing these results to the corresponding Rayleigh range which was calculated previously.

Evidently, the deviation $\Delta x^{(\lambda)}$ of the focal position of the imaging light, especially $\Delta x^{(855.2)}$, is far beyond the Rayleigh range and depth of focus, namely by two orders of magnitude. This means, that despite using the objective the chromatic aberration is still considerably high. From these findings it definitely has to be concluded that the objective should not be aligned with respect to only one of its tasks such as perfect dimple beam alignment. Rather, a compromise should be made between high resolution and an ideal profile of the dimpled ODT.

Since Rydberg imaging is less important than a reliable dipole potential for experiments performed within this thesis the weighting shall certainly be in favour of the dimple beam. As soon as resolution becomes essential, the objective can then be realigned.

Effect of Alignment Errors

In the next step it will be analyzed how sensitive the dimple beam is towards slight variations from the calculated configuration. Therefore, the effect of errors in the misalignment of the lenses on the beam characteristics is studied by considering both the *relative* lens positions x_2 as well as the objective's *absolute* position in terms of the distance x_1 to the glass chamber.

x_0 is again set to the fixed value due to its immovable nature in the experimental setup. Additionally, with the previous knowledge of the final realization, this analysis is conducted for the wavelength $\lambda_{dODT} = 855.2\,\text{nm}$ as only this is relevant regarding later measurements.

The procedure then looks as follows: First, in order to examine the effect of variations[21] δx_2 in the relative lens positions, x_1 was fixed to the optimum value. Respectively, the same is done vice versa for studying effects of δx_1 next. Changes of the resulting RMS spot radius

---

[21] Please note that lowercase deltas δ are used for errors in the causing variable and capital ones Δ for the variables that are affected by them. All deltas denote the difference of the particular quantity y with respect to its corresponding optimized value in case of perfect alignment which means $(\delta$ or $\Delta)y = y^{(err)} - y^{(opt)}$.

in units of the Airy disk radius $\Delta\left(\frac{r_{RMS}}{r_{Airy}}\right)$ are used in both cases as a criterion to evaluate the effects of misalignment. Additionally, the deviation Δx_i of the respective unfixed distance with respect to its optimum value is calculated. For every error value δx_1 (or δx_2) the *Zemax* optimization procedure is computed while using x_2 (or x_1 respectively) as the only variable.

Results of the optimization protocol and effects of the according misalignment are specified in tables 2.5 and 2.6, both in absolute (penultimate column of each table) and in relative numbers (last column).

For studying the effect of the relative as well absolute misalignment of the lens configuration, the according quantities x_1 and x_2 are varied by $\delta x_i = \pm 5\,\%$ (first column) which corresponds to absolute deviations on the order of tenth of millimeters for δx_1 (compare italic typed values in 2nd column to first value) and roughly one order of magnitude bigger for δx_2 (compare italic typed values in 3rd column to first value). These deviations seem to be reasonable since the lenses are mounted within a tube, which makes it pretty hard to exactly adjust the lens positions. Furthermore, it is challenging to perfectly position the objective with respect to the glass chamber on the sub-millimeter scale. Additionally, it cannot be fully guaranteed that the distance between the atomic cloud and the glass chamber might slightly vary from the assumed value.

Alignment	$x_0^{(fixed)}$ [mm]	x_1 [mm]	x_2 [mm]	$\|\Delta x_i\|$ [mm]	$\left\|\Delta x_i / x_i^{(opt)}\right\|$
Perfect	*54.9*	**8.933**	**18.343**	—	—
$x_1 = 0.95 \cdot x_1^{(opt)}$	*54.9*	*8.486*	**24.316**	**5.973**	**32.56** %
$x_1 = 1.05 \cdot x_1^{(opt)}$	*54.9*	*9.380*	**12.174**	**6.169**	**33.63** %
$x_2 = 0.95 \cdot x_2^{(opt)}$	*54.9*	**9.000**	*17.426*	**0.067**	**0.75** %
$x_2 = 1.05 \cdot x_2^{(opt)}$	*54.9*	**8.865**	*19.260*	**0.068**	**0.76** %

TABLE 2.5: ***Zemax optimization results for investigating the influence of alignment errors on the objective's optical performance.*** *The lens configuration was optimized using dimple light at* 855.2 nm *for various different cases:* ***First row:*** *Lens assembly is optimized by setting both relative lens distances $x_{1/2}$ variable (= perfect case).* ***Row 2 and 3:*** *Results of optimization procedure for 5% deviation of absolute position x_1 of the objective from the optimal value given in the first row. To this end x_1 was fixed to the faulty value and only x_2 was optimized in this defective configuration. $\|\Delta x_2\|$ (4th column) then numbers the deviation of x_2 compared to the perfect case. For such a wrong absolute alignment (x_1) the relative lens position x_2 differs by about 33% (compare values for $\|\Delta x_2 / x_2^{(opt)}\|$ in last column) with respect to the perfect case.* ***Row 4 and 5:*** *The same procedure has been conducted for 5% misalignment of the relative distance x_2 between the lenses which is therefore fixed to the respective faulty value. Optimization was then conducted using x_1. Obviously, relative lens misalignment does not influence optimized configuration equally severely as errors of the absolute position (compare values in last column) do.*
Again values of fixed variables (denoted by (fixed)) are italicized, those ones resulting from optimization (opt) are bold. x_0 is always fixed to the real value in the experiment.

The results listed in table 2.5 provide information about the sensitivity of the focal position of the dimple beam to errors of the lens configuration. The relative numbers in the last column reveal that it is of particular importance to position the whole objective as perfect as possible.

Alignment	r_{RMS}	r_{Airy}	$\left\lvert \Delta\left(\frac{r_{RMS}}{r_{Airy}}\right)\right\rvert$	$\left\lvert\frac{\Delta\left(r_{RMS}/r_{Airy}\right)}{\left(r_{RMS}/r_{Airy}\right)^{(opt)}}\right\rvert$
Perfect	1.256 µm	1.909 µm	—	—
$x_1 = 0.95 \cdot x_1^{(opt)}$	2.867 µm	1.939 µm	0.821 µm	124.73 %
$x_1 = 1.05 \cdot x_1^{(opt)}$	1.710 µm	1.879 µm	0.252 µm	38.32 %
$x_2 = 0.95 \cdot x_2^{(opt)}$	1.110 µm	1.904 µm	0.075 µm	11.39 %
$x_2 = 1.05 \cdot x_2^{(opt)}$	1.453 µm	1.913 µm	0.102 µm	15.44 %

TABLE 2.6: *Zemax optimization results for investigating the influence of alignment errors on the objective's optical performance.* *The first two columns comprise resulting values of the RMS- and the Airy disk radius for all five cases described in the caption of the previous table 2.5. Effects on the objective's optical performance in the defective configurations are quantified by the deviation of the respective ratio r_{RMS}/r_{Airy} from the perfect ratio $(r_{RMS}/r_{Airy})^{(opt)}$ which is given by the values in the first row. Both the absolute (3rd column) deviations $|\Delta(r_{RMS}/r_{Airy})| = |(r_{RMS}/r_{Airy}) - (r_{RMS}/r_{Airy})^{(opt)}|$ and the relative (4th column) ones are listed.*

Obviously, for misalignment of 5% the relative distance x_2 between the lenses would have to be modified by about 33% in order to restore optimized performance. Misalignment of x_2 as well by 5%, however, does not have these tremendous effects. Then the objective's absolute position x_1 would only have to be adjusted by less than 1% in order to optimize the optical performance again.

These findings are confirmed by the results listed in the lower table 2.6. The values in the last two rows are a measure for misalignment effects on the spot radius in units of the Airy disk radius. Obviously, these results for impairment of the radial beam characteristics as well suggest that the objective's optical performance is very susceptible to the absolute positioning of the objective.

Finally, it can be concluded that lens alignment highly influences the optical performance, namely in such a way that not only the focal position is shifted along the optical axis but also its waist is increased finally resulting in spot radii that exceed the diffraction limit specified by the Airy disk radius.

Focal Length

As a last aspect, the effective (EFL) and the back focal length (BFL) of this objective are calculated, again with the help of *Zemax*[22] which delivers values of $EFL = 80.03$ mm and $BFL = 54.88$ mm in the case of perfect alignment. Thus, the choice of lenses made for the objective significantly reduces the system's focal length compared to the previous optical setup, which consisted only of the single plano-convex lens with $f = 100$ mm for detecting the imaging light. This in turn means that the angle of aperture is larger now which enables to capture a higher amount of imaging light.

However, even though a smaller focal length allows for saving space, the setup of the objective is definitely larger than before, such that effectively more space is needed.

---

[22] *Zemax*: Flag "Reports" → Option "System Data" → "Effective Focal Length" and "Back Focal Length"

2.4.4 Conclusion

Finally, based on the outcomes presented and discussed above, the following alignment of the objective and its constituent lenses is recommendable:

Since the main focus for the setup of upcoming experiments lies on the modification of the crossed ODT towards a dimpled one and since chromatic aberration turns out to not being negligible, the lenses should be positioned pursuant to 2.3 such that they introduce the dimple beam into the experiment in an optimized way. However, most likely this will strongly deteriorate the objective's feature of high resolution imaging. For measurements in the scope of this thesis, though, this property is not of vital importance. Effects of the dimple on the shape of the atomic cloud in the ODT anyway have to be monitored by means of vertical imaging. For the purpose of observing the cloud shape in the y-z-plane via horizontal imaging, the objective's resolution should still be sufficient. As soon as high-resolution imaging in horizontal direction will become of higher interest as well, the objective's position can then be readjusted by taking into account all results presented before.

By the way, this proposed lens arrangement significantly differs from the one initially suggested in [39]. This is due to the fact that there the distance between the glass chamber to the atomic cloud was neither fixed nor set to the correct value. For the analysis here, though, this value was fixed and adapted to the one measured in the current experiment setup.

It should be noted, that another type of aberration that has not been examined above is astigmatism. This monochromatic effect can always be induced by a specific optical component if one or more previous optical elements are misaligned in such a way that the beam strikes this subsequent optical component under a specific angle of inclination with respect to the optical axis. If the beam is then composed of two or more components oriented along different radial directions, the foci will no longer coincide. Consequently, astigmatism will result in blurred images.

Of course, the same effect arises if the optical components are tilted relative to the propagation direction of the beam.

As astigmatism is a common effect induced by misalignment of basically all optical parts and since it is not inherent to special setups but can rather occur in every complex optical assembly, it is not investigated further in the context of this objective. The system set up in the context of this thesis is actually not more susceptible to astigmatism than any other arrangement.

Exactly the same is true for the aberration phenomena called coma. This effect describes divergency of the focus due to radial shifts which result from an incident monochromatic and collimated beam which does not strike the optical system perfectly parallel to its optical axis.

Furthermore, spherical aberration was as well not investigated since this kind of aberration is also inherent to every optical system. Anyway, spherical aberration will more strongly be determined by beam characteristics such as the diameter of the collimated beam than by the optical system. Reducing spherical aberration by means of the optics would necessitate the use of lenses with aspherical surface. However, in most cases this is not reasonable bearing in mind their much higher prices.

Chapter 3

First Approach
Using Thorlabs Laser Diode

Based on the design and related calculations presented in the previous chapter, subsequently, the actual practical implementation of the dimpled optical dipole trap as an extension of the existing setup will be outlined. In order to adhere to the overall structure of describing the course of events of this thesis, the two approaches which have been made for producing the dimple laser beam are described separately. Therefore, this chapter covers practical tasks related to the first laser source that has been used, namely the standard Thorlabs *laser diode.*

The chapter starts with an outline of the diode's specified characteristics which is directly followed by the description of setting up required optics and an intensity stabilization circuit for the laser beam. Afterwards, all steps related to the characterization of the beam such as the inspection of its mode structure and according measurements are presented and discussed in-depth. Based on these results, the chapter is closed by presenting attempts for improvement of the diode's

FIGURE 3.1: *Picture of the used* Thorlabs *laser diode. (taken from [40])*

performance and a final conclusion which resulted in the abandonment of this approach. Reasons for this decision will be discussed in detail there.

The adjacent chapter 4 will then comprise the final and successful realization of the dimpled trap.

This chapter 3 mainly contains very technical and elaborate explanations of the practical course of action. By sometimes actually mentioning every nut, bolt and screw these descriptions are also supposed to provide an instruction which affords the reader to reproduce the setup and perform related measurements in exactly the same way.

As already mentioned before, initially it was planned to employ a simple *Thorlabs* laser diode to serve as the light source for the dimple beam. This decision was made based on the *MATHEMATICA* simulations of the optical dipole potential. According to the diode's specifications it was in principle approved to be well suited and to fully comply with the requirements deduced from these calculations.

However, after having characterized the beam, especially concerning the mode structure and its stability, this plan for realizing the dimpled ODT was abandoned. Thus, the diode itself was only pursued up to the step of finally applying the beam to the experiment. Though, as the third segment of the optical setup between the fibre and the experiment chamber is basically independent of the light used source, the respective assembly could be used as well for the second light source. That is why this optical setup is described in this chapter whereas

the next chapter only briefly sketches the specific pre-fibre optics required for modifying the output beam of the *Toptica* diode laser before being coupled into the fibre.

3.1 Laser Diode Specifications

The selected laser diode[23] which is shown above was bought from *Thorlabs* and according to its data sheet [40] it is supposed to operate in single transverse mode and emit light at 824 nm. According to *Optomark*, one of *Oclaro*'s distributors, this type of laser diode is originally manufactured by *II-VI LASER ENTERPRISE* in vertical-cavity surface-emitting laser (VCSEL) structure [50]. These types of laser diodes feature perpendicular laser beam emission from the surface instead of edge-emission as it is common for conventional semiconductor laser diodes. Pursuant to the data sheet the laser diode is supposed to show both lateral as well as transverse single-mode characteristics [40].

> *Unfortunately, it can soon become confusing when it comes to the meaning of the identification of the mode directions. Generally, in optical semiconductor devices the term longitudinal is used for the direction of light emission [51]–[53]. On the other hand, the transverse direction always denotes the plane which is perpendicular to the longitudinal axis. Consequentially, in free isotropic space the field's transverse electric (TE) and transverse magnetic (TM) modes span this plane [51], [54], [55]. Normally, the transverse plane is in turn subdivided into vertical and lateral transverse directions with the vertical one being perpendicular to the active layer of the semiconductor device and the lateral one being parallel to it [56], [57].*
>
> *Usually, laser diodes lase in TE mode since the threshold gain is smaller for TE than for TM modes. Then, the vertical transverse direction is conventionally used to denote the TM mode and the lateral one for the TE mode [57].*
>
> *For standard edge-emitting laser (EEL) this is a consistent way of identifying all three orthogonal spatial directions. However, for VCSELs, which are surface-emitting, this terminology becomes contradictory because it implicates that the vertical transverse direction is both parallel as well as perpendicular to the longitudinal emission direction. This is because on the one hand vertical means perpendicular to the active layer but transverse in turn always has to be orthogonal to the longitudinal direction. In order to resolve this conflict, in the context of VSCELs the following notation can regularly be found: The term transverse still denotes a direction being perpendicular to the longitudinal axis which is still the direction of light emission [54], [55]. The same is true for the lateral one [58], [59].*
>
> *Thus, the difference to the case of EEL is that the term vertical is abandoned and transverse is declared to be the direction that is orthogonal to the lateral one. Thus, transverse is downgraded from denoting a plane to just indicating one axis [60] which is not perpendicular to the active layer anymore.*

Finally, to cut a long story short, the main conclusions to bear in mind in context of the laser diode used here are, that

- the wavelength λ can be used to identify the longitudinal modes and that

---

[23] Type: *Oclaro*, SM830-200-TO56-R0x

- the intensity profile in terms of the TEM_{mn} is determined by the transverse and the lateral laser diode modes [53], [54].

Thus, translated to the particular case here, the laser diode was supposed to only show one single TEM mode. However, literature research also reveals the following:

Generally, cavity lengths in VCSELs are very small. Therefore typically they are intrinsically single-longitudinal-mode devices [52], [55] whereas they often exhibit multiple transverse and polarization modes [55], even though transverse single-mode operation is commonly claimed [61].

Due to these dubieties, it was definitely advisable to thoroughly characterize the laser diode before implementing it, especially concerning its emission spectrum which is presented in sections 3.6 and 3.7. Not until the diode provides proof of performing satisfactorily it should finally be inserted into the experiment setup for the purpose of providing the light source for the dimple beam.

Before this beam characterization could be carried out several other steps had to be taken first. Especially, the diode had to be mounted properly and all required optical parts had to be arranged according to the design described in chapter 2. Furthermore, the diode's intensity was to be locked by means of an active stabilization loop.

3.2 Setup: Mounting

First of all, the laser diode was mounted inside a home-made distributed feedback (DFB) laser box which consists of a massive copper block that encloses both a thermistor (NTC) and a Peltier element for active cooling. A transparent box made of acrylic glass is placed on top in order to insulate all parts inside especially the diode itself from any thermal and electric contact. The diode is placed inside a tube which in turn is attached to the inside of one wall of the box. This tube additionally contains the socket for the diode[24] and a collimation lens with $f = 4.51\,\text{mm}$ and $NA = 0.55$. The electric currents which are applied to both the diode and the Peltier element are delivered to the box by means of a 15-pin D-subminiature (D-sub) plug at its back which is also used to read out the resistance of the thermistor.

The temperature and the current applied to the laser diode are actively controlled by a *Thorlabs* OEM laser driver that includes both a temperature and a laser current controller and is connected to the box via the D-sub cable.

3.3 Setup: Optics

In order to test and characterize the diode's performance under similar conditions as they will be given in the experiment, all optics which might modify either the beam profile itself or features such as the intensity or the mode characteristics, ought to be assembled in exactly the same way as it was designed previously. In order to avoid impact on measurements which have been executed on the experiment table at that time, this was done in the framework of a test setup on a separate breadboard. A drawing of the corresponding test assembly is sketched in figure 3.2. The constituent parts are described in the following subsections, split up into two

---

[24] Before inserting the diode one has to make sure that the diode is grounded in the right way. Additionally, it is recommended to ground oneself in order to prevent the diode from being shorted and damaged.

parts, the setup before and the one behind the fibre. The fibre will later serve as a means to transfer the beam between the different locations.
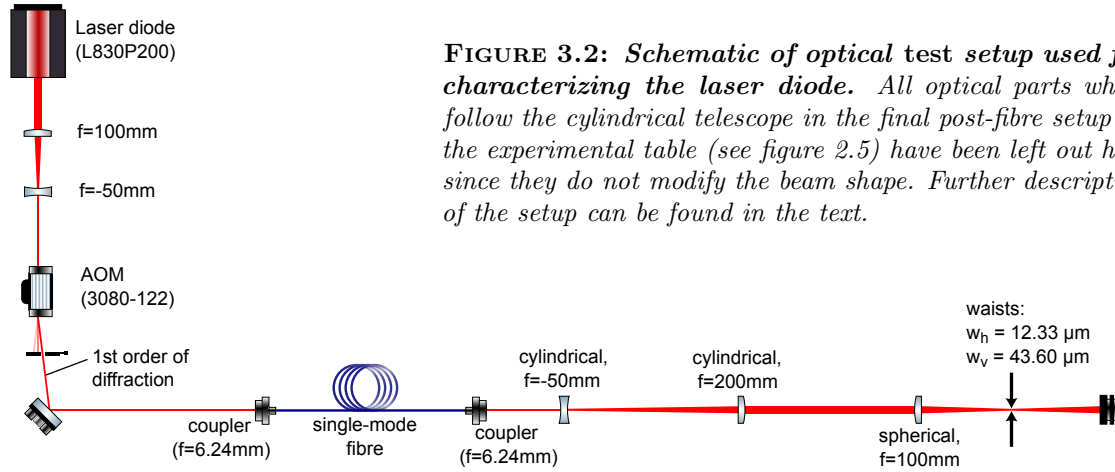
FIGURE 3.2: *Schematic of optical test setup used for characterizing the laser diode.* *All optical parts which follow the cylindrical telescope in the final post-fibre setup on the experimental table (see figure 2.5) have been left out here since they do not modify the beam shape. Further description of the setup can be found in the text.*

3.3.1 Pre-Fibre Configuration

The main purpose of the optics prior to the fibre is to provide the option for modifying the intensity of the laser beam without having to change the laser current. This is typically achieved by means of an AOM, where basically the applied RF power determines the fraction of light in the different orders of diffraction [25]. The required RF signal is provided by the AOM driver, which in turn offers two input ports, one for analog signals and one for digital ones. As the signal applied to the analog port is internally processed at lower speed than the TTL-signals at the digital port, the latter one should be preferred for switching tasks. On the other hand, analog signals ranging from $0\,\text{V}$ to $10\,\text{V}$ can be used in order to continuously adjust the optical power of the beam in the desired way.

In order to fully and efficiently couple the laser beam into the AOM its waist is scaled down by a factor of two by means of a simple spherical telescope. The AOM's first order of diffraction was then filtered out and coupled into the single-mode fibre which guides the light to the subsequent optics later found on the experiment table.

The remaining orders of diffraction were coupled into a multi-mode fibre in order to establish a permanent connection to the wavemeter.

The lens used for coupling the beam into the single-mode fibre was selected on the base of a rough beam waist measurement. Therefore, an image of the output beam's cross section, which is shown in figure 3.3, was taken directly behind the laser diode by means of a simple webcam which is totally sufficient for this purpose. An evaluation of the Gaussian beam profile using a *MATLAB* script called *BeamMaster* yields a spot radius ($1/e^2$ radius) of about $550\,\mu\text{m}$.

This picture also shows the typical elliptically shaped beam profile of laser diodes. The polarization direction of the light is normally parallel to either one of the ellipse's main axes. In the case here, the ellipticity is relatively small so that it does not have to be compensated for by means of an additional cylindrical telescope.

---

[25] For more details on AOMs refer to appendix A.

The summed cross section which is shown underneath the actual picture reveals that the beam exhibits a slightly non-Gaussian profile in horizontal direction and this even directly behind the source without any additional optics placed in between. As it will turn out later, this feature becomes even more pronounced after transmission through subsequent optical components so that it will finally prohibit certain mode characterization measurements (see section 3.7.3).

By reproducing the lens arrangement and the beam by means of the lens configurator tool called *GaussianBeam* an in-coupler lens with $f = 6.24\,\mathrm{mm}$ was found to be adequate.
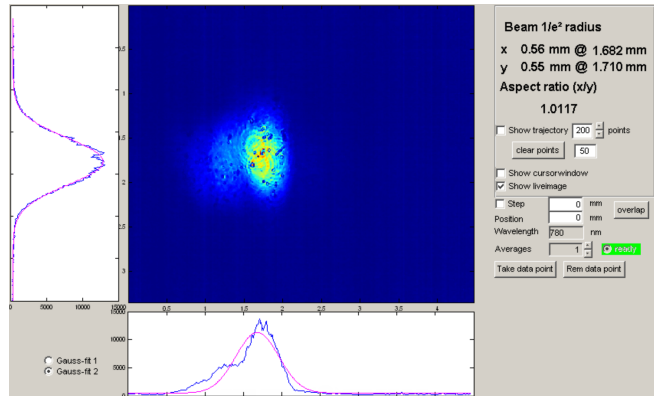
FIGURE 3.3:
Image of cross section of laser diode output beam. *The image was captured by means of a simple webcam directly behind the laser diode. $1/e^2$-radii of $550\,\mu\mathrm{m}$ and $560\,\mu\mathrm{m}$ have been evaluated for the horizontal and vertical direction respectively using a MATLAB script.*

3.3.2 Post-Fibre Configuration

Additionally, on the separate breadboard the optical components which succeed the fibre, especially the cylindrical telescope, were arranged in the way it is planned to be done on the experiment table according to the design described in section 2.3. The only difference was, that in this test setup the PBS and all mirrors including the periscope were left out since they are not expected to modify beam properties which are examined by means of the test setup. For focussing the beam a standard $f = 100\,\mathrm{mm}$ lens was used similar to the one which was part of the imaging setup so far.

After having optimized fibre coupling, the fibre output power was measured to be $90\,\mathrm{mW}$ at the maximum laser current of $I_{LD} = 200\,\mathrm{mA}$ that can be supplied by the laser driver.

At this point, it should be noted that so far no optical isolator was placed behind the laser diode as commonly recommended for these kinds of setups in order to suppress optical feedback caused by reflections at successive optical components. This has not been done because even for perfect alignment the use of an optical isolator will reduce the optical power of the transmitted laser beam, typically by about 20%[26]. Since the power measured behind the fibre is already close to the critical value for producing a considerable dimple in the ODT, for the time being, it was tried to omit the isolator. Nevertheless, most likely this will impair the diode's output performance.

3.4 Setup: Intensity Stabilization

Before the diode's mode properties have been examined, the setup of the laser was completed by locking the beam intensity using an active stabilization loop that includes the AOM driver

---

[26] This is mainly due the isolator's inherent insertion loss, which is a low loss for forward-propagating light induced by imperfections due to both fabrication and alignment. Further loss might be caused if the collimated beam behind the diode is slightly too large in diameter to fully pass the isolator.

as the regulating device. Generally, it is always recommendable to establish such an intensity lock as laser diodes can never be expected to emit radiation with an intensity that is sufficiently stable for typical applications in quantum optics.

3.4.1 Composition and Constituent Parts

For the implementation into the experiment the stabilization loop shall be established according to the scheme which is schematically illustrated in figure 3.4. The experiment chamber shown here, though, could of course not be included in the test setup.
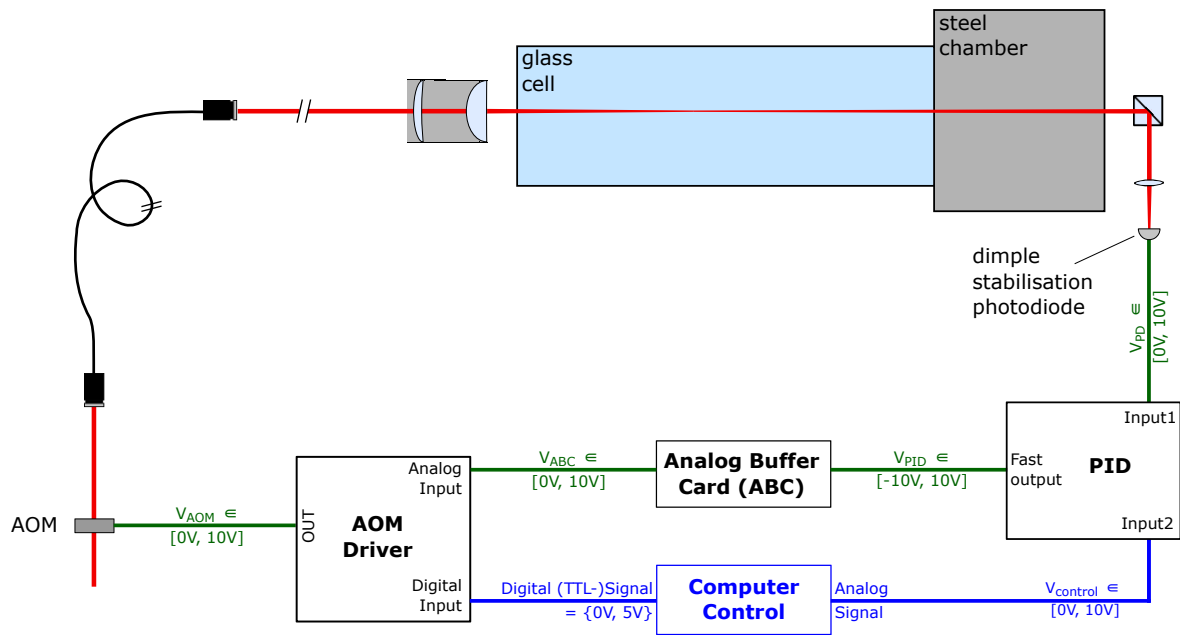
FIGURE 3.4: *Schematic of the setup for the intensity stabilization loop. The intensity of the dimple beam is actively stabilized by controlling the input voltage at the AOM via a PID. The mechanism and all related components are described in the text.*

Generally, setting up the intensity lock necessitates three additional devices, namely

- a photo diode (PD) for continuously detecting the light intensity of the beam and converting this optical signal into an electrical one. For the time being in the test setup, the PD was placed directly behind the fibre and a subsequent PBS. As the PBS splits the beam up according to its polarization, it enables to not simply take intensity but also polarization fluctuations into account. Thus, by only detecting one polarization the intensity will be locked to exactly this one.
  In the final implementation the PD will be mounted behind the experiment chamber so that the intensity will be stabilized onto the transmitted dimple laser light which, due to the PBS in front of the objective (see 2.5), will as well only be composed of one polarization component.

- Next, a proportional–integral–derivative (PID) controller, representing the loop's building block, is used to generate the feedback signal. A control voltage $V_{control}$ is applied to the PID's second input channel and required as a reference value to compare the PD's

signal to. It can be set either manually by means of a potentiometer or remotely via the computer control. Once the desired laser intensity has been identified, this second channel is the loop's interface that offers to set the circuits working value by parameterizing this intensity by the control voltage $V_{control}$. The method of determining the correct control voltage which corresponds to the desired intensity is described in the subsequent section 3.4.2.

The version of the PID used here, offers to attenuate both input signals separately by means of variable resistors. Sometimes this might be useful in order to weigh the inputs differently enabling the error function, which is basically the weighted difference between both inputs, to be tuned in the desired way. In the particular case here, however, this option was not employed, rather, both attenuation were set to one.

- Last, a so called Analog Buffer Card (ABC) is required to adapt the feedback signal to the permitted input range of the AOM driver. As the PID's output range of $V_{PID,out} = [-10\,\text{V}, 10\,\text{V}]$ does not match the AOM driver's input range of $V_{PID,out} = [0\,\text{V}, 10\,\text{V}]$ the ABC just comprises an electric circuit who fulfills the task of mapping the first range to the second[27].

The loop is finally closed via the AOM and its driver which are already implemented in the setup. By performing their task of converting electrical signals back to optical intensity they represent the devices that provide access to the experimental setup. They serve as connecting elements which apply the feedback signal back to the laser beam by adjusting the fraction of light intensity that is diffracted by the AOM into the first order.

3.4.2 Realization

Subsequently, it is explained in more detail how the lock was established and applied to this laser diode beam. Furthermore, the loop's mode of operation is described and a final characterization of its performance is presented. Before measurements could be performed the following preparatory task of identifying its working voltage had to be made:

Setting Working Voltage

The intensity stabilization loop is designed to lock the diode's output intensity to a certain value. This value has to be chosen according to the purpose of the laser beam and in some way has to be transferred to the loop and finally to the beam itself. As the AOM represents the interface between feedback generation and the laser beam, this can only be achieved by altering the AOM's performance which, in turn, is governed by its input voltage supplied by the AOM driver.

However, as sketchily mentioned above, the only port granting external access to the loop is the PID's second input ("Input2") which is internally compared to "Input1" which is the voltage measured by the PD and which corresponds to the present intensity of the beam. Thus, the desired beam intensity has to be set in the following way:

First of all, it needs to be determined which voltage V_{AOM} has to be applied to the AOM so that the resulting intensity in the first order of diffraction matches the desired intensity. In

---

[27] How well the mapping can finally be realized of course depends on the available and used electric components. More details on the ABC's circuit diagram can be found in the next subsection 3.4.2.

order to identify this voltage, the AOM's characteristic curve has to be measured. Additionally, in order to identify the full range which the intensity lock can operate on, the corresponding maximum working voltage of the AOM should as well be extracted from this curve.

Though, as the RF power in the AOM is governed by only one parameter, namely the voltage supplied by the AOM driver, it makes sense to determine the relation between the beam intensity (in terms of the voltage V_{PD} at the PD) and the input voltage $V_{AOM,Driver}$ at the driver[28]. Eventually, from this curve the required PID output voltage can be calculated by considering the transfer function of the ABC. How this PID output can finally be achieved by means of controlling the voltage at Input2 is explained later.

Thus, the first preparatory step was to measure the voltage V_{PD} at the PD as a function of the AOM driver's input voltage $V_{AOM,Driver}$. Therefore, a function generator[29] was directly connected to both an oscilloscope and the AOM driver. In this way the latter one's input voltage was scanned between $0\,\mathrm{V}$ and $10\,\mathrm{V}$ by means of a triangular signal at a frequency of $0.5\,\mathrm{Hz}$. Simultaneously, the optical power of the laser beam was measured with the help of an amplifying photo diode[30], which is connected to the second channel of the oscilloscope. Plotting the first over the second channel finally yields the sought dependence which is visualized in 3.5.
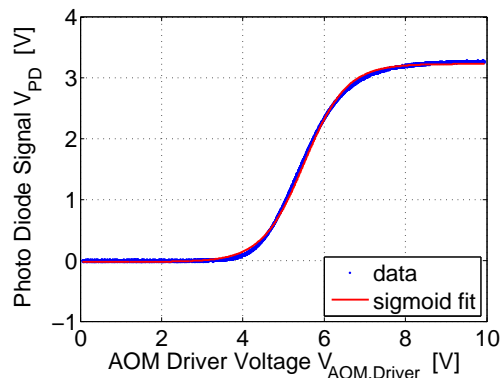
FIGURE 3.5: *Measurement of characteristic AOM curve. While scanning the AOM driver input voltage $V_{AOM,Driver}$ over the full range of $[0\,\mathrm{V}, 10\,\mathrm{V}]$ the optical power in the AOM's first order of diffraction was monitored on a photo diode. The resulting photo diode voltages V_{PD} are plotted against $V_{AOM,Driver}$. This curve can then be used to figure out the particular value of $V_{AOM,Driver}$ that corresponds to the desired optical power.*

As mentioned, for the purpose of this test setup and the characterization of the intensity lock the photo diode was placed directly behind the fibre as the beam is not expected to lose a considerable amount of power due to subsequent optical components. The calibration of the PD signal, which means to identify the scaling between optical power and detected PD-voltage, anyway has to be renewed once the whole arrangement is implemented in its final configuration into the experiment. This is due to the fact that the dimple beam power will then be measured after transmission through the glass chamber and the atomic cloud which definitely induces additional attenuation of the optical power.

Now, the required value for the AOM driver input voltage could be extracted from the AOM characteristics. Normally, prior to this, the mentioned scaling factor between optical power and the voltage that has been detected on the PD would have to be identified first. This can be accomplished by setting the laser to the desired power which it is supposed to emit and detecting the corresponding voltage at the photo diode.

However, this last step was omitted for the test setup and was was not carried out until

---

[28] This input voltage is applied to the driver via port "AnalogIn".
[29] Type: *Agilent*, 33522A (2-Channel, 30MHz Function/Arbitrary Waveform Generator)
[30] Type: *Thorlabs*, PDA10A-EC

the laser source was finally implemented[31]. For the time being, a rather arbitrary value was selected which only complied with the following requirement:

Ideally, the driver's input voltage should be chosen as to maximize the fraction of light which is deflected by the AOM into the first order of diffraction. However, it should not be *fully* maximized in order to still leave some little space for the intensity loop to regulate the voltage into both directions.

Remark about Input Impedances

At this point another technical aspect, namely the matter of input impedance, should be pointed out which emerges during the arrangement of the intensity lock and its characterization. As this is an important aspect which generally has to be kept in mind while setting up electric networks especially those operating at high frequencies, it is definitely worth to briefly delve a little bit deeper into this matter. To this end appendix B presents the basics concepts of input and output impedances and their proper matching depending on the particular purpose of the electric network.

Finally, translating the discussion there back to the particular case of measuring the photo current which is generated by the PD, it becomes clear why in fact large load input impedances of the measurement devices are desirable. Once the photo diode is connected to it, the generated photo current will drive this load impedance and the corresponding voltage drop is eventually detected and put out. Thus, the higher the input impedance the more does the measured voltage match the real output value which is displayed at the oscilloscope for instance.

This, however, implicates that the displayed voltage does not only depend on the current that has to be observed but also highly on the load's input impedance as its simple presence will manipulate the measured signal. This aspect always needs to accounted for when different devices such as a simple multimeter and an oscilloscope which exhibit unequal input impedance are employed one after another to measure the same current.

Total Bandwidth of the Circuit

However, especially if the simple application of measuring photo currents is extended complete intensity lock circuit, the case becomes considerably more complex so that a more sophisticated treatment of impedances is required. This is because now, not only voltage transfer matters but also the overall bandwidth of the loop becomes extremely important since the intensity lock's reaction time should be as short as possible. This reaction time scale τ_{loop} of the closed stabilization loop which is anti-proportionally related to its total bandwidth BW_{loop} is mainly limited by the following factors:

- The photo diode features a rise time on the order of several hundreds of nanoseconds which is defined as the time that it takes for the signal to rise from 10% to 90% of the maximum value.

- An additional delay time that is inherent to the AOM reduces the total bandwidth even further. This delay time is equal to the time that it takes for the modified sound wave to fully traverse the beam, since not until then the beam is completely diffracted. This, in turn, depends both on the speed of sound in the crystal which is a given quantity

---

[31] This calibration has been done in context of setting up the second light source and is described in section 4.1.4.

and on the diameter of the beam inside the AOM. Of course, the smaller the beam waist in the AOM, the shorter is the delay time which is typically as well on the order of few hundred nanoseconds for a beam diameter of about $500\,\mu$m. However, it is not recommended to attempt by all means to demagnify the beam diameter to reduce this delay time because the AOM's diffraction efficiency will then be deteriorated. Rather, it should be compromised between achieving high efficiency or reducing delay times.

- All other retardations induced by the speed of operation other devices or by signal transit times are very small compared to the two delay times mentioned above so that they can be neglected. Total cable lengths of several metres for example would lead to time lags of only few nanoseconds.

The total bandwidth of the circuit BW_{loop} is then composed of all individual bandwidths BW_i which correspond to these times which delay the round-trip of the signal [62]:

$$BW_{loop}^{-2} \approx \sum_i BW_i^{-2} \tag{3.1}$$

where bandwidths that result from rise $\tau_{rise,i}$ and fall times $\tau_{fall,i}$ are given by [62]

$$BW = \frac{0.76}{\tau_{rise} + \tau_{fall}} \tag{3.2}$$

As expected, these expressions implicate that the total bandwidth will be deteriorated most by the longest retardation time.

At this point again impedances come into play since the photo diode's rise time, in fact, highly depends on the actual load impedance of connected devices which is in this case the PID's input resistance.

Generally, higher bandwidths are obtained for smaller load impedances which however counteract high signal-to-noise ratios (SNR) due to a lower magnitude of the input voltage signal. Thus, here again a compromise has to made.

In case of amplifying photo diodes such as the particular one used here[32] the bandwidth shows an antiproportional dependence on the load impedance which however cannot be expressed in a simple way [63].
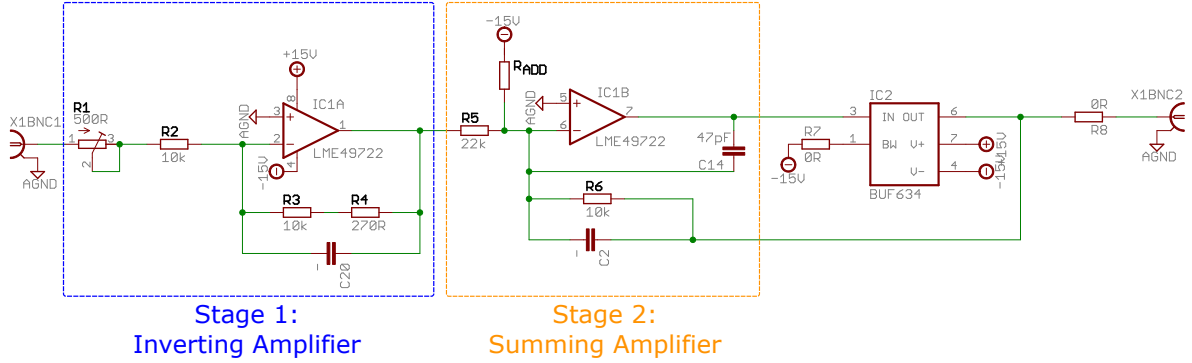
Analog Buffer Card

The last preparatory step was the modification of the Analog Buffer Card such that it maps the PID's output voltage V_{PID} correctly onto the AOM driver's input range as sketched in 3.4. Basically, this mapping f_{ABC} relates both ranges in such a way that both their minimum and, respectively, their maximum values coincide with each other. This results in a linear transfer function $V_{out}(V_{in})$ that assigns all incoming voltages $V_{in} = V_{PID}$ to defined output values $V_{out} = V_{ABC}$ according to

$$f_{ABC}: \ [-10\,\text{V}, 10\,\text{V}] \ \rightarrow \ [0\,\text{V}, 10\,\text{V}], \ \ V_{in} \ \mapsto \ V_{out}(V_{in}) = m \cdot V_{in} + b \tag{3.3}$$

Thus, the adjustment of the circuit consists of setting both the proportionality factor m and offset b by choosing appropriate values for the responsible electric components. To this end basically two stages of the circuit have to be considered as visualized in schematic 3.6:

---

[32] Type: *Thorlabs*, PDA10A-EC

FIGURE 3.6: ***Detail of the electric circuit of the Analog Buffer Card.*** *Mainly two stages are responsible for setting the desired transfer function f_{ABC}: The inverting amplifier with unity gain in the first stage only needs to be considered due to its property of inverting the voltage and for offering fine-tuning by means of the potentiometer R_1. The mapping can then be adjusted by choosing the correct additional resistance R_{add} in the second stage.*

- The first stage enclosed by the blue box simply represents an inverting amplifier with roughly unity gain $G_1 = (R_3 + R_4)/(R_1 + R_2) \in [0.98, 1.03]$ which modifies the input voltage according to $V_{out,1} = -G_1 \cdot V_{in}$.

- Next, the parts enclosed by the orange box build up a regular summing amplifier that transforms $V_{out,1}$ into

$$V_{out,2} = -R_6 \left(\frac{V_{out,1}}{R_5} - \frac{15\,\text{V}}{R_{add}} \right) \approx -10\,\text{k}\Omega \left(-\frac{V_{in}}{22\,\text{k}\Omega} - \frac{15\,\text{V}}{R_{add}} \right)$$

Thus, in order to obtain the desired mapping, R_{add} had to be chosen such that $V_{out,2}$ obeys $V_{out,2} \in [0\,\text{V}, 10\,\text{V}]$. For $V_{in} \in [-10\,\text{V}, 10\,\text{V}]$ this could be roughly satisfied by using the combination $R_{add} = R_{fixed} + R_{poti}$ of a fixed resistor $R_{fixed} = 22\,\text{k}\Omega$ and a variable resistor $R_{poti} = 20\,\text{k}\Omega$ in series. Adjusting the resistance of both potentiometers R_1 and R_{poti}, finally resulted in a measured output range of $V_{out} \in [1.1\,\text{V}, 10.0\,\text{V}]$ which almost agrees with the desired range.

3.4.3 Characterization

After having connected all additional components to the according devices in the test setup, the performance of the intensity lock in terms of its response time was measured next. In practice, this involves on the one hand to specify the AOM's delay and the PD's rise time and additionally to characterize the overall response of the loop. However, instead of separately measuring all retardation times of every single involved device, the overall delay and rise times of the whole circuit have directly been measured.

Therefore, rectangular pulses with an amplitude of $5\,\text{V}$ and both a duration and spacing of $5\,\upmu\text{s}$ (corresponding to a frequency of $f = 100\,\text{kHz}$) have been applied as a control voltage $V_{control}$ to the second input channel of the PID using the function generator. Where possible, cable lengths were already chosen similar to the planned final realization in order to conduct the measurement under exactly the same conditions. The electric circuit of the PID allows

to separately vary the gain of all stages by means of potentiometers. For the purpose of the intensity lock only the P- and I-stages have been used. For all measurements presented below, the corresponding gains have been optimized in such a way as to minimize the delay times.

Response Times of Photo Diode and AOM

For the quantification of the loop's rise and fall times the terminating resistor at the oscilloscope has to be chosen such that the PID's input impedance dominates the overall load impedance that is experienced by the photo diode. Only then the measuring device does not have large impact on the measurand, in this case the response times.

By interconnecting the PID between the oscilloscope and the PD, it is no longer solely the oscilloscope that introduces a load but also the PID. As all connections have been established by coaxial cables, they effectively represent shunt circuits. In order to minimize the oscilloscope's impact on the lock's performance it should be terminated by highest possible resistances[33]. Only then the current coming from the photo diode will fully drain off via the PID so that negligible currents flow into the oscilloscope, thus, making it an almost perfect voltage measurement device.

The PID's circuit allows to add a certain input resistance. In order to maximize the bandwidth as described in section 3.4.2, this option was made use of by attaching a $56\,\Omega$ resistor. Since the photo diode contains a final amplifying stage this choice should also yield a sufficiently high SNR. Moreover, it complies with the requirement that the PID represents the dominant load.

With the oscilloscope being terminated by $1\,\text{M}\Omega$ the loop's rise and fall times were measured to be $\tau_{rise} = 200\,\text{ns}$ and $\tau_{fall} = 201\,\text{ns}$. Both the control voltage pulse that was applied to the PID and the corresponding PD-signal are plotted in figure 3.7. According to equation (3.2) the resulting bandwidth amounts to $BW_{analog} = 1.90\,\text{MHz}$. As the PID output is connected to the *analog* input channel of the AOM driver the quantity symbol BW is indexed with "analog".
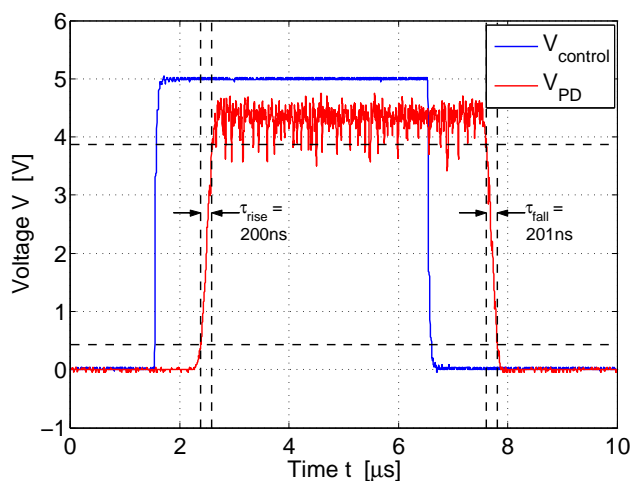
FIGURE 3.7: *Measurement of the "analog" response of the intensity stabilization loop after optimization. The blue line shows the control voltage signal $V_{control}$ which was generated in a pulsed way by the function generator and has been applied to the PID which is connected to the* analog *input channel of the AOM driver. The red line represents the response of the stabilization circuit in terms of the detected voltage on the photo diode. The dashed lines indicate the positions of 10% and 90% of the maximum voltage which are required to evaluate rise and fall times. The delay times are obtained similarly.*

As shown in figure 3.4, the AOM driver does not only possess an analog but also a digital

---

[33] The oscilloscope which was used for this measurement already features an input impedance of $1\,\text{M}\Omega$. This is why principally no additional termination resistor is necessary if very high load resistances are required.

input channel which allows to switch it off directly by using a TTL- instead of an analog pulse as done so far. Applying digital signals at a frequency of $f_{digital} = 200\,\text{kHz}$ directly to the driver instead of to the PID resulted in rise and fall times of $\tau_{rise} = 72\,\text{ns}$ and $\tau_{fall} = 93\,\text{ns}$ yielding $BW_{digital} = 4.61\,\text{MHz}$. An exemplary pulse as well as the corresponding response are plotted in figure 3.8. It should be noted that in this case the PID did not contribute to the retardation times so that τ_{rise} and τ_{fall} have been induced mainly by the photo diode.

The detected speed-up response, though, can only be exploited for purposes where the AOM only has to be switched on or off but not for modifying the light intensity.
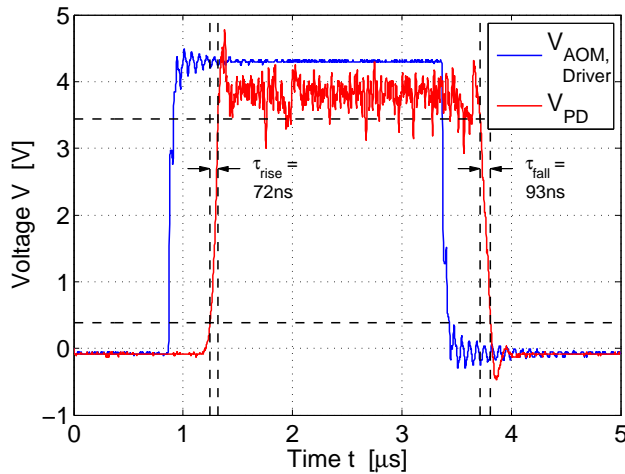
Figure 3.8: *Measurement of the "digital" response of the intensity stabilization loop after optimization. The measurement procedure was similar to the one described in caption 3.7. However, this time the blue line shows the control voltage signal V_{AOM} which was directly applied to the* digital *input channel of the AOM driver which especially means that the PID does not contribute to the response times here.*

The delay times were extracted as well from both measurements presented above. In the case of generating and applying analog signals to the AOM driver, delay times of $\tau_{ON} = 946\,\text{ns}$ for switching on and $\tau_{OFF} = 1162\,\text{ns}$ for switching off have been determined. In the digital mode they have been measured to be $\tau_{ON} = 419\,\text{ns}$ and $\tau_{OFF} = 393\,\text{ns}$, again revealing a considerable speed-up due to restriction of involved devices. Using equation (3.2) this leads to bandwidths of $BW_{delay,analog} = 360.5\,\text{kHz}$ and $BW_{delay,digital} = 936.0\,\text{kHz}$.

By comparing the measured retardation times of the analog and the digital mode it can be deduced to what extent the PID influences the overall response. Apparently, both the rise and the delay times are significantly deteriorated by the PID. However, the time differences might also partly originate from the analog buffer card and differing internal AOM driver processing of analog and digital signals[34].

Overall Performance

If combined according to equation (3.1), these delay times finally result in overall bandwidths of about $BW_{loop,analog} = 354.2\,\text{kHz}$ for the analog and $BW_{digital} = 917.2\,\text{kHz}$ for the digital mode of operation respectively.

Finally, the response curve of the complete stabilization loop was measured in order to identify its working range. Therefore the development of the optical power is measured while increasing the control voltage $V_{control}$ which represents the parameter that is finally used to define the light intensity. For this purpose a triangular signal with a voltage range of

---

[34] The influence of other sources of retardation such as signal transmission lines was assumed to be negligible here.

$V_{control} \in [-3.2\,\mathrm{V}, 7.9\,\mathrm{V}]$ and a frequency of $1\,\mathrm{Hz}$ was applied to the PID while the corresponding light intensity was monitored on the photo diode.

Up to the diode's maximum optical output power the light intensity which is measured in terms of V_{PD} is supposed to show exactly the same rising behaviour as the control voltage. At control voltages which would correspond to higher light intensities, the signal at the PD is then expected to stay constant at the maximum value. At the time scale that has been used for this measurement, delay times should not become noticeable at all. The measurement of the response curve is shown in figure 3.9.
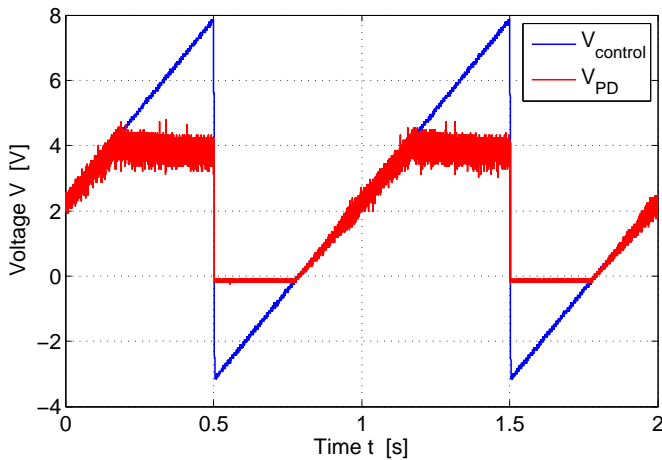
FIGURE 3.9: *Measurement of working voltage range of intensity stabilization circuit. The range of possible working voltages has been determined by applying control voltages $V_{control}$ to the PID which exceed the range of possible photo diode voltages V_{PD}. For this measurement the input signal has been set to a much lower frequency so that response times do not have any influence.*

Obviously, it qualitatively agrees with the expectations, however, another problem that has regularly been observed but has not been mentioned so far becomes apparent again: All detected photo diode signals shown above reveal that the intensity is not stable at all but rather fluctuates a lot around the maximum values. This is even the case for the closed stabilization circuit. From these observations it can be deduced that the frequency of the fluctuations necessarily has to exceed the lock's bandwidth.

The fact, that the amplitude of the intensity fluctuations changes if the laser current is varied, suggests that they are definitely not caused by signal transmission but rather by the laser diode itself. This is already strongly hinting at a very non-stable laser diode output. Further investigations concerning this matter and to what extent this might be improved is discussed within the next sections.

3.5 General Beam Characterization

After having finalized the dimple beam setup, the laser diode itself was to be characterized, first simply in terms of the shape of its output beam but then also with regard to its mode structure.
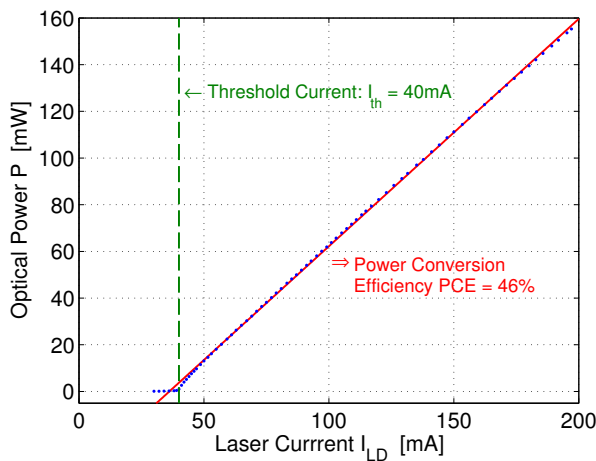
3.5.1 L-I-Characteristics

As a first characterization step, the diode's output light versus input current, also known as *L-I* or *P-I* characteristic was measured. Therefore, the current I_{LD} was increased in steps of about $\Delta I_{LD} = 1\,\mathrm{mA}$ from $30\,\mathrm{mA}$ to the driver's maximum output current of $200\,\mathrm{mA}$. Simultaneously,

its optical output power P_{LD} was measured at a distance of about $2\,\mathrm{cm}$ behind the collimator lens by means of a laser power meter.

The curve in figure 3.10 clearly shows the progressive behaviour that is typical for laser diodes. As soon as the current exceeds the threshold current I_{th} stimulated emission is initiated. Subsequently, the optical power increases approximately linear with the current. The measured laser threshold of $I_{th} = 40\,\mathrm{mA}$ exactly agrees with the value specified in the data sheet [40]. Furthermore, the diode's performance of converting electric power to optical power which is quantified by the value PCE was evaluated by fitting a linear function to the data. Using the measured operating voltage of $V_{op} = 2.1\,\mathrm{V}$ the conversion efficiency amounted to 46% which exceeds the specified value by six basis points.

The laser driver that was used here is not capable of supplying currents which are sufficiently large to observe the typical rollover of the optical power caused by self-heating [64].

FIGURE 3.10: *Measurement of the L-I characteristic of the laser diode. The blue dots show the measured optical power P for different applied laser currents I_{LD} between $30\,\mathrm{mA}$ and $200\,\mathrm{mA}$. The power conversion efficiency PCE can be extracted from a linear plot (red line) to the data points above the laser threshold current of $I_{th} = 40\,\mathrm{mA}$ which is marked by the dashed green line.*

3.5.2 Beam Profile

In the next step the beam profile was to be precisely measured. First of all, a picture of the beam's cross section at the focal position[35] was taken by means of the CCD-camera with and without a 40-fold magnifying objective being attached. The captured image of the magnified profile is pictured in figure 3.11. The evaluation in terms of a Gaussian fit to the intensity distribution that is shown next to the picture yielded waists of $w_{0,y} = 14.3\,\mathrm{\mu m}$ and $w_{0,z} = 62.8\,\mathrm{\mu m}$.

This image, though, should only be consulted for qualitative judgment of the beam profile. This is owing to the fact that during this measurement it could not completely be ensured that the beam stroke the objective exactly perpendicularly which in turn might induce image aberrations. Due to coma the beam waists might then appear to be larger than they really are. Furthermore, astigmatism might result in different focal positions in horizontal y- and vertical z-direction[36].

The existence of aberration was confirmed by the fact that waists which have been extracted from the picture without using the additional objective, deviate from the ones given above.

---

[35] It should be kept in mind that the characterization was still conducted in the framework of the setup where the beam was focussed by means of a single focussing lens instead of using the objective (compare figure 3.2).

[36] These coordinates still comply with the system shown in figure 2.2 where the dimple beam propagates along the x-axis and z denotes the vertical direction.
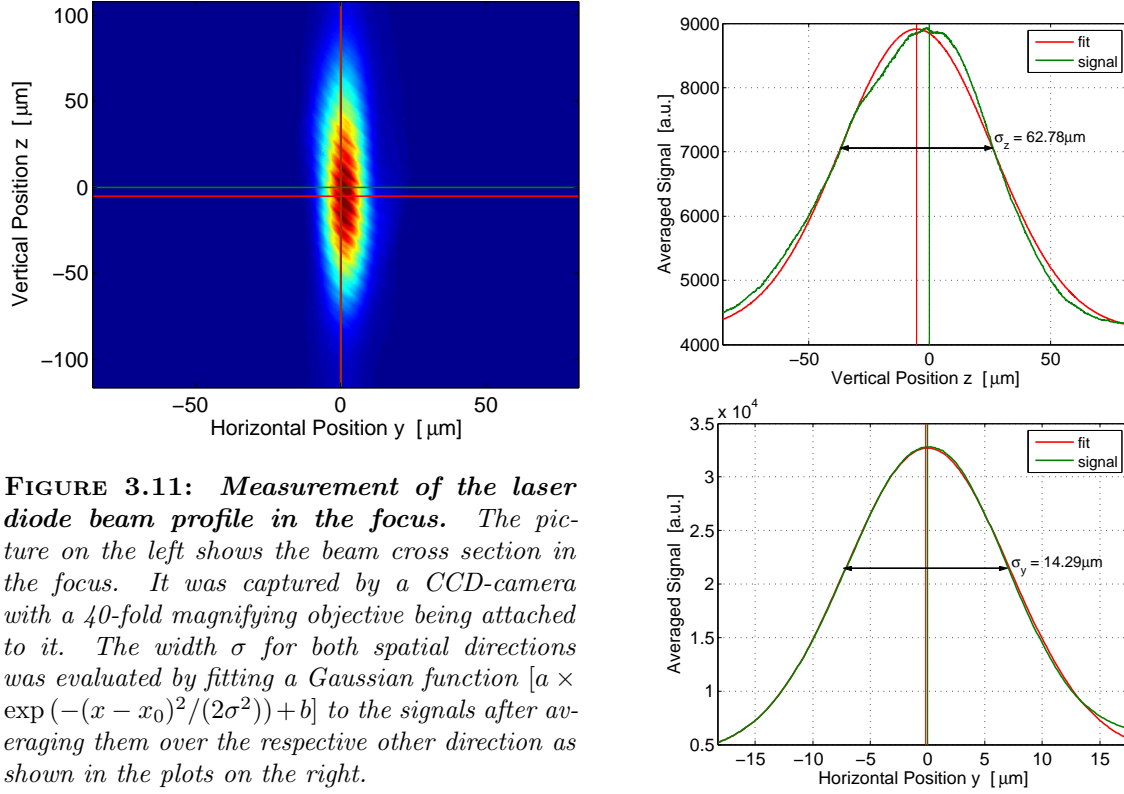
FIGURE 3.11: *Measurement of the laser diode beam profile in the focus. The picture on the left shows the beam cross section in the focus. It was captured by a CCD-camera with a 40-fold magnifying objective being attached to it. The width σ for both spatial directions was evaluated by fitting a Gaussian function $[a \times \exp{(-(x-x_0)^2/(2\sigma^2))}+b]$ to the signals after averaging them over the respective other direction as shown in the plots on the right.*

Without magnification the waists have been evaluated to amount to $w_{0,y} = 12.5\,\mu$m and $w_{0,z} = 43.6\,\mu$m.

Thus, in order to obtain a more precise value especially for the smaller waist in horizontal direction a much more precise quantitative technique was applied, the so called knife edge method.

Therefore, a razor blade was mounted onto a *Thorlabs* manual translation stage. Successively it was then horizontally inserted into the beam at various longitudinal positions x, thereby acting as a partial beam blocker in y-direction. While moving the razor blade in steps of $\Delta y = 10\,\mu$m the optical power of the extant amount of light that passed the blade was detected by the power meter. This procedure was repeated for numerous knife edge positions along the direction of propagation at intervals of $\Delta x = 50\,\mu$m around the focal position and larger spacings further away from the focus. The evolution of the horizontal beam waist as a function of x around the focus is plotted in figure 3.12. This curve was evaluated by fitting an error function to every single data set that corresponds to a certain position x and plotting the resulting beam diameters against x. Finally, a waist of $w_{0,y} = 12.33\,\mu$m and a Rayleigh range of $z_R = 580.7\,\mu$m could be extracted by fitting a function of the type given by equation (1.16) to the calculated data points.

This waist agrees very well with the value that was obtained by the initial *MATHEMATICA* simulation presented in the context of designing the dimpled ODT. As long as the wavelength will not change too much, the second light source is expected to exhibit a similar waist since image-shaping properties of the optics behind the fibre is independent of the source.
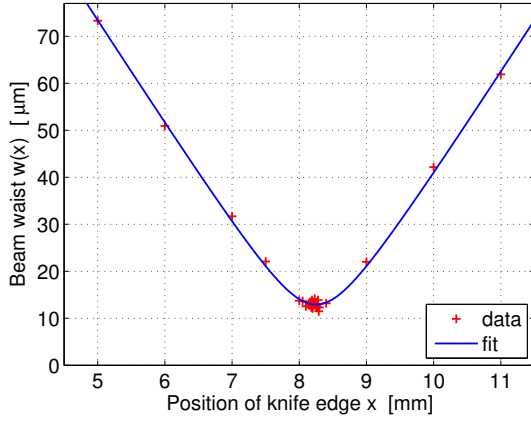
FIGURE 3.12: *Knife edge measurement of the horizontal beam waist in the focus. Each red data point was retrieved from an error function fit to the knife edge measurement of the beam waist w at the respective position x. Around the focal position the razor blade has been shifted by only* $50\,\mu m$ *from one measurement position to the next. The minimal waist* $w_{0,y} = 12.33\,\mu m$ *was evaluated by fitting equation (1.16) to the red data points.*

3.6 Preliminary Mode Characterization

As already mentioned in section 3.1, oftentimes inconsistent specifications can be found in the context of the mode structure of laser diodes. This is why in cases where stable mode emission is of high importance such as for the present purpose of generating the dimpled ODT, one should by no means only rely on the specifications. Rather, before being finally utilized, the particular laser diode should first be thoroughly examined with regard to its mode structure.

In the present case, though, there is another aspect that necessarily demands for scrutiny of the diode's emission spectrum. All measurements that have been conducted in the context of setting up the intensity stabilization reveal significant intensity noise which could not be eliminated by the lock and which is definitely not acceptable with regard to the intended purpose. Therefore, the diode's emission was to be studied in more detail by switching to the frequency space.

In general, a lot of different, also quite sophisticated techniques can be employed [65], [66] for the investigation of the mode characteristics of a laser diode. However, in the present case, simple methods were expected to be sufficient for monitoring the diode's emission spectrum and for drawing conclusions on the diode's performance.

A first preliminary analysis has been carried out by means of the wavemeter. Related observations are described next.

3.6.1 Expectations

Generally, in stable laser resonators different transverse modes oscillate at distinct frequencies which do not necessarily have to be equal [67]. This establishes a connection between the transverse and longitudinal mode structure.

The spectral position of the respective modes depends on their mode numbers (q,m,n), where q indicates the longitudinal modes and m and n the transverse TEM_{mn} modes. The according resonance frequencies inside the resonator are given by [65], [68]

$$\nu_{qmn} = \frac{c}{2L} \cdot \left[q \ + \ (m+n+1) \ \frac{\arccos(\pm\sqrt{g_1 g_2})}{\pi} \right] \tag{3.4}$$

where $c/(2L) \equiv \nu_{00}$ denotes the frequency of the fundamental TEM_{00} mode. Thus, equation

(3.4) implies that different transverse TEM_{mn} modes are separated by

$$
\begin{aligned}
\Delta\nu &= \nu_{q(m+1)n} - \nu_{qmn} = \nu_{qm(n+1)} - \nu_{qmn} \\
&= \nu_{00} \cdot \frac{\arccos(\pm\sqrt{g_1 g_2})}{\pi}
\end{aligned}
\tag{3.5}
$$

Due to this relation monitoring the spectral features can already indicate the number of transverse modes that a laser beam can be expected to comprise. However, it should be noted that the observation of multiple spectral peaks does not allow for drawing distinct conclusions on multi-mode emission. Rather, a laser diode can also operate single-mode but jump between different modes with different frequencies which as well leads to the observation of more than one single peak in the wavemeter spectrum.

In the case of a laser diode that runs stable and is specified to provide single transverse mode emission as the particular one used here, though, one would expect to monitor only few peaks at distinct, equidistant frequencies given by equation (3.4) which belong to different harmonics of the single mode. These peaks should become more and more pronounced the further the laser current exceeds the lasing threshold. This is because then the diode's radiation becomes more and more coherent. The larger the current is the more dominant becomes stimulated emission in all the diode's possible cavity modes. For currents much larger than the lasing threshold current I_{th} the stimulated emission will soon outweigh the spontaneous emission which the diode exhibits at $I_{LD} < I_{th}$ [69].

According to its data sheet the laser diode emits radiation in single *transverse* mode[37] around the central wavelength of $\lambda_0 = 824\,\text{nm}$ with deviations of $\pm 6\,\text{nm}$ if operated at the maximum optical output power of $P_{LD} = 200\,\text{mW}$. At 90% of this power the spectral bandwidth is specified to be $\Delta\lambda_{90} = 0.5\,\text{nm}$ [40].

Based on these specifications the emission spectrum is expected to show one distinct peak at a frequency that corresponds to the single transverse mode and is given by equation (3.4). This peak should additionally exhibit a linewidth which, in terms of λ, does not exceed the specified value of $\Delta\lambda_{90} = 0.5\,\text{nm}$.

3.6.2 First Observations

First observations of the spectrum by means of the wavemeter (compare figure 3.18) did not confirm the specifications at all, neither the single transverse mode emission nor the claimed spectral bandwidth. In fact, first measurements revealed large and fast fluctuations of the output signal on a spectral range of $\Delta\lambda = 6\,\text{nm}$. Furthermore, regular mode jumps in terms of abrupt changes of the central wavelength could be observed, especially at very high currents.

Simultaneously to wavemeter observations, the diode's output beam intensity was detected on a photo diode. These measurements revealed that the mode jumps have always been accompanied by considerable jumps between different intensity levels. Additionally, between two hopping events the intensity did not remain at stable values but rather fluctuated a lot.

---

[37] For details on the indication of the different mode directions in a laser diode with respect to the direction of light emission, please refer to the remark at the beginning of section 3.1.

3.6.3 Approaches to Improvements

As both the laser current and the temperature of the diode are typically expected to highly influence the output radiation of a laser diode, it was attempted to use these two parameters in order to improve the spectral width and mode stability. According to the data sheet, a change in temperature should result in wavelength shifts of $d\lambda/dT = 0.25\,\text{nm}/^\circ\text{C}$.

In fact, the active stabilization of the diode's temperature by means of its driver made it possible to slightly narrow the spectral width resulting in more stable intensities. However, these effects stayed very rudimentary as they have by no means been large enough to meet the specifications.

The best result was achieved for a thermistor resistance of $R_{TEC} = 6.8$ where spectral fluctuations were reduced to the range of $\pm 1\,\text{nm}$ around a distinct λ_0. For the purpose of the dimpled ODT, though, the intensity and wavelength should remain at a constant level on much longer time scales and should additionally vary much less so that the trap depth ideally remains constant during experiments. Changes in the trapping potential on the time scale of single experiment runs would induce unwanted heating and loss of the atoms. The *MATHEMATICA* simulations of the dipole potential reveals that the present fluctuations would impair the trap depth by more than 3%.

Variations in the laser current could as well not significantly improve the spectral features of the diode's output. Here, highest stability was achieved only on a range of about $\pm 1\,\text{nm}$ at a current of $I_{LD} = 195.0\,\text{mA}$.

3.6.4 Preliminary Conclusion

In fact these observations seem to be strong evidence for multi transverse mode operation which additionally does not comply with the specifications regarding the spectral bandwidth.

Nevertheless, observations that are only based on wavemeter measurements do not allow for drawing unambiguous conclusions on the beam's mode structure. In fact the wavemeter spectrum simultaneously contains all modes which the beam consists of. It is not capable of separating the modes and verifying the existence of multiple modes.

Possibly, the diode's output might not be as bad as it appears to be since mode hopping can in fact be a common feature of single-mode laser diodes. Also, accompanying intensity fluctuations can regularly be observed; precise control of the operation parameters might sometimes not be sufficient [70].

Furthermore, the wavemeter does not feature very high resolution which demands for using another measurement technique.

3.7 Cavity Mode Characterization

For these reasons, as a next step a scanning Fabry-Pérot cavity (SFPC) was to be employed for systematic scrutiny of the diode's emission spectrum. The output of such a cavity is much more suitable for monitoring modes of the incoming laser light since it is also capable of separating the modes. Moreover, SFPCs feature a resolution that only depends on the properties of used parts and which therefore can be of very high quality.

Appendix C comprises a detailed introduction into the concept of a scanning Fabry-Pérot cavity. Next to a description of the basic setup it includes a discussion on the stability of

resonator configurations. Furthermore it presents the most important parameters that are used to characterize a cavity.

As a start, the following fact should be noted and kept in mind for this section: Generally, the observation of special intensity patterns in the cavity output which represent different transverse modes does not necessarily have to be inherent to the beam itself. In fact, these modes can very well be a consequence of imperfect mode matching which means that the features of the Gaussian beam coupled into the cavity do not conform with the parameters set by the cavity configuration [71]. This is especially true if the beam is transmitted through a single-mode fibre before being coupled into the cavity since the fibre serves as a mode filter which only emits Gaussian fundamental modes. Consequently, if in this case the cavity output deviates from the fundamental mode it can be concluded that mode matching has not been optimized yet.

Expected Spectrum

The basic introduction into the concept of resonators that is presented in appendix C, suggests that the following spectral features can be observed when using a tunable SFPC under the assumption of perfect mode matching.

Generally, the spectral width of all resolvable peaks is determined by the cavity's ability to enhance the captured light field which mainly depends on the mirrors' reflectivities and potential losses due to scattering, absorption or diffraction errors. The higher the reflectivities $|r|^2$, the larger is the finesse and thus the more does the light become self-enhanced. Consequently, the cavity properties define the minimum resolvable spectral mode separation.

This resolution capacity, though, should not be too relevant when using Gaussian beams that only comprise the fundamental TEM_{00} mode. This is because in this case, the corresponding spectrum does not show peaks which spectrally come very close together. Rather they are equidistantly separated by $q\lambda$ as they satisfy the resonance condition $L = q\lambda/2$.

Only in the case that the mode characteristics of the light is unknown that means whether it is composed of more than one mode, resolution becomes important and should therefore be maximized. If multi-mode laser light is coupled into the cavity, several peaks within one free spectral range will be anticipated. Their spectral position depends on the mode numbers (q,m,n) and is given by equation (3.4).

For the purpose of analysing the observed spectrum, it should be pointed out again, that different transverse modes do not necessarily have to be inherent to the particular input beam but can also originate from imperfect mode matching. The preconditions and realization of mode matching, also concerning practical restrictions, will be briefly discussed in the following subsection 3.7.1 in conjunction with designing the SFPC for the purpose of investigating the laser diode's emission spectrum.

3.7.1 New SFPC Setup

A new SFPC has been constructed for scrutiny of this particular laser beam with regard to its mode structure. For illustration of the setup the final cavity is pictured in figure 3.13.

For the purpose of building this SFPC, only two kinds of mirrors, namely planar-planar and plano-concave ones with a radius of $R = 500\,\text{mm}$ and a refractive index of $n = 1.5$ have been available. The mirrors feature diameters of $12.6\,\text{mm}$ and are $6.3\,\text{mm}$ thick. One of their

surfaces is coated[38], which is the curved one in case of the plano-concave mirror, and exhibits best reflectivity of 98.75 % for wavelengths between 760 nm and 795 nm. According to equation (3.6) this yields a finesse of $\mathcal{F} = 249.75$. In the ideal case without accounting for loss or other factors such as misalignment that might deteriorate the cavity's quality, this finesse should be sufficiently large for the purpose here.

Furthermore, only one type of hollow metal tube with internal and external diameters of $d_i = 10\,\mathrm{mm}$ and $d_a = 30\,\mathrm{mm}$ respectively and a length of 83.5 mm could be used as a casing for the cavity. Due to various additional spacers the total length between the reflecting surfaces of the mirrors will amount to 100 mm which will yield a free spectral range of $\Delta\nu_{FSR} = 999.31\,\mathrm{MHz}$ pursuant to equation (3.3).

These practical restrictions of available components significantly limit the number of possible configurations.

In order to offer tunability of the resonator length, one of the mirrors shall not be directly glued to the tube, but rather a ring-shaped piezoelectric actuator (called piezo) has to be inserted between mirror and tube. In order to prevent its electrodes from shorting which will put the piezo out of operation, it should be made sure that the glued joint is not conducting. This can be achieved for example by using a layer of Kapton polyimide film in-between.

Piezoelectric Actuator

By applying high voltages[39] V_{piezo} to the piezo, its height h changes linearly according to $\Delta h = d_{piezo}V_{piezo}$ where d_{piezo} denotes the characteristic piezoelectric coefficient of the piezo material. This piezoelectric effect is a completely reversible process and results from linear electro-mechanical interaction in crystalline materials. That means a piezoelectric crystal can either internally generate electric charges as a result of mechanical force or it can exhibit the reverse effect in terms of inducing mechanical strain by means of an applied electric field. d_{piezo} parameterizes the mechanical strain per unit applied electric field [72].

FIGURE 3.13: *Pictures of self-made scanning Fabry-Pérot cavity. The cavity consists of a planar (left mirror in the top picture) and a concave mirror. While the last one was directly fixed to the casing the planar mirror was first glued onto a piezo and then attached to the tube as shown in the picture below. Further specifications are given in the text.*

In the present case, the required voltages have been generated by means of a self-made amplifier with an amplification of -40.

The only available type of piezo features a ring-like shape with an outer diameter of 10 mm and a length of 6.3 mm. Further specifications have not been known.

Moreover, in the beginning it has been insecure whether the piezo worked properly at all so that it had to be inspected for functionality before being implemented. A rough estimation could be obtained by measuring the piezo's resistance which is typically in the order of MΩ

---

[38] Type: *LASEROPTIK*, B-11035
[39] Voltages of up to 400 V can be applied to the piezo used here without destroying it.

for properly operating crystals. Shorted or damaged actuators will of course possess lower resistances.

A more thorough way to check the functionality of the device is to apply a frequency-tuned AC signal to it. Generally, piezos exhibit a distinct resonance frequency where they convert the electric energy most efficiently into mechanical energy. At this particular frequency the crystal strongly vibrates which can even be heard if the frequency is part of the audible domain. Typically, this characteristic frequency can be found in the kHz range for ring piezos such as the one employed here. By carrying out this test, the piezo's functionality could be proven. The corresponding resonance frequency became noticeable in terms of high-pitched humming at frequencies between $f_{res} = 28.5\,\mathrm{kHz}$ and $31.5\,\mathrm{kHz}$ and an applied voltage of $V = 120\,\mathrm{V}$.

Realizable Cavity Configurations

Due to the previously mentioned practical restriction of available parts, only two resonator configurations have been feasible:

(a) **Plano-Concave Resonator:**
As sketched on the left hand side in figure 3.14 this type of cavity is composed of one concave and one planar mirror. With the dimensions given above the configuration is characterized by $(g_1, g_2) = (1, 0.8)$ which definitely yields a stable resonator (compare figure C.1).

(b) **Concave-Concave Resonator:**
The second option is a cavity setup that consists of two plano-concave mirrors with their reflecting and curved surfaces facing each other as shown on the right hand side in figure 3.14. In the present case it is described by $(0.8, 0.8)$ which also results in a stable configuration.
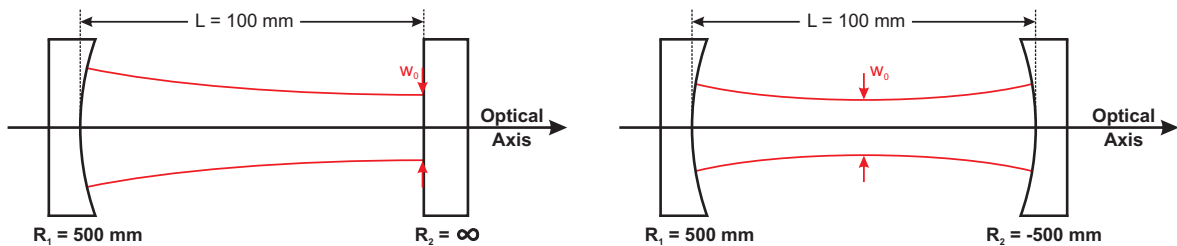
FIGURE 3.14: *Schematics of possible resonator configurations. All values comply with the specifications of available parts. The beam waist w_0 indicates the position of the focus.*

The third possible option, the plano-plano configuration was not even considered due to its position on the hyperbola in the stability diagram which is illustrated in C.1. As it is located on the edge of the region of stability, small deviations from perfect alignment such as slightly non-parallel relative orientation of the mirrors could already lead to an unstable configuration. Especially in the case here, it is expected that cavity coupling experimentally cannot be carried out this precisely due to various shortcomings concerning beam collimation and shape, as described later.

Principally, both described resonator configurations are equally suitable. Therefore, the choice of which of them to implement was based on the outcome of the calculation of required mode matching optics.

An illustrative argument supporting the plano-concave cavity might be that this configuration is indeed similar to a concave-concave setup of double the length which is folded along the vertical symmetry axis. Extending the cavity length implies that the beam which is coupled into the resonator does not have to be focussed that tightly as in the case of shorter cavities that utilize the same mirrors. This, in turn, allows their wavefronts to exhibit a smaller curvature and thus to diverge less so that this configuration might finally be less sensitive to imperfect coupling.

3.7.2   Mode Matching

In general, a Gaussian beam can only be coupled efficiently into a Fabry-Pérot cavity if its beam shape agrees with the profile of the constituent mirrors that means that its wavefront at the mirror positions equals their curvature. This condition can be satisfied by means of mode matching which is based on the principle that the Gaussian beam is a mode of the spherical-mirror resonator [30]. Only if this is fulfilled, the mirror will reflect the beam in such a way that it is refocussed resulting in self-enhancement of the light field.

Therefore, the laser beam which shall be coupled into the cavity first has to be modified by additional optical components in front of the cavity according to the resonator configuration. In the case of the plano-concave cavity, the focus has to agree with the position of the reflective surface of the flat mirror whereas for the concave-concave setup it has to be placed exactly in the middle of the resonator. In both cases the beam has to evolve in such a way as to match the mirrors' curvatures.

Based on the particular boundary conditions defined by the radii and positions of the mirrors, this mode matching condition can mathematically be expressed in the following way. Thereby, equation (1.17) which describes the evolution of the curvature of the Gaussian beam is sufficient in order to derive conditions for the required focal waist w_0 or, equivalently, the Rayleigh range z_R as a function of the cavity's characteristic parameters R_1, R_2 and L.

Assuming that the two mirrors are located at positions z_1 and z_2 and the beam's focal position defines the origin, the radii R_1 and R_2 of the reflecting mirror surfaces are related to the beam curvature according to[40]

$$-|R_1| = R(z_1) = z_1 + \frac{z_R^2}{z_1} \qquad \text{and} \qquad |R_2| = R(z_2) = z_2 + \frac{z_R^2}{z_2} \qquad (3.6)$$

The third equation required to derive expressions for z_1, z_2 and z_R in terms of the radii R_1, R_2 and the cavity length L is given by

$$z_2 = z_1 + L \qquad (3.7)$$

---

[40] This derivation is based on the mirror sign convention introduced in footnote 92. Note, that the two conditions in (3.6) already account for the fact that negative signs for wavefront curvatures are attributed to converging Gaussian beams and positive signs to divergent ones respectively. In the present case the focus is supposed to define the origin and the beam is intended to propagate along the z-axis so that convergence of the focussed beam is always given for $z < 0$ and divergence for $z > 0$. This leads to a change of signs at the origin.

On the other hand, the sign of the mirror radii does not rely on the relative position to the origin so that signs do not change there. For example, negative radii are always assigned to surfaces with the centre of curvature located on the left, whatever position they are placed at.

This discrepancy explains the necessity of absolute value bars in equation (3.6) and the different shape of the corresponding conditions.

This system of equations (3.6) and (3.7) can be solved for each z_1, z_2 and z_R yielding the following sought-after expressions in terms of the cavity parameters R_1, R_2 and L or, alternatively, of the stability parameters g_1 and g_2. Actually, the latter expressions should be preferred since they are consistent with all different sign conventions used in literature [41].

$$
\begin{aligned}
z_1 &= -\frac{L(|R_2| - L)}{|R_1| + |R_2| - 2L} = -\frac{g_2(1 - g_1)}{g_1 + g_2 - 2g_1g_2} \cdot L \\
z_2 &= \frac{L(|R_1| - L)}{|R_1| + |R_2| - 2L} = \frac{g_1(1 - g_2)}{g_1 + g_2 - 2g_1g_2} \cdot L \\
z_R^2 &= \frac{L(|R_1| - L)(|R_2| - L)(|R_1| + |R_2| - L)}{(|R_1| + |R_2| - 2L)^2} \\
&= \frac{g_1g_2(1 - g_1g_2)}{(g_1 + g_2 - 2g_1g_2)^2} \cdot L^2
\end{aligned}
\tag{3.8}
$$

By means of these equations the required values for z_1, z_2 and especially z_R can be evaluated for both possible cavity geometries:

(a) **Plano-Concave Resonator:**
Using $(g_1, g_2) = (1, 0.8)$ as stability parameters, the mirrors have to be placed at $z_1 = 0$ and $z_2 = L$ as expected. These values are consistent with equation (3.7) and the assumption that the beam's focus is located in the origin, where by definition (1.17) the wavefront curvature is supposed to be infinitely large.
The much more important result is the beam's Rayleigh range which has to be $z_R = 200\,\mathrm{mm}$ in order to achieve perfect mode matching and maximized resonator performance. Consequently, according to equation (1.16), for coupling the beam into the plano-concave resonator it must be focussed down to a focal waist of $w_0 = 228.90\,\mu\mathrm{m}$ assuming a wavelength of $\lambda_{LD} = 823.6\,\mathrm{nm}$.

(b) **Concave-Concave Resonator:**
The stability parameters $(g_1, g_2) = (0.8, 0.8)$ in this case yield mirror positions of $z_1 = -50\,\mathrm{mm}$ and $z_2 = 50\,\mathrm{mm}$. This again reproduces the anticipated focal position or origin to be located exactly in the middle of the resonator.
Furthermore, the beam coupled into this cavity geometry is required to feature a Rayleigh range of $z_R = 150\,\mathrm{mm}$ and a focal waist of $w_0 = 198.23\,\mu\mathrm{m}$. As expected, this cavity design demands for stronger focussing.
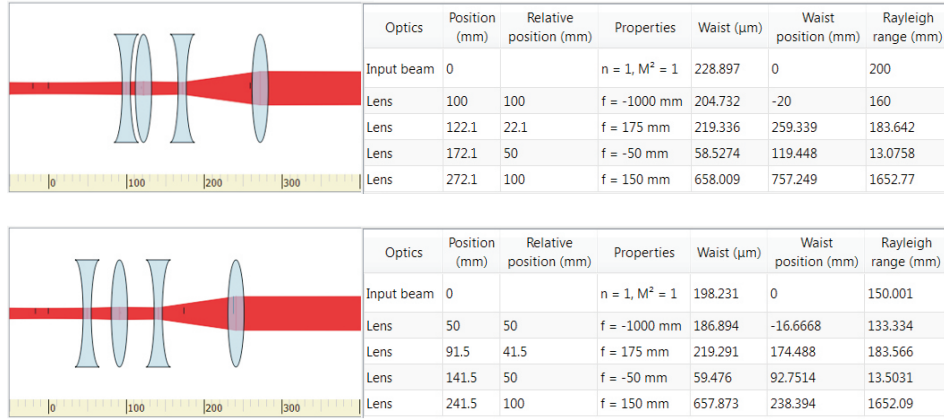
Optics and Choice of Resonator Configuration

Consequently, before the beam can be coupled into the cavity, some additional mode matching optics is required in order to modify the beam shape such that it satisfies these conditions.
Next, this mode matching optics was determined for both possible cavity configuration (a) and (b) in order to figure out which setup is more suitable for the purpose here. Therefore a software, called *GaussianBeam*, was employed which computes the development of a Gaussian beam according to the optical elements that are defined and placed by the user. The resulting optical setups are schematically pictured in figure 3.15.

---

[41] If literature is consulted for the purpose of mode matching, the problem of non-conforming mirror sign conventions should be kept in mind as described in footnote 93.

Optics	Position (mm)	Relative position (mm)	Properties	Waist (µm)	Waist position (mm)	Rayleigh range (mm)
Input beam	0		n = 1, M² = 1	228.897	0	200
Lens	100	100	f = -1000 mm	204.732	-20	160
Lens	122.1	22.1	f = 175 mm	219.336	259.339	183.642
Lens	172.1	50	f = -50 mm	58.5274	119.448	13.0758
Lens	272.1	100	f = 150 mm	658.009	757.249	1652.77

Optics	Position (mm)	Relative position (mm)	Properties	Waist (µm)	Waist position (mm)	Rayleigh range (mm)
Input beam	0		n = 1, M² = 1	198.231	0	150.001
Lens	50	50	f = -1000 mm	186.894	-16.6668	133.334
Lens	91.5	41.5	f = 175 mm	219.291	174.488	183.566
Lens	141.5	50	f = -50 mm	59.476	92.7514	13.5031
Lens	241.5	100	f = 150 mm	657.873	238.394	1652.09

FIGURE 3.15: *Evaluation of required mode matching optics for the two possible resonator configurations. Starting from the focussed beam inside the cavity, required lenses for mode matching have been calculated with the help of the software* GaussianBeam*. Lens positions have been optimized in such a way that the resulting beam characteristics agree with the laser diode output beam. The upper calculation belongs to the plano-concave and the lower one to the concave-concave configuration.*

Due to practical reasons, instead of starting with the laser beam profile and successively evaluating the optical components which are necessary to obtain the required cavity mode, the calculation was carried out in the reversed direction. Starting with the cavity mode (on the left in figure 3.15) which is characterized by the previously calculated values z_1, z_2 and z_R an assembly of three lenses was arranged which will finally yield a collimated beam that exhibits a waist of about $w_0 = 650\,\mu$m. This is the value which has been measured for the dimple beam directly behind the AOM. In case of the plano-concave geometry it was assumed that the beam will be coupled into the cavity through the concave mirror.

This reversed approach is justified due to the fact that the beam evolution is invariant towards the direction of propagation so that a given optical setup will always produce the same overall beam structure independent of which side the beam arrives at.

For these calculations it should be kept in mind, that the curved mirror will act as a concave lens for transmitting instead of reflecting the light. Its focal length f is given by the lensmaker's equation

$$\frac{1}{f} = (n_l - 1)\left[\frac{1}{R_-} - \frac{1}{R_+} + \frac{(n_l - 1)d_l}{n_l R_- R_+}\right] \tag{3.9}$$

where R_- and R_+ indicate the radii of the lenses' left (-) and right (+) surface. n_l denotes the refractive index of the lens material and d_l is its thickness along the optical axis [73]. Thus, for light transmission the right cavity mirror with radii of $R_- = -500\,$mm and $R_+ = \infty$ and $n_l = 1.5$ will act as a lens with $f = -1000\,$mm.

Two of the calculated lenses are solely required to constitute a telescope which is needed to adjust the diameter of the collimated beam. For them only the ratio of focal lengths is relevant and the absolute values are in fact of little importance. The third lens which represents the focussing lens directly in front of the cavity, finally has to produce the required Rayleigh range or waist respectively. Due to the fact that the latter one's focal length could only be chosen from a small and limited amount of available lenses, it could not be expected that the mode matching conditions will be entirely satisfied.

Finally, it turned out that for both cavity configuration the same selection of lenses would deliver the best result, namely a focussing lens with $f = 175\,\text{mm}$ and a telescope with a magnification of three which consists of lenses with $f = 50\,\text{mm}$ and $f = 150\,\text{mm}$. As indicated by the schematics in figure 3.15, the only difference between the two cavity configurations are differing lens positions. Obviously, the total lengths of the optical setups are roughly equal so that this quantity could not be used as a decisive selection criterion.

Thus, the final decision on which cavity configuration to be realized could not be based on the argument of mode matching feasibility but rather had to fall back on the Rayleigh range z_R which represents the only parameter that distinguishes one setup from the other. Generally, pursuant to (1.18), the smaller z_R, the bigger is the divergence and the more strongly the beam diverges the less tolerant it finally is towards misalignment of beam-shaping optics. Therefore, the decision was made in favour of the ***plano-concave geometry*** as this was assumed to be slightly less sensitive to mode matching errors.

3.7.3 Pre-Fibre Beam Inspection

The full mode structure of the laser diode's output beam can only be observed before it is transmitted through the single-mode fibre. This is owing to the fact that the fibre inherently acts as a mode filter so that the output light can only be examined with regard to the resonance frequency of existing modes as given by equation (3.4). It is not possible though, to clearly determine the corresponding TEM_{mn} mode by detecting the output on a CCD-camera. This is why as a first step the cavity was to be coupled to the beam in front of the fibre.
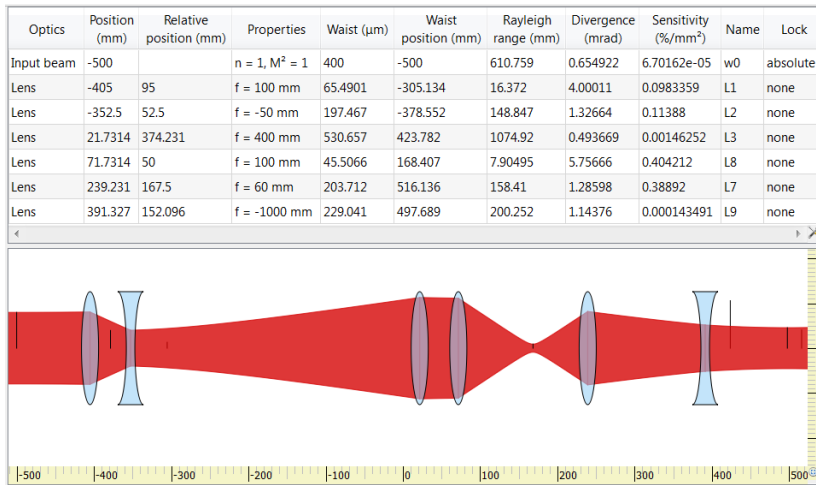
At this point the calculation of mode matching has been carried out again in order to figure out the exact lens positions. However, this time it was done in "correct" forward direction and the evaluation was not only based on the waist of the collimated laser diode beam but also on its divergence which first had to be evaluated from beam profile measurements at various positions along the propagation direction.

The reason for also considering the beam divergence was the observation that the beam exhibits slight divergent behaviour of unknown extent. This is due to the fact that the lenses of the telescope directly behind the diode have been aligned for optimized fibre coupling instead of cavity coupling. As a result, their distance marginally deviated from the perfect value of $50\,\text{mm}$ which induces a small divergence.

Even slightly uncollimated beams might in turn necessitate considerably different lens positions compared to the case of a perfectly collimated beam. The evolution of beam parameters should be known as good as possible in order to optimize mode matching which is crucial for best cavity performance.

In order to identify the present divergence, pictures of its profile were taken by means of the CCD-camera at various positions between diode and cavity. A subsequent evaluation of the detected beam waist evolution $w(z)$ revealed that the divergence amounts to $\theta = 1.3266\,\text{mrad}$ which corresponds to a Rayleigh range of $z_R = 148.85\,\text{mm}$. These values represent a divergence that is significantly larger than anticipated. That is why a recalculation of the mode matching optics was all the more required. In doing so, different focal lengths turned out to be more suitable for mode matching. The resulting optical setup is illustrated in schematic 3.16.

Additionally, from the pictures captured by the CCD-camera it became apparent that the beam's profile behind the AOM does not exhibit a Gaussian shape at all, but rather seemed to consist of much more than only the fundamental mode. An exemplary shot is shown in figure 3.17. Generally, it is very challenging to couple such a beam into the cavity. Especially the

Optics	Position (mm)	Relative position (mm)	Properties	Waist (μm)	Waist position (mm)	Rayleigh range (mm)	Divergence (mrad)	Sensitivity (%/mm²)	Name	Lock
Input beam	-500		n = 1, M² = 1	400	-500	610.759	0.654922	6.70162e-05	w0	absolute
Lens	-405	95	f = 100 mm	65.4901	-305.134	16.372	4.00011	0.0983359	L1	none
Lens	-352.5	52.5	f = -50 mm	197.467	-378.552	148.847	1.32664	0.11388	L2	none
Lens	21.7314	374.231	f = 400 mm	530.657	423.782	1074.92	0.493669	0.00146252	L3	none
Lens	71.7314	50	f = 100 mm	45.5066	168.407	7.90495	5.75666	0.404212	L8	none
Lens	239.231	167.5	f = 60 mm	203.712	516.136	158.41	1.28598	0.38892	L7	none
Lens	391.327	152.096	f = -1000 mm	229.041	497.689	200.252	1.14376	0.000143491	L9	none

FIGURE 3.16: GaussianBeam *calculation of the mode matching optics required for the diverging laser diode beam.* The first two lenses are used to generate a beam that exhibits the measured parameters. The following three lenses are required to bring this beam into agreement with the cavity mode. The last lens represents the concave mirror of the resonator.

spectral resolution will in this case definitely suffer from imperfect mode matching. Moreover, these coupling imperfections will most likely produce many additional modes in the transmission spectrum of the cavity.
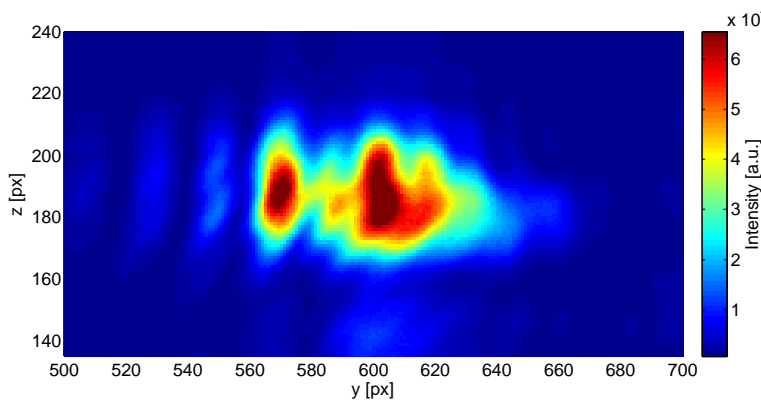
FIGURE 3.17: Pixelfly *shot of the laser beam cross section used for cavity coupling.* The picture was taken directly behind the flip-mirror which is shown in figure 3.18. The unusual beam profile highly impeded cavity coupling.

After having arranged the mode matching optics according to the calculation as illustrated in figure 3.18 cavity coupling could finally be performed.

As expected this turned out to be challenging. Even the very alignment of the cavity with respect to the laser beam was not easy but could finally be accomplished by first adjusting the height and afterwards successively rotating and shifting the cavity perpendicularly to the beam propagation direction. Simultaneously, the transmitted light was detected on the CCD-camera so that the perfect cavity alignment was found by maximizing the detected light power.

In spite of these difficulties, ultimately a significant amount of light could be obtained. However, as expected, this transmission signal did not only consist of the fundamental Gaussian mode. Instead, even in the cavity's non-scanning mode that means when the piezo was turned off, the detected spatial intensity distribution revealed the presence of several higher-order modes which quickly alternated with the fundamental mode. Exemplary shots captured by the *pixelfly* CCD-camera are pictured in figure 3.19.

Though, whether the multitude of modes was caused by imperfect mode matching or
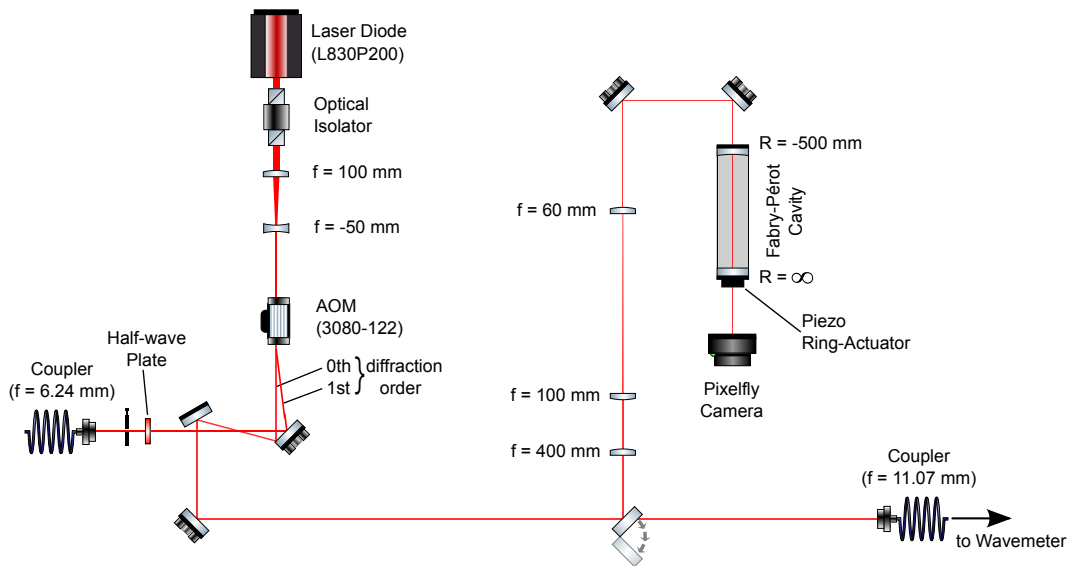
FIGURE 3.18: *Required optical setup for pre-fibre cavity coupling. AOM diffraction orders that are not coupled into the fibre have been used for mode characterization with the SFPC. All following lenses between the flip mirror and the cavity have been set up according to the* GaussianBeam *calculation that is shown in figure 3.16.*
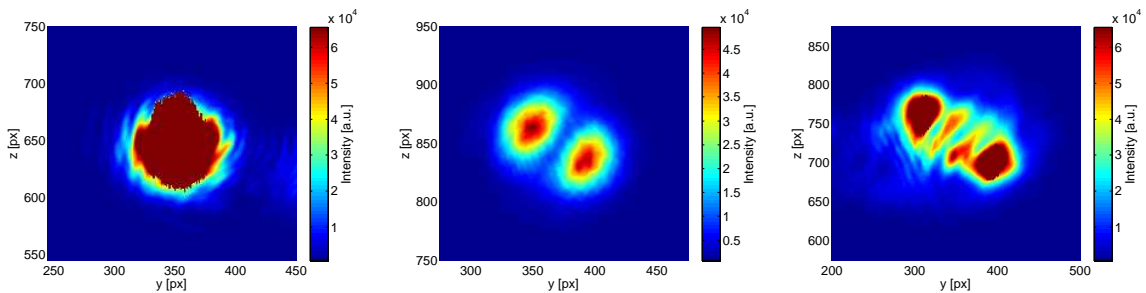
FIGURE 3.19: *Pixelfly shots of the cavity output signal (pre-fibre). The pictures have been captured at different times while the piezo was turned off. Even with the fixed resonator length several alternating higher-order Gaussian modes could be observed.*

whether they are inherent to the input beam, could not be clearly identified due to the poor input beam profile.

The detected signal did as well not change for variations of the laser current. At least, fluctuating currents could be eliminated as a possible source of noise since they were measured to be stable on the order of parts per thousand.

This observation might be an indication that the higher-order modes have been induced by incorrect mode matching. However, it can as well hint at a very unstable laser diode output.

Consequently, even after optimized cavity coupling, using the cavity with the beam in front of the fibre did not prove to be suitable for investigations of the diode's mode structure. Due to the fact that optimized mode matching could not be guaranteed to the full extent, it was not possible to clearly attribute the obtained results to the input beam so that no clear statement could be made about its emission spectrum.

3.7.4 Post-Fibre Beam Inspection

As a second approach to investigate the emission spectrum, the beam was coupled into the cavity after fibre transmission. Up to now this way of realization was avoided due to the filtering property of the single-mode fibre. Since the fibre output does not preserve the mode's intensity distribution, the output beam cannot be used to identify the mode numbers m and n of existing beam modes. It can only be subject to a detailed scrutiny of their spectral position and width.

Piezo Voltage for One Free Spectral Range

Before the cavity was used for the beam of the laser diode, though, it was coupled to the output beam of a *Toptica TA pro* diode laser at a wavelength of 780 nm. This was done in order to identify the piezo voltage which corresponds to one free spectral range.

For this purpose, only one focussing lens with a focal length of $f = 300$ mm was required for mode matching due to the beam's convenient profile. In this case cavity coupling turned out to be much less challenging so that it was very straightforward to obtain a significant signal on the camera behind the cavity. Once the fundamental resonator mode was found, the cavity was switched to the scanning mode and the input voltage of the SFPC piezo was tuned over the range from 0 V to 240 V by means of a triangular signal from the function generator and the interconnected voltage amplifier. Both the signal from the function generator and the photo diode voltage were simultaneously detected on an oscilloscope. From this measurement it could be deduced that in the case of input light at $\lambda = 780$ nm, one free spectral range of the SFPC corresponds to a piezo input voltage range of 200 V.

Not until this value is determined, peaks in the spectrum of the SFPC can be clearly identified. Spectral signals for instance which appear at piezo voltages exceeding this value can then be assigned to higher harmonics of a fundamental mode which can already be observed at a lower voltage.

This result could now be translated to the case of using the laser diode beam as cavity input. Due to the slightly higher light frequency it was expected that for $\lambda_{LD} = 823.6$ nm one free spectral range will be covered by an piezo voltage range of about 210 V.

Investigation of Mode-Filtered Laser Diode Beam

Now, the SFPC was applied to the actual laser diode beam behind the fibre. This time, mode matching necessitated an optical setup only consisting of a single focussing lens with a focal length of $f = 300$ mm since the used fibre out-coupler lens provided a relatively small collimated beam waist.

Subsequently, cavity coupling was executed in the following systematic way: First, the beam was roughly coupled into the resonator by aligning the cavity with respect to the propagation direction. As soon as a transmission signal was observed on the camera, no matter which mode, the piezo was turned on and scanned at a high frequency on the order of several kHz over the full input voltage range which covers significantly more than one free spectral range. As a result, the detected spot on the camera became considerably intensified and enhanced. This is because at this scanning speed the camera cannot timely separate and resolve all alternately appearing modes, but rather averages over the full observable spectrum. Therefore, the detected signal comprises all the modes popping up within the measured spectral range which are effectively summed up to one signal.

This multitude of modes, however, was still caused by cavity coupling which has not been optimized yet. For this purpose, the beam was walked until only one big bright spot was visible on the camera. At this optimized coupling, the cavity transmission signal did no longer contain any higher-order Gaussian modes induced by imperfect cavity coupling. Now the observed signal was rather only the sum over all occurring fundamental modes within the considered spectrum.

At this point, the scanning frequency was turned down to a value which is also resolvable by the human eye so that the alternating modes could be observed on the camera picture. Next, additionally to the camera, a photo diode was employed by means of a beamsplitter in order to detect the optical power of the cavity output and to plot it on the oscilloscope together with the scanned piezo voltage range. Resulting plots are depicted in figure 3.20[42].
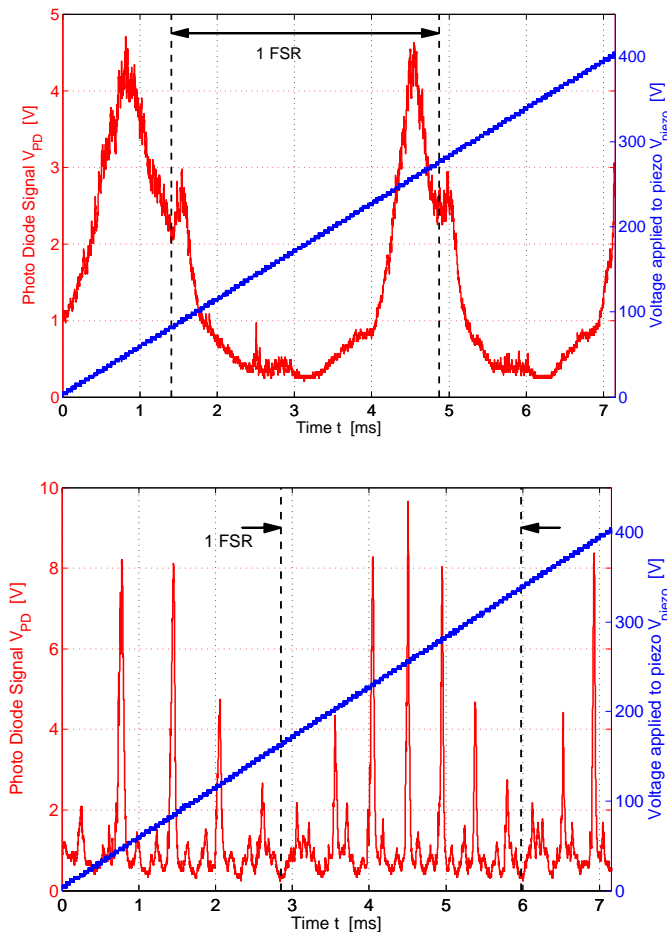
FIGURE 3.20: *Measurement of the cavity output signal using the filtered beam after fibre transmission.* While the cavity length was scanned over the full possible range (blue line showing voltage V_{piezo} applied to the piezo) the optical power of the cavity output signal was monitored on the photo diode (red). One free spectral range is marked by two dashed lines. The upper plot represents the measurement directly after cavity coupling was optimized. After less than a minute the signal already revealed the presence of further modes (lower plot).

---

[42] In this context, it should be noted that the measured curves have not been plotted as functions of the wavelength or frequency as it is typically done. This is due to the fact that the type of piezo and thus its characteristic electro-mechanical relation have not been known exactly and the measurement of one FSR in terms of the piezo voltage was not considered to be precise enough. Anyway, these plots were not supposed to be analyzed quantitatively but only consulted for qualitative evaluation of the mode stability of the laser beam.

3.7.5 Results and Conclusion

The upper plot in figure 3.20 was detected immediately after optimized cavity coupling. However, after less than a minute the signal regularly changed in the way that much more peaks arose within one free spectral range as it can be seen in the lower plot. By means of the detected camera picture it could be confirmed that all of them corresponded to fundamental modes. Furthermore, the occurrence of this multitude of modes could not be reduced by optimizing cavity coupling again.

These findings highly suggest that the deterioration of the cavity transmission signal must have be inherent to the laser beam itself. A bad cavity performance should not be considered as a possible cause for this observation since the SFPC was found to work very reliable in its application to the 780 nm light.

The occurrence of several peaks can be explained in the following way: If the laser diode emits several modes which correspond to different wavelengths, these modes will be resonant with the cavity at distinct resonator lengths. If the cavity is now scanned over the full free spectral range, all of these existing modes are tuned to resonance and become observable in the transmission signal.

Variations of the diode's operating parameters namely its supply current I_{LD} and temperature did not yield any improvement of the output in terms of a reduced number of detected peaks. Instead, at distinct current or temperature settings the output was deteriorated even more.

Based on all the results that have been gained in the context of mode investigation, it can definitely be stated that this particular laser does not perform in the specified way. In fact it emits light at a time-varying number of different wavelengths.

3.8 Optical Feedback

Finally, one last feature should be discussed that was regularly observed during investigations of the laser diode, especially in measurements of the optical power. Here regularly high-frequency noise was detected in the intensity signal. This disturbance could not be eliminated by means of the intensity stabilization which suggests that the signal fluctuates on time scales that are not covered by the lock's bandwidth.

Moreover, fluctuating laser currents have certainly not been the reason for the noise since the driver output was measured to be very stable. Therefore, it was strongly assumed that the noise was induced by optical feedback into the cavity. Up to now, it was tried to avoid the use of an optical isolator in order to provide for a maximum of power for the realization of the dimpled ODT. However, the high noise amplitude suggested that the application of an optical isolator is inevitable.

3.8.1 An Optical Isolator

To begin with, the working principles of an optical isolator should be briefly outlined:

An optical isolator is a device capable of suppressing transmission in reverse direction so that light can only pass in forward direction. Thus, it can be used to prevent unwanted optical feedback into precedent optical components such as laser diodes. Thereby, the degree of isolation, also known as return loss, is determined by the isolator's design and typically amounts to values higher than 30 dB.

The phenomenon of one-way transmission of light rests upon an magneto-optic effect, the so called Faraday effect which describes the rotation of the light polarization by an angle of $\alpha = V \int \vec{B} \cdot d\vec{r}$ as a consequence of applying a magnetic field $\vec{B}$ where V denotes a characteristic material constant, the Verdet constant [74]. In case that the field is both homogeneous and isotropic within the medium of length d, this expression simplifies to $\alpha = V|\vec{B}|d$.

This physical effect is exploited inside the isolator's building block, the so called Faraday rotator. For the use in an optical isolator the parameters are typically chosen in such a way that $\alpha = 45\,°$.

Optical isolators exist in different versions: For example, they can be sensitive to input polarization according to the way of internally separating the propagation directions. Furthermore, in order to enhance an isolator's suppression performance, they can also comprise two Faraday rotators. These latter types, which can feature degrees of isolation of more than 60 dB are called double-stage isolators.

Typically, the use of optical isolators will to some extent implicate insertion loss in forward direction which is mainly caused by imperfect polarizers and slightly imprecise polarization rotation [75]. These factors also influence the return loss.

Of course, the optical isolator performs best on a distinct wavelength range. Thus, regarding the application to the laser diode here, it should be noted that the degree of isolation might be worsened by an unstable wavelength or by the fact that the laser beam is composed of more than one single wavelength. Therefore, it was assumed that in connection with the laser diode an optical isolator would most likely feature both a reduced degree of isolation and some amount of insertion loss.

3.8.2 Feedback Suppression

Next, a double-stage optical isolator[43] was inserted into the optical path directly behind the laser diode in order to suppress the permanent optical feedback observed so far. By adjusting the relative orientation of the polarizer in the middle, the isolation performance was optimized to maximum transmission. In this context it should be mentioned, that this adjustment does not necessarily imply maximized suppression in reverse direction [74]. However, due to the fact that the diode's output power was already near the marginal value for generating a substantial dimple, maximum transmission instead of optimized suppression was declared to be of first priority.

After optimization, the optical power was measured at a laser current of 192.5 A for three configurations:

1. First the power without using the optical isolator was determined to be 146.0 mW. This value serve as a reference which the following measurements can be compared to.

2. Next, after inserting the isolator which first has been optimized to transmission, the optical power declined to a value of 121.5 mW. This corresponds to an insertion loss of 0.798 dB which is well below the specified maximum value of 1.4 dB[44]. Furthermore, in this setup the corresponding fibre output was measured to be 59.5 mW. Such a beam would finally yield a dimpled ODT depth of 128.8 μK compared to 156.7 μK without

---

[43] Type: *Laser 2000*, I-80U-4

[44] According to the data sheet, the particular type of optical isolator that has been used here provides for an isolation of at least 60 dB, an insertion loss not exceeding 1.4 dB and a transmission of typically 81 % [76].

optical isolator and 74.3 μK for the crossed ODT. Consequently, with the optical isolator inserted into the optical path, presumably it would not be possible to double the dipole trap depth.

3. Finally, the whole optical isolator was turned around in order to determine the degree of isolation. In this arrangement, the optical power in the beam amounted to 15.5 μW which results in an attenuation of 39.74 dB compared to the case without isolator. As anticipated for the reasons outlined above, the isolator's capabilities can by no means be exploited to the full extent. Rather, this measurement revealed a degree of isolation which is significantly smaller than the specified value of more than 60 dB [76].

By applying the isolator to the laser diode, the feedback could indeed be reduced considerably. However, judging from the detected signal on the photo diode, optical feedback still persisted to a small extent, even though at a smaller frequency. This observation suggests that either the degree of isolation has not been sufficient or that the fluctuations are indeed caused by unstable mode emission.

3.9   Final Conclusion

Finally, after having performed a comprehensive and systematic characterization of the laser diode, it can be concluded that the chosen *Thorlabs* photo diode is presumably not suitable for the realization of the dimpled optical dipole trap.

Especially based on investigations of the mode structure using the cavity the claimed single transverse mode operation could not be verified. Rather, it was observed that the emitted beam consists of a time-varying amount of modes at different wavelengths. This in turn would translate to fluctuations of the dipole potential and thus to unwanted heating of the trapped atoms.

Another problem which would deteriorate the trap performance even more, is the constantly detected optical feedback into the laser diode leading to permanent occurrence of considerable intensity noise. Generally, optical feedback really is an important aspect to be taken into account for the application of semiconductor lasers [77] that should possibly be suppressed by means of an optical isolator. However, in this particular application, it is in fact arguable whether it makes sense to use an optical isolator or not due to additional insertion loss.

In the configuration without isolator, though, the degree of heating will probably become unacceptable.

Considering this variety of accumulating issues, it was concluded that the diode does not at all meet initial expectations that were based on its specifications. In their entirety, the observed problems suggest that the diode will most likely not operate reliable enough for the purpose of a dimpled ODT. Therefore, at this stage, the laser diode implementation was ultimately abandoned.

Chapter 4

Final Realization
Using Toptica TA-SHG pro

Instead of attempting to realize the initial plan to use the laser diode without high chances of success, another way of implementing the dimpled trap was tackled. The new light source used for generation of the dimple beam is a Toptica TA-SHG pro *diode laser system which can definitely be expected to provide very reliable light emission with respect to both the wavelength as well as constant emission of the Gaussian fundamental mode.*

This chapter starts with briefly outlining the required optical setup. This also comprises one new aspect, namely the importance of polarization and how its conservation has been achieved.

As anticipated, the dimple beam generation by means of this laser source turned out to be fruitful so that final experimentally obtained characteristics of the dimpled trap can be presented after outlining necessary alignment tasks and adjustments of the experiment control.

4.1   Laser and Optical Setup

According to the requirements for establishing the dimpled ODT (see section 1.2.2) the corresponding laser source should provide an output beam at sufficiently large detuning which is in turn mainly limited by the maximally available optical power: Pursuant to equation (1.20), large detunings necessitate higher optical laser intensities in order to obtain the same trap depth.

In case of the *Toptica* laser system, it can be chosen between two different wavelengths: The TA output at 855.2 nm and the SHG beam at 427.2 nm. Only the first option would yield red-detuning which is essential for producing an attractive potential by means of a focussed Gaussian beam. This is why only the TA output beam came into consideration for the generation of the dimple laser beam. The SHG stage was never used within the scope of this thesis.

At temperature and current settings of $T_{DL} = 21.4\,°\mathrm{C}$ and $I_{DL} = 127\,\mathrm{mA}$ for the seed diode laser and $T_{TA} = 19.9\,°\mathrm{C}$ and $I_{TA} = 2320\,\mathrm{mA}$ respectively for the tapered amplifier, the output power was measured to be 882 mW directly behind the casing. According to the *MATHEMATICA* simulation this beam should definitely be suitable for generating the dimple in the optical dipole trap.

According to experience with exactly this laser system, its output frequency is stable on the order of about 300 kHz without employing any locking technique. By means of a permanent connection to the wavemeter, this empirically obtained linewidth could also be confirmed in the setup here. Since this linewidth was considered to be stable enough for the dimple beam, no laser frequency stabilization was set up.

Subsequently, the optical setup for the *Toptica* laser will be briefly described similarly to the way it was presented before in the context of the *Thorlabs* laser diode. Again this part is split up into two parts, first the optical assembly which is placed on the laser table and afterwards the optics on the experiment table will be presented.

4.1.1 Pre-Fibre Optics

Similarly to the case of the laser diode, all optical components in front of the fibre are necessitated either for establishing remote access and control of the beam intensity or for final fibre coupling. The assembly is illustrated in figure 4.1.

As usual, remote access is obtained by means of the same AOM used before. For this purpose, the beam first passes through a simple telescope consisting of two spherical lenses with focal lengths of $f = 100$ mm and $f = 30$ mm which adapts its diameter to the aperture of the AOM. After alignment, the power in the first order of diffraction was measured to be 640 mW. Finally, this fraction of the beam is coupled into a single-mode fibre[45], which is identical to the one used so far but five times longer. The power

FIGURE 4.1: *Optical pre-fibre setup for the* Toptica *diode laser. After leaving the laser the beam gets horizontally polarized by passing the PBS. The final wave plate in front of the in-coupler is required for fine-tuning of polarization maintaining fibre coupling. The purpose of all remaining optical parts is described in the text.*

behind the fibre was measured to amount to 326 mW which is a value that is supposed to produce a decent trap depth.

In order to quantify leakage light, the AOM was digitally turned off at the computer control via the AOM driver and the optical power was measured behind the fibre. There, a tiny amount of 2.56 μW was detected whereof 16 nW account for background light. This persistent fraction will produce a permanent dipole trap even if the ODT is turned off completely via the AOM. However, the corresponding trap frequencies of $(\omega_x, \omega_y, \omega_z) = 2\pi \cdot (0.10\,\text{Hz}, 9.10\,\text{Hz}, 2.57\,\text{Hz})$ are not expected to impair the performance of the experiment at all.

4.1.2 Post-Fibre Optics

Due to the filtering property of the single-mode fibre, the shape of the beam after fibre transmission will always feature the same profile independent of the used light source. Only the frequency of the light is changed correspondingly.

Therefore, the optical components on the experiment table which succeed the fibre did not have to be adjusted when the *Thorlabs* diode was replaced by the *Toptica* laser. Rather, the setup on the experiment table remained exactly similar to the one shown in figure 2.5.

---

[45] Type: *OZ Optics*, PMJ-3AF3AF-850-5/125-3A-15-1

4.1.3 Polarization Maintenance

Between both locations, namely the laser table where the light source is placed and the experiment table, the light has to be transferred in such a way as to conserve all of its properties as well as possible. This does not only mean to maximize the fibre output power for example, but also to preserve the polarization of the input light. As outlined below in the context of the present setup, this condition requires a slightly more sophisticated technique than simple fibre coupling.

Required Polarization

For the dimple beam setup, polarization maintenance becomes important due to the way of introducing the dimple light into the experiment chamber, namely by means of the polarizing beamsplitter cube. In order to provide maximum optical power in the chamber, the beam has to be polarized in such a way as to maximize reflection at the cube, that is vertical polarization here. This polarization should already be adjusted right at the beginning and maintained throughout the whole subsequent optical setup.

Appendix D presents further details on polarization maintaining fibre coupling. Before describing the coupling technique itself and how to optimize it, some basics of polarization maintaining fibres are given in order to make clear why the optimization of coupling can be carried out as suggested.

After having performed fibre coupling in the way described there, long-term stability of the polarization maintaining light transmission could be confirmed by monitoring the detected ratio between cube-transmission and -reflection over a period of several hours. Fluctuations were observed to be smaller than 1%.

In the next step the intensity lock had to be set up in its final configuration:

4.1.4 Intensity Stabilization

Optimization

First of all, the stabilization loop's performance had to be optimized once again according to the scheme described in section 3.4. Therefore, a rectangular control voltage signal $V_{control}$ with an amplitude of 1.9 V and a frequency of 50 kHz was applied to the second input channel of the PID by means of the oscilloscope's built-in function generator, called *WaveGen*. By optimizing the gain of both the P- and I-stage the loop's response times could be minimized to a delay time of $\tau_{delay} = 890$ ns and a rise time of $\tau_{rise} = 272.5$ ns for analog switching. These values are in the same range as in the application to the *Thorlabs* diode. Both the control voltage and the resulting voltage signal generated by the photo diode are plotted and pictured on the left hand side in figure 4.2.

After optimization, a long-term measurement of the optical power behind the experiment chamber was performed which is shown in the right plot in figure 4.2. This over-night log yields intensity fluctuations of at most $\pm 1.15\%$ on the timescale of hours.

Setting the Working Voltage

As explained before in section 3.4.2, the last step which has to be carried out in order to determine the working voltage of the intensity stabilization and finally put it into execution, is
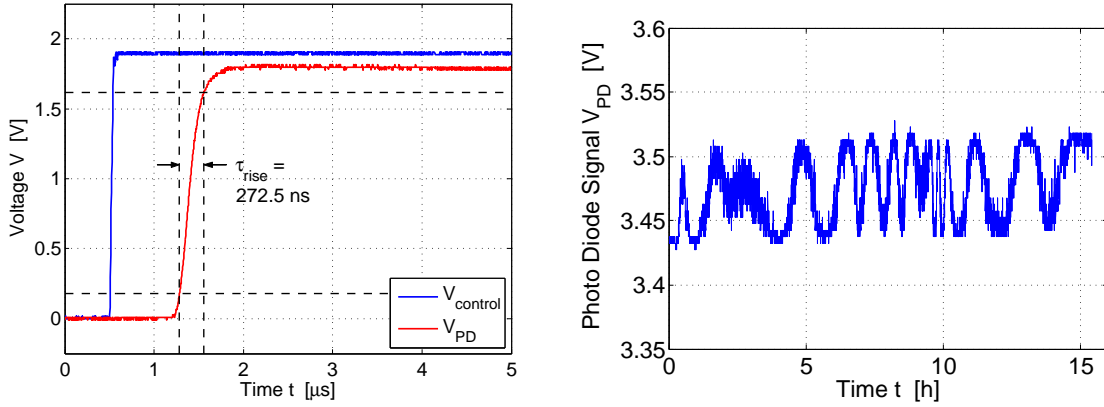
FIGURE 4.2: *Left: Measurement of the response of the intensity stabilization loop after optimization. The measurement procedure is exactly the same as already described in the context of the laser diode (compare caption of figure 3.7). **Right:** A long-term measurement of the optical power of the dimple beam behind the experiment chamber reveals only small intensity fluctuations.*

represented by a final calibration, that means to identify the relation between the generated photo diode voltage and the corresponding optical power of the dimple beam behind the chamber.

For this purpose, first of all the optical power of the dimple beam was measured as a function of the AOM driver input voltage $V_{AOM,Driver}$ both in front of and behind the experiment chamber by means of the power meter. Therefore, a low-frequency[46] triangular signal that covers the AOM driver's full input voltage range $V_{AOM,Driver} = [0\,\text{V}, 10\,\text{V}]$ was applied to it by means of the function generator.

Afterwards, the photo diode was used instead of the power meter in order to detect the optical power behind the chamber, again by applying the same input signal to the AOM driver. The generated photo diode voltages V_{PD} were then plotted as a function of $V_{AOM,Driver}$. All three measurements are shown in figure 4.3.

The calibration curve is obtained by relating each value measured with the power meter to the photo diode signal that corresponds to the same AOM input voltage. All resulting data pairs can then be put together to the calibration curve as depicted on the right in figure 4.3. Thus, calibration just means to plot the data of the power meter measurement as a function of the photo diode signal.

Remark about Non-Injective Behaviour of Calibration Curve

The calibration curves which are plotted on the right in figure 4.3 show one peculiarity which is closely connected to set theory, a special branch of mathematics. Obviously, in the measurements shown on the left in 4.3, usually more than only one optical power value (y-values, representing the "codomain") is assigned to the same AOM driver voltage

---

[46] In contrast to the bandwidth measurements, here a low frequency of 0.5 Hz was chosen in order to avoid impairment of calibration measurements due to delay times.
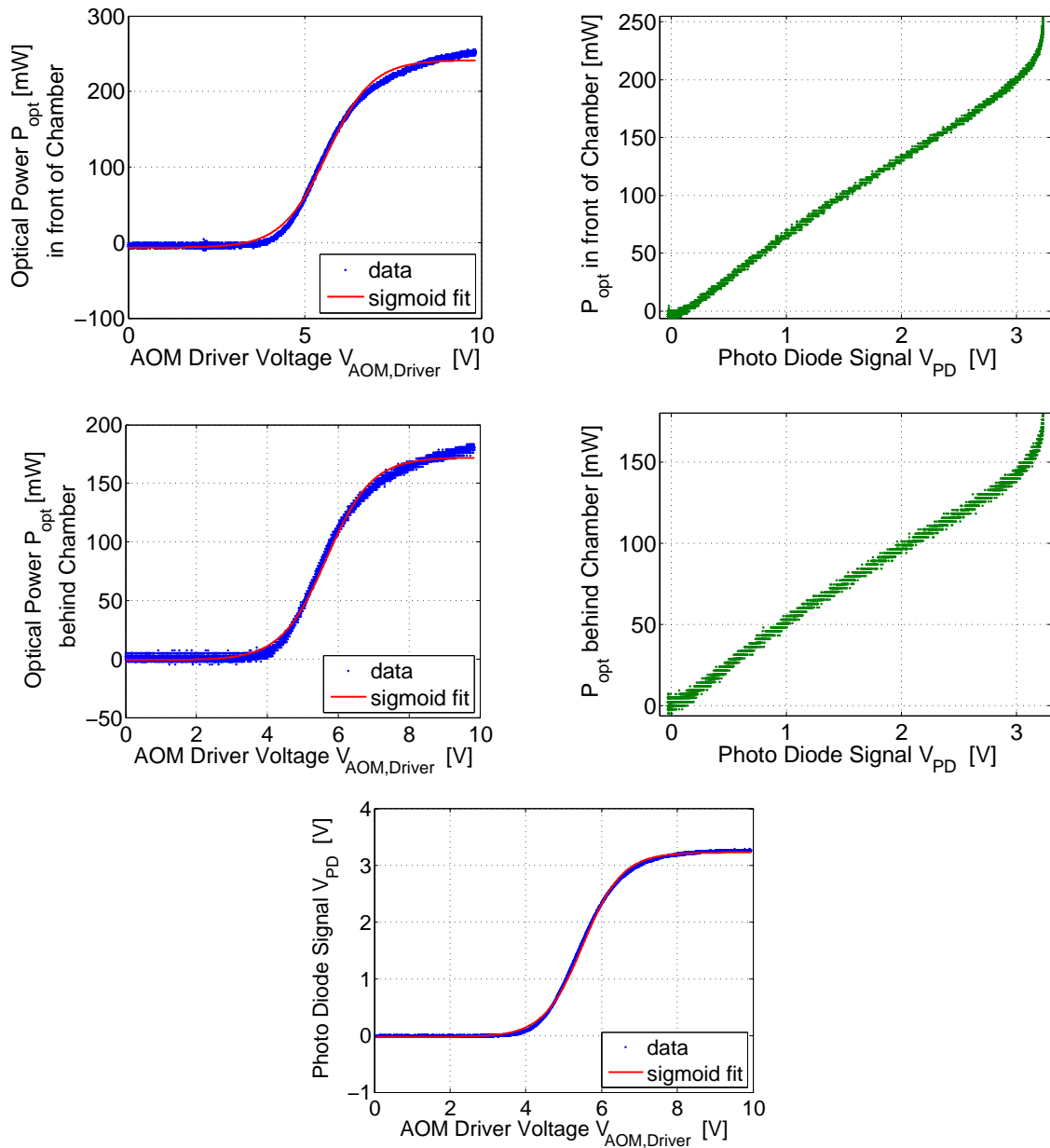
FIGURE 4.3: ***Calibration of Dimple Beam Power.*** *For evaluation of the green calibration curves (plots on the right) of the dimple beam the optical power was first measured in three different ways as a function of the full range of the AOM driver's input voltage $V_{AOM,Driver}$: In front of (top left) and behind (middle left) the experiment chamber using the power meter and behind the chamber using the photo diode (bottom). All three plots show both the measured data (blue) and a sigmoid fit in red. The calibration curves of the optical power both in front of and behind the chamber can then be obtained by plotting the respective P_{opt} data set against the photo diode signal V_{PD}.*

(the "domain") on the x-axis. Thus, the function is not injective which basically means that it does not preserve distinctness.

The same is true vice versa for the inverse function, that means several AOM driver voltage values (x-values) belong to the same optical power value on the y-axis. Speaking in terms of domain and codomain, this means that the inverse function, which maps $V_{AOM,Driver}$ (now the codomain) to the values for the optical power (the domain), is as well not injective.

This specific feature originates from the way of acquiring the underlying data and calculating the calibration curve: As explained, the final calibration relation is based on two separate function, either the optical power or the photo diode voltage as functions of $V_{AOM,Driver}$. The underlying data sets for each of these two functions were obtained in the following way:

All voltages, that means $V_{AOM,Driver}$, the optical powers measured with the power meter and finally the photo diode signals, were monitored on the oscilloscope at different input channels. Typically, if one particular input channel is to be plotted, the input voltages are traced as a function of the acquisition time. Thus, if the time steps for data acquisition become very small compared to changes of the input signal, it happens that successive input signals differ by an amount smaller than the resolution. This is especially the case, if the input measuring range becomes large. Consequently, the same input voltage might be recorded at later times again.

If, subsequently, different input channels are plotted against each other, as it was done for the optical power measurements shown in figure 4.3, this matter of fact causes the resulting function to be non-injective since several y-values (that means belonging to a particular input channel) can then be associated to the same x-value which belongs to another channel.

Finally, the calibration curves on the right in figure 4.3 have been obtained by plotting y-data sets of separate (already non-injective) functions shown on the left against each other, namely the optical power against the photo diode signal. Relating these non-injective functions to each other necessarily has to result as well in a non-distinct mapping. This explains the broadening of the calibration curves.

Obviously, the resulting relation between optical power and photo diode signal does not necessarily have to exhibit a linear behaviour. This is due to the fact that the voltage generated by the photo diode does not increase linearly with the optical power over the full range.

Based on these calibration curves the PID control voltage could be set to the voltage which corresponds to the desired optical power of the dimple beam. This step finalized the whole setup for the dimple beam so that now everything was prepared to put the dimpled ODT into operation.

4.2 Realization of the Dimpled ODT

4.2.1 Dimple Beam Alignment

After having commissioned the laser source and set up corresponding optics, the objective had to be aligned in such a way that the dimple beam is focussed exactly to the centre of the atomic cloud. Ideally, this should be the case by positioning the objective according to the results which have been obtained from the *Zemax* calculations and which are presented

in table 2.3. These investigations revealed that the alignment of the lenses is a crucial parameter for optimized performance of the objective. However, as already anticipated there, the experimental positioning of the lenses became challenging due to their mounting inside a metal tube. Consequently, precise measurements of both the lenses' relative as well as absolute distances to the experiment chamber were partly obstructed by the setup so that perfect alignment turned out to be demanding.

Fine-tuning of the dimple beam was performed according to the following procedure:

The use of light at a wavelength of 855.2 nm, which is part of the infrared spectrum, prohibits to directly observe the laser beam by the human eye. Furthermore, the detection of effects of the trapping light on the atoms is also impeded due to the fact that its wavelength is typically chosen such that the light only changes external degrees of freedom of the atoms by generating an additional optical dipole potential. It is not capable, though, of manipulating internal degrees, for example by exciting transitions or driving Rabi oscillations. The only exception to this is the Stark effect which induces shifting and splitting of spectral lines due to strong external electric fields.

For this reason, alignment was initially performed by attaching another laser system[47] to the fibre which emits light at a wavelength of about 780 nm. This laser beam, in contrast to the dimple beam, is capable of exciting atomic transitions which belong to the characteristic Rubidium D_2-line, that means the transition between the $5^2S_{1/2}$ and the $5^2P_{3/2}$ state. Thus, now the interaction between light and matter can be made visible by means of absorption imaging.

For the purpose of alignment, the light emission was not fixed to a certain wavelength but the laser frequency was rather permanently tuned around resonance by means of the respective laser control module. This ensures highest absorption rate by resonantly exciting the full range of allowed transitions also including shifted levels.

Now the beam was walked by adjusting both the mirror behind the cylindrical telescope and the upper periscope mirror in order to align the focal position of the beam. Simultaneously, the atomic cloud was detected by absorption imaging so that effects of walking the beam could immediately be observed [48]:

Once the beam is aligned in such a way that first parts of its cross section begin to overlap with the cloud, scattering of photons at the atoms will set in. If then the light power is sufficiently high[49], all atoms which are addressed by the laser are sort of 'shot away' due to momentum transfer. This impact on the atomic cloud can then be observed by using absorption imaging of the x-y-plane.

Once the 780 nm-test beam hit the cloud for the first time, in an iterative procedure its optical power was successively reduced and at each power the focal position was optimized anew. The reason for carrying out alignment like this is that imaging becomes more sensitive at reduced power. If the light power exceeds the value for saturation, the maximum amount of atoms is addressed. However, at smaller power, the inhomogeneous density of the cloud will

---

[47] Type: *Toptica*, TA pro

[48] The exact wavelength used for absorption imaging is 780.247 nm which is resonant with the transition between the hyperfine states $F = 2$ to $F' = 3$. Although possessing roughly the same wavelength as the test light for alignment, the imaging light originates from yet another laser source.

[49] In the beginning the light power should be turned up as far as possible via the responsible AOM in order to provide best detectability.

gain influence in terms of higher detection signals the closer the focus comes to the centre of the cloud. In this way, the vertical focal position could be adjusted very precisely.

Of course, so far adjustment of the focal position was restricted to the transverse plane that means to displacements in y- or z-directions. Alignment along the direction of propagation can only be performed by shifting focussing lenses or, the whole objective respectively. However, due to chromatic aberration, the focal position of the 780 nm-beam will not conform to the one for 855.2 nm. This is why now the laser source which is applied to the optical dimple setup was switched back to the original 855.2 nm-dimple light. Fine tuning of the focal position along the x-axis was then accomplished by altering the distance of the whole objective relative to the experiment chamber that means by displacing the mounting tube which contains both lenses. Absorption images of the cloud, which have been taken according to the time-of-flight (ToF) technique that means at a certain delay after switching off the ODT, revealed that the focus was initially located slightly in front of the atoms. Therefore, the optimal longitudinal position could be established by moving the whole objective towards the chamber and thereby pushing the focus towards the cloud.

As a side note it should be mentioned that the objective was now aligned with regard to perfect dimple beam alignment instead of second possible purpose of high-resolution horizontal imaging. Consequently, in this configuration the focus of the imaging light is expected to be located about 200 μm in front of the centre of the atoms. This value can be extracted from the analysis of chromatic aberration of the objective which has been presented in section 2.4.3 and listed in table 2.4.

4.2.2 Loading Atoms into Dimpled ODT

After optimization of alignment the experiment sequence had to be modified and extended in order to allow for efficient transshipping of the atoms from the crossed trap into the dimpled one. Therefore, especially the following four channels which control four parallel but related processes had to be considered. Their timing schedule is sketched in figure 4.4.

1. After state preparation the atoms are laser cooled in the **MOT** by driving the cooling transition[50] between the states $(5^2\mathrm{S}_{1/2}, F = 2)$ and $(5^2\mathrm{P}_{3/2}, F = 3)$ in a red-detuned way (compare figure 2.1). As a consequence of subsequent spontaneous emission they will lose energy due to a net loss of momentum during one cooling cycle.
   However, the atoms will not necessarily decay back into the initial state. Rather, a small fraction will leave the cycle by decaying into the ground state level that belongs to the quantum number $F = 1$. Therefore, the cooling cycle is closed by a repumper which drives the transition from $(5^2\mathrm{S}_{1/2}, F = 1)$ to $(5^2\mathrm{P}_{3/2}, F = 2)$.

2. However, as visualized in figure 4.4, the **repumper** is not turned on during the complete cooling period but ramped down earlier so that the atoms will afterwards only be addressed by the MOT light field. This is because after a certain time cooling and heating processes in the MOT which are induced by transfer of momentum will equilibrate and compensate for each other. At this point the so called Doppler temperature limit will be reached where the atoms cannot be cooled any further.

   Thus, the atoms now have to be loaded into the dipole trap where evaporative cooling is performed. Therefore, they are forced to leave the cycle by transferring them to a state

---

[50] For an overview of the most important states and transitions refer to figure 2.1.

where they do not feel the MOT light field anymore. This is achieved by ramping down the repumper while the MOT light remains unchanged. This inherently results in the transfer to the $F = 1$ state which is a "dark" state for the MOT lasers.

At the same time, the repumper should not be ramped down too early that means prior to the point where the atom's temperature is low enough for efficient evaporative cooling.
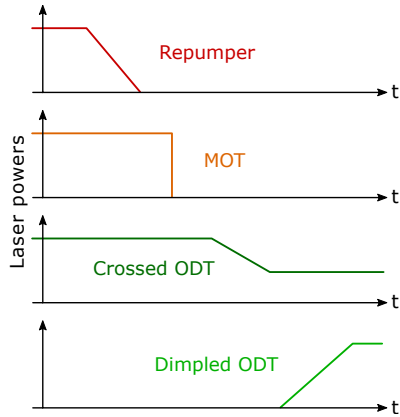
FIGURE 4.4: *Schematic of an excerpt of the experiment timing sequence. The illustration only comprises the timing of the four most important experiment parts with regard to loading of the dimpled ODT. The y-axes specify the power of the respective light field. (Timing is not true to scale.)*

3. The crossed laser beam which is responsible for producing the **crossed dipole trap** is turned on right from the beginning as the dipole potential anyway will not influence the atoms as long as they still feel the MOT lasers and as long as their temperature is still high compared to the dipole trap depth.

 Once the atoms have been transferred to the crossed ODT, evaporative cooling can be performed by adiabatically ramping down the laser power to a certain level. This will reduce the trap depth so that only atoms with a maximum temperature that corresponds to the present depth can be kept inside the trap. This cooling technique intrinsically comes at the expense of atom numbers.

 The performance of experiments based on EIT such as the one here, strongly depends on the optical depth (OD) of the atomic medium. Since the area of confinement stays constant during evaporative cooling the atom number becomes a crucial parameter for providing high OD at a given absorption cross section [78]. This is why evaporative cooling should not be pushed too far. High optical depths should also be regarded as benchmarking the transfer to the last stage of preparing the cloud, the dimpled ODT.

4. Before the atoms are transshipped from the crossed into the **dimpled ODT**, they are cooled down further by Raman sideband cooling (RSC), a quite elaborate sub-recoil and low-loss cooling technique that basically makes use of Raman scattering within the framework of a superimposed lattice. As it comprises numerous operational steps including switching of lasers and magnetic fields according to a sophisticated timing schedule, this technique will not be described in more detail here. Rather, reference should be made to the Bachelor thesis carried out by Christoph Braun [79].

 After Raman sideband cooling the atoms are transshipped into the dimpled dipole trap by ramping up the intensity of the dimple beam as sketched in figure 4.4. This is managed by regulating the control voltage at the PID of the intensity lock. Appropriate timings and ramping parameters have to be optimized in an iterative and empirical way by monitoring related effects, especially on the atom number.

4.3   Results

Execution of this optimized loading sequence of the dimpled ODT yields an atom number of about 2.5×10^4, a cloud length of less than $2\sigma_y \approx 24\,\mu$m and an unchanged radial width of maximally $2\sigma_x \approx 50\,\mu$m. These values can be extracted from the absorption image pictured in figure 4.5 and the time-of-flight measurements which are presented below[51]. For comparison figure 4.5 additionally shows the image of the elongated cloud in the crossed ODT. Both pictures have been taken by means of vertical absorption imaging from top of the setup.

Based on experimental measurements of the EIT spectrum it was evaluated that the optical depth in the dimpled trap amounts to $OD = 10$.

Additionally, the temperature of the cloud has been determined by means of time-of-flight measurements. Therefore, the trap is turned off and the atomic cloud are subsequently observed during free expansion by means of absorption imaging. Assuming a non-interacting ensemble and neglecting any kind of loss, the atoms' thermal energy is completely converted to kinetic energy so that they escape from the region of confinement at a velocity that is given by their previous temperature T. If σ_v is the Gaussian width of the velocity distribution this relation is given by

$$\frac{m}{2}\sigma_v^2 = k_B T \tag{4.1}$$

where m denotes the atomic mass and k_B the Boltzmann constant [80].

During free expansion the cloud size in terms of its Gaussian width σ_i $(i = x, y)$ will then develop according to

$$\sigma_i(t) = \sqrt{\sigma_{i,0}^2 + \sigma_v^2 t^2} \tag{4.2}$$

which after long delay times will show a linear behaviour proportional to σ_v. Thus, the temperature can be obtained from the slope of a linear fit to the observed time development of the cloud width.

Figure 4.6 shows time-of-flight measurements of the atoms in the dimpled trap after two stages of Raman sideband cooling, for both the x- and y-direction. The corresponding set of measurement data consists of five time-of-flight runs where each of them again comprises twelve data pairs (t_{ToF}, σ_i).

Obviously, the cloud size in x-direction is initially bigger than in y-direction. Due to this difference in compression of the atoms, the respective energy distribution will differ as well so that the cloud will expand at different speed in both directions. This could be confirmed by evaluating the measured data which yielded temperatures of $T_x = 5.43\,\mu$K in x- and $T_y = 8.08\,\mu$K in y-direction.
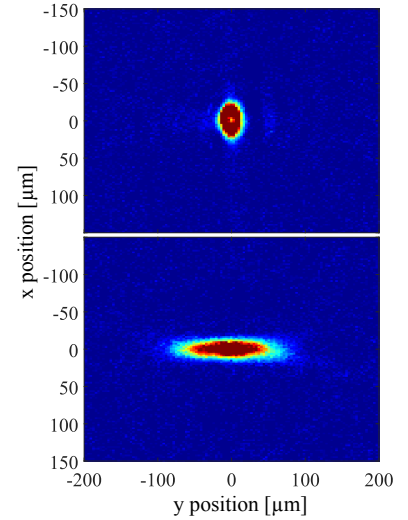
FIGURE 4.5: *Absorption images of the atomic cloud. The pictures that have been taken by means of vertical absorption imaging show the atomic cloud that is confined in either the dimpled (top) or the crossed (bottom) ODT. The origin of the coordinate system lies in the centre of the cloud; x is the dimple beam propagation direction.*

---

[51] Recent measurements reveal that significantly smaller cloud sizes can be reached by further optimizing the loading sequence. Furthermore, it should be noted that these lengths scales are close to the resolution of the imaging system. For this reason the measured values should be considered as upper bounds.

Additionally, figure 4.7 shows exemplary absorption images of the cloud taken from the first run at six successive time of flights.
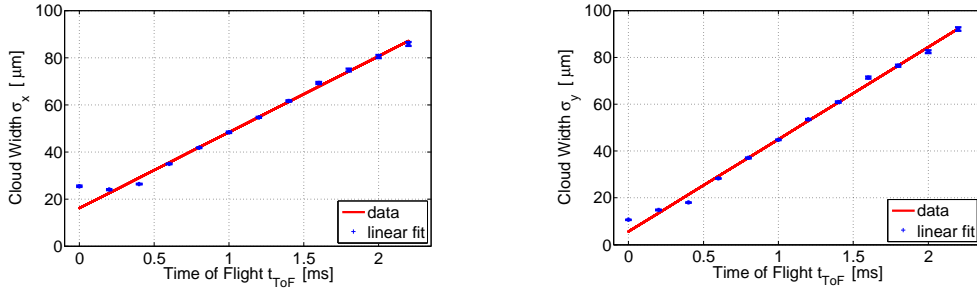
FIGURE 4.6: *Time-of-flight measurement of atomic cloud in dimpled ODT after Raman sideband cooling. For both horizontal directions x (left) and y (right) the width σ of the cloud has been extracted from absorption images (compare figure 4.7) at different times t_{ToF} after releasing the atoms from the trap (blue data points). The temperature of the ensemble can be evaluated by fitting a linear function to the data points at higher t_{ToF} (red line).*
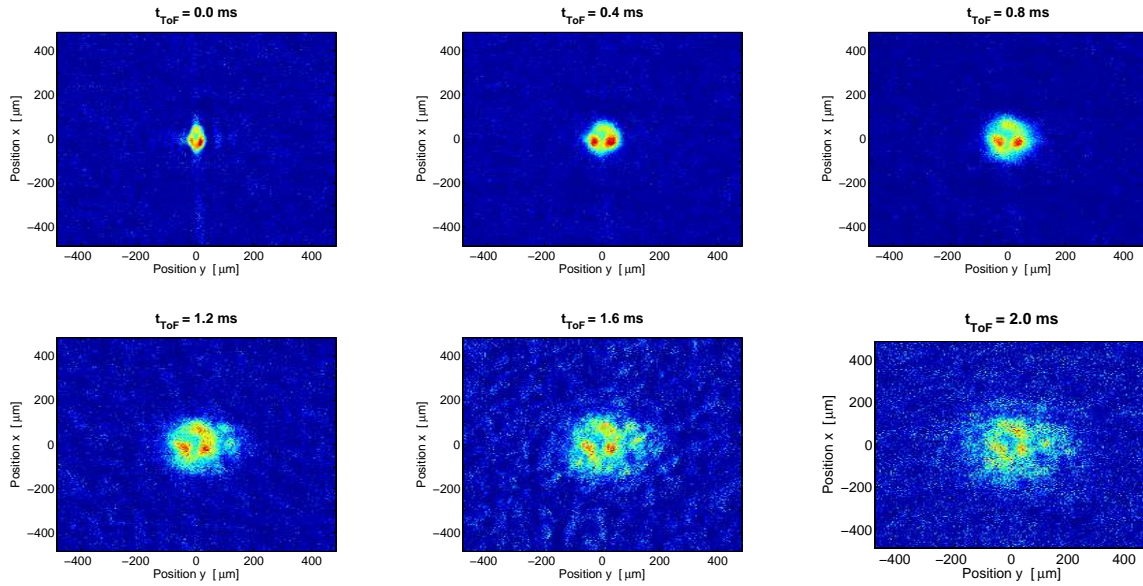
FIGURE 4.7: *Absorption images taken during time-of-flight measurement. The expansion of the released cloud is monitored by means of vertical absorption imaging which is shown here for six different time of flights t_{ToF}. The cloud width σ can be extracted from these pictures in order to evaluate the ensemble temperature.*

Eventually, these characterization steps finalized the setup for the new trap configuration. Now, actual measurements using the modified ultracold cloud of atoms could be conducted in order to investigate and answer open questions in the field of quantum optics. Problems which have been studied first, namely the coherent all-optical single-photon transistor and the single photon absorber, are presented in the following part of this thesis.

Part II

Single Photon Gates in the Dimpled Optical Dipole Trap

Chapter 5

Coherent All-Optical Single-Photon Transistor

Practical tasks concerning the modification of the experimental setup have been finalized by the characterization of the dimpled optical dipole trap. The new configuration of the experiment now enables the investigation of various open physical questions and the implementation of respective applications.

First of all, measurements that have finally been conducted in the former optical dipole trap configuration shall be resumed. In order to comply with the course of events during this thesis, the next chapter will treat exactly this plan.

As the actual subject of these measurements relies on a fairly complex and sophisticated physical system, the first part of this chapter briefly outlines the underlying physical processes that are conveniently provided by the combination of the ultracold atomic cloud and appropriate light fields.

Based on this the principle of operation and the corresponding experimental scheme of the particular quantum mechanical application that theses measurements served for, will be presented.

Next, this is followed by explaining in which way the modified dipole potential allows for advancement of this scheme. This basically relies on the fact that it is now possible to account for the intrinsically quantum mechanical aspect of coherence.

Finally, the chapter is closed by outlining which requirements have to be fulfilled in order to realize the enhanced scheme within the present experiment.

5.1   Atom-Light Interaction in the Ultracold Atomic Cloud

Prior to the modification of the optical dipole trap, the existing experimental setup was used in order to realize an outstanding photon gate which has so far only been known from the field of electronics, namely the transistor. This realization, however, does not only satisfy the general transistor tasks of switching and amplifying signals but, which is much more significant, to also incorporate the quantum mechanical nature of the light resulting in an *all-optical single-photon transistor* [81].

Whereas the electronic component is constructed in a fairly simple way, its quantum optical counterpart requires a much more sophisticated setup. This is owing to the fact that its mechanism mainly relies on two distinctive physical phenomena that are provided by the combined features of an ultracold atomic cloud and light fields capable of manipulating the atoms.

The foundation for the first mechanism which is known as electromagnetically induced transparency (EIT) is laid by the level structure of the atoms in the cloud. Based on this and a light field with convenient properties, transmission of photons can be established where they normally experience maximized absorption.

The second phenomenon of Rydberg excitations as well relies on the combination of the atomic properties and photons entering the cloud. By exciting the atom to states with high principal quantum numbers n Rydberg atoms are formed which enhance inter-atomic interaction ranges inside the cloud to scales only known from Coulomb interaction.

In order not to blow up this thesis too much the quite extensive fundamentals of Rydberg physics will not be presented here and basic knowledge is assumed to be known[52]. Only the main effects that are required to explain and understand in which way the new trap setup enables an advanced transistor scheme, are given where appropriate in the course of this chapter. The same is true for the first mentioned phenomenon of EIT.

The combination of both processes, also referred to as Rydberg-EIT, yields an astonishing effect. Indeed, the interplay between the Rydberg medium and appropriate light fields enables the realization of interactions between photons which in free space can normally not be achieved. In contrast, by mapping the photons onto material properties of the Rydberg medium, atomic Rydberg interactions can be exploited to effectively control the behaviour of a light field by single photons that have excited Rydberg atoms inside the cloud. Thus, the whole mechanism is simply based on the atom's capacity of acting as a mediator for realizing inter-photonic interactions and thereby enabling the implementation of a single-photon transistor.

The incorporation of the quantum mechanical nature of the system can only be achieved by boiling the transistor scheme down to the single-particle level by exploiting the very strong and long-range Rydberg interaction which allow for amplifying the effect of a single photon onto several thousands of atoms and thereby make the effect large enough to be measured. Only on this single-photon level the laws of quantum mechanics will then rule the evolution of the system.

Even though the system inherently exhibits quantum mechanical properties, up to now the transistor scheme did not conserve coherence and was therefore referred to as the *incoherent* all-optical single-photon transistor. Before explaining in which way this might be changed, it is necessary to understand the real mechanism of the scheme itself which is explained in the following section.

---

[52] For further study refer for example to [82].

5.2 Incoherent Transistor - Principle of Operation

In contrast to the electronic device that works with arbitrary electric potentials and currents, in case of the all-optical single-photon transistor these input signals are represented by light pulses on the level of only few photons. In order to adhere to the transistor terminology, in the present system a "source" signal is as well controlled by the "gate".

For realizing the transistor tasks of amplification and switching the medium has to provide for a mechanism that enables to control the propagation of several source photon by only one gate photon. Explicitly, this is achieved in the following way in term of the combination of Rydberg excitations yielding strong interactions and EIT which enables to map these interactions onto photons:

Level Scheme and Pulse Sequence

As sketched in figure 5.1 the source light itself comprises two separate pulses, a strong "control" Ω_s and a weak "probe" pulse[53] $\mathcal{E}_s$.

These light pulses feature wavelengths such that in combination they excite a ladder-type three-level EIT scheme consisting of the ground state $|g\rangle$, the intermediate level $|e\rangle$ and an upper level $|r\rangle$ as shown in figure 5.1. In the present case this level scheme is conveniently provided by the Rubidium atoms[54].

Thus, in the absence of any external influences that might induce level shifts, the source probe pulse $\mathcal{E}_s$ will be transmitted through the cloud ideally without loss. As a second consequence of EIT the dispersion curve which is basically the real part of the optical susceptibility and which determines refractive properties of the light, features a steep rising behaviour on resonance (compare right plot in figure 6.1). This effect intrinsically reduces the group velocity of the transmitted photons so that they propagate as "slow-light" polaritons through the cloud.

The inter-photonic control mechanism can now be realized by gating this transmission of EIT-photons:

If an EIT-atom feels any kind of interaction which induces energy level shifts as illustrated in figure 5.1 the corresponding transitions are tuned out of resonance. In this case the condition for lossless transmission is no longer fulfilled so that the source probe photons are scattered at the intermediate level $|e\rangle$.

This represents the basic mechanism that allows for the task of switching photonic signals.

Mediating Interaction Process

So far it has not been mentioned which kind of interaction process serves as mediator for this switching between transmission and scattering that preferably should influence as many photons as possible.

As explained at the beginning the inherent strong dipole-dipole interactions of Rydberg atoms allow for extending the range of inter-atomic interactions to scales known from Coulomb interaction[83].

For long ranges, in the so called van-der-Waals (vdW) regime, where the energy defect between contributing Rydberg levels is considerably larger than their dipole-dipole interaction

---

[53] The latter indication originates in the fact that the corresponding transition is effectively used in order to probe the cloud for Rydberg excitations.

[54] As a reminder, the corresponding Rubidium level scheme is shown in figure 2.1.
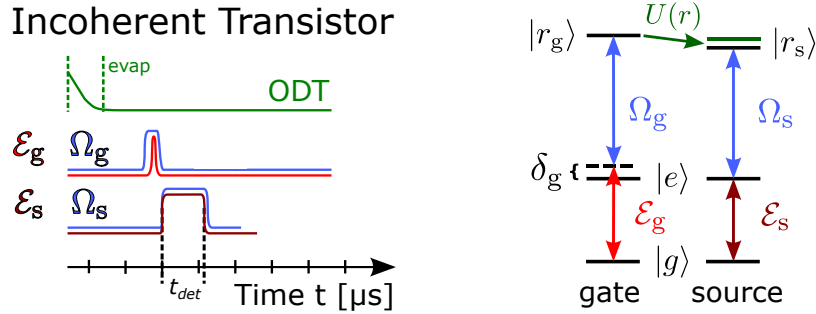
FIGURE 5.1: *Sequence of incoherent transistor. **Left:** Timing sequence of probe $\mathcal{E}$ and control Ω pulses for each the gate (middle, index g) and source (bottom, index s) excitation. Note that the probe pulse is always fully enclosed by the respective control pulse in order to ensure optimized atom-light interaction. Additionally, the green line sketches the power of the crossed ODT showing an evaporation ramp in the beginning. **Right:** The excitation scheme gives an overview of all transitions that correspond to the pulses shown on the left. Refer to figure 2.1 for a more detailed level scheme. The amplitude as well as the sign of the Rydberg level shift which is caused by dipolar interaction depends on the respective C_6 coefficient.*

energy, the energy shift can be well modeled by $U(r) = -C_6/R^6$. The C_6-coefficient is the characteristic parameter serving as a measure for the interaction strength and scales proportional to n^{11}.

If the Rydberg atoms approach each other so much that the interaction energy exceeds the energy defect, the system can no longer be treated within the van-der-Waals regime. Here, the energy shift has a r^{-3}-dependence which is associated with two interacting static dipoles [84].

Without employing any interaction-enhancing processes such as tuning to so called Förster resonances [85], the present transistor scheme is well described by the van-der-Waals model. The interaction range is then parameterized by the Rydberg blockade radius R_b which corresponds to the sphere around a Rydberg excitation in which the interaction energy is still large enough to influence all other atoms inside in such a way as to prevent further excitations due to shifting energy levels [4]. Therefore, it is defined in terms of an equalization of the interaction energy and the linewidth γ of the excitation and expressed by [7]

$$R_b = \left| \frac{\gamma C_6}{\Omega_0^2} \right|^{1/6} \tag{5.1}$$

where $\Omega_0 = \mathcal{E}\Omega/(2\delta)$ denotes the effective single-atom two-photon Rabi frequency of the corresponding EIT transitions which are driven by the probe and control fields with $\mathcal{E}$ and Ω at single-photon detuning δ from the intermediate energy level $|e\rangle$ [18], [86].

In order to return to the transistor application this Rydberg interaction process can now be exploited to implement the amplification task: If the upper EIT-level $|r_s\rangle$ is chosen to be a Rydberg level[55] the long-range character of the interaction allows for enhancing the region of influence, thereby offering the control of the transmission of several EIT-photons in the following way.

---

[55] This explains why the upper level is indicated by r for Rydberg.

Once one atom in the cloud has been excited to a Rydberg level [56] $|r_g\rangle$, all atoms inside the corresponding blockaded area can no longer provide the unperturbed EIT-level scheme so that all source photons entering this sphere will be scattered and the detection signal of transmitted source probe photons will considerably drop.

Now it becomes clear in which way the Rydberg-EIT combination effectively establishes a photon-photon interaction: After exciting one atom in the cloud to a Rydberg state and thereby mapping the "Rydberg-light field" onto the atom (see figure 5.1), the transmission of subsequent source probe photons can be gated by so to say switching the EIT condition on and off. This is why the "Rydberg-light field" which also consists of two pulses, the probe $\mathcal{E}_g$ and control Ω_g, is also referred to as the "gate".

The inter-atomic Rydberg interaction between the gate excitation and the upper EIT Rydberg level will then serve as a mediator to control a *large* number of other photons. Thus, the single stored gate photon effectively interacts with subsequent[57] photons via inherent atomic processes.

Obviously, in the ideal case of maximum Rydberg absorption the gate source pulse solely has to contain one photon on average in order to create the Rydberg excitation. This aspect represents the single-photon character of the scheme so that the whole system represents an *all-optical single-photon transistor*.

It should be noted, that the performance of the transistor can be quantified in terms of the attenuation of the source probe pulse as a consequence of photon scattering at the Rydberg excitation induced by the single gate source photon. This means that it is sufficient to simply detect the transmitted source probe light in order to also evaluate the gain of the transistor.

This is the point where quantum mechanical coherence comes into play: The current transistor scheme so far only exhibits an incoherent character. This matter of fact immediately motivates to advance the system by taking coherence into account and thereby paving the way towards the realization of quantum gates.

5.3 Theoretical Concept of Coherence in the Rydberg Medium

In order to understand how coherence is linked to the transistor scheme, the process of gating the transistor by means of a Rydberg excitation has to be examined in much more detail.

5.3.1 Collective Character of the Rydberg Excitation

In a Rydberg medium such as the present ultracold cloud of atoms, it is no longer possible to treat every single atom independently. This is mainly due to the many-particle nature of the atomic cloud combined with the characteristic property of Rydberg atoms to introduce strong and long-range interactions into the system.

Consequently, Rydberg excitations which are normally produced by the interaction of light with only one atom become collective phenomena in the cloud. Naturally, this in turn demands for a theoretical Rydberg model which similarly takes into account all contributing atoms.

---

[56] In order to distinguish between source and gate excitations, the gate control pulse Ω_g typically couples the intermediate state $|e\rangle$ to another Rydberg level $|r_g\rangle$ than the source control Ω_s does. This prevents the source control pulse to read out the gate excitation again which is the one that should exhibit longest possible life times.

[57] As depicted on the left in figure 5.1 in the gated mode, the corresponding gate photon is stored in the cloud immediately the irradiation of source photons sets in.

It should explicitly be noted that the long-range character of Rydberg-Rydberg interactions demands for extending the length scale under consideration from the range of atom-light interaction to the one of dipole-dipole interaction.

As previously explained in the context of the incoherent scheme, this interaction is parameterized by blockade Radius R_b which is basically a measure for the range on which one Rydberg atom can influence others. The consequence of preventing the existence of more than one excitation inside the blockaded volume offers the possibility to control following photons.

5.3.2   The Coherent Spin Wave Representation

Rydberg interaction implies that the Rydberg excitation is collectively shared by all N non-interacting atoms in the ensemble [87] which means it is dynamically created and annihilated amongst all involved atoms. Therefore, the excitation might be located anywhere within the blockade so that the quantum mechanical state of the ensemble has to be expressed in terms of a so called collective spin wave state Ψ_{sw}

$$|\Psi_{sw}\rangle \;=\; \frac{1}{\sqrt{N}} \sum_{n=1}^{N} \left(e^{-\imath \varphi_n} |r\rangle_n \langle g|_n \right) |G\rangle \;=\; \frac{1}{\sqrt{N}} \sum_{n=1}^{N} e^{-\imath \varphi_n} |w\rangle_n \qquad (5.2)$$

which describes the simple case that only one excitation is stored in the cloud which has been chosen here for the sake of clarity[58].

The spin wave state Ψ_{sw} is a superposition of $|w\rangle$-states with distinct phase relations φ_n, where $|w\rangle_n = |g_1, g_2, ..., r_n, ..., g_N\rangle$ denotes the state of a single Rydberg excitation $|r\rangle_n$ of atom n at position $\vec{r}_n$. The ket $|G\rangle = \prod_{j=1}^{N} |g\rangle_j$ represents the collective ground state where all atoms reside in their corresponding single-atom ground states $|g\rangle_j$. The individual phases $\varphi_n = \vec{k}_0 \cdot \vec{r}_n$ are derived from the position $\vec{r}_n$ of the particular atom and the collective wave vector $\vec{k}_0 = \vec{k}_1 + \vec{k}_2$ of the spin wave where $\vec{k}_1$ and $\vec{k}_2$ indicate the wave vectors of the exciting fields, in this case represented by probe and control fields $\mathcal{E}$ and Ω respectively [83], [86].

By representing a superposition of the single-atom excitation states, expression (5.2) inherently contains the aspect of delocalization of the excitation [9]. As the notation bears strong resemblance to spin waves that are disturbances of magnetic ordering, the collective Rydberg excitation is also referred to as a Rydberg spin wave which is generated by coherently driving the ensemble of atoms. Thus, the excitation process represents the mapping of the according light field onto a Rydberg spin wave [83]. If the treatment refers to ensembles whose dimensions exceed the blockaded sphere, also states with more than only one excitation have to be accounted for.

The Superatom Picture

Theoretically, the transition matrix element of the collective Rydberg excitation which is shared by N blockaded atoms is expected to be enhanced by a factor of $\sqrt{N}$ [16]. By experimentally exploring this scaling it was possible to verify the existence of spin waves as a representation of the excitation [4]. As all these collective phenomena such as the cooperation of N atoms that results in an enhanced transition dipole remind of features of one big atom, the shared excitation is often referred to as a "superatom".

---

[58] A complete expression which also takes into account the case of multiple excitations in the cloud can be found in [83] and [86].

Loss of Coherence

The existence of one Rydberg excitation inside the cloud indirectly affects the propagation behaviour of succeeding photons by shifting energy levels and preventing further excitations within the blockaded volume. Depending on the excitation scheme, namely the detuning δ, this leads to scattering or transmission. Intuitively, it might be anticipated that superposition states consisting of N single-atom states such as the one in (5.2) are very vulnerable to directly lose spin wave coherence due to processes like scattering for example. However, since these superpositions of $|w\rangle_n$ states are very robust for instance against particle loss [88], coherence turns out to be quite stable if dephasing is induced by single-particle processes [16].

Theoretical calculations reveal as well that during the process of photons being scattered off the spin wave under certain conditions the excitation itself should stay unaffected so that the spin wave coherence can be preserved [9]. This in turn enables subsequent mapping of the properties of the spin wave including its coherence back onto a photon which can conveniently be achieved in the framework of the present EIT scheme. Then, detection of probe transmission instantaneously allows to draw a conclusion about the existence of Rydberg excitations, thus, representing a non-destructive optical detection scheme [89]. Thereby, the single-atom components that build up the spin wave are retrieved in such a way as to restore the initial photon propagation direction [90].

5.3.3 Transfer of the Concept to the Transistor Scheme

These fundamental concepts can now be easily transferred to the special transistor application whose mechanism is only enabled by exploiting exactly this characteristic Rydberg interaction within the cloud. Moreover, based on this treatment of Rydberg excitations in terms of coherent and collective phenomena it becomes clear at which point the present transistor scheme allows for advancement by integrating coherence.

Model System

In a simple model the transistor is considered as a system of an ultracold atomic gas that allows for transmission of single photons via resonant excitation of the EIT scheme. This transmission in turn can be gated by a single Rydberg excitation which is stored in the cloud as a coherent spin wave. It should be noted here that the previous treatment of the Rydberg superatom did not account for dynamical effects but has been completely restricted to static processes. The extension to propagating excitations through the cloud necessitates a treatment in terms of polaritons [91]. However, in the context of the gate this is not necessary due to the fact that the excitation is stored inside the cloud as a static spin wave rather than propagating through.

Next, based on this model, the procedure of gating the transmission takes place in the following way:

Non-Gated Cloud

In the first and obvious case that no gate excitation is stored inside the cloud all atoms can provide for the original unmodified EIT scheme and enable transmission of source photons. In contrast to the gate excitation, here the light propagation has to be considered in terms of slow-light polaritons which are strongly coupled atom-light superpositions formed by the

electromagnetic wave character combined with the dipole-carrying Rydberg excitation [91]. Thus, as soon as the source photon enters the cloud without any additional gate excitation being stored inside, it is converted into a slow-light polariton whose Rydberg component can be passed on in an undisturbed way [92] finally resulting in the transmission of the respective photon.

It should be noted, though, that for sufficiently high rates of incoming source probe photons even without gate excitation the transmission can be blocked due to mutual source photon interaction [5]. This interaction is mediated by the source polaritons' Rydberg components which will interact among themselves once consecutive photons will come closer together than the respective blockade radius. This process introduces an optical nonlinearity to the system which is mediated by Rydberg-EIT. Due to the fact that is only caused by the interaction between source probe photons themselves and does not require any gate excitation, it is also referred to as the self-blockade effect.

FIGURE 5.2: *Measurement of optical nonlinearity.* *The transmission of photons from the weak probe field $\mathcal{E}_p$ has been detected as a function of the detuning δ for different incident photon rates (black and red). A strong nonlinearity can be observed on resonance ($\delta = 0$). (same plot as in [93]*

It should explicitly be pointed out that this cooperative optical nonlinearity is not mediated by an optical field but rather by the long-range interaction that is immanent to Rydberg atoms[59].

The plot in figure 5.2 shows the suppression of probe photon transmission with increasing intensity which is due to this self-blockade effect. The corresponding measurement has been conducted in the present experiment [93].

Gated Cloud

Next, the much more interesting case of stored gate excitations should be examined:

Once a Rydberg gate excitation is stored in the cloud incident source photons will experience the presence of the stored gate photon in terms of level shifting induced by dipolar interaction. As a result the source photons are incoherently scattered in the medium so that the source transmission T, which is the quantity to be measured, will become significantly reduced.

Analytic calculations reveal that this source scattering at the gate spin wave is actually very efficient which means that virtually no source photons will transmit the gated cloud, Additionally, this is independent of the ratio between blockade radius R_b and cloud length L [9] as shown in figure 5.3. Obviously, in the gated case, the medium will always be rendered opaque for incoming source photons which in turn ensures maximized single-photon switch contrast.

Once more this illustrates that photon-photon interaction can be realized by exploiting inherent inter-atomic interaction processes. By mapping the Rydberg interaction between the gate spin wave and the Rydberg component of the source polariton onto photons the gate photon can be used to control subsequently incoming source photons.

---

[59] For a more detailed theoretical explanation also including measurements of this nonlinearity, refer to [5].

Cloud Length versus Blockade Radius

Much more profound, though, is the way the scattering process affects the coherence of the gate spin wave. In contrast to the transmission T this will highly depend on the ratios R_b/L, as described next.

Intuitively, the scattering process can be considered as a localization; a measurement of the position of the Rydberg excitation with an accuracy on the order of the blockade radius [9]. Hence, if the cloud is significantly bigger than the blockade or respectively than the Rydberg interaction range, the spin wave and thus its coherent character will collapse as the corresponding Hilbert space is restricted to the scale of the blockade.

This illustrative conclusion is confirmed by results obtained from an elaborate theoretical investigation of the system [9]. Studies of the gate spin wave coherence as a function of the interaction strength in terms of R_b, the cloud length L and the bandwidth of the incident photon pulse reveal that the coherence of the gate spin wave can only be conserved in case of sufficiently strong interactions or respectively small systems such that $L \lesssim R_b$.

Thus, as the intuitive argument already suggests, the present experimental system where the cloud is considerably longer than the blockade radius, at least in direction of polariton propagation, the transistor scheme cannot be expected to fully preserve the gate spin wave coherence. Rather, scattering of incoming source photons partly destroys this distinctive feature in the sense that it not only probes the pure existence of gate excitations but also their positions within the cloud which finally forces the spin wave to partially collapse.

Figure 5.3: *Analytic calculation of coherent transistor performance. Both the transmission T of probe photons (blue) and the fidelity F (red) in the gated cloud are plotted as a function of the normalized blockade radius R_b/L. While the fidelity which quantifies the conservation of coherence approaches unity only for $R_b \approx L$ the transmission is already negligible for smaller ratios R_b/L. (taken from [9])*

Furthermore, the length ratio L/R_b in the crossed ODT allows for the existence of more than only one gate excitation in the cloud. This feature of course represents some kind of defect regarding the single-photon character of the transistor scheme which then can only be claimed after performing post-selection of the measured transmission with respect to the number of simultaneously stored Rydberg excitations.

Towards Conservation of Coherence

Based on this analysis of the former experiment configuration it becomes evident where to modify the system in order to realize the conservation of coherence, namely by reducing the ratio L/R_b. It should explicitly be noted here, that it is not the goal to only reach the case where $L = 2R_b$, as one might hastily assume since the blockaded volume has a length of $2R_b$, but where $L \lesssim R_b$. Only then it is guaranteed that the blockade covers the whole cloud for all configurations, also including the case where the excitation is momentarily located at the outermost atoms.

In the case that $L \lesssim R_b$, scattering of incoming photons is no longer capable of resolving the position of the gate excitation so that the final Rydberg spin wave $\hat{\rho}_f$ fully agrees with the

initial one $\hat{\rho}_i$ and spin wave coherence is preserved. This can be quantified by the fidelity

$$F = \left[\text{Tr} \, | \sqrt{\hat{\rho}_i} \sqrt{\hat{\rho}_f} | \right]^2 \tag{5.3}$$

which then reaches unity as shown in figure 5.3 [9].

5.4   Experimental Realization of the Coherent Transistor

5.4.1   Coherent Storage of Gate Spin Wave

Thus, in order to enhance the transistor scheme and allow for conservation of gate spin wave coherence the length ratio L/R_b has to be modified experimentally. Practically it can become quite challenging to enhance the interaction strength that is parameterized by R_b and typically on the order of about $(15 - 20)\,\mu\text{m}$ depending on the particular Rydberg state combination of gate and source excitations $|r_g\rangle$ and $|r_s\rangle$, for example $R_b = 17.9\,\mu\text{m}$ in case of $|r_g, r_s\rangle = |90S, 90S\rangle$.

Enhancement of Interaction

The choice of larger C_6-coefficients for instance oftentimes requires to choose higher principal quantum numbers. However, this is accompanied by shorter storage times due to higher susceptibility to external influences such as stray fields leading to faster decay of the excitation.

Alternatively, exploiting interaction enhancement processes such as electrically tuned Förster resonances [85] might facilitate to maintain spin wave coherence. However, these phenomena are not expected to boost the blockade radius to the range of the current cloud length.

According to (5.1) the single-atom two-photon Rabi frequency Ω_0 of the combined EIT transitions represents another quantity that might be used to adjust the Rydberg interaction strength. However, this value should not be reduced too much as this might go at the expense of the transistor performance in terms of declined absorption efficiency for instance. Additionally, smaller control Rabi frequencies would impair the EIT transmission where the width of the transmission window around resonance $\delta = 0$ is given by

$$\Delta\omega_{EIT} = \frac{\Omega^2}{\Gamma\sqrt{OD}} \tag{5.4}$$

which is the power-broadened width of a Gaussian function. Γ denotes the decay rate of the intermediate state that is mainly determined by spontaneous emission [18]. OD is the optical depth of the medium.

Additionally, weaker control laser beams will not only result in a smaller transmission bandwidth but will also impair the transmittivity itself by reducing the amplitude of the transmission peak. This means transmission can no longer be ensured for all probe photons.

In this context it should be noted, that the EIT transmission window is neither shifted nor experiences a broadening as a consequence of the self-blockade effect. The latter effect only results in a suppression of the transmission which becomes apparent by decreased absolute transmission [5].

Reduction of the System

Alternatively, instead of modifying the length ratio L/R_b by enhancements of the interaction, the goal of conservation of gate spin wave coherence can also be achieved by reducing the cloud length. From the experimental point of view, this is expected to be possible in a very straightforward way by modifying the optical dipole potential.

Obviously, this represents the method of choice in this thesis for realizing the coherent single-photon transistor. In case of sufficiently small blockade radii the system will only allow for a single gate Rydberg excitation in the cloud which immediately justifies to use of term "single-photon" to characterize the application.

5.4.2 Coherent Readout

On the way to the implementation of quantum gates, besides realizing coherent storage of the gate spin wave it is equally important to enable readout of the stored gate excitation in a non-destructive coherent way.

This requirement necessitates an extension of the current transistor experiment sequence which is presented in [81] and sketched on the left in figure 5.1. Actually, the incoherent transistor scheme did not care much about the nature of the gate excitation so that readout has not been of high interest so far. However, readout of the excitation becomes of vital importance for further processing of the stored photon, not only regarding the implementation of the coherent transistor but also for possible advancements towards the general implementation of quantum gates.
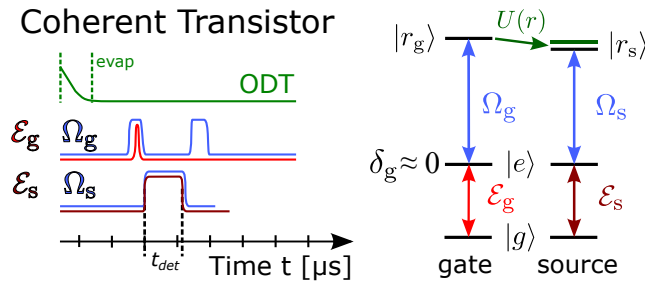
FIGURE 5.4: *Timing sequence and excitation scheme of coherent transistor. For further description of the labelling can be found in the caption to figure 5.1 which shows similar diagrams for the incoherent transistor. The only two differences of the coherent sequence are the final gate control pulse and a gate control detuning of $\delta_g \approx 0$. The reason for this and resulting effects are discussed in the text.*

In fact, the stored gate photon can be retrieved in a rather simple way as visualized in figure 5.4:

After having performed the incoherent transistor scheme according to the well-defined time sequence, only one additional laser pulse will suffice to convert the gate excitation back into a photon: By means of a final gate control pulse the Rydberg excitation is stimulated to decay back to the intermediate level $|e\rangle$ of the excitation scheme. This process will inherently be accompanied by the emission of a photon.

In case that coherence of the excitation does not exist anymore, the propagation of this photon can be orientated into all spatial directions due to the loss of the coherent phase relations between the $|w\rangle_n$ components of the spin wave.

However, in case of a coherently stored Rydberg spin wave the stimulation by the control pulse stimulates all contributing single-atom components, the $|w\rangle_n$-states, to interfere in such

a way as to restore the original light propagation direction during collective conversion back to the photon. This directional emission which is based on the mentioned fixed phase relations between the single-atom components can only be obtained if the phases are coherently conserved throughout the full process and if they are afterwards coherently converted back to photonic components.

It should be noted, that loss of coherence does not necessarily have to be caused by scattering events. Rather, even in case of sufficiently small clouds, where scattering does not localize the excitation, the coherence of the gate spin wave might get impaired by external influences that induce dephasing during execution of the transistor sequence.

One last comment should be made on the transistor sequence shown in figure 5.4. Apparently, compared to the incoherent transistor sequence shown in figure 5.1, the coherent one only comprises an additional final gate control pulse. However, there is another slight deviation which does not stand out that much. In order to maximize readout efficiency, the gate control light field in fact has to be resonant with the transition between $|e\rangle$ and $|r_g\rangle$. This peculiarity also affects the way the gate photon is stored in the cloud in the beginning of the sequence:

In case of the incoherent transistor the gate detuning δ_g is so large that the 3-level system can effectively be considered as a 2-level system. In this case the gate photon is stored by sending a so called π-pulse into the medium. This means that the gate pulse which basically drives Rabi oscillations between $|g\rangle$ and $|r_g\rangle$ is timed in such a way that the pulse exactly ends at the time where the population of the excited state $|r_g\rangle$ is maximized.

Though, if δ_g approaches zero as it is the case for the coherent transistor scheme (compare figure 5.4) the gate pulse has to be stored in a different way: Now, the gate control pulse is turned off in such a way that the polariton is slowed down until it finally comes to rest. This technique is based on the fact that the group velocity of the polariton which travels on EIT through the medium depends on the intensity of the control light field.

The reason for not choosing this way of storage for the incoherent scheme, is the slightly enhanced excitation efficiency for the storage method explained first.

5.5 Conclusion

As described to the full extent, practical work on modifying the optical dipole trap has been successfully completed in terms of a considerable reduction of the length of the ultracold atomic cloud. However, whether the cloud can now be fully enclosed within one blockaded volume, has not been investigated yet.

That is why the implementation of the coherent transistor temporarily stays work in progress which means that related measurements will be postponed. Although this project could not be experimentally realized in the scope of this thesis, it will definitely stay on the agenda of the RQO experiment.

Before the coherent transistor will be implemented, the system shall be subject to a thorough investigation regarding its dimension relative to the blockade radius. Actually, this is achieved by implementing another type of single-photon gate, namely the single-photon absorber, whose scheme is as well based on Rydberg phenomena. As discussed in the next chapter its realization, though, should not be restricted to only serve for testing the cloud size. Rather, this gate itself offers a variety of promising quantum mechanical applications.

Chapter 6

Single Photon Absorber

This chapter comprises comprehensive studies, analysis and discussions of the mechanism of the single photon absorber. These investigations are not restricted to the pure experimental implementation but also extended by a digital replication of the experiment on the basis of Monte-Carlo simulations.

The chapter is opened by a detailed description of the fundamental concepts behind the scheme of the single photon absorber which is especially focussed on an implementation in the framework of the available experimental setup. Regarding data evaluation, the correlation technique is introduced as a major way of analyzing the single photon absorber mechanism.

Next, the structure of the simulation is outlined and methods that have been employed during its implementation are described. This is followed by simulation-based investigations of the absorber performance with respect to various physical properties of the scheme. These examinations are not only based on effects on the pulse shapes and photon number statistics but also include studies of related correlation effects.

After presenting and discussing the experimental implementation and final measurement results, the simulation outcome is finally compared to the evaluation of experimental data. This makes it possible to figure out crucial properties of the system.

6.1 Fundamental Concept

Next to the coherent transistor the present modified experimental setup facilitates the realization of another very promising quantum mechanical application, the single photon absorber. Even though initially only being intended to represent a means to test the new setup for particular characteristics, the application itself should definitely be considered as an equally potent single-photon gate as the coherent transistor.

Next to enabling the simple task of investigating the length of the Rydberg medium the single photon absorber indeed opens up a huge variety of possible application:

Of course, as its name suggests the elementary operation of single photon absorption primarily serves for extracting one photon from an arbitrary light field independent of the particular physical system. The scheme might for example be employed to experimentally explore distinct quantum mechanical constructs such as inherent properties of coherent states [94]. Thereby, the investigation of particular physical phenomena is by no means restricted to fundamental physics but can easily be expanded to practical applications of quantum mechanical effects such as the investigation of quantum communication rules [95] or quantum networks in general [96].

Furthermore, within the field of quantum mechanics the subtraction of single photons from light fields represents a powerful tool which in particular allows for the creation of artificial

quantum mechanical states [97] that so far only existed in the ivory tower of theoretical physics. In this context, one might in the first instance think of the prominent realization of Schrödinger cat states which might indeed be an interesting tool for quantum information processing [98], [99]. However, the creation of non-classical states [100] might also represent a means to simply perform arithmetic operations [101].

Intuitively, one might expect that the realization of single photon absorption should be accomplishable in a quite straightforward way. In fact, though, it is far more challenging and complex than it initially assumed even though there exist various possible implementation schemes which are for example based on standard techniques from the fields of linear and non-linear optics [102]–[104]. Recently, a new scheme for deterministic subtraction of a single photon from a light field was reported which employs a totally different process, namely single-photon Raman interaction (SPRINT) [105].

However, the usability of all these schemes is usually impaired by various drawbacks. Indeed single photon absorption by means of pure optical processes can for example be implemented in a fairly simple setup, their extension to the single photon level, though, is oftentimes on the expense of success rates [101]. Beyond that, within these schemes the detection of extracted photons is inherently accompanied by the loss of their quantum mechanical character [105]. Other implementations which might yield high efficiency, in turn require highly sophisticated setups.

6.1.1   Implementation Based on Rydberg Medium

Considering these shortcomings, the present setup of an ultracold Rydberg medium provides for a truly promising way of realizing single photon absorption from arbitrary light fields: It might not only yield near-unity fidelity [100] but also allows for a free-space implementation which might furthermore preserve the coherent character of the subtracted photon. Not least, it directly offers various modifications of the scheme which in turn enable further applications such as a single-photon transmitter [7].

In contrast to the single-photon transistor the subtraction of individual photons from a light pulse only relies on one physical process in the cloud. Whereas proper functioning of the amplifying switch is only possible by combining Rydberg physics and EIT, the realization of single photon absorption solely depends on the Rydberg character of the cloud. The effect of on-resonant EIT transmission is no longer necessitated here since the scheme does not require any kind of effective photon-photon interaction or any other control mechanism.

In case of the single photon absorber an interaction between the special (absorbed) single photon and subsequent photons is in fact explicitly unwanted. This is because the latter ones are here supposed to represent the artificially created state of light which transmits the cloud. This implicates that the propagation behaviour of all photons except for the absorbed one should preferably be unaffected by the presence of the extracting medium, the atomic cloud.

6.1.2   Excitation Scheme

The single photon absorber (SPA) can be implemented within an excitation scheme comprising the same atomic energy levels that have already been used for the transistor, however, with slightly modified excitation light fields. The scheme which is shown on the left in figure 6.1 solely consists of a 2-photon Raman transition with combined Rabi frequency $\Omega_0 = \mathcal{E}\Omega/(2\delta)$ to the highly excited Rydberg state $|r\rangle$ [4] where the two constituting light fields are both

far detuned by δ from the intermediate state $|e\rangle$. If the corresponding laser pulses are in combination resonant with the transition from the ground $|g\rangle$ to the Rydberg state $|r\rangle$ a Rydberg excitation can be introduced into the cloud of ground state atoms.
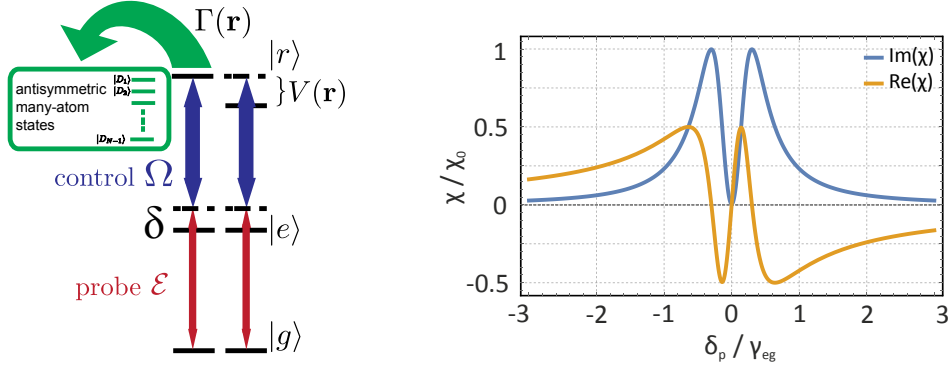
FIGURE 6.1: ***Left:*** *Excitation scheme of the single photon absorber. By off-resonant 2-photon Raman transition via probe $\mathcal{E}$ and control Ω field an atom can be excited to the Rydberg level $|r\rangle$ which inhibits further excitations within the blockaded volume due to dipolar interaction and resulting level shifts $V(\vec{r})$. Life times of the collective excitation can be enhanced by means of dephasing $\Gamma(\vec{r})$ which distributes the coherent spin wave over all antisymmetric states including $N-1$ dark states $|D_i\rangle$.* ***Right:*** *Optical response of the 3-level system that is shown on the left, in terms of the normalized susceptibility χ/χ_0 as a function of the probe detuning δ_p/γ_{eg} (in units of the radiative linewidth γ_{eg}). At large detuning the absorption of probe photons which is determined by the imaginary part (blue curve) can be minimized.*

The upper transition is again driven by the strong control laser with Rabi frequency Ω that couples the intermediate state $|e\rangle$ to the Rydberg level $|r\rangle$. Whereas this control pulse is only required to finally facilitate the Rydberg excitation the weak light field with Rabi frequency $\mathcal{E}$ that excites the lower transition is actually the significant one here. Pulses that belong to this light field typically comprise only few photons. During transmission through the cloud ideally only one of them is absorbed and converted to a Rydberg atom [60].

Obviously, the name "probe" again originates from its property of testing the cloud for Rydberg excitations since transmitted pulses are ideally only modified if there is a finite chance to excite an atom. In case of insufficiently small clouds or Rydberg decay multiple excitations can take place which can directly be observed in the detected signal. Thus, in case of long excitations life times, transmission detection is a way to verify whether the cloud can really be blockaded by one single excitation.

At this point it becomes clear why the scheme necessitates significant detuning δ from the intermediate state $|e\rangle$. If the combined 2-photon transition stopped over resonantly at the level $|e\rangle$, scattering of probe photons would set in once a Rydberg atom has been created which renders the medium opaque for subsequent probe. In case of large detuning, though, the atoms will only feel the present light if no Rydberg atom has been excited yet so that only then one photon will be subtracted from the pulse. Once a Rydberg atom exists, the blockade effect prevents further excitations due to level shifts that tune the coupling light field

---

[60] Of course, maximized interaction of the probe light with the Rydberg medium can only be achieved if the probe beam is strongly focussed into the cloud. Especially the beam's transverse mode area is required to be smaller than the transverse size of the cloud.

out of resonance. Since the far detuned probe field only weakly couples the ground to the intermediate state so that almost no scattering will take place and following probe photons can be transmitted trough the cloud.

The effect of detuning on the transmission of probe photons becomes apparent by visualizing the analytically obtained response of the atomic 3-level system to the excitation light fields. The right plot in figure 6.1 illustrates the imaginary part (blue line) of the optical susceptibility χ, as a function of probe detuning δ_p in units of the radiative linewidth γ_{eg}. This quantity basically determines the absorption of probe photons.

Obviously, by working on the outermost tail of the Lorentzian curve the system is so far detuned that absorption and scattering at the intermediate level becomes negligible and a maximum of probe photons is transmitted. Practically, sufficiently narrow absorption profiles can of course only be obtained if the intensity of the strong control laser in terms of its Rabi frequency stays significantly below the power-broadened linewidth Γ of the intermediate level $|e\rangle$ [18].

6.1.3 Single Photon Character and Coherence

Of course one might wonder why the SPA scheme relies on Rydberg excitations at all. Why can the single photon not simply be absorbed as a result of a 2-photon transition to any low-energy state?

This is the point where the single-photon aspect of the absorber scheme comes into play as this special feature can only be realized by exploiting Rydberg physics. Rydberg excitations are a straightforward means to restrict the number of absorbed photons to exactly one. By blockading the whole atomic cloud and thereby preventing further excitations which in turn would subtract further photons from the pulse, the single-photon character can easily be ensured.

This finally makes clear why single photon absorption has not been possible within the former experimental setup and why it can now be used in order to investigate the present setup regarding the ratio of cloud size and blockade radius R_b. The dimple in the dipole potential makes the difference by enabling full blockade by only one Rydberg atom.

Beyond that, this particular way of realizing single photon absorption by means of Rydberg physics inherently allows for the conservation of coherence which makes this scheme superior to many others. In fact, the Rydberg excitation is not only coherently stored in terms of a spin wave, which all atoms contribute to, but in the end it can even be coherently retrieved again, thereby offering further processing of the absorbed photon. As this feature is the crucial building block of quantum information processing and enables a huge range of consecutive applications it should definitely be considered as an outstanding consequence of this single photon absorption scheme.

6.1.4 Enhanced Life Time by Transfer of the Superatom

Of course, retrieval of the Rydberg spin wave and further processing of the resulting photon is only possible provided that the life time of the excitation is sufficiently long.

Long life times essentially require the excitation to be shielded from any influences that possibly induce decay. This by no means only restricted to external factors such as stray fields but especially also demands for abruptly ceasing atom-light interaction once the Rydberg

excitation is created. If the excited atom stayed addressed by the light field, stimulated emission might force the excitation to decay resulting in a severely reduced life time.

In order to circumvent this effect it was proposed to induce artificial collective dephasing Γ that couples the present spin wave state $|W\rangle$ to the $N-1$ remaining collective states $|D\rangle$ in a medium of N atoms. Consequently, the coherent excitation becomes distributed over all N available states [100] as illustrated by the schematic on the left in figure 6.1.

The crucial property of the $|D\rangle$-states is that they are inherently "dark" with regard to the irradiated light. This means once being transferred to one of them the superatom no longer feels the presence of the light field so that finally the probability for retrieval is significantly reduced.

This transfer of the Rydberg superatom could in the present scheme be achieved for example by artificially inducing AC-Stark shifts or any other processes yielding equivalent dephasing $\Gamma(\vec{r})$.

6.1.5 Effects of Photon Absorption on Statistics

Experimentally, the single photon character of the absorber scheme can directly be verified by performing conducting photon statistics measurements of the transmitted probe pulses. For input pulses with a number of photons that is Poissonian-like distributed around the mean value λ, the transmitted pulse is supposed to comprise an average number of $\lambda-1$ photons. However, since the variance of the corresponding probability density function stays unchanged the number of photons per pulse does not obey Poissonian statistics anymore but is called as to exhibit super-Poissonian character.

The number of absorbed photons can simply be obtained by monitoring the transmitted pulse and comparing it to a reference pulse that is detected in the absence of atoms.

A slightly enhanced detection setup provides for investigating another effect of photon subtraction. Splitting up the transmission signal at a beamsplitter and subsequently detecting on two separate counters allows for exploring the intensity correlation of the transmitted pulses.

6.1.6 Conceptual Scheme for Correlation Studies

Correlation measurements are a typical way of studying photon bunching or anti-bunching effects where the first phenomenon is of main interest here. In general, correlation effects between two separate signals from the same source are referred to as photon bunching if more photon pairs are detected closer together than further apart [106]. Thus, they effectively arrive at the detectors in a bunched way. Translated to the special case of the single photon absorber the source is represented by the input probe pulse which becomes modified during transmission of the cloud.

As mentioned above, the typical setup for correlation measurements is built up of a regular beamsplitter that routes the incoming photons randomly with equal probability to one of the two identical detectors. As this kind of detection setup was first implemented by Robert Hanbury Brown and Richard Q. Twiss for the purpose of astrophysical studies [107] it is also known as Hanbury Brown-Twiss (HBT) interferometer and the correlation effect as Hanbury Brown-Twiss effect.

Second-Order Correlation

Due to the super-Poissonian character of the photon number per transmitted pulse the normalized second-order correlation function

$$g^{(2)}(t_1,t_2) = \frac{\langle n_1(t_1) n_2(t_2) \rangle}{\langle n_1(t_1) \rangle \langle n_2(t_2) \rangle} \tag{6.1}$$

is supposed to exhibit such a bunching feature [108]. Here $n_i(t_i)$ indicates the rate of detected photons at counter i and time t_i and is basically the time-dependent detection signal of the light intensity. In this definition the angle brackets $\langle ... \rangle$ explicitly denote the ensemble average which in the present case corresponds to an average over all measurement runs. This is an important aspect to keep in mind.

Generally, if working with classical states of light which also includes laser light with Poissonian distribution, the allowed values for the second-order correlation function $g^{(2)}(t_1,t_2)$ range from 1 to infinity ($1 \leq g^{(2)}(t_1,t_2) \leq \infty$) with $g^{(2)}(t_1 \neq t_2) < g^{(2)}(t_1 = t_2)$. Conversely, this implies that any measurement that reveals $g^{(2)}(t_1,t_2) < 1$, which is known as antibunching, has been conducted on quantum states of light [84], [109].

Detection Process

Typically, detection temporally proceeds in a discrete way. That means that the detected signal is divided up into equidistant time bins. Since the two detectors are supposed to be identical this detection procedure is equal for both of them. It should explicitly be noted that the separately detected signals are indicated by independent detection times t_1 at the first counter and t_2 at the second one.

In case of the single photon absorber an evaluation of the second-order correlation function $g^{(2)}(t_1,t_2)$ then yields a distinct bunching effect that depends on *both t_1 and t_2*.

Correlation measurements of one signal pulse in an HBT detection setup basically means to correlate each transmission pulse with itself which is also called auto-correlation. Except for all values belonging to $t_1 = t_2$ same effects would be observed if the pulse was detected by only one *perfect* counter that does not possess any dead time. Actually, the need to circumvent exactly this shortcoming of real counters is the only reason for splitting the pulses up, measuring them on two separate counters and finally "cross-correlating" them[61].

Auto-correlation measurements on one perfect detector and cross-correlations of two signals from the same source only differ in the values $g^{(2)}(t_1 = t_2)$. In the case of auto-correlation the value at $t_1 = t_2$ is evaluated by correlating all photons that arrive at the detector within the same time bin t_1 with themselves. In contrast, if the signal is first split up and afterwards cross-correlated, the same photon can intrinsically never be correlated with itself since it has only been counted at one of the detectors. Thus, the cross-correlation signal at $t_1 = t_2$ does not comprise this additional auto-correlation contribution so that $g^{(2)}_{cross}(t_1 = t_2) < g^{(2)}_{auto}(t_1 = t_2)$.

With regard to evaluations presented below, it should be noted that this peculiarity of similar auto- and cross-correlation effects of a single signal pulse can be exploited to enhance the signal-to-noise ratio. By averaging over all three correlation functions the bunching effects can be intensified and noise can be reduced which is exemplarily illustrated in figure 6.2.

---

[61] In this context it should explicitly be noted that auto- and cross-correlation effects are only similar for signals that originate in the same source.

Stationary and Non-Stationary Processes

It is common practice to transform t_1 and t_2 into a set of an absolute time t and a relative one τ and subsequently time-averaging over t which finally results in

$$g_t^{(2)}(\tau) = \frac{\langle n_1(t) n_2(t+\tau) \rangle_t}{\langle n_1(t) \rangle_t \langle n_2(t) \rangle_t} \qquad (6.2)$$

where $\langle ... \rangle_t$ denotes the time average. Consequently, τ is supposed to completely absorb the time-dependence of the correlation function and is therefore the only quantity to be employed further on. This approach, however, effectively reduces the dimensionality of the time dependence so that parts of it automatically get lost.

This transition from the ensemble to the time average and thereby from $g^{(2)}(t_1, t_2)$ to $g_t^{(2)}(\tau)$, though, can only be performed if the system fulfills the condition of ergodicity. Thus, it is only valid for correlation functions that belong to time-invariant that means stationary processes. Therefore, the investigation of non-stationary processes necessarily requires to preserve the complete two-dimensionality of the correlation function. Anyway, a thorough examination of bunching effects is generally only possible by means of the generalized correlation as a function of independent times t_1 and t_2.

In case of stationary processes, physical events can happen at any time totally independent of the past state of the system. From this matter of fact it becomes directly clear in which way the particular realization of the single photon absorber in the Rydberg medium

FIGURE 6.2: *Exemplary plots of the simulated correlation function* $g^{(2)}(t_1, t_2)$*. The SNR can be enhanced by adding the auto-correlations of both detected signals (bottom) to their cross-correlation (top).*

has to be treated: As it is known from elaborate explanations in the previous chapter, in the context of Rydberg physics it is absolutely necessary to consider the instants of time that special events occurred at. Especially in a cloud that is blockaded by one single excitation, physical processes such as further Rydberg excitations highly depend on the current and past state of the system. If one Rydberg excitation prevents all other atoms of the ensemble to be excited as well before it decays, it is important to always consider the relative time to a previous excitation.

Translated to the absorber scheme the instance of time of the generation of a Rydberg atom corresponds to the subtraction of a photon from the incoming pulse. Thus, if the pulse is sufficiently short compared to the coherence time of the Rydberg spin wave, ideally no subsequent photons within this pulse will be absorbed by the cloud. This is also expected to be observed by intensity correlation measurements.

Since the condition of ergodicity is not satisfied here, it is not only useless but simply wrong to investigate the correlation in terms of a fixed relative time τ. Assuming the photon is absorbed at time t_{abs} it definitely makes a difference whether the state of the system at

$t_0 < t_{abs}$ is compared to the one at $(t_0 - \tau)$ or at $(t_0 + \tau) > t_{abs}$. Negligence of this peculiarity by performing the transformation from t_1 and t_2 to t and τ and time-averaging, would immediately absorb distinct time-dependent properties of the bunching signal.

Consequently, as simple as the explanation of sole appearance of photon bunching seems to be, the much more difficult it is to understand all its distinct characteristics within the present absorber scheme. Measurements reveal that special features such as the relation between the exact time of photon absorption and the correlation time are highly nontrivial. This is why systematic scrutiny of the system is required to answer these questions.

For this purpose, parallel to the experimental realization and investigation of the single photon absorber, a numeric simulation of the system with the help of *MATLAB* has been conducted. It is supposed to reproduce the experiment and serve as a means for studying the single photon absorber scheme in general but also for understanding physical processes behind distinct bunching features.

6.2 Simulation

6.2.1 Motivation

The initial goal of a numerical simulation of the single photon absorber was to reproduce the experiment to such an extent as to understand or even verify results obtained from the experimental implementation of the single photon absorber. In fact, this turned out to be much more complex than initially assumed so that the simulation developed to be a rather independent project of this thesis that finally represents a thorough reproduction of the whole absorber scheme. Due to the fact that it was written parallel to the experimental implementation it was also possible to already include various features that have been observed and measured in the experiment.

Basically, the numerical implementation of the SPA scheme is based on a so called Monte-Carlo simulation that means events which only happen with certain probabilities are repeated sufficiently often as to finally yield reliable and converging results.

As the simulation is primarily supposed to generate the photon statistics of the single photon absorber scheme, it should explicitly not reproduce the experimental implementation one-to-one. In particular, various imperfections which distort the photon statistics such as the counter's immanent inability of detecting more than one photon at a time due to finite dead times should not be considered. All other peculiarities of the experiment that do not impair the statistical outcome, though, are supposed to be implemented entirely.

Thus, for the benefit of conserving the full photon statistics the code simulates a perfect implementation scheme that slightly deviates from the experiment.

6.2.2 Structure and Methods

The following section describes the basic structure and methods employed in context of the numerical SPA implementation. Besides presenting the general approach it also emphasizes important aspects that had to be taken into account.

Basic Structure

Basically, the simulation procedure is built up equivalently to the experiment cycle: First of all various parameters of the input pulse and the overall scheme such as the number of runs are initialized. Additionally, it can be defined in which way other characteristics should be taken into account such as the probability for Rydberg decay or photon loss. Subsequently, so called "reference" and "signal" pulses are generated, detected in a simulated HBT setup and finally correlated. In the last step results of both the photon statistics and the correlation are plotted and saved if desired.

The terms "reference" and "signal" pulses that have just been introduced are used for the two different modes of the experiment: As the name suggests, the first one represents a pulse with initially defined characteristics that passes the experimental setup in the absence of the atomic cloud. Therefore, it serves as a reference which the actual signal can then be compared to.

Of course the initial signal pulse exhibits exactly the same properties as the reference, however, it will subsequently be modified due to light-matter interaction during transmission of the cloud. The resulting transmitted signal is finally used for studying correlation effects produced by the single photon absorber.

For the sake of clarity of the code, various simulation steps have been sourced out. While parameters are defined in the main script where also pulse initialization and calculation of certain statistical quantities is performed, all remaining simulation steps such as signal pulse generation, simulation of the detection, correlation of respective pulses and finally plotting and saving are processed within separate functions which called by the main script and supplied with all required parameter values.

Parameters

At the beginning of the code, the following parameters are defined and, where required, values are assigned to them:

1. Numerical simulations innately require discretization of continuous quantities into tiny fractions. In the present case this also allows for considering the counters' specific time-resolved detection in terms of equidistant time bins. This is why all pulses in the simulation are divided up into a initially defined number of time ***bins***. Depending on the exact pulse shape, informative results can already be obtained for 50 bins per pulse.

   The length of time that is assigned to one bin depends on both the pulse length and the number of bins. If it was the detection method at the counters that is intended to be reproduced, the duration of one bin would have to be fixed to the value that is technically defined by the counter. Otherwise, however, the duration of one bin is given by the ratio of pulse length and number of bins and is therefore rather arbitrary.

2. In order to deliver reliable results the simulation should comprise a large enough number of experiment ***runs***. The term reliable means that the outcome should not exhibit any conceptually induced deviations caused by an insufficient number of repetitions. Values of more than 10^5 turned out to be a good choice.

3. The length of a pulse in the simulation should preferably be equivalent to the one in the experiment. Only then time scales that are extracted from measurements can also be numerically reproduced. Typical ***pulse lengths*** are in the order of few microseconds.

If the pulse length is fixed to the real value, the number of bins yields the time resolution of the simulation which therefore does not necessarily have to agree with the specification of the counter. Useful results are also obtained for larger time bins.

4. Not only the length of the incoming pulses can be specified but also its **shape**. The simulation allows for defining arbitrary amplitude functions for the intensity of the pulse. Next to Gaussian-shaped pulses also signals with constant intensity and especially tukey-shaped ones have been used here. The latter intensity function, a tapered cosine window, exactly reproduces the experimentally generated pulse shape.

5. Each pulse is contains a certain number of photons which is Poissonian-distributed around the **mean number of photons** λ. Basically, this is the value used for normalizing the amplitude function. The exact value for λ which ranges between one and about ten should again agree with the one used in the experiment.

6. The final parameter to be initialized is the **life time** τ_{Ryd} of a Rydberg excitation which represents the time constant of the corresponding exponential decay rate. In order to generally reproduce experimentally observed correlation time scales it is important to choose the life time relative to the pulse length. Measured life times amount to several microseconds. In the context of a comparison between simulation and experiment it will be discussed to which extent simulation results based on the measured life time match experimental observations.

Next, a number of **probabilities** for certain physical mechanisms are introduced which are related to the SPA implementation. Again, their values are defined pursuant to experimental observations. Some of them belong to features that can be used optionally so that they are only considered if explicitly desired.

1. The most important probability to be set is the likelihood p_{exc} of absorbing a photon at a certain time for the purpose of exciting a Rydberg atom. Due to the system's non-stationary character, this probability is by no means constant during the whole experiment cycle. In fact, the value changes over time and depends on the Rydberg absorption probability $p_{abs}^{(1st)}$ itself but also on the decay rate of the excitation which is given by the decay constant $1/\tau_{Ryd}$.

   The first quantity $p_{abs}^{(1st)}$ represents the chance for exciting a Rydberg atom in the case that the ensemble resides in the ground state G. It is mainly determined by the efficiency of atom-light interaction in the medium.

   The second parameter then defines the time evolution of the excitation probability $p_{exc}(t)$: After a certain time the Rydberg excitation will decay due to various possible influences such as spontaneous or stimulated emission or induced by external stray fields. Only if this happened, a second photon can be absorbed for the purpose of creating a new excitation. On average the Rydberg decay obeys an exponential function with time constant τ_{Ryd} so that at a certain time t relative to the last excitation the probability for a new excitation is given by

$$p_{exc}(t) = p_{abs}^{(1st)} \left[1 - \exp\left(-\frac{t}{\tau_{Ryd}}\right) \right] \tag{6.3}$$

2. Depending on the principal quantum number of the chosen Rydberg level it might be possible that a single Rydberg excitation does not blockade the full cloud due to insufficient interaction strength. In these cases it can happen that a second photon is absorbed to excite a second Rydberg atom while the first excitation is still alive. It should be noted, that strictly speaking these events of second excitations directly put the name "single photon absorber" into question.

   In the simulation such an event can be accounted for by means of the parameter $p_{abs}^{(2nd)}$. If possible at all, the likelihood for a second excitation is as well defined in a dynamical way. This function, however, cannot be expressed in an equally compact way as equation (6.3) for the first excitation. This is due to the way the probability for first and second excitations are evaluated in the code.

   In the simulation Rydberg atoms are only called second ones if there is still another one alive. Therefore, the parameters $p_{abs}^{(1st)}$ and $p_{abs}^{(2nd)}$ are processed in a nested way and $p_{abs}^{(2nd)}$ is only incorporated in the overall probability if the cloud has been successfully tested for a still existing Rydberg atom. This is why the final evaluation of excitation probabilities exhibits a pretty elaborate structure.

3. Besides getting absorbed or being transmitted through the cloud there is a third path incoming photons can take: While passing the atomic cloud photons might get scattered at one of the atoms. In this case the photon is effectively "lost" as it can no longer be detected at one of the counters. In the simulation photon loss is implemented by means of the parameter p_{loss}. Typically measured loss probabilities amount to about 5%.

By means of certain flags individual parameters can be enabled or disabled so that different experiment modes can be simulated. The most important cases to be mentioned are the option for decay and loss. Parameters will then only be considered for the simulation if corresponding flags are activated.

General Data Structure

Concerning their data structure all pulses in the simulation are defined in an equivalent way. Throughout the whole simulation procedure both the reference as well as the signal pulses are handled by means of two-dimensional arrays where each row represents a separate experiment run and each column stands for one bin. With this definition all experiment runs can be processed at the same time in each simulation step such as transmission of the cloud or detection. This data structure also allows for simultaneous initialization of all pulses. By using only one command respective bins can be filled with photons.

Reference Pulse Initialization

The investigation of photon statistics intrinsically relies on the properties of the incoming reference pulses. Here, the basic idea is to model them in such a way that on average the number of photons per pulse obeys a Poissonian distribution with mean number λ.

Keeping in mind their discretized structure the reference pulses are therefore generated in the following way: First of all, a certain intensity value is assigned to each bin in every run according to the initially defined amplitude function which is normalized to the mean number of photons λ. Now, Poisson statistics is introduced by generating for each bin a random number

from the Poissonian distribution around a mean value that is equal to the bin's amplitude. Consequently, the photon numbers comprised by the bins in one column will be Poissonian-like distributed around a mean value equal to this column's intensity. Furthermore, the number of photons per row, or pulse respectively, will yield the same probability density function (pdf), however, with the mean number λ.

This way of initialization can easily be performed by nesting the two *MATLAB* commands *poissrnd()* and *repmat()* so that the whole array can be processed at once.

Signal Pulse Generation

Whereas the treatment of the reference pulses only comprises two simulation steps, namely initialization and detection, signal pulse generation additionally includes the step of transmission of the cloud. Since various processes have to be considered here, this step is the most challenging and complex one in the simulation. Especially the need to comply with all defined probabilities requires a quite sophisticated implementation approach:

In the typical case where the number of bins clearly exceeds the number of photons per pulse, a large fraction of bins is just empty. In order to keep demands on computing time as low as possible, instead of successively handling each bin only those ones are processed which contain photons at all. Thereby it has to be kept in mind that the occurrence of repeated events such as the excitation of Rydberg atoms depends on the time of preceding events. Therefore, it is not possible to process the whole pulse array at once. Rather, all photons comprised by one pulse have to be treated one after another.

In some cases, though, for example if the option for Rydberg decay is disabled and coexisting excitations are not allowed for, the processing of one pulse can be aborted after the first photon has been subtracted.

Several nested loops are now used in order to test for all possible cases and probabilities. This is done by generating a random number between 0 and 1 and comparing it with the corresponding probability value. In case of time-dependent processes the probability first has to be calculated based on the time bin of the current photon with respect to previous photon absorption times.

Starting from the reference pulse array, each filled bin is handled successively in the following way: Before absorption is tested for, a first loop is used to consider for photon loss. Afterwards, all possible cases of absorption are processed for the remaining photons. Therefore, the bin of last subtraction and in case of coexisting Rydberg atoms also penultimate excitation times have to be remembered.

Furthermore, it is important to nest all loops in the correct way. Absorption of more than one photon for example is either possible in the case of decay or if coexisting excitations are enabled. Thereby, it is crucial to consider the order of testing corresponding probabilities.

Simulation of Pulse Detection

The third and last experiment step to be simulated is photon detection within the HBT setup. The first component which the pulses strike is the 50/50-beamsplitter which routes the photons with equal probability to one of the counters. Which counter a certain photon is assigned to is again determined by generating a random number from the uniform distribution and comparing it to the probability of 50% for each path.

Depending on which way the photon goes, it is afterwards registered in one of two additional arrays. Each of them comprises all those photons that have been assigned to the same counter. During beamsplitting the index of each photon is preserved that means the photon is written into the same bin as prior to the detection stage.

This way of splitting also incorporates the actual step of detection since the two resulting arrays already represent the detection outcome of the two (perfect) counters.

Evaluation of Photon Statistics

For both the reference and the signal pulse array certain statistical properties are evaluated in the course of the experiment simulation: The photon statistics of one array are visualized by taking the mean value of each row, normalizing the values with the overall number of photons in the whole array and generating a histogram from this data. The resulting probability density functions are an important means to analyze the transmission of signal pulses through the cloud. Additionally, the mean number of photons per pulse is calculated by averaging the number of photons per row.

Whereas the photon statistics of the signal pulses represent the base for investigations of the single photon absorber, the statistical properties of the reference pulses are used to verify the Poissonian character of the photon number distribution.

Correlation of Detected Pulses

Besides photon statistics the study of the single photon absorber is based on the correlation of the detected signals.

The calculation of the second-order correlation function $g^{(2)}(t_1, t_2)$ is performed according to the expression given by equation (6.1). However, additionally to this cross-correlation term the auto-correlation functions of each detected signal are used as well. After correcting them for the values belonging to $t_1 = t_2$ for the reason outlined above, they are added to the cross-correlation term for enhancement of the SNR.

In practice, the intensity correlation function $g^{(2)}(t_1, t_2)$ is obtained by evaluating outer matrix products of relevant arrays.

It should explicitly be noted here that the built-in *MATLAB* function *xcorr()* cannot be employed for the purpose of calculating correlation functions that depend on both t_1 and t_2. This is owing to its way of processing input data which is equivalent to definition (6.2) and therefore intrinsically inappropriate for the present case.

In the simulation the computation of the correlation function is sourced out into a separate *MATLAB* function so that it is universally applicable to any kind of input data. For this reason it is used for both the data generated in the simulation and the data that is acquired in experimental measurements.

6.3   Simulation-Based Analysis of the Single Photon Absorber

The outcome of the SPA simulation will now be analyzed separately once only concerning the photon statistics and afterwards with respect to the bunching effect that is observed in the correlation function. Due to connections between photon bunching and pulse shapes, though, investigations of the correlation will also refer to corresponding pulse shapes and statistics where required..

Before starting studies on the absorber mechanism some remarks should be made on the general approach to the analysis which is based on a variation of underlying parameters:

1. Each data set which is used for generating one of the following plots, represents the simulation of the SPA scheme for 10^6 **repetitions**. By using such a high number of repetitions it can be assumed that resulting mean values will not be affected by statistical errors anymore. This eliminates misleading conclusions based on inaccurate photon statistics. This is why all peculiarities observed in corresponding statistical values are assumed to be completely caused by the absorber scheme itself.

2. Furthermore, for this analysis, all generated pulses with each of them constituting one run, are divided up into 112 **bins**. The choice of this number results from reproducing exactly the same parameters as for detected pulses in the experiment.

3. In particular also the simulated pulse shape is similar to the one in the experiment which is a **tukey-shaped pulse** with distinct rise and fall times and a **pulse width of about** 4.5 μs.

4. It should be noted, though, that the **length of the bins** set in the experiment does not agree with the real duration of the time bins that the counter's in the experiment exhibit, which is 10 ns. Rather, for the sake of justifiable computing efforts and time it was chosen to amount to 50 ns which is determined both by the fixed pulse length and the number of 112 bins.

    In this context, it should be mentioned that it was prioritized to reproduce the exact pulse length instead of the duration of one time bin. In place of the pulse length one could as well fix the length of a bin to the real 10 ns which would than yield a pulse width of about 1 μm using the same number of bins which should not be changed to keep computing time low. However, this would in turn complicate the comparison of experimentally obtained time scales with the simulation outcome. Anyway, it could be verified that an increased bin length of 50 ns does not at all affect statistics.

5. All figures that are tabularly constructed and presented below are arranged according to the same method:

    All plots which are listed in the same column rely on an equal mean number of photons per pulse λ. On the other hand, plots in the same row belong to the same value of the specific parameter that is to be analyzed in this particular figure. They only differ in the mean number of photons per pulse λ. If for example the influence of the life time is under examination, each plot in one row shows simulated data with the same underlying decay rate.

    Values λ for the mean number of photons per pulse have again been chosen in compliance with the experimentally defined parameters. There, measurements have been conducted for three different probe pulse intensities which directly correlate with mean numbers of $\lambda = 2.2$, 6.0 and 10.5.

6. In general, one figure serves to investigate as well only one parameter which is varied from one row to the next. This is done parallel for all three mean numbers λ.

    Therefore, all parameters that are not under examination have been fixed to one value for all plots comprised by one figure. In the case of the **absorption probability** for the first

photon, a value of **90%** was chosen pursuant to measurements. The ***fixed life time of*** $1\,\mu s$, however, represents the value that has to be used in order to bring simulation results into best agreement with the evaluation of experiment data. More details on this will be given later.

Finally, the chance for exciting more than one Rydberg atom at a time was assumed to be negligible. That is why the parameter $p_{exc}^{(2nd)}$ was set to zero for all simulation runs except for the ones of course which explicitly serve to explore the effect of $p_{exc}^{(2nd)}$. This complies with observations based on ionization measurements which reveal that coexisting excitations are only possible at lower principal quantum numbers of the Rydberg level.

7. A last comment should be made on detection efficiency and loss: Of course the photon counters integrated within the experiment do not perform in a perfect way. Rather, their inherent dead times prohibit to detect every single photon. However, since this technical shortcoming simply sorts out arbitrary photons, it only impairs the contrast of measurement and does not lead to any deeper physical effect. For this reason the detection efficiency was set to 100% in the simulation.

   The same is partly true for photon loss caused by scattering at atoms in the cloud. As this as well only deteriorates the amplitude of detected signals, it is not investigated further. However, in the simulation this parameter was initialized to a value of 5% pursuant to experimental measurements.

6.3.1 Analysis of Pulse Shapes and Photon Statistics

The discussion of the absorber performance begins with systematic studies on photon statistics. Below, four different cases are treated in order to separately investigate the effect of the parameters $p_{exc}^{(1st)}$, $p_{exc}^{(2nd)}$ and τ_{Ryd} on the SPA outcome. All unvaried parameters are always set to the fixed values given above.

Perfect Case

In the perfect case the simulation reproduces an experimental implementation of the SPA where Rydberg excitations do not exhibit any decay and second Rydberg atoms are as well not possible. This implicates that maximally one photon can be absorbed per pulse.

Therefore, corresponding pulse shapes and statistics are supposed to illustrate expected characteristics resulting from the absorption of one photon. They are intended to serve as a reference to compare the next three cases to.

Each of the split plots in figure 6.3 shows both the pulse shape (upper plot) and the corresponding photon statistics (underneath). All three mean photon numbers λ are studied simultaneously (different columns). Throughout this whole section the following colour code is used: Whereas blue-coloured lines represent reference pulses, those ones marked in red identify the actual signal pulses. Furthermore, the plotted pulse shapes always depict the average over all 10^6 pulses generated per experiment run.

As shown in the lower plots, photon statistics are typically visualized by means of histograms which specify the probability $p(N)$ for detecting a certain photon number N per pulse. The histogram in the first column additionally contains the likelihood for absorbing a certain number of photons from one pulse (green bars). This is only presented for the lowest mean photon number $\lambda = \langle N \rangle$ since for higher values the y-scale of the corresponding histogram would
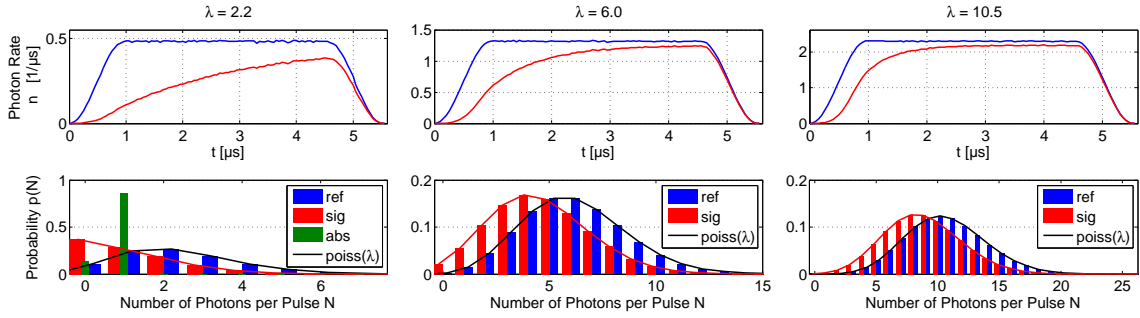
FIGURE 6.3: **Simulation of pulse shapes and photon statistics in the perfect case** (no decay, $p_{abs}^{(1st)} = 0.9$, $p_{abs}^{(2nd)} = 0.0$). *Each of the upper plots shows the averaged pulse shapes of both the reference (transmission in the absence of the cloud; blue line) and the signal (red) pulses for one of the three different mean numbers of sent photons per pulse $\lambda = 2.2$ (left), 6.0 (middle) and 10.5 (right). Corresponding photon statistics including all simulated runs are plotted beneath. For clarification each plot also comprises the envelope of the signal bars (red) and a perfect Poisson distribution (black) around the respective mean value λ. The plot on the left additionally shows the statistics of absorbed photons (green). Further explanations and a discussion are given in the text.*

change to such an extent that reference and signal bars would be compressed too much. In order to check whether enough data has been gathered that means whether enough experiment runs have been simulated to yield stable ensemble average values, a perfect Poissonian density distribution function is drawn in black into each plot.

Several characteristic features illustrate the perfect mechanism of the single photon absorber:

First of all it can be observed that the signal pulses never reach the level of the reference pulses, independent of the mean photon number λ. This can be explained by the fact that generally 5% of all photons per pulse get lost during transmission of the cloud.

From the green histogram it becomes apparent that not in all runs a photon has been absorbed from the pulse which is no wonder if keeping in mind a Rydberg excitation probability of 90%. Of course this aspect becomes most pronounced for low photon numbers λ since this probability value applies to every photon and the more photons a pulse contains the more often an absorption can take place.

An excitation (or absorption) probability that deviates from 100% also causes absorption events to be shifted to later times which can clearly be seen from the pulse shapes. Of course, the lower $p_{exc}^{(1st)}$, the less likely it becomes that the first photon in each pulse will be absorbed. Again, this feature becomes most pronounced for low mean photon numbers due to the fact that the probability for absorbing a photon at all increases with λ.

Unsurprisingly, the photon statistics especially of pulses with high λ reveal the system's basic task of subtracting one photon from a transmitted pulse. It can clearly be seen that the resulting red distribution function of the signal pulses still exhibits the same variance but is shifted to the left by one compared to the reference histogram. This illustrates the absorber's expected effect of rendering the Poisson distribution of incoming photon numbers to super-Poissonian statistics.

For the signal pulses this mechanism finally results in a nonlinear dependence between the mean photon number of sent pulses $\langle N_{in} \rangle$ and the mean number $\langle N_{out} \rangle$ of transmitted photons which is visualized in figure 6.4. Due to a loss rate of 5% the resulting red curve does

not perfectly converge to a straight line that exhibits the same slope as the reference but is shifted down by one. This would only the case if pulses did not experience any loss during transmission of the cloud, as shown in green in figure 6.4.

The line which indicates perfect performance for high mean numbers of incoming photons is drawn in black into each plot to serve as a guide to the eye.
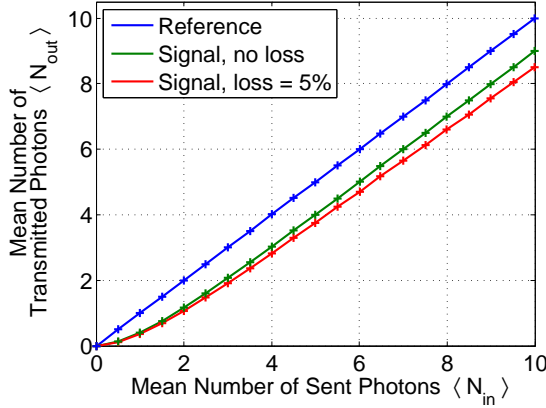
FIGURE 6.4: *Simulation of signal nonlinearity.* *The mean number of transmitted photons* $\langle N_{out} \rangle$ *is plotted against the mean number of sent photons* $\langle N_{in} \rangle$ *for the reference pulses (blue) and the signal pulses once for the perfect case (green) and once considering a typical photon loss rate of 5% due to scattering (red). In both cases the signal pulses show a clear nonlinearity with* $\langle N_{in} \rangle$. *In the perfect case* $\langle N_{out,sig} \rangle$ *converges to* $\langle N_{out,ref} \rangle - 1$. $(p_{exc}^{(1st)} = 0.9)$

Influence of Decay

Next, it should be studied in which way the life time of the single Rydberg excitation affects photon statistics. Corresponding plots can be found in figure 6.5.

Obviously, faster Rydberg decay significantly deteriorates the absolute level of transmitted signal pulses. At a life time of $\tau_{Ryd} = 0.1\,\mu s$ for example (lowermost row) it does not even reach a quarter of the reference level anymore. In order to comprehend this effect it is advisable to relate the life time which is the time constant of the decay to the time scale of the pulse length of about $5\,\mu s$. Thus, if the length of one pulse is about 50 times higher than the life time itself (as it is the case on the lowermost row) the excitation will on average decay up to 50 times during one pulse so that finally much more photons will be absorbed. Once an exiting Rydberg excitation decays the next photon can be subtracted from the pulse with a probability of $p_{exc}^{(1st)}$. As this process starts right after the pulse enters the cloud and continues during its entire transmission time, the pulse level is attenuated throughout its full length.

Concerning photon statistics, shorter life times evidently lead to an increase of the probability for lower photon numbers per transmitted pulse. This observation is actually no big surprise as it is in full agreement with increasing absorption. Of course, the more photons are extracted from the pulse the higher is the probability of detecting respectively fewer photons in the transmitted signal.

However, in contrast to the process of perfect absorption of a single photon which preserves the variance of the distribution function, in the present case of reduced life times *both* the mean number of photons *and* the variance are influenced. The underlying mechanism that causes the probability density function to change in this way is in fact not trivial:

The perfect absorber mechanism yields a pronounced nonlinearity of transmitted photon numbers where the resulting relation $\langle N_{out} \rangle (\langle N_{in} \rangle)$ tends towards the shifted straight line described by $\langle N_{out} \rangle = \langle N_{in} \rangle - 1$ which indicates the extraction of only one single photon. In this case the number of absorbed photons is totally independent of the actual number of
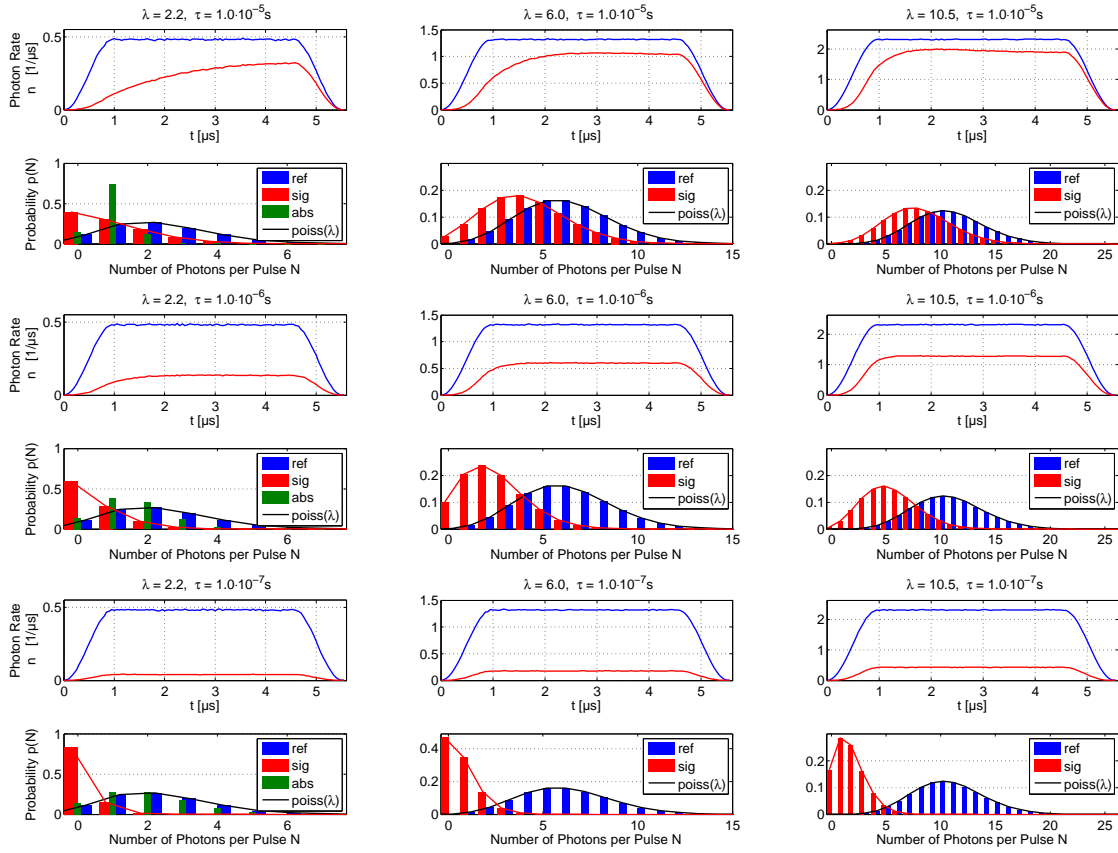
FIGURE 6.5: *Simulation of pulse shapes and photon statistics for exploring the effect of Rydberg decay* $(p_{abs}^{(1st)} = 0.9, p_{abs}^{(2nd)} = 0.0)$. *Plots in the first row are generated from simulated data for a life time of $\tau_{Ryd} = 0.1\,\mu s$, those in the middle for $\tau_{Ryd} = 1\,\mu s$ and the ones in the last row from data for $\tau_{Ryd} = 10\,\mu s$. (refer to caption 6.3 for further details on denotations)*

incoming photons which in turn results in a probability density function with unchanged mean variation but shifted mean value λ compared to the reference.

However, as soon as decay or loss gains influence on the absorber performance these dependencies become severely modified: These processes inherently destroy the limit of single photon extraction even though they are not necessarily absorbed for the purpose of Rydberg excitation. As a result the number of subtracted photons per pulse is no longer independent of the number of sent photons. Rather, under these conditions, the more photons enter the cloud the more will also be extracted. In the extreme case of perfect absorption efficiency $p_{exc}^{(1st)} = 1.0$ and fast decay this finally leads to a complete depletion of transmitted pulses.

Such a deteriorated *single photon* absorber mechanism in turn also erodes the pronounced nonlinearity. Instead of rising slowly and adapting to a shifted straight line with unchanged slope of one, the whole resulting relation $\langle N_{out}\rangle\,(\langle N_{in}\rangle)$ is now more and more flattened tending to a line with significantly reduced slope. This behaviour becomes increasingly severe for faster decay as shown in figure 6.6.

Such an absorption behaviour which moreover persists for the whole pulse duration translates to a probability density function that is not only shifted but also squeezed. This kind of
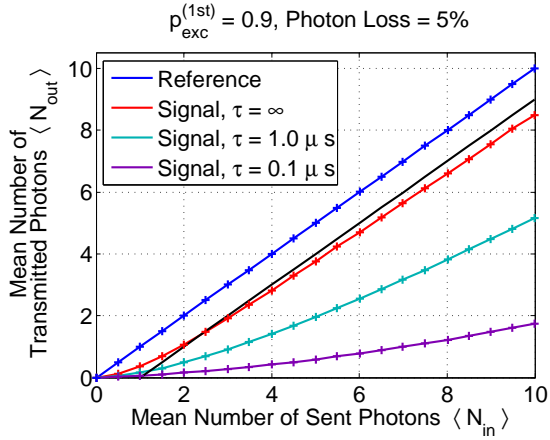
FIGURE 6.6: *Simulation of signal nonlinearity with decay. The mean number of transmitted photons $\langle N_{out} \rangle$ is plotted against the mean number of sent photons $\langle N_{in} \rangle$ for the reference pulses (blue) and the signal pulses for three different Rydberg decay rates. The signal nonlinearity becomes significantly attenuated for faster decay. The perfect absorption behaviour for large $\langle N_{in} \rangle$ is additionally shown as a guide for the eye (black). ($p_{exc}^{(1st)} = 0.9$, 5% loss)*

modification of the pdf reveals that in case of photon loss the Poissonian nature of the original incoming photon number becomes more and more preserved.

These observations are in sharp contrast to the resulting statistics in the perfect case without any loss induced by either decay or scattering. There, the pdf is only shifted by exactly one to the left with unchanged spread of photon number probabilities.

Consequently, the (partial) conservation of Poissonian pulse character can be interpreted to be a clear sign of imperfections in the system which introduce additional (unwanted) absorption processes such as loss or decay.

In which way certain parameters modify statistics will be discussed in more detail at the end of this section 6.3 after having analyzed corresponding correlation functions.

Impact of Absorption Probability

Studies on the impact of Rydberg absorption efficiency on the signal photon statistics are based on simulated data for three different absorption probabilities $p_{abs}^{(1st)} = \{0.6, 0.8, 1.0\}$ which is plotted in figure 6.7. It should be kept in mind that $p_{abs}^{(2nd)} = 0$ here, that means the number of simultaneously existing Rydberg atoms is still limited to one. Again, the plots are arranged such that the first row presents the absorber outcome for perfect excitation efficiency which successively declines towards the last row.

All plots rely on simulations with a Rydberg life time of $\tau_{Ryd} = 1.0\,\mu s$. Why exactly this value has been chosen here becomes clear later on in section 6.5 where simulation results are compared to the outcome of experimental measurements.

Obviously, imperfect Rydberg absorption probabilities affect the statistics similarly to faster decay (see figure 6.5), however, in the expected reversed way: Whereas shorter life times lead to more frequent photon subtraction, impaired Rydberg excitation efficiency of course impedes the absorption of photons which becomes directly apparent in higher pulse levels.

The overall reduction of the signal pulse amplitude which can be observed in all plots in figure 6.7 is caused by the finite life time. This is also why the pulse shapes do not exhibit the same slow rising behaviour as under perfect conditions (compare figure 6.3). Instead they directly reach a steady level which they remain at throughout the whole detection time.

Furthermore, reduced excitation efficiency $p_{abs}^{(1st)}$ is reflected in changed photon statistics. Since less photons will be absorbed at reduced excitation probability the pdf spreads and is shifted to higher mean numbers of transmitted photons compared to the perfect case. It more
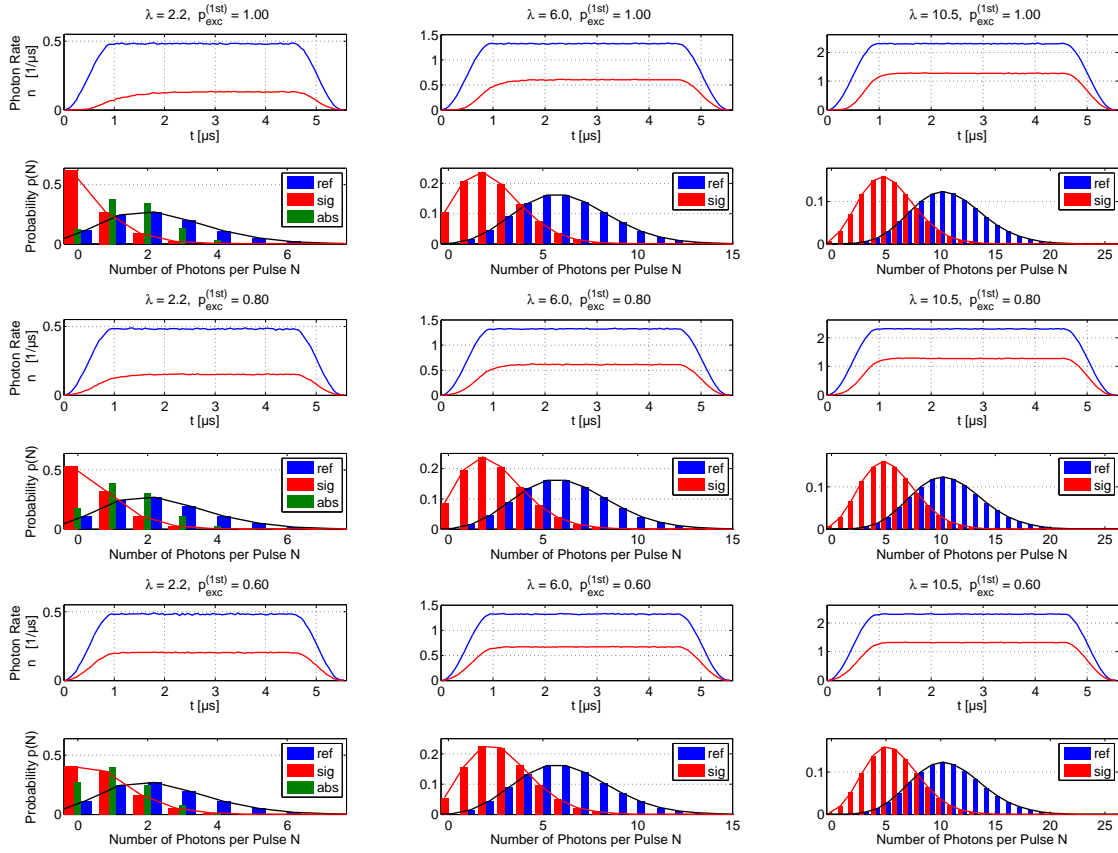
FIGURE 6.7: *Simulation of pulse shapes and photon statistics for investigation of Rydberg excitation efficiency* $(\tau_{Ryd} = 1\,\mu s,\ p_{abs}^{(2nd)} = 0.0)$. *Plots in the first row are generated from simulated data for highest possible efficiency of sole Rydberg excitations* $(p_{abs}^{(1st)} = 1.0)$, *those in the second row for* $p_{abs}^{(1st)} = 0.8$ *and the ones in the last row from data for* $p_{abs}^{(1st)} = 0.6$. *(refer to caption 6.3 for further details on denotations)*

and more approaches the reference distribution which it would finally match for $p_{abs}^{(1st)} = 0.0$ without considering loss. Thus, impaired Rydberg excitation efficiency as well, at least partly, maintains the Poissonian nature of the photon number of incoming pulses.

Chance of Coexisting Excitations

The last characteristic physical property of the absorber scheme that shall be examined here is the chance for two coexisting Rydberg excitations in the cloud. In the simulation this is accounted for by setting $p_{abs}^{(2nd)} \neq 0$. Figure 6.8 comprises plots for three different probabilities of coexisting excitations, namely $p_{abs}^{(2nd)} = \{0.0\,,0.2\,,0.4\,\}$. Again, the plots in the first row embrace the ideal case of sole excitations, however, allowing for non-perfect first excitation efficiency with a typically measured value of $p_{abs}^{(1st)} = 0.9$.

In order to comply with experimental observations the likelihood for coexisting excitations has been limited to 40%. Even though this value already represents a fairly large chance, it might still be too low to clearly highlight the effect of coexistent excitations on the realistic

SPA performance including loss. That is why Rydberg decay was not taken into account for the investigation of $p_{abs}^{(2nd)}$.
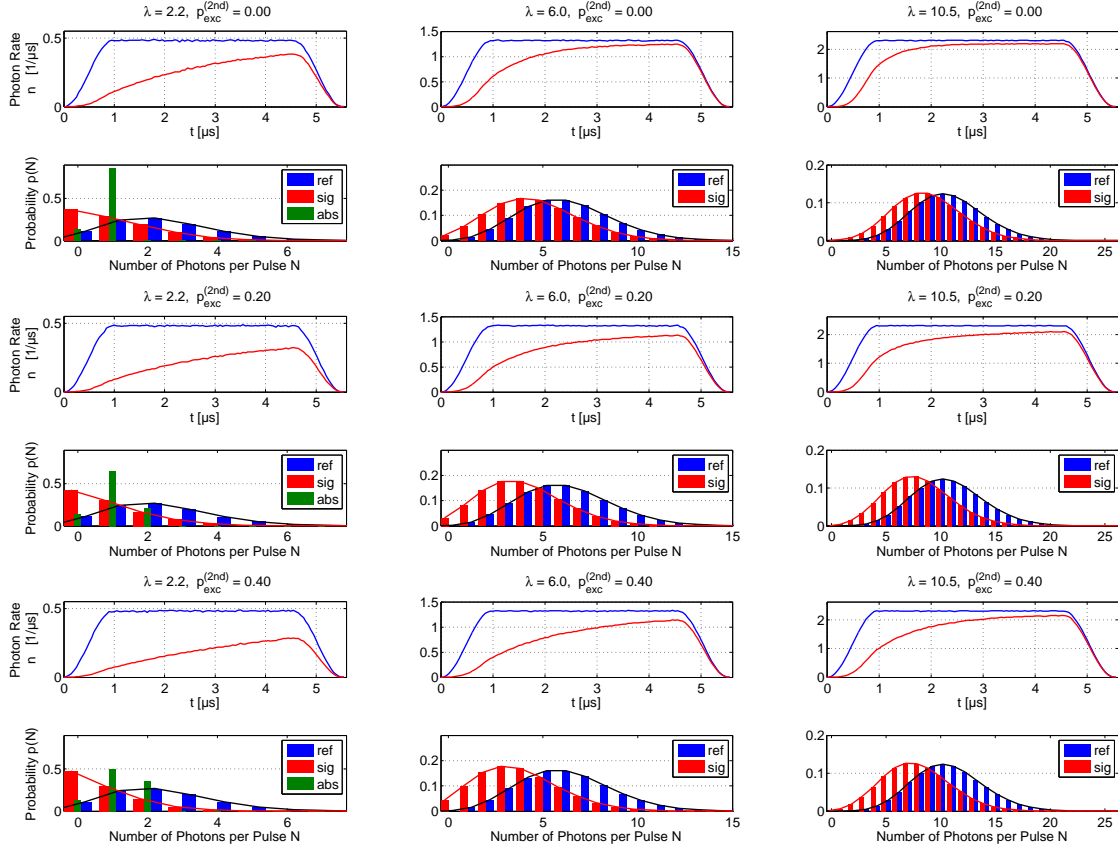
FIGURE 6.8: *Simulation of pulse shapes and photon statistics for exploring the effect of coexisting Rydberg excitations* $(\tau_{Ryd} = \infty,\ p_{abs}^{(1st)} = 0.9)$. *Plots in the first row are based on simulated data with vanishing likelihood for coexisting excitations* $(p_{abs}^{(2nd)} = 0.0)$, *those in the second row for* $p_{abs}^{(2nd)} = 0.2$ *and the ones in the last row are based on data for* $p_{abs}^{(2nd)} = 0.4$. *(refer to caption 6.3 for further details on denotations)*

Generally, finite chances for coexisting excitations intrinsically enable the absorption of a second photon within the life time of a present excitation. This matter of fact especially translates into a pulse shape that rises more slowly to the steady state because the second photon can already be extracted right from the beginning of the pulse.

This makes the difference compared to all previous cases where second absorption for the purpose of Rydberg excitations is, if at all, only possible after the existing one decayed. This implies that the minimal time-lag of photon absorption is defined by the life time so that in particular only one photon can be subtracted from the beginning of the pulse.

Furthermore, an increasing possibility of coexisting Rydberg atoms apparently affects the pdf of transmitted photon numbers in a significantly different way than impaired excitation efficiency $p_{abs}^{(1st)}$ or faster Rydberg decay.

In the latter cases the probability density function is both shifted *and* compressed which represents, at least to some extent, the discussed (unwanted) conservation of the Poissonian

character of incoming photon numbers. However, in the case here, the photon number distribution is solely shifted to the left, its variance, though, stays nearly unchanged. This becomes especially apparent from the plots for higher mean input photon numbers λ. Only very small deviations from perfect shifting can be observed in terms of marginally enhanced amplitude of most probable photon numbers and slightly smaller variances (especially visible in the left plot in the last row). These subtleties are caused by the influence of slightly imperfect efficiency for first excitations ($p_{abs}^{(1st)} = 0.9$) and some small amount of experimentally measured loss.

In fact, it was to be expected that the pdf will only shift as a result of allowing for coexistent excitations. This is due to the fact that the underlying physical process is similar to the mechanism of first excitations: Without considering decay, in both cases the number of extracted photons is either limited to one or two. Consequently, all input photon numbers will as well be reduced by maximally one or two. Since higher numbers of subtracted photons are not possible this absorption behaviour only affects the mean number of the pdf but preserves its original variance. Thus, in case of coexisting excitations the initial Poissonian character of input photon numbers will as well be converted to super-Poissonian distribution.

This is in sharp contrast to the effect of the other two analyzed parameters, decay and impaired Rydberg excitation probability. In the case of decay the number of subtracted photons per pulse is not restricted to a certain number. Rather, all numbers of photons can be absorbed provided that the pulse contains a sufficiently high quantity. On the other hand, deteriorated excitation efficiency impedes the extraction of a photon so that more and more pulses will just go through the cloud in the way they entered it. Consequently, both mechanisms (at least partly) preserve Poissonian statistics which indicates that they inherently counteract the intended mechanism of the *single photon* absorber.

6.3.2 Analysis of Correlation Effects

The second part of the studies on the SPA mechanism is based on the correlation function $g^{(2)}(t_1, t_2)$ defined in equation (6.1). All plots below are calculated from the simulated signal pulse after being split and detected. Additionally, as explained previously, the auto-correlation of each detector signal has also been used in order to enhance the contrast.

The fundamental observation that can be made from the correlation function is the appearance of photon bunching that highly depends on the detection times at the counters. Therefore, the development of the bunching feature can immediately be related to the pulse shape since temporal positions within the pulse are directly connected to the detection time.

Again, each of the next three subsections separately treats the effect of the variation of one characteristic physical property of the absorber scheme on the photon bunching, either decay, absorption efficiency or the chance of coexisting excitations. Related plots are arranged in exactly the same way as in the previous chapter so that each correlation plot can be easily compared to the corresponding pulse shape and photon statistics.

The following investigations are primarily supposed to comprehend distinct characteristics of the bunching effect and especially of its connection to certain physical processes taking place within the SPA framework.

Perfect Case

Again, first the perfect case shall be considered for the purpose of explaining all general features that can be extracted from the correlation plots. Therefore, the absorber scheme has been simulated for typical parameters of $p_{abs}^{(1st)} = 0.9$, $p_{abs}^{(2nd)} = 0.0$, infinitely large Rydberg life times and photon loss of 5% for each of the three mean photon numbers $\lambda = 2.2$, 6.0 and 10.5 yielding the data sets visualized in figure 6.9.
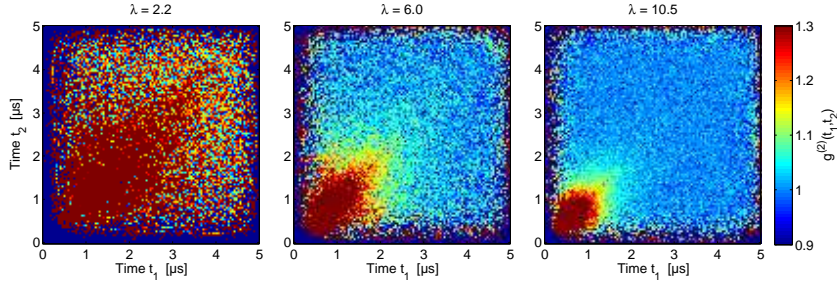
FIGURE 6.9: *Simulation of signal correlation function* (no decay, $p_{abs}^{(1st)} = 0.9$, $p_{abs}^{(2nd)} = 0.0$). *Each of the colour plots shows the correlation function $g^{(2)}(t_1,t_2)$ for the three mean numbers of sent photons $\lambda = 2.2$ (left), 6.0 (middle) and 10.5 (right) as functions of the independent detection times t_1 and t_2. Values $g^{(2)}(t_1,t_2)$ are encoded in colours ascending from blue ($g^{(2)}(t_1,t_2) < 1$) over green ($g^{(2)}(t_1,t_2) = 1$) to red ($g^{(2)}(t_1,t_2) > 1$). (corresponding pulse shapes and photon statistics that are based on the same data sets are shown in figure 6.3)*

Obviously, the position but also the duration of the bunching effect relative to the detection time highly depends on the mean number of photons λ per incoming pulse. The higher it is, the more does the bunching get compressed in the beginning of the detection. This indicates that at higher λ the underlying physical processes that are responsible for photon bunching happen increasingly early.

In the present scheme the bunching can definitely be ascribed to photon absorption leading to Rydberg excitations in the cloud since this is the only possible process to be triggered by pulse transmission through the cloud. This explains the observed λ-dependence of the bunching appearance: Of course, the higher the pulse intensity, the more photons are available at earlier times and the faster first absorption takes place.

Another feature that becomes apparent in figure 6.9 and shows up in all following figures as well, is the strongly impaired contrast and high noise at low photon numbers due to fewer absorption events at such a low light intensity. Therefore, plots belonging to $\lambda = 2.2$ are not really suitable for the purpose of detailed investigations and only shown as a means to illustrate general λ-dependences.

Influence of Decay

The plots generated from data for different decay rates that are merged in figure 6.10 confirm the observations that have already been made in the context of analyzing corresponding pulse shapes (compare figure 6.5 and related text).

At reduced excitation life times, the number of photons that are extracted from the same pulse for exciting Rydberg atoms rises considerably which directly results in reduced signal pulse levels. Additionally, the absorption of photons is no longer restricted to the beginning of
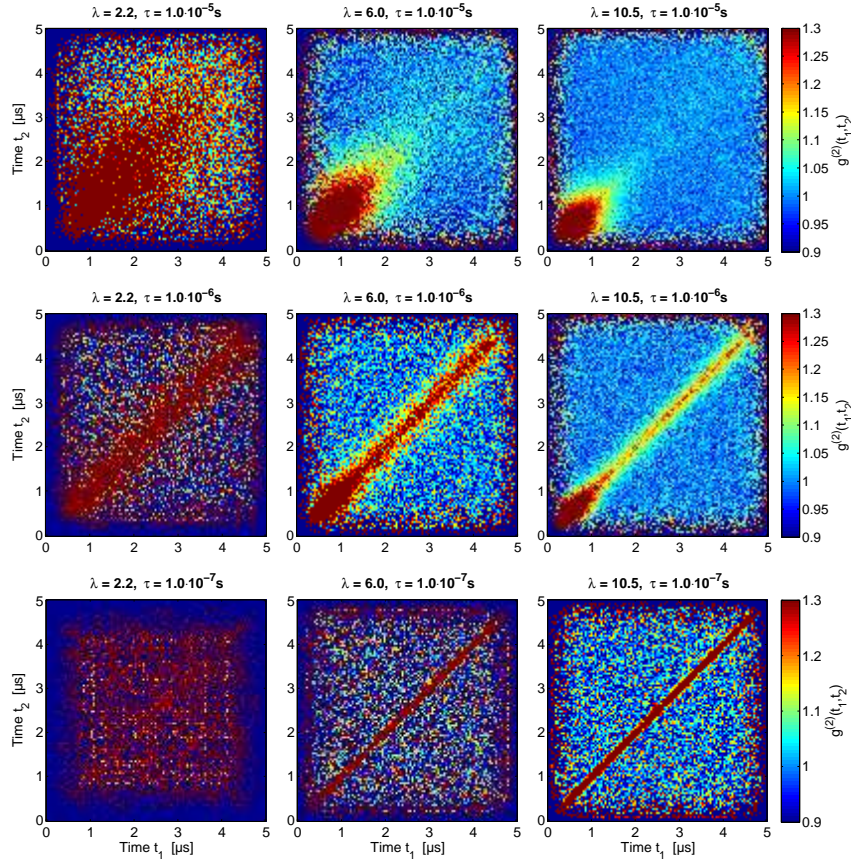
FIGURE 6.10: *Simulation of signal correlation function for exploring the effect of Ryd-berg decay* $(p_{abs}^{(1st)} = 0.9, p_{abs}^{(2nd)} = 0.0)$ *Plots in the first row are based on simulated data using a life time of $\tau_{Ryd} = 0.1\,\mu s$, those in the middle for $\tau_{Ryd} = 1\,\mu s$ and the ones in the last row are based on data for $\tau_{Ryd} = 10\,\mu s$. Results are analyzed and discussed in the text. (corresponding pulse shapes and photon statistics that are based on the same data sets are shown in figure 6.5; similar structure and colour code as in figure 6.9)*

the pulse but can rather take place throughout the whole transmission. As explained previously, this is due to the fact that for finite decay the number of subtracted photons is by no means limited to only one which is typically absorbed right after the pulse enters the cloud. In case of Rydberg decay, photons are in fact regularly extracted once an existing superatom collapses so that absorption events occur throughout the whole pulse. Thus, the number of absorbed photons is no longer limited to one but rather determined by both the life time and the total number of photons per pulse: The shorter excitations stay alive the more do pulses become depleted during its full transmission time.

The permanent occurrence of absorption events becomes especially apparent in the way the bunching feature changes. With increasing decay (from top to bottom in figure 6.10) it becomes clearly extended over the full detection, and pulse transmission time respectively, coming along with correspondingly reduced vertical spread.

In order to understand the latter effect it might be helpful to become aware of the actual meaning of one specific correlation value $g^{(2)}(t_1, t_2)$ that belongs to a distinct pair (t_1, t_2) of

detection times at the counters. According to the definition of the correlation function, values of $g^{(2)}(t_1,t_2) = 1$ simply indicate that on ensemble average the detected signal at time t_1 does not correlate with the one at t_2 which means that events that happened at the corresponding pulse positions and respectively at the corresponding cloud transmission times on average are not connected to each other.

In the concrete case of the single photon absorber this means that the product of photon numbers detected at t_1 and t_2 on average does not differ from the product of the individual mean values at these times. Thus, correlation values only depart from one if the averaged product deviates more often and more severely from its mean value than statistically allowed. Only photon numbers at t_1 and t_2 that in combination regularly exceed the product of their individual mean numbers can finally result in bunching. Exactly this is only the case if the photon numbers at both t_1 and t_2 on average obey super-Poissonian statistics.

Thus, photon bunching that becomes restricted to the diagonal $t_1 = t_2$ indicates that single photon absorption is more and more deteriorated in terms of multiple absorption per pulse. This is caused by imperfections that superpose the ideal mechanism and lead to conservation of the Poissonian character at these distinct time bins[62].

By the way, it would not have been possible to analyze the vertical spread of bunching solely based on the reduced correlation function $g_t^{(2)}(t_1,t_2)$ where the two-dimensional time dependence has been boiled down to one relative time τ and where the ensemble average has been replaced by the time average. Thus, now it becomes clear why this transformation should not be carried out here. Since the bunching effect is in general not uniformly distributed with similar width along the whole diagonal, conclusions based on $g_t^{(2)}(t_1,t_2)$ are not equally reliable as those ones using $g^{(2)}(t_1,t_2)$. Effects of any kind of imperfection for example can not be distinguished as easily as with the help of the general correlation function $g^{(2)}(t_1,t_2)$.

Impact of Absorption Probability

With the help of the pulse shapes and corresponding histograms (compare figure 6.7) it has already been realized that impairment of Rydberg excitation efficiency mainly affects the absorber scheme by degrading its task of single photon subtraction. This as well becomes apparent in the correlation plots in figure 6.11 which rely on the same data.

It should be kept in mind here that the elongation of the bunching signal over the whole diagonal that can be observed in basically all nine plots is caused by the influence of decay. All plots are based on simulation data with a life time of $\tau_{Ryd} = 1\,\mu s$.

The main effect of gradually worsened absorption probability (from top to bottom in figure 6.11) becomes evident in terms of vanishing contrast. Actually, this is coherent with the way the underlying physical process is modified: At low excitation efficiency it cannot be ensured that a photon is absorbed from every incoming pulse so that consequentially not all input pulses will contribute to photon bunching. More and more detected pulses only add to the background signal of constantly $g^{(2)}(t_1,t_2) = 1$. Therefore, the contrast is degraded and the bunching signal erodes.

This effect can also be explained by means of Poisson statistics: As discussed in the context of decay, correlation values $g^{(2)}(t_1,t_2)$ will only exceed one if the product of the signals at t_1 and t_2 on average over all runs exhibits larger spread than the product of their individual

---

[62] Especially for the purpose of this discussion it should be kept in mind that not only the photon number in the whole pulse is distributed according to Poisson statistics but also especially the photon number in each bin.
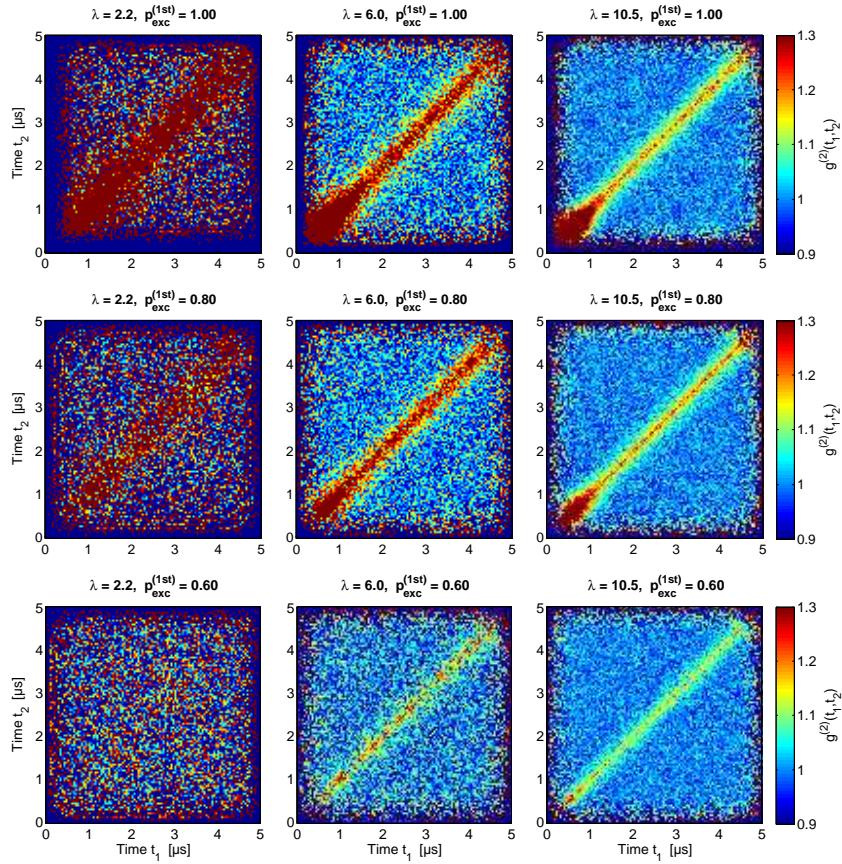
FIGURE 6.11: *Simulation of signal correlation function for investigation of Rydberg excitation efficiency* $(\tau_{Ryd} = 1\,\mu\text{s},\ p_{abs}^{(2nd)} = 0.0)$. *Plots in the first row are generated from simulated data for highest possible efficiency of sole Rydberg excitations* $(p_{abs}^{(1st)} = 1.0)$, *those in the second row for* $p_{abs}^{(1st)} = 0.8$ *and the ones in the last row belong to data for* $p_{abs}^{(1st)} = 0.6$. *Results are analyzed and discussed in the text. (corresponding pulse shapes and photon statistics that are based on the same data sets are shown in figure 6.7; similar structure and colour code as in figure 6.9)*

mean values. This is in turn only the case if the detected signals at both t_1 and t_2 are super-Poissonian.

Thus, from reduced values $g^{(2)}(t_1,t_2)$ it can be deduced that, due to missing absorption, fewer detection signals, that are assigned to either t_1 or t_2, exhibit super-Poissonian character and therefore do not contribute to photon bunching.

Chance of Coexisting Excitations

As discussed previously, in case of slight chances of coexisting Rydberg excitations a second photon can already be extracted from the pulse for the purpose of Rydberg excitation as long as the existing one is still alive. It was observed that this possibility mainly affects the pulse shape directly after entering the cloud because both photons can already be absorbed right from the beginning. In consequence, the transmitted intensity rises more slowly than in the case of single excitations.

This effect also appears in the corresponding correlation functions that are visualized in figure 6.12, namely in the following way: Since the frequency of absorption events becomes enhanced in the front of the pulse, photon bunching agglomerates as well at the beginning of detection and declines towards the end. Thereby, especially the vertical extent of the bunching signal in the front is broadened.

Translated to the picture of Poissonian character of detected signals this means that single photon absorption or, in other words, generation of super-Poissonian statistics is now true for more bins in the front than without the possibility of coexisting excitations. This also explains why the signal slightly expands in vertical direction: In more and more cases both the signal detected at t_1 and the one at t_2 show super-Poissonian character.
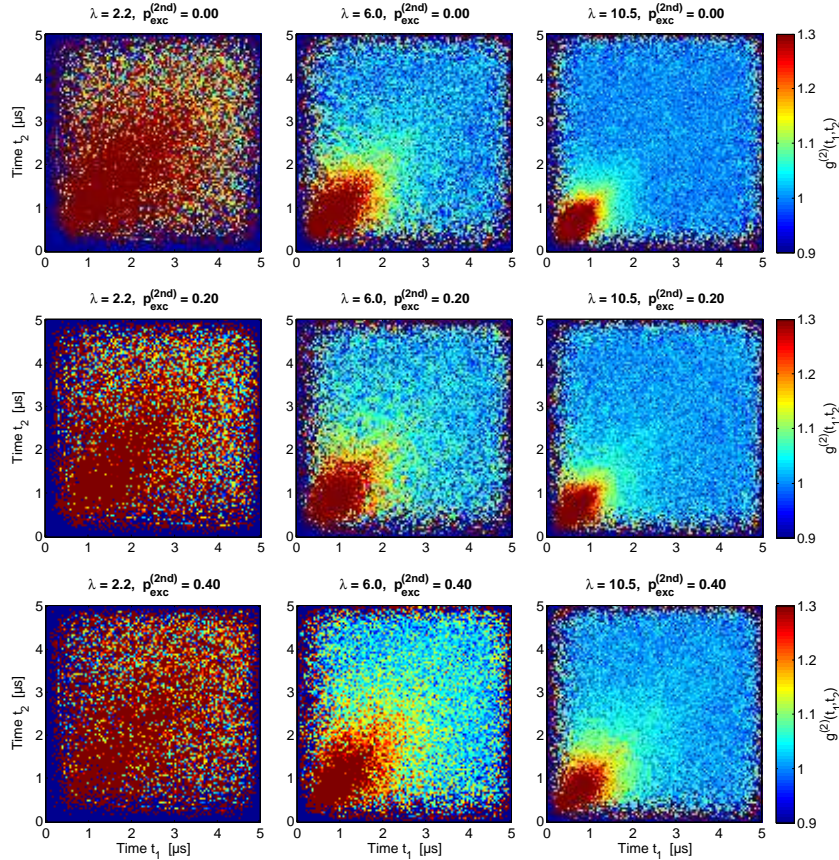
FIGURE 6.12: *Simulation of signal correlation function for exploring the effect of coexisting Rydberg excitations* $(\tau_{Ryd} = \infty, p_{abs}^{(1st)} = 0.9)$. *Plots in the first row are based on simulated data for vanishing likelihood for coexisting excitations* $(p_{abs}^{(2nd)} = 0.0)$, *those in the second row for* $p_{abs}^{(2nd)} = 0.2$ *and the ones in the last row rely on data for* $p_{abs}^{(2nd)} = 0.4$. *Results are analyzed and discussed in the text. (corresponding pulse shapes and photon statistics that are based on the same data sets are shown in figure 6.8; similar structure and colour code as in figure 6.9)*

Reason for Different Transmission Statistics

Of course one might wonder why the variation of different characteristic physical properties of the present SPA implementation scheme modifies the statistics of transmitted photon numbers in quite different ways. The reason has already been outlined above in context of analyzing the influence of decay on pulse shapes. However, this will now be discussed in detail after having identified the connection between statistics and photon bunching in the correlation functions. Now the question is: Why do some parameter result in the preservation of Poissonian character which in turn simply leads to correlation values of $g^{(2)}(t_1,t_2) = 1$ and why does the influence other parameters finally yield super-Poissonian light which enables the observation of photon bunching effects?

The only difference in the way certain properties can influence the photon number statistics lies in the number of *subtracted* photons per pulse. Therefore, it is worth having a closer look on exactly this number statistics of absorbed photons which is visualized in figure 6.13 for two exemplary cases:

The upper plot shows the case of absorption for mean input photon numbers of $\lambda = 10.5$, allowing for coexisting excitations with a probability of 40%, however, prohibiting their decay. The underlying data is exactly the same as for the plots in the lower right hand corner of both figure 6.8 and 6.12.

In contrast, the lower plot is based on the same data that has already been used for generating the plots in the lower right hand corner of figures 6.5 and 6.10, as well with $\lambda = 10.5$, however, with a life time of $\tau_{Ryd} = 0.1\,\mu s$ and only single excitations.

Each plot depicts the statistics of both the number of subtracted photons per pulse (turquoise or purple) and as a reference in blue the distribution of the number of incoming photons which exhibits typical Poissonian character. It should be noted that the y-scales have been chosen differently for the two plots.

Each plot illustrates the effect of the according underlying process regarding photon extraction and thereby reveals the different influence on the transmitted photon number statistics. Generally, as shown in the upper plot, in the perfect case without decay and only small loss, the number of extracted photons is limited to the maximally possible number of coexisting excitations.

However, if decay is accounted for (lower plot), suddenly much more photons will be absorbed. Now the number of extracted photons is no longer restricted to the number of maximally coexisting excitations. Rather, it is now only
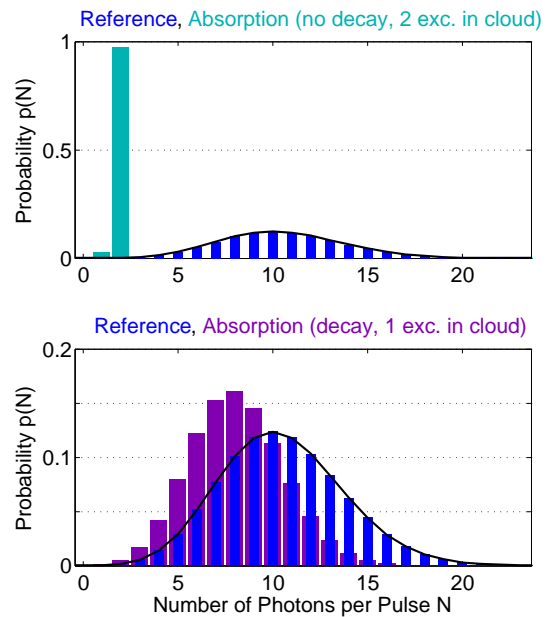
FIGURE 6.13: *Simulated statistics of absorbed photon numbers.* *Each of the two plots shows the photon statistics of both the reference pulses (blue) and the number of absorbed photons per pulse for two different choices of parameters. Whereas the upper one represents the perfect absorber mechanism in case of finite chance for coexisting excitations* ($\tau_{Ryd} = \infty$, $p_{abs}^{(2nd)} = 0.4$), *the lower plot illustrates the case of highly deteriorated performance due to decay* ($\tau_{Ryd} = 0.1\,\mu s$, $p_{abs}^{(2nd)} = 0$).

restricted by the number of available photons per pulse. Additionally, even more important is that not always an equal amount of photons is absorbed. As shown in the lower plot the distribution of extracted photons is in fact as well Poissonian, similar to the one of incoming photons[63].

So how does this now translate to the statistics of transmitted photons which finally gives rise to correlation effects?

If the number of incoming photons is modified in Poissonian-like way which means that from each pulse a different number of photons is subtracted, the outcome still obeys a Poisson distribution. In contrast, if, as in the case of the perfect single photon absorber, always the same number of photons is absorbed, only the mean number of transmitted photons is modified, the corresponding variance, however, is maintained. This results in super-Poissonian statistics which represents the precondition for photon bunching.

Thus, the observation of correlation effects directly depends on the distribution of subtracted photons which in turn is ruled by the number of maximally extractable photons. All imperfections such as Rydberg decay which deteriorate the perfect mechanism by lifting this limit, inherently annihilate photon bunching.

6.3.3 Conclusion and Possible Advancements

In fact, in its current version the numerical simulation of the single photon absorber already allows for a comprehensive and systematic study of the three most important physical processes within the present scheme. Especially Rydberg decay and impaired excitation efficiency have thereby been identified as to deteriorate the perfect mechanism by partly preventing the complete adaption to super-Poissonian transmission. This is an important result with regard to the analysis of experimental data.

However, there is still some room left for improvements of the simulation since some peculiarities about the scheme have not been considered so far. This becomes of special interest for the purpose of comparing the simulation results to the evaluation of experimentally acquired data.

Therefore, it would be most important to implement all details of light-matter interaction taking place within the SPA scheme. In this context it is especially not sufficient to restrict the treatment to the excitation of Rydberg atoms. Rather, following photons from the same pulse can of course induce stimulated emission. This process is not only accompanied by Rydberg decay but particularly also by the emission of a photon that joins the transmitted pulse and can subsequently be detected as well. Thus, both the life time and the number of transmitted photons will then be modified. The underlying mechanism is exactly the same as previously described in the context of the coherent single-photon transistor where a final control pulse is used to retrieve the stored photon.

In the simulation version that was employed to provide the data for the plots presented here, photon retrieval has not been taken into account yet. This should be kept in mind for the following comparison to experimental results.

---

[63] In order to emphasize this difference in subtracted photon statistics two extreme cases have been chosen which cannot be experimentally observed like this in the present setup. Especially, the measured life time is typically two orders of magnitude higher.

Furthermore, a value of $\lambda = 10.5$ has been chosen since the effect becomes most pronounced for high mean photon numbers where the number of maximally extractable photons is not additionally limited by the number of available photons.

Another interesting modification of the simulation is on-resonant two-photon Raman excitation to the Rydberg level. This can actually be implemented in a quite straightforward way and has already been done rudimentary within this thesis. In this on-resonant case the scheme is not supposed to *absorb* single photons but to *transmit* a train of single photons where the minimal time lag is mainly limited by the group velocity of the light in the medium. Thus, a slight modification of the scheme would yield a totally different outcome which in turn enables many further applications. However, it has to be kept in mind that a comprehensive implementation of on-resonant excitation necessarily requires to also consider excitation dynamics which was so far more or less legitimate to be swept under the curtain.

6.4 Experimental Realization

6.4.1 Implementation Scheme

Whereas in the simulation only the HBT setup was digitally replicated, the experimental measurement procedure is not restricted to the detection of transmitted light on avalanche single-photon counters that build up the Hanbury Brown-Twiss setup. Additionally, after transmission of each pulse ionization measurements are performed in order to detect the number of simultaneously existing Rydberg excitations in the cloud. This is achieved by applying an electric field which is sufficiently strong as to ionize the Rydberg atom by removing the weakly bound, highly excited electron. The resulting ion is subsequently detected using a so called micro-channel plate[64].

Conveniently, the laser setup for the single photon absorber is similar to the one for the coherent transistor. The most important parts of the setup are schematically illustrated in figure 6.14.

For the experimental realization of the single photon absorber different Rydberg levels have been used. Ionization measurements reveal that exclusive excitations can only be ensured for large principal quantum numbers n. This is due to the previously mentioned fact that the interaction strength which is parameterized by the blockade radius R_b can be enhanced with increasing n. Indeed, this represents an important result concerning the success of all practical work conducted before in the context of modifying the optical dipole trap. At this point it was finally possible to probe the cloud size by determining the number of coexisting excitations. Now, it could experimentally be verified that the dimpled trap really performs in the intended way as to establish the system of an ultracold cloud of
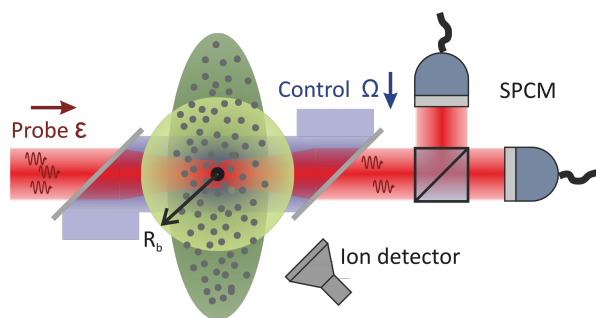
FIGURE 6.14: *Schematic of experimental setup of single photon absorber. The optical setup for providing both the probe $\mathcal{E}$ and the control Ω light fields are the same as for the single-photon transistor (compare also figure 2.3) except for using only one beam for each of them. In probe propagation direction the cloud is fully covered by a single Rydberg excitation with blockade radius R_b. The transmitted probe pulses are detected on the two single photon counting modules (SPCM) in the HBT setup. The cloud can be probed for Rydberg excitations by ionization and subsequent detection of the ion on a micro-channel plate.*

---

[64] For more information about micro-channel plates refer to [110].

atoms which is completely blockaded by one single excitation, thereby enabling the realization of various single-photon gates such as the coherent transistor or the SPA.

Finally, the state $|r\rangle = |121S_{1/2}, m_j = 1/2\rangle$ was used as the Rydberg level for the implementation of the single photon absorber. Here, the corresponding blockade is always large enough to cover the whole cloud so that not more than one Rydberg atom can exist at the same time.

Furthermore, the choice of this state allows for enhanced dephasing of the bright spin wave state $|W\rangle$ to one of the $N-1$ collective dark states $|D\rangle$ due to broadening of the Rydberg molecule lines in the excitation spectrum [111]. As explained in the beginning of this chapter, such a dephasing is required in order to avoid driving Rabi oscillations between the collective ground state and the bright spin wave state $|W\rangle$. Instead, the two-photon Raman transition which is facilitated by the combination of the weak probe field $\mathcal{E}$ and the strong coupling field Ω that is blue-detuned by more than $40\,\mathrm{Mhz}$ from the intermediate state $|e\rangle$, allows for reliable conversion of a probe photon to a Rydberg atom. In order to maximize the Rydberg excitation efficiency the coupling field lasts $2\,\mu\mathrm{s}$ longer than the probe.

Additional dephasing is finally achieved by means of a spatially dependent AC-Stark effect. This is induced by keeping the dimple laser switched on while performing experiments.

In the experiment the probe field is pulsed in the way that tukey-shaped pulses with a length of about $5\,\mu\mathrm{s}$ are sent into the medium. The same pulse properties have also been used in the simulation. The number of photons per pulse can be precisely controlled by the probe laser intensity enabling values of λ on the single-photon level.

In order to eliminate statistical errors one experiment run which consists of the transmission and detection of a single pulse is repeated for more than 30000 times.

6.4.2 Experimental Results

Finally, in this implementation scheme both the pulse shapes and the corresponding correlation functions have been measured separately for mean incoming photon numbers per sent pulse of $\lambda = \{2.2, 6.0, 10.5\}$. This is why the simulation of the experiment has also been based on these values. Figure 6.15 shows plots that have been generated using this measured data.

In order to comply with the previous notation for simulation results the sent pulses (blue lines) are again called reference and the transmitted ones (red lines) referred to as signal.

Obviously, in all three cases the measured pulse shapes do not rise up to the level of the reference pulses. This is a clear sign for some kind of "loss" mechanism taking place which means that the ideal task of single photon absorption is to some degree impaired. This can either be caused by general photon loss during transmission of the cloud due to coupling to the intermediate state $|e\rangle$ or by decay of the Rydberg atom which immediately allows for a new excitation and thus photon absorption. Since measurements reveal that 95% of all probe photons pass the cloud in the absence of any control field, Rydberg decay definitely contributes to lower pulse levels as well. Only this explains why also photons from the end of the pulse are absorbed and the bunching signal stretches across the full detection time.

Furthermore, even for the largest mean photon number $\lambda = 10.5$ the transmitted pulses do not immediately climb up to their final steady level but show a distinct rise in the beginning. This indicates efficient Rydberg excitation in terms of first extractions taking place right after the pulse enters the medium.

As photon absorption times are directly related to the shape of photon bunching, both
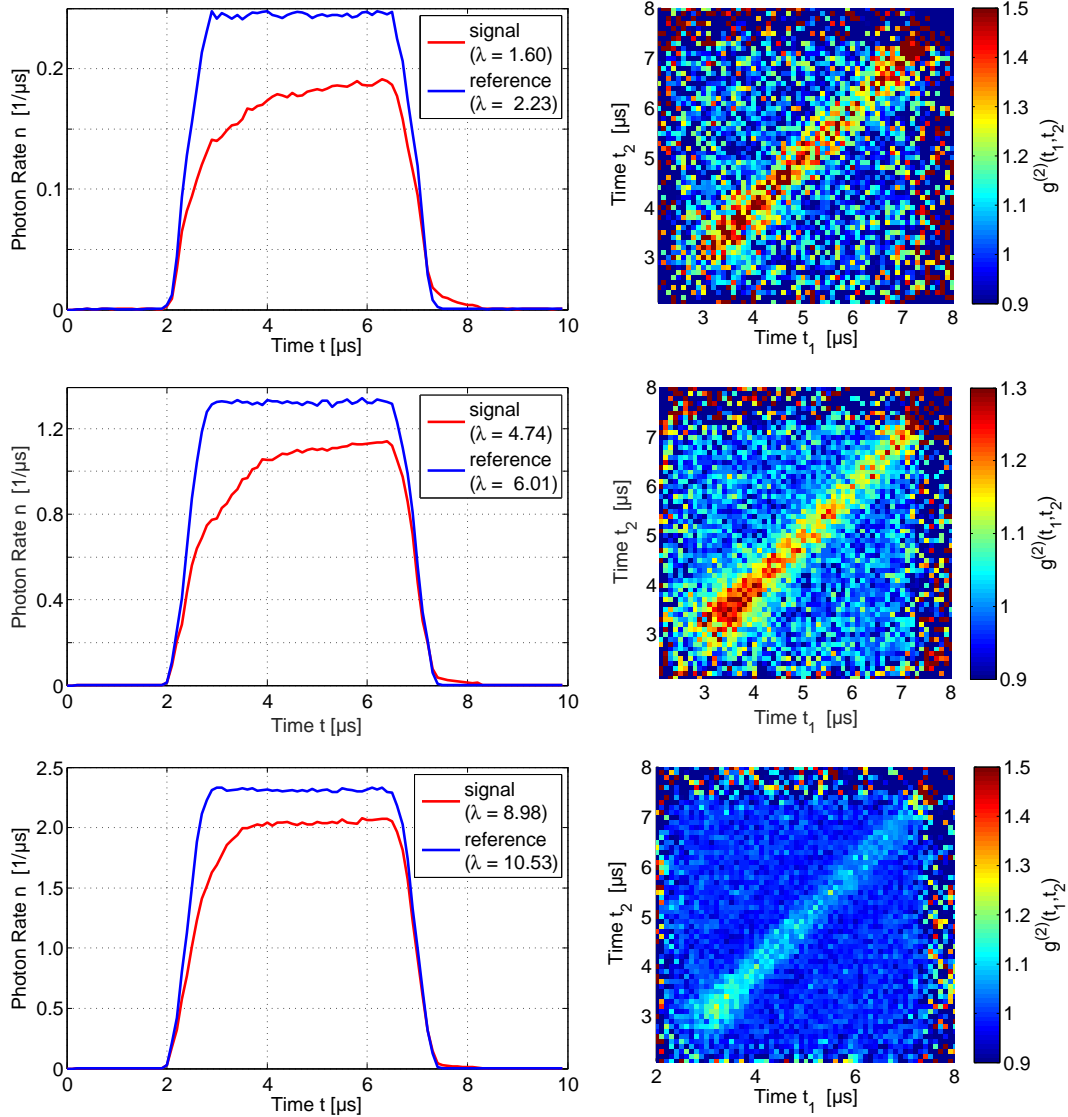
FIGURE 6.15: *Measurement of pulse shapes and correlation functions.* *Each of the plots on the left show the shapes of the sent reference pulses (blue) as well as the detected signal pulses (red) averaged over all experiment runs. The colour plots on the right illustrate the correlation function $g^{(2)}(t_1,t_2)$ of the respective signal pulses on the left. Plots in different rows only differ in the mean photon number per pulse λ. The ones in the first row show the measurement for sent photon numbers around the mean value $\lambda_{ref} = 2.23$, the ones in the middle for $\lambda_{ref} = 6.01$ and the plots in the last row present measured data for $\lambda_{ref} = 10.53$.*

features can also be observed in the correlation plots. In fact, photon bunching is enhanced in the beginning but also lasts throughout the whole detection.

6.5 Simulation versus Experiment

Next to these qualitative statements quantitative results can be obtained by comparing the evaluation of experimental data to the outcome of the simulation. By iterative variation of all parameters in the simulation both the pulse shapes and the correlation function can be brought into agreement with measurements which finally allows for the determination of physical properties of the experimental SPA scheme.

The parameters in the simulation which above investigations of the SPA mechanism are based on, have already been chosen with regard to this comparison. This for example explains why coexisting excitations have generally not been permitted, except for the purpose of studying their general influence. The choice of $p_{abs}^{(2nd)} = 0.0$ originates in ionization measurements which reveal that in the case of $|r\rangle = |121S_{1/2}\rangle$ the cloud is fully blockaded by one single excitation.

Appropriate parameters for matching simulation and experiment can now be figured out by comparing plots based on experimental data to the simulation outcome. Since the parameter $p_{abs}^{(2nd)}$ can for the just-mentioned reason not be used for this purpose only the life time τ_{Ryd} and the excitation efficiency $p_{abs}^{(1st)}$ are left over.

On the basis of the rising behaviour of signal pulses and the shape of the correlation function a value of $p_{abs}^{(1st)} = 0.9$ is determined as to match the simulation data and the experiment results in the best way. This value confirms the observation that Rydberg excitations are created quite efficiently. In contrast, concerning the life time, no distinct value can be figured out which brings both the pulse shapes and the correlation functions into agreement.

By comparing the plots of the simulated pulse shapes to the measured ones, here best agreement seems to be achieved for a life time of $\tau_{Ryd} = 10\,\mu s$ which is approximately the same value that can also experimentally be obtained by means of ionization measurements.

Simulated correlation plots (compare figure 6.10), however, reveal that for such a long life time photon bunching does not stretch across the full diagonal but already ceases within the first half of the whole detection time. In order to match the correlation functions rather a value of about $\tau_{Ryd} = 1\,\mu s$ should be chosen which is one order of magnitude smaller than the one that fits best for the pulse shapes. However, such a decay time constant in turn yields pulse amplitudes that are far below the measured ones (compare figure 6.5). If Rydberg excitations decay that quickly too many photons will be absorbed for exciting new Rydberg atoms.

This apparent contradiction, though, should most likely be solvable by accounting for the entire atom-light interaction during pulse transmission. For the reason outlined above, readout of the stored Rydberg excitation will definitely influence the transmission signal. In fact, then also for longer life times, which directly result in increased transmitted pulse amplitudes, the bunching signal will very probably extend over the complete diagonal. Thus, by considering the readout effect it should be possible to match both the pulse shapes and the exact shape of the photon bunching feature.

6.6   Conclusion

First and not least important, the implementation of the single photon absorber delivers several important results with regard to practical works conducted in the scope of this thesis. In this context, it should be mentioned that it was not only possible to experimentally realize this new single-photon gate but also to comprehensively replicate its mechanism by means of a Monte-Carlo simulation. Only minor extensions are missing for an entire digital reproduction of its experimental implementation scheme.

Regarding this thesis, one of the most important results retrieved from final absorber measurements is the observation that the new ODT setup now allows for trapping the atomic cloud in such a way that it is fully blockaded by one single Rydberg excitation. Thus, the implementation of the single photon absorber finally revealed that practical work carried out in the beginning of this thesis has in fact been successful in terms of satisfying the initially defined goal of an entirely "single-blockaded" cloud.

However, the usefulness of the single photon absorber should by no means be restricted to the simple purpose of probing the cloud for its size. The outcome of systematic studies on its mechanism rather reveal that the now available free-space SPA realization represents a truly promising single-photon gate that in turn offers a huge range of further applications.

Conclusion and Outlook

Conclusion

Pursuant to the course of events, all activities that have been performed in the scope of this thesis can basically be divided up into two parts:

Tasks comprised by the ***first*** part were mainly related to a significant reduction of the confinement area of the former optical dipole trap and therefore very technically oriented. This especially aimed at establishing a Rydberg gas of ultracold atoms that enables the implementation of *single-photon* gates which have been realized in the ***second*** part of this thesis.

This plan was approached by considerably downsizing the atomic cloud by means of a dimpled optical dipole trap. Finally a state should be reached where the ensemble is fully blockaded by only *one* Rydberg excitation. This in turn makes it possible to radically modify the transmission behaviour of light pulses by means of only *one* preceding photon.

First of all, the realization of this state necessitated to calculate the light field that provides the required dipole potential and to formulate requirements on the according light source. Based on this an appropriate optical setup was designed which also includes the modification of the absorption imaging setup by replacing the existing focussing lens by a high-resolution objective. For this purpose the optical performance of the objective was analyzed regarding a simultaneous application to both the imaging and the dimple light at different wavelengths. This revealed that the objective cannot perform both tasks at the same time to complete satisfaction:

Even though the design of the objective aims at minimizing image defects, it induces significant chromatic aberration. If it is simultaneously used for the two wavelengths of 780 nm for imaging and 855.2 nm for the dimple light, the focal positions of both beams differ by more than 200 µm. Furthermore, its performance is very sensitive to alignment errors.

Although the laser diode which was initially selected to serve as the dimple light source should, according to its specifications, satisfy all requirements for the according light field, a comprehensive characterization of its output beam revealed the opposite. In fact, investigations of its mode structure could not verify the claimed way of light emission. For this purpose a scanning Fabry-Pérot cavity was designed, constructed and finally coupled to the output beam. Cavity coupling was strongly impeded due to the very abnormal beam shape prior to fibre transmission. From the cavity spectrum in use with the filtered beam behind the fibre it could be deduced that the laser diode emits light at different wavelengths at the same time. Moreover, it was observed that the emission is not stable in time but rather fluctuates on the time scale of minutes.

Furthermore, intensity fluctuations due to optical feedback into the diode could not even be completely eliminated by using an optical isolator which would moreover significantly impair the available optical output power. The intensity could as well not be compensated by setting up an active intensity stabilization loop.

For these reasons the dimpled optical dipole potential was finally realized by means of the

Toptica diode laser system in a very straightforward way. In the context of the subsequent characterization of the resulting trap a significant reduction of the cloud size could be measured. Moreover, the final ensemble temperature of only $T = 5.43\,\mu\text{K}$ in the new configuration was extracted from time of flight measurements. This ultracold cloud of about 2.5×10^4 ^{87}Rb atoms still yields a large optical depth of $OD = 10$.

The results of these practical activities now offer the realization of applications on the single photon level due to the fact that the narrow confinement of the atomic cloud allows for blockading the entire ensemble by only one Rydberg atom. Two single-photon gates, namely the coherent all-optical transistor and the single photon absorber have been studied in the scope of this thesis.

In order to continue measurements that have been conducted last within the former experiment setup, activities were first focussed on the implementation of the coherent all-optical single-photon transistor. In fact, compared to the formerly incoherent transistor the new scheme does not solely represent a small extension but rather constitutes an independent new application.

It was theoretically suggested by Weibin Li and Igor Lesanovsky that a "single-blockaded" Rydberg medium allows for introducing the quantum mechanical aspect of coherence to the transistor scheme. Now, the Rydberg excitation is in fact coherently distributed over all atoms in the cloud in terms of a collective spin wave. Coherent retrieval at the end of the sequence then represents a crucial step towards further processing of the photon which inherently converts the transistor into a quantum mechanical gate.

However, before actual measurement of the coherent single-photon transistor will be performed the small cloud was first to be comprehensively analyzed, especially with the objective of proving the existence of the single-blockade-sized Rydberg medium.

To this end the present experimental setup and atomic excitation scheme was employed for the implementation of a completely different quantum gate, namely the single photon absorber.

The basic mechanism of the absorber application was first systematically studied and analyzed by simulating the entire experimental implementation scheme. From these Monte-Carlo simulations crucial conclusions could be drawn regarding the influence of various physical properties of the present implementation scheme. In doing so, Rydberg decay and impaired Rydberg excitation efficiency could be identified as to degrade the ideal outcome of the single photon absorber by impairing the conversion of Poissonian input to super-Poissonian output pulses with unchanged variance but shifted mean number of photons. It could be shown that this transformation can only be brought to perfection if single or multiple coexisting Rydberg atoms can be stored in the cloud throughout the entire transmission time of one pulse.

Furthermore, it was worked out in which way the creation of super-Poissonian light translates into the characteristic correlation effect of photon bunching. Simulation of correlation measurements confirmed previous observations concerning the influence of above-mentioned physical properties.

Parallel to the simulation the single photon absorber was experimentally implemented in the dimpled trap and related measurements were conducted. First of all, they revealed that the initial aim of a single-blockade-sized cloud can successfully be established if working at a high principal quantum number $n = 121$ of the Rydberg level.

More important, though, was the measurement of photon bunching and corresponding photon statistics of both the input and the transmitted light pulses.

128

Finally, these measurements were compared to the simulation outcome in order to work out values of the physical system. In doing so, the measured excitation efficiency of about 90% could be confirmed. However, no value for the Rydberg life time could be determined which brings both the measured pulse shapes and the photon bunching signal into agreement with simulation results. This directly demands for the extension of the simulation in terms of an implementation of the entire atom-light interaction especially concerning the process of reading out existing Rydberg atoms.

Outlook

Enhancement of the single-photon absorber is not restricted to optimization of the simulation method. Rather, on the experimental side a "local repumper" could be used to solely address all atoms residing in the dimple of the trap. This additional laser beam could be introduced to the experiment via the same optical path that is already used for the dimple beam itself. By means of the repumper it can be ensured that really only atoms in the dimpled trap contribute to experimental measurements.

The present experiment setup and excitation scheme exhibit the outstanding property that only slight variations already allow for totally new applications. In the scope of this thesis, the transistor scheme could for example easily be adapted to serve for the implementation of the single photon absorber. In the same way the latter one could now straightforwardly be adjusted to enable the realization of a further photon gate, the single-photon transmitter. Resulting trains of single photons directly offer the realization of photon-photon gates, the creation of artificial states of light or the investigation of many-body phenomena based on strongly correlated photons [7].

Finally, as already proposed in this thesis, it is definitely worth to finalize the *coherent* single-photon transistor. Its successful implementation in turn would directly pave the way towards the realization of quantum gates which represent the building block of quantum information processing. All these developments suggest a truly promising future for the present experiment and for Rydberg quantum optics in ultracold gases in general.

Appendix A

Two-Frequency AOM Driver

This appendix contains the description of a two-frequency AOM driver which is especially designed for applications requiring high beam pointing stability. The basic setup of such a driver had to be modified in order to make fast switching of the laser beam possible.

The first section briefly summarizes the basics of acousto-optic modulation. This is directly followed by motivating the necessity of a two-frequency driver. Finally, the last section comprises a detailed instruction of the implementation of this device. This also includes a rather technical step-by-step instruction of how to carry out the calibration procedure.

A.1 Basics

Acousto-optic modulators (AOMs) are mainly used to deflect laser beams, shift their frequency or modulate their intensity. In the field of atomic, molecular and optical physics (AMO) especially the last two applications are relevant. Especially the ability to switch beams on and off with high speed and electronically controlling their intensity is crucial in experiments using laser light to manipulate matter.

AOMs are based on the physical phenomenon of Brillouin scattering which, in this case, describes the diffraction of light by sound waves within a crystal, predicted for the first by Brillouin in 1922 [112]. Sound waves passing the crystal provoke periodic density perturbations which finally result in periodic changes of the refractive index in the crystal. The periodicity is given by the wavelength of the moving sound wave.

In the case of thick gratings that means when the optical path length is much bigger than the sound's wavelength λ_s, this process can be described by Bragg diffraction. Here, constructive interference of different light paths always occurs if the difference in the corresponding path lengths of two scattered beams is an integer multiple m of their wavelength λ. The angle, under which this is the case, is called Bragg angle θ_B. Mathematically this condition is expressed by

$$2\lambda_s \sin \theta_B = m\lambda \tag{1.1}$$

where m is an arbitrary integer number corresponding to the order of diffraction.

In the opposite limit of thin gratings only small differences in the optical path lengths occur. Thus, these small phase shifts result in diffraction into many different orders. This case is called Raman-Nath regime [113]. As AOMs are typically operated in the Bragg regime where thick gratings dominate, Raman-Nath diffraction will not be considered here.

Besides switching and modulating laser beam intensities, shifting the light's frequency is a second useful feature in the application of AOMs. In a simplified description this effect can be

considered as a consequence of the Doppler effect. Due to the fact that the sound wavefronts are moving through the AOM crystal at a certain velocity c_s, diffracted light experiences a small frequency shift which is given by c_s.

In a more sophisticated approach, the particle picture, the frequency shift is described by the absorption and stimulated emission of phonons representing the sound wave. In the case of a scattering event, energy and momentum always has to be conserved. Assuming that one phonon with a distinct energy $\hbar\omega_s$ and momentum $\mathbf{k}_s$ is absorbed by an incoming photon $(\hbar\omega_{in}, \hbar\mathbf{k}_{in})$ this results in an outgoing photon with

$$
\begin{aligned}
\omega_{out} &= \omega_{in} + \omega_s \\
\mathbf{k}_{out} &= \mathbf{k}_{in} + \mathbf{k}_s
\end{aligned}
\tag{1.2}
$$

accounting for the momentum's vector character. Thus, the corresponding frequency shift is $\Delta f = \omega_s/2\pi$.

The sound waves travelling through the AOM's crystal are generated by a radio-frequency (RF) signal which is applied to a piezoelectric transducer. A commonly used crystal material is Tellurium Dioxide TeO_2. After having passed the crystal, the sound wave is absorbed at the opposite end [114]. Absorption is crucial in order to suppress unwanted standing waves and maintain the AOM's frequency-shifting property. The fraction $\frac{I_0 - I_1}{I_0}$ of incoming light being diffracted into the first order by the moving sound waves is determined by the sound's intensity P_s and, thus, by the RF-power [113]:

$$
\frac{I_0 - I_1}{I_0} = \sin^2\left(\frac{\pi}{\lambda}\sqrt{10^7 * M' * P_s}\right)
\tag{1.3}
$$

where the acousto-optic figure of merit M accounts for various material and acoustic beam parameters. Consequently, the RF power P_{RF} corresponding to the maximum fraction of light in the first order of diffraction depends as well on these parameters. Typical values lie in the range of some volts leading to Bragg angles on the order of mrad [65].

A.2 Motivation

In our experiment, amongst others, AOMs are used in order to control the laser intensity of the laser beams for the optical dipole. This enables precise and fast changes of trap characteristic such as the trap depth. At the same time it is crucial to ensure a high stability of the trap position on the sub-micrometer scale. In the case of low laser powers this can easily be achieved by using a fibre between the AOM and the experiment. However, this method cannot be implemented if high power lasers are required. Here the beam has to be directly applied to the experiment demanding for a high pointing stability of the beam. Consequently, it is necessary to keep both the absolute value of the diffractive index and its spatial pattern inside the crystal as constant as possible.

However, if the light intensity needs to be varied, this cannot always be guaranteed in the simple setup of only one RF frequency applied to the AOM. Significant changes in the power of the sound waves, caused by altered RF power, lead to varying power dissipation in the crystal accompanied by thermal fluctuations. This, in turn, induces changes in the diffractive index,

---

[65] For AOM 3080-194 [115]: P=2.5W leading to 10.1mrad

finally resulting in movements of the diffracted beams on the order of mrad and timescales of several seconds [116].

In order to compensate for this movement, the RF frequency could be adjusted simultaneously to changes in the RF power. However, this method is difficult to realize since the calibration depends on the speed of change in RF power [66].

High pointing stability can more easily be obtained by driving the AOM with constant RF power. This is realized by simultaneously applying two different RF signals to the AOM at fixed frequencies f_1 and f_2 with distinct powers P_1 and P_2. The power P_2 of the second auxiliary RF signal is then adjusted such that the condition $P_{tot} = P_1 + P_2 = constant$ is permanently fulfilled. Though incoming light will now be diffracted into various different orders [67] both the intensity of diffracted light as a whole and the power dissipation within in the crystal can be maintained at a constant level.

However, beams corresponding to the same order of diffraction will only be clearly separated if either the difference $\Delta f = f_2 - f_1$ in frequency is big enough or the distance from the AOM is sufficiently large. Although Δf should be maximized, both frequencies still have to be within the bandwidth of the AOM. Moreover, the amount of power being reflected by the AOM at one frequency should be equal to the similar amount in the second frequency. Only then, it is guaranteed that RF power stays constant both directly behind the RF source and in the crystal during changes either in P_1 or P_2. Of course, at the same time reflectivity should be minimized in order to achieve high diffraction efficiency.

Assuming proper calibration of the auxiliary RF signal, this two-frequency AOM scheme finally provides for high beam pointing stability even in the case of high laser intensities.

A.3 Implementation and Calibration

The fundamental setup of the two-frequency AOM driver consisting of two identically constructed AOM drivers and a device called 'voltage adjustment' which is required in order to adapt the second driver's input voltage such that the combined RF output power of both drivers stays constant. The two individual RF outputs of each driver are merged by means of a combiner [68] and amplified [69] before being applied to the AOM.

However, for purposes which require fast switching on the timescale of several nanoseconds the whole setup had to be modified. Up to now switching times were limited to milliseconds by the AOM drivers. Furthermore, calibration of the present setup was carried out with another type of AOM [70]. Every exchanged or added part such as a fast switch, though, will influence the transfer function describing the relation between the individual input powers of each AOM driver. The overall input signal which is applied to the whole setup is directly applied both to the first AOM driver and to the voltage adjustment which generates a control voltage for the second driver based on the overall input voltage. This nonlinear transfer function between input and control voltage is calculated and finally set by the voltage adjustment during calibration. Thus, re-calibration has to be conducted again after modifying the whole device.

---

[66] The slower the variation in RF power the more likely the temperature will follow correspondingly.

[67] Besides higher orders of diffraction due to absorption and stimulated emission of more than one phonon [117], every order will now be generated twice, one for each frequency.

[68] *Mini-Circuits*, ZSC-2-1

[69] *Mini-Circuits*, ZHL-1-2W-S

[70] previously: *Crystal Technology*, 3110-199 [116], [118]; now: *Crystal Technology*, 3080-194

Besides re-calibration, replacing the AOM additionally requires another change to be made. Every single AOM features an individual RF-frequency-dependent back-reflection curve since an AOM can be considered Consequently, the two RF-frequencies have to be chosen anew in order to ensure that both signals are equally reflected by the AOM.

Thus, for choosing appropriate frequencies, first of all the AOM's back-reflectivity curve

$$R(f) = \frac{P_{refl}(f)}{P_{out}(f)} \tag{1.4}$$

has to be determined. Here, watt [W] instead of decibel [dBm and dB] should be used as a unit [71]. Hence, both the RF power $P_{refl}(f)$ reflected by the AOM and the AOM driver's output power $P_{out}(f)$ as a reference value have to be measured. This can be done by directly attaching the *output* channel (OUT) of a RF directional coupler [72] to the output of one AOM driver. In the first case (measurement of $P_{refl}(f)$) the AOM is connected to the *input* (IN) of the coupler and a spectrum analyzer (SA) [73] to its *coupled* channel (CPL) [74] as shown in figure A.1. For the case of $P_{out}(f)$ the SA is simply connected to IN and CPL is terminated by a $50\,\Omega$ resistor.

Due to their equality of structure, principally, it does not matter which AOM driver is used for the measurements. However, as the output behaviour might be slightly different that driver is used which generates the frequency dedicated for the experiment.
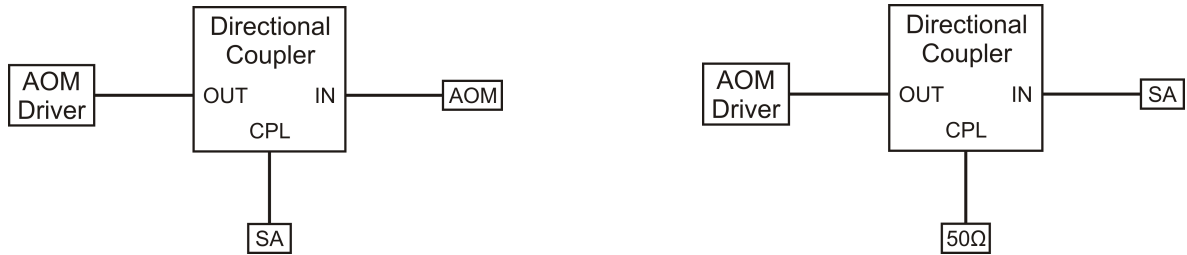
FIGURE A.1: *Setup for the measurement of the RF-power reflectivity by the AOM.*
Left: The RF-signal generated by the AOM driver and reflected by the AOM is measured via a spectrum analyzer (SA) (= $P_{refl}(f)$). The generated RF-signal is directed from its source (AOM driver at OUT) to the AOM (at IN). The reflection can then be measured at the couled port (CPL) using the SA.
Right: The reference data $P_{out}(f)$ for calculating the reflectivity $R(f) = {P_{refl}(f)}/{P_{out}(f)}$ is taken by connecting the SA to the input of the coupler and directly measuring the signal arriving here. Therefore, the CPL connection has to be terminated by a $50\,\Omega$ resistor.

The measured RF-power back-reflectivity curve for the AOM in use is shown in figure A.2. It should be noted that for calculating P_{refl} from the measured signal at CPL the latter one has to be corrected by the loss of $11.50\,\mathrm{dB}$ (according to [119]) between IN and CPL.

Finally, based on this data the two frequencies are chosen while keeping in mind the following three requirements: Δf should be sufficiently large, both f_1 and f_2 have to be within

---

[71] Conversion: $P[\mathrm{dBm}] = P[\mathrm{dB}] + 30 = 10 \cdot \log_{10}\left(P[\mathrm{W}]/1\,\mathrm{w}\right) + 30$ and $P[\mathrm{W}] = 1\,\mathrm{W} \cdot 10^{((P[\mathrm{dBm}]-30)/10)}$ respectively. Consider following calculation rules: $[\mathrm{dB}] \pm [\mathrm{dB}] = [\mathrm{dB}]$; $[\mathrm{dBm}] \pm [\mathrm{dB}] = [\mathrm{dBm}]$; $[\mathrm{dBm}] - [\mathrm{dBm}] = [\mathrm{dB}]$; $[\mathrm{dBm}] + [\mathrm{dBm}]$ is not defined.
[72] *Mini-Circuits*, ZDC-10-1+ (0.5 to 500MHz)
[73] *HAMEG*, HMS3000, 3GHz
[74] An attenuator is attached to the input connection of the SA taking into account its limited input power.
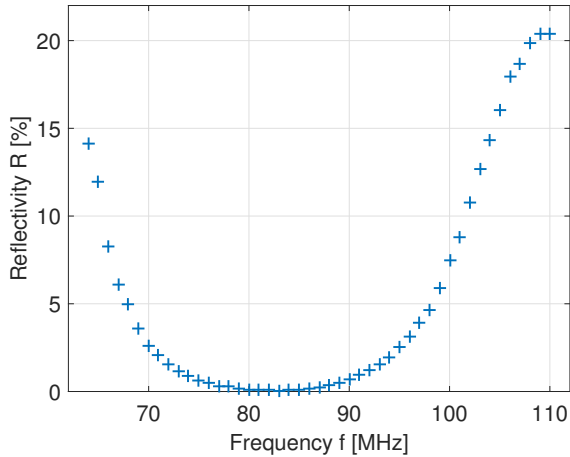
FIGURE A.2:
***Measured reflectivity curve of the RF-power reflected by the AOM of type* Crystal Technology*, 3080-194.** For a wide range of frequencies between approx.* $75\,\text{MHz}$ *and* $92\,\text{MHz}$ *the AOM shows very little reflection of the applied RF-signal. At the edges of this flat range the reflectivity slowly starts to increase and finally reaches unfeasible high values.*
Due to these characteristics, f_1 *and* f_2 *required for the two-frequency AOM driver were chosen to be* $f_1 = 71\,\text{MHz}$ *and* $f_2 = 94\,\text{MHz}$ *with a almost equal reflectivity of* $R_1 = 2.070\,\%$ *and* $R_2 = 1.963\,\%$ *respectively.*

in the AOM's bandwidth and the reflected power should be equal and as low as possible. Here, $f_1 = 71\,\text{MHz}$ and $f_2 = 94\,\text{MHz}$ are considered to be a good choice. The respective reflectivities at these frequencies are $R_1 = 2.070\,\%$ and $R_2 = 1.963\,\%$.

A.3.1 Setup

Typically, a standard single-frequency AOM driver mainly consists of three series connected parts as shown in figure A.3: a voltage-controlled oscillator (VCO) [75] for generating the RF signal, an electronic attenuator [76] for modulating the amplitude and a power amplifier [77] with constant gain. The attenuator can be controlled externally via an input voltage U_{in}. Subsequently, the output is directly applied to the AOM's transducer which makes use of the piezoelectric effect to convert the RF signal to an acousto-optic wave.
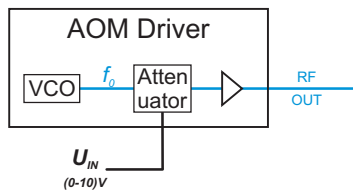
FIGURE A.3: ***Schematic diagram of a typical single-frequency-driven AOM driver.** It consists of a voltage-controlled oscillator (VCO) generating the RF-signal with the desired frequency* f_0*. The signal's amplitude can then be modified by an attenuator which is externally controlled by an input voltage* U_{in} *on the range of* $(0...10)\,\text{V}$*. Before the signal is finally emitted, it is attenuated by a constant gain.*

Basically, the setup for the two-frequency AOM driver only contains two of these single-frequency AOM drivers, an electronic device named voltage adjustment [78] plus a combiner [79] used for unifying the two RF-signal and a final amplifier [80] with constant gain G (as shown in figure A.4). Aiming at a constant total RF output power $P_{tot} = G \cdot (P_1 + P_2)$ of the whole setup the voltage adjustment is used to transform the input voltage, which is directly applied to the first AOM driver, to a voltage controlling the second driver. The corresponding transfer function $U_{control}(U_{in})$ describes the relation between the input voltage and the required control

---

[75] In this setup: *Mini-Circuits*, POS-150
[76] Here: *Mini-Circuits*, PAS-3
[77] Here: *Mini-Circuits*, ZHL-1-2W
[78] Details on the electronic circuit can be found in [116], [118].
[79] *Mini-Circuits*, ZSC-2-1
[80] *Mini-Circuits*, ZHL-1-2W-S

voltage $U_{control}$. Due to the nonlinear response of one driver's RF output power on the input control voltage, $U_{control}(U_{in})$ has to be nonlinear as well.
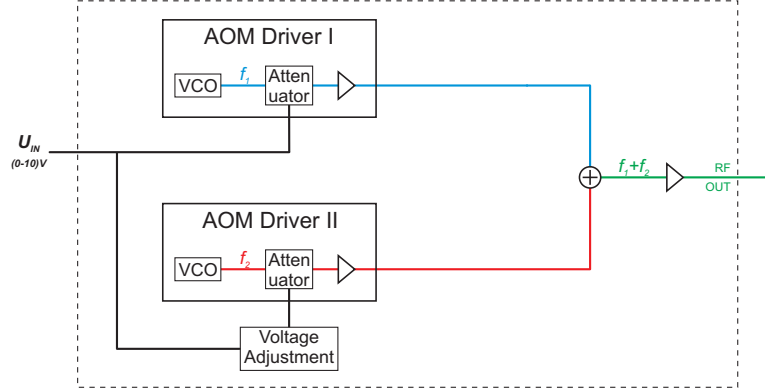
FIGURE A.4: *Schematic diagram of the basic setup for a two-frequency AOM driver. The two required frequencies f_1 and f_2 are separately generated by AOM driver I and II respectively. The drivers can be externally controlled by the common input voltage $U_{in} \in [0, 10] V$. However, in order to fulfill the purpose of keeping the total RF-power output $P_{tot} = G \cdot (P_1 + P_2)$ constant U_{in} first has to be modified before being applied to the second driver. This is done by the electronic circuit which the device voltage adjustment consists of.*
Both individual RF-signals are then merged together to one signal with constant amplitude and finally amplified by the factor G.

Furthermore, measurements show that the final amplifier's performance changes if two instead of only one RF signal is applied to it. Due to both this characteristic and the fact that the amplifier's saturation might have an effect on the calibration, the power should always be measured behind the last amplifier. Moreover, this is why the control voltage for the second driver cannot simply be calculated from the input voltage or output power of the first driver but has to be set in a calibration procedure.

When putting the two-frequency AOM driver into operation, either for calibration or its real purpose, three technical aspects about the amplifier have to be kept in mind: First of all, before it is turned on, the load has to be connected before the input is applied and the amplifier is turned on. Secondly, the input RF power must never exceed its maximum value [81]. Ultimately, take care that the amplifier's output will not exceed the AOM's maximum RF input power [82].

A.3.2 Calibration Procedure

Principally, during calibration, the electronic circuit successively approximates the nonlinear transfer function with step-wise linear functions between the data points. This is why a sufficient number of measurement points should be used. Thus, the voltage adjustment works by means of a digital list comprising numerous pairs of values of U_{in} and the corresponding output voltage $U_{control}$ being directed to the auxiliary AOM driver.

---

[81] For *Mini-Circuits*, ZHL-1-2W-S: maximum RF input voltage $= +10 \, \text{dBm}$

[82] With the parts used here this could be the case, since the maximum output of one individual AOM driver is approximately $+5 \, \text{dBm}$ and the gain of the amplifier was measured to be $34 \, \text{dBm}$ at a frequency of $94 \, \text{MHz}$. This results in $+39 \, \text{dBm}$ which is bigger than the AOM's maximum RF input power of $2.5 \, \text{W}$.

In the following the calibration procedure for obtaining and setting the transfer function will be briefly described. Beforehand, it should be pointed out that calibration should not be performed before having set up the final configuration of all parts, since every modification could affect the transfer function.

Before calibration is conducted, the desired value for the total RF output power P_{tot} has to be fixed. As this will directly be applied to the AOM, it should never exceed the AOM's saturation power P_{sat} [83] as for higher values the RF power cannot be fully absorbed by the AOM anymore leading to excessive heating and damage. However, P_{tot} should be close to P_{sat} since this is the RF power where the AOM's diffraction efficiency, defined as the ratio between laser power in the first order (with RF power turned on) and the zeroth order (with RF power turned off), typically peaks. However, in order to actively stabilize the laser intensity with the help of the AOM driver later on and, for this purpose, to be able to alter the RF power applied to the AOM into both directions, P_{tot} should be slightly below P_{sat} [120].

Additionally, in order to fix P_{tot}, the maximum RF output power $P_{1,max}$ and $P_{2,max}$ of both driver has to be measured separately. This is done by applying input voltages on the full working range $U_{in} = (0...10)\,\text{V}$ to each of them. Presumably, P_{max} will be reached either at $U_{in} = 0\,\text{V}$ or $10\,\text{V}$. If P_{max} of both drivers exceeds P_{sat}, the latter one should be used as P_{tot}. Otherwise [84] the smaller one of $P_{1,max}$ and $P_{2,max}$ should be chosen. Only this will ensure that P_{tot} can be kept constant for all U_{in} in the combined two-frequency setup since then one driver will always output its (negligibly small) minimum power if the other one's is maximized, thus, not being able to significantly contribute to P_{tot}.

Now calibration can be executed by obeying the following scheme:

1. **Choosing set of data points:**
   A sufficiently large number of reasonable spaced input voltage values U_{in} have to be chosen as data points for approximation of the transfer function. For higher precision, U_{in} should always be read on the display of the voltage adjustment instead of the power supply.

2. **Determining required P_2:**
   For each of these values successively the output power $G \cdot P_1$ behind the final amplifier has to be measured with the spectrum analyzer. Subsequently, the required value for P_2 should be calculated such that $P_{tot} = G \cdot (P_1 + P_2)$ is fulfilled.

3. **Initializing and performing programming:**
   The *programming mode* of the voltage adjustment that means setting the transfer function, has to be started at $U_{in} = 0\,\text{V}$. It automatically terminates at $U_{in} = 10\,\text{V}$. After having set $U_{in} = 0\,\text{V}$ programming is initiated by pressing knob (1) (see figure...) for about three seconds. Via the potentiometer knob underneath, the output voltage can then be adjusted such that the measured output of the second driver P_2 comes into agreement with the calculated value. In order to save this control voltage of the voltage adjustment (which is given to AOM driver II) the upper knob has to be pressed shortly.

   Step 3 has to be repeated for every chosen value of U_{in} until $U_{in} = 10\,\text{V}$ is reached which means to set U_{in} to the desired value and the control voltage is adjusted until P_2 equals the calculated value.

---
[83] For *Crystal Technology* AOM 3080-194: $P_{sat} = 2.5\,\text{W}$ [115]
[84] This was the case for the setup and AOM used here.

4. **Finishing programming:**
   After having saved the control voltage for the last data point $U_{in} = 10\,\mathrm{V}$ the electronic circuit will calculate the transfer function from the saved list. If this was successful that means no error message was displayed, the voltage adjustment will return automatically to the *running mode*.
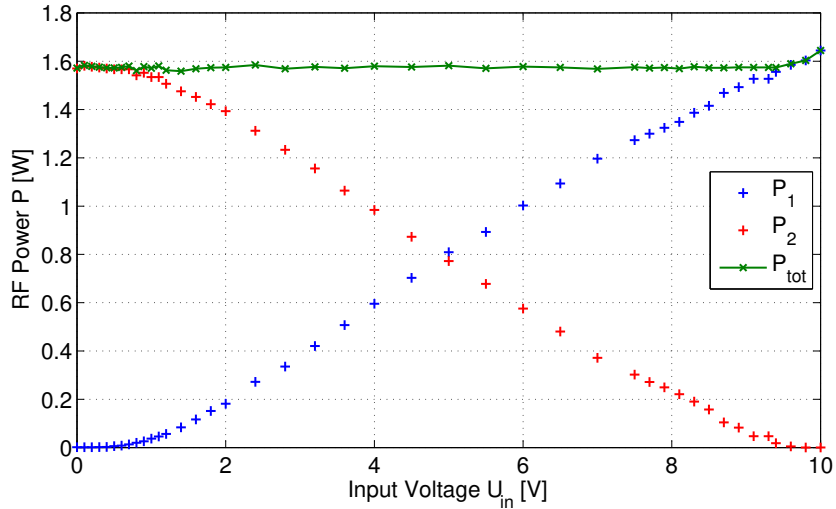
FIGURE A.5: *Transfer function established during calibration of the setup shown in A.6. The RF-output power P_1 (blue) and P_2 (red) of each AOM driver is a nonlinear function of the input voltage U_{in}. These powers were measured using a spectrum analyzer behind the final amplifier. For a individual series of measurements of P_1 (or P_2) U_{in} was only applied to AOM Driver I (or Driver II respectively).*
However, by calibrating the voltage adjustment and applying U_{in} to both drivers at the same time, the total RF-output power P_{tot} (green) of the whole device can be kept constant. A detailed instruction describing the calibration procedure is given in the text.

Finally, the combined total output power can be checked for consistency by adding the values for $P_2(U_{in})$ measured in step 3 to the corresponding (that means for the same U_{in})[85] $P_1(U_{in})$ determined in step 2. This sum should be constant as a function of the input voltage.

The resulting measurement data for the setup used here is shown in figure A.5. The nonlinear relationship between each driver's output and the controlling input voltage can be clearly seen (red and blue). Furthermore, obviously the calibration has been conducted successfully as the total output power stays pretty much constant (green) except for $U_{in} > 9.5\,\mathrm{V}$. This is due to the fact, that P_{tot} was chosen to be the smaller one of the individual driver's maximum outputs $P_{i,max}$, namely the second driver, which reaches its maximum of $P_{2,max} = 1.58\,\mathrm{W}$ at $U_{in} = 0\,\mathrm{V}$ (red). Thus, $P_{1,max}$ (blue) peaks at a higher value leading to an increased overall output power. This is another reason [86] why the AOM should not be driven at boundary values of U_{in}.

---

[85] As a reminder: U_{in} is the input voltage applied both to AOM driver I and to the voltage adjustment.
[86] Besides being able to integrate the AOM into an active stabilization loop.

A.3.3 Fast Switching

Typically, experiments in AMO physics require fast switching application of AOMs to externally turn them on and off or fast modification of laser power on small timescales such as for evaporative cooling. However, the AOM driver as described above (A.3.1) does not qualify for fast switching purposes as measurements show that it only works on a millisecond timescale.

For this reason, it is convenient to additionally use a customary RF-TTL-switch [87] directly behind AOM Driver I which generates the frequency used in the experiment, as it is shown in figure A.6). Typically, these switches feature rise/fall times on the range of only a few nanoseconds [121].

However, in order to still keep the total RF output power constant, AOM driver II has to be set to maximum output at exactly the same time. As this one is controlled by the voltage adjustment, that means that the appropriate input voltage has to be applied to the latter one. In order to satisfy this requirement, another fast analog switch has to be used being able to manipulate the input voltage U_{in} (see scheme in figure A.6). This switch will be controlled be the same TTL-signal as the RF-TTL-switch.

As a convenient side effect, the analog switch will set U_{in} such that not only Driver II is set to maximum output but also that Driver I emits its minimum RF-power. Though, in order to completely suppress P_1, which is the RF-signal coming from Driver I, the RF-TTL-switch will stay integrated. Furthermore, as the analog switch is a self-built electronic circuit based on the Integrated Circuit DG419 with a switching speed of about $100\,\mathrm{ns}$ [122], the RF-TTL-switch will perform faster by two orders of magnitude.
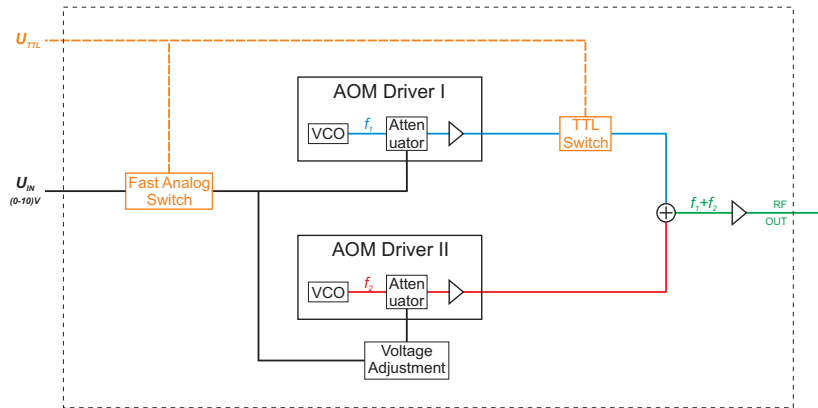
FIGURE A.6: *Schematic diagram of a fast version of the two-frequency AOM driver. This configuration is designed to fastly turn on and off the RF-power at the frequency, whose corresponding first order of diffraction is used in the experiment. For this purpose, compared to the basic setup illustrated in figure A.4, additionally two different switches are required.*
The first fast analog switch is capable of setting Driver I to minimum and Driver II to maximum output by pulling U_{in} to $0\,\mathrm{V}$. This can be controlled by a TTL-pulse U_{TTL} which at the same time is applied to the second TTL-switch. This switch is only inserted between Driver I and combiner for the reason of even faster switching. While the analog switch performs on the timescale of approx. $100\,\mathrm{ns}$ [122] the TTL-switch is faster by two orders of magnitude.

The whole circuit diagram of the fast analog switch is shown in figure A.7 and figure A.8

---

[87] *Mini-Circuits*, ZASWA-2-50DR+

schematically depicts the functional principle of the electrical component IC DG419 with a functional block diagram on the left and the corresponding truth table on the right. Basically, this Integrated Circuit, based on a monolithic CMOS architecture, is designed for precisely performing fast switching of analog signals with high precision. Depending on the input TTL-signal at IN a connection will be established from pin D to either pin S_1 or S_2. Thus, the potential of the unconnected pin will be undefined.
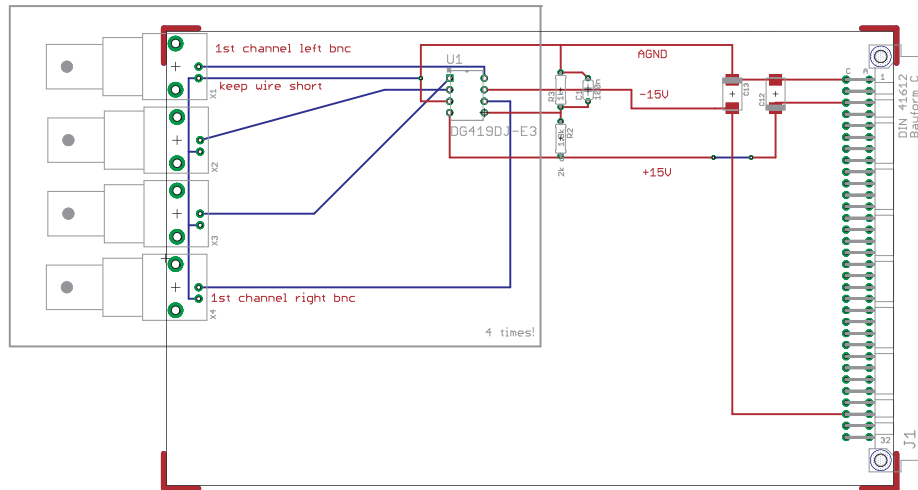
FIGURE A.7: **Circuit Diagram of the fast analog switch.** *In principal, this electronic device is based on the integrated circuit of the type DG419. This component switches the output between two different input signals depending on the TTL level to it. Its functional principle is schematically depicted in figure A.8. The voltage follower of the type BUF634 which is shown in figure A.9 is missing here.*

TRUTH TABLE DG419		
Logic	SW$_1$	SW$_2$
0	ON	OFF
1	OFF	ON

Logic "0" $\leq$ 0.8 V
Logic "1" $\geq$ 2.4 V
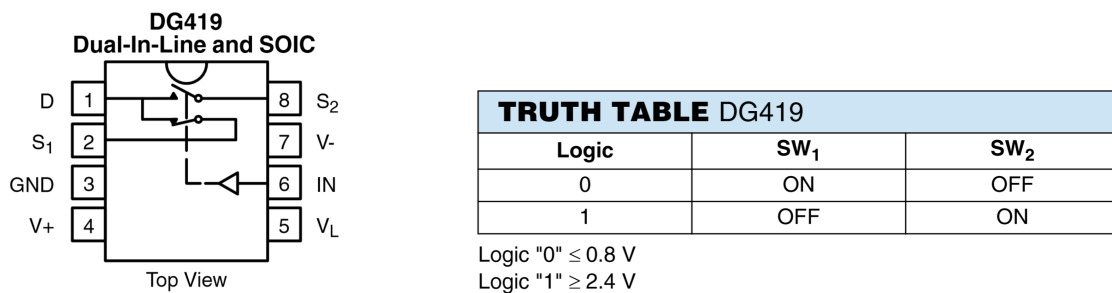
FIGURE A.8: **Functional principle of the integrated circuit DG419 used in the fast analog switch [122].**
Left: *By means of the TTL-signal applied to IN the output at D can be switched between S_1 and S_2.*
Right: *Consequently, switch 1 (SW$_1$) being capable of creating a connection between D and S_1 is either closed for low TTL-signals and open for high ones respectively. The reversed case applies to switch 2 (SW$_2$) between D and S_2.*

As it is the task of the analog switch to pull down U_{in} to ground (GND) for TTL LOW and let it pass for TTL HIGH respectively, it has to be integrated into the circuit of the two-frequency driver as shown in figure A.9. Pin D is used as output either being connected to GND at S_1 (TTL LOW) or receiving the input signal U_{in} from S_2 (TTL HIGH).
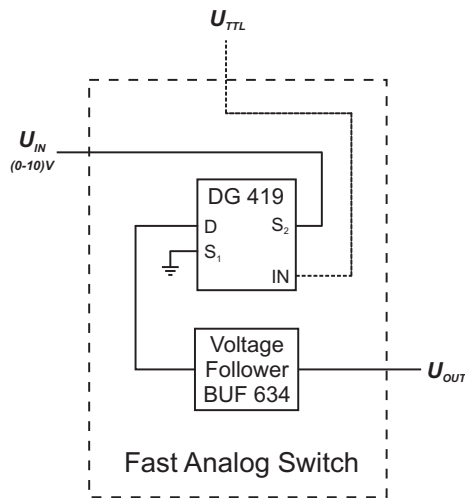
FIGURE A.9: *Detail of the complete schematic diagram of the fast analog switch.* Compared to the basic circuit shown in figure A.7 and additional voltage follower of the type BUF634 is employed behind the output of DG419 with the reason being a too little maximum continuous current output of the latter electronic component. For details refer to the text.

The analog switch DG419 features a maximum continuous current output of $30\,\mathrm{mA}$ which is equal to the maximum control current of the input signal applied to one of the AOM drivers [88]. Though, as the analog switch is inserted previously to both drivers the current flowing through DG419 might exceed this threshold of $30\,\mathrm{mA}$ and even reach values of up to $60\,\mathrm{mA}$.

In order to solve this problem, the additional electronic component BUF634 follows the analog switch (compare figure A.9). This high speed, unity-gain open-loop buffer is, among other purposes, especially designed to increase output currents, thus acting as an voltage follower. It operates on the full range of its supply voltage ($\pm18\,\mathrm{V}$) and provides output currents of up to $250\,\mathrm{mA}$.

In this final configuration, the two-frequency driver is ready to be used for fast-switching high-laser-power AOM applications meeting the demand of high beam pointing stability.

---

[88] This is valid for the particular attenuators of the type *Mini-Circuits* PAS-3 that are implemented in the driver setup here.

Appendix B

Impedances in Electric Networks

Generally, the issue of input and output impedances depends on the specific situation and application. Basically two cases have to be distinguished, either that the network is intended to reliably transmit voltages or that it is designed to maximize power transfer.

In the context of this thesis especially the first case is the more interesting one. For better understanding, the following treatment is simplified by only considering the real part of the impedance Z, namely the resistance R. In the end, a short comment will be made on the general case of complex impedances.

Voltage Transfer

As a start it should be outlined in which way the present problem is related to the issue of impedances:

Typically, a photo diode is read out by monitoring the signal in terms of voltages by means of a measuring device.

Intrinsically, photo diodes are devices which internally convert incoming light into an electric photo current. Thus, when detecting continuous light beams the PD represents a constantly emitting source of current. If this generated current is then to be quantified, the photo diode will be connected to the measuring device, which implicates that in either device the photo current somehow has to be converted into a voltage. This is also the reason why this system is constructed to reliably transmit voltages.
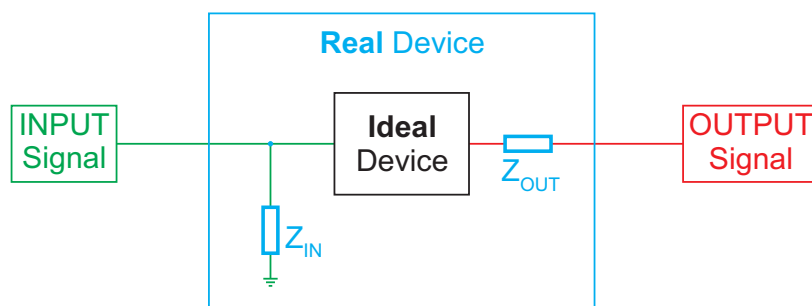
FIGURE B.1: *Schematic illustrating difference between real and ideal devices. While an ideal device does not require any input current and supplies unlimited output currents, real devices generally need some little input current and cannot provide infinitely high output power. This matter of fact is typically accounted for by attaching an input and output impedance Z_{IN} and Z_{OUT} to the ideal device which in combination with the ideal device yields the real device.*

Input and Output Impedances

At this point, input and output impedances come into play and it makes sense to switch to a more generalized picture[89] of a network designed for voltage transfer:

As schematically illustrated in figure B.1, in general an electronic device can by no means be considered as an ideal device which would not demand for any input current but starts working by simply applying a voltage to it. However, a real device rather always demands some little current to flow in. In a simple model, this can easily be accounted for by inserting a grounded resistor preceding the ideal device's input which in combination represents the real device. The imaginary resistor then represents its input impedance[90] Z_{in}.

As a consequence, this input resistance diminishes the input voltage such that the voltage that reaches the ideal device is not equal to the applied voltage at the real device anymore.

Similarly, a device cannot supply unlimited output currents at any required voltage which would imply to effectively provide infinitely high power. Instead, with increasing output currents a rising voltage drop can be observed which in turn can be modelled as the output impedance Z_{out}.

Electric Networks

If, as a next step, a connection between two devices is established, the ratio between output impedance of the first (called source) and input impedance of the second real device, the load, becomes important and should be chosen according to the actual application. For the purpose here, this discussion aims at the task of reliably transferring voltages.

By connecting both stages the respective impedances that are involved build up a voltage divider such that the voltage reaching the second ideal device is reduced by a factor of $\frac{Z_{in,2}}{Z_{in,2}+Z_{out,1}}$ with respect to the voltage emitted by the first ideal device. Therefore, for the case of voltage transfer it is advisable to choose the load's input impedance to be as high as possible assuming DC signals or at least one at very low frequencies. Typically, it is recommended to use ratios between input and output impedances that exceed a value of ten [123]. The more precise the voltage in an analog circuit has to be transmitted the higher should the ratio be set.

As a result, according to Ohm's law $V = I \cdot |Z|$, this will also relieve the source in the sense of minimizing the current and hence the power which is required by the source to drive the load at a given voltage. In the ideal case of infinitely large input impedances, any desired voltage could be fed into the load without inducing any absorption of power.

Impedance Matching for Power Transfer

Next, as promised the matter becomes significantly more intricate, if the electric network is intended for power transfer as then impedance matching becomes of higher interest than simply maximizing the input impedance. This is due to the fact that power depends on both voltage and current. Whereas for given output voltages the input voltage will increase with higher input impedance, the current will simultaneously decrease. Due to this reverse behaviour, some

---

[89] Even though generalized, the treatment is simplified by only using resistances. This is only justified for signals at DC or very low frequencies. At higher frequencies the imaginary part of the impedance, the reactance, becomes significant and has to included as well.

[90] Although only resistances are used as impedances here, the corresponding quantities are denoted by the correct symbol Z for complex impedances.

kind of compromise has to be made in a way as to maximize their product, the power. This is satisfied exactly in the case that the input impedance matches the output impedance [124].

Moreover, in order to minimize overall losses by keeping the total resistance of the connection low, the source's output impedance should in general be reduced as much as possible while keeping in mind to reduce the load impedance by the same amount. Lower output impedances which result in lower currents will also allow for enhanced source capabilities since the power stays bounded above.

Obviuosly, the conditions for maximized power transfer collide with the ones for perfect voltage transfer where input impedances need to be maximized. As a consequence of impedance matching, the input voltage is cut in half compared to the output, which implicates that both power and voltage transfer cannot be optimized at the same time.

Impedance Matching for Minimizing Reflections

Impedance matching not only demands attention when working with networks that are intended for power transfer. Rather the issue becomes equally important in the case that they are designated to reflectionless transmission of signals. This is simply due to the fact that reflections are mainly caused by impedance mismatches. Actually, minimizing reflections is closely related to maximizing power transfer as reflections can cause considerable loss of power.

Additionally, this effect will gain more and more influence when working at higher frequencies which has not been considered yet. The higher the frequency the more easy standing waves will establish so that not the full amount of power will be transferred anymore [125].

Complex Impedance

The situation becomes even more complicated, if the real device does not only feature a resistance but also a capacitance or inductance. Then, the simple picture of the impedance only comprising a real part is not sufficient anymore but rather has to be extended to the generalized impedance identified by a complex quantity. While its real part is related to the resistance R, its imaginary part results from the reaction of the capacitance C or inductance L to a change in voltage or current respectively. This is why it is also called reactance.

The reactance can cause trouble in the sense that capacitors feature lower resistance at higher frequencies, while inductors exhibit lower resistance at lower frequencies. For example, if voltage transfer has to be optimized at high frequency, high input capacitances can counteract this goal by reducing the impedance. However, in general input impedances are required to be as high as possible for the purpose here.

Thus, if a device features significant capacitive or inductive input or output impedances, the actual frequency which the circuit operates at, always has to be kept in mind.

Conclusion

In general the task of choosing appropriate impedances and matching them in the right way can soon become highly challenging. The restriction to this simplified treatment was only adequate for easy voltage transfer application such as measuring photo currents. In order to not blow up this discussion too much, the explanation of impedance matching and effects of higher frequencies was intended to outline the problem and solutions regarding the special purpose here. Therefore it was kept rather superficial and short. Another aspect, which has not been mentioned at all, are transmission lines which is mainly about the issues induced by

connecting elements between different devices by means of coaxial cables for example. Since the latter ones are typically constructed to feature an impedance of $50\,\Omega$, matching between cable and device can always easily be achieved by terminating the respective device with a resistor equal to $50\,\Omega$.

Conclusively, the matter of impedances can be briefly summarized by the following rules of thumb which should be kept in mind when working with respective networks. They purpose and intended application mainly determines which impedances should be chosen:

- For voltage transfer low output but high input impedances should be preferred.

- Optimized power transfer, though, requires low output impedances which are matched by the input impedances.

- When operating at high frequencies, it is advisable to match impedances as well. The loss of 50% in voltage should be accepted in favor of avoiding reflections as far as possible. The higher the frequency the more important this requirement becomes. At this point it is essential to consider the characteristic impedances of the transmission lines as well.

- Finally, if necessary, impedances should always be treated in a complete sense of accounting for their full complex nature and frequency-dependence. This requires to extend the simplification of impedances only induced by resistances to the complete picture which also includes capacitances and inductances that give rise to the complex reactance.

Appendix C

A Scanning Fabry-Pérot Cavity

Generally, the mode structure of a Gaussian beam can be detected by coupling the beam into a cavity and monitoring the transmitted light on either a photo diode or a camera. The latter option should be preferred as only this enables to resolve the beam's spatial intensity distribution which is an indicator for the explicit TEM_{mn} mode. This information cannot be obtained by solely monitoring the beam on a wavemeter.

In order to observe the full spectrum of the different modes building up the beam and to detect them separately, the beam has to be coupled into a cavity with variable length. By tuning the resonator length, modes with different wavelength can be brought into cavity resonance. Typically, for this purpose a so called Fabry-Pérot cavity is used. Such a type of optical resonator is built up of two parallel and highly reflecting mirrors at a well-defined distance which is referred to as the resonator length. The tunability of this cavity is achieved by attaching one of the mirrors to a piezoelectric actuator. By applying appropriate voltages to the actuator the piezoelectric effect can be exploited in order to modify the resonator length on the order of the optical wavelength. These kinds of tunable Fabry-Pérot cavities are called scanning Fabry-Pérot cavities, short SFPCs. This appendix presents the basic concept behind SFPCs including the criterion for resonator stability and quantities used for characterizing them.

Resonator Setup

The setup of a Fabry-Pérot cavity is very simple: Two mirrors with complex reflection coefficients r_i and reflectivities[91] $|r_i|^2$ of almost 100% are arranged in a parallel way such that their reflective surfaces face each other. Light is then coupled into the cavity at one of the non-reflecting sides of a mirror, if possible along the cavity's symmetry axis. At any given distance between the mirrors, electromagnetic waves with certain wavelengths will fit into the resonator, mathematically expressed by

$$L = q \cdot \frac{\lambda}{2} \tag{3.1}$$

with q representing the longitudinal mode number. If this condition is fulfilled, that means if the resonator length L matches multiples q of $\lambda/2$, the corresponding wave is reflected at the mirrors in such a way that the phase shift $\delta = 2qL \cdot 2\pi/\lambda$ between successive reflections becomes a multiple of π. This yields constructive interference and self-amplification of the

---

[91] While the reflection coefficients $r = |r|e^{i\varphi_r/2}$ are associated with the complex electric field amplitude, the reflectivity $|r|^2$ is related to the light intensity which is basically equivalent to the electric field squared [73]. Typically, the reflectivity is also indicated by the symbol $R = |r|^2$. However, for the sake of consistency, throughout this thesis $|r|^2$ is used instead of R in order to avoid confusion with the symbol R for denoting a mirror's radius of curvature.

circulating wave inside the resonator. Then the wave is called to be in resonance with the cavity.

The properties of the two mirrors, especially their radii of curvature[92] R_1 and R_2, have to be chosen according to the cavity's intended application. Next to the resonance condition 3.1 which represents a criterion for permitted wavelengths at a given resonator length, there is a second requirement which the beam coupled into the cavity has to comply with. This condition is related to the mirrors' curvatures, namely that in the case of Gaussian beams the curvature of its wavefronts at the position of the mirrors has to be exactly equal to the mirrors' curvatures. Only then perfect reflection and interference can be guaranteed. Generally, this is achieved by using additional mode matching optics, in particular a focussing lens in front of the cavity.

Resonator Stability

The curvature of the mirrors also determines the stability of the resonator which is a measure of its ability to trap light between the mirrors. A resonator is called stable if the intracavity beam is refocussed again after every reflection. Otherwise, if the beam waist continuously increases, the cavity is unstable since this will result in a loss of the beam. Stable resonators will also be less sensitive to slight misalignment in terms of the beam's angle of incidence or its focal waist.

For a particular resonator length L stability is given if the radii of the mirrors satisfy the following condition[93] [30], [67]:

$$0 \leq \left(1 - \frac{L}{R_1}\right)\left(1 + \frac{L}{R_2}\right) \leq 1 \tag{3.2}$$

This stability criterion can also be illustrated by plotting it as a function of the stability parameters which are defined as $g_{\{1/2\}} = 1 \mp L/R_n$. This is depicted in figure C.1.

g_1 and g_2 are also used as indicators for the various two-mirror cavity configurations such as (-1, -1) denoting a concentric setup consisting of two identical spherical[94] concave mirrors in a distance of twice the radius. Another configuration which will become important in this thesis, is the plano-concave type of cavity which is composed of a combination of a planar and concave mirror and indicated by $(1, g_2)$. This configuration is stable if $g_2 \in [0,1]$, that means if the radius of curvature of the right mirror's reflecting surface is equal to or exceeds the separation L between the mirrors. However, if the cavity additionally comprises an amplifying medium also other effects that are not considered here can stabilize the resonator.

---

[92] Conventionally, the radius of curvature is supposed to be negative (positive) if the centre of curvature is located to the left (right) of the curved surface. In the case of a plano-concave mirror with the left surface being flat and the right one concave, the latter one's radius is positive. The right surface of a plano-convex lens, however, features a negative sign.
In the case of cavities the radius of a mirror always refers to its reflecting surface.

[93] Often, in literature one can find a slightly different notation, namely with a negative sign in the definition of g_2. This difference is caused by differing sign conventions for the mirrors. Sometimes, the signs are defined in such a way as to attribute positive/negative signs to surfaces whose centre of curvature is located towards/away from the cavity (for example in [67]). In this picture the sign of the right mirror's curvature will then be exactly inverse compared to the definition generally used in lens optics [126] which is given in 92 and does not rely on any reference system.
For the sake of consistency, throughout this thesis the general definition is used so that the stability criterion has to be written like this.

[94] Throughout this thesis, mirrors which are part of a cavity, are always supposed to be spherically shaped, even if not stated explicitly.
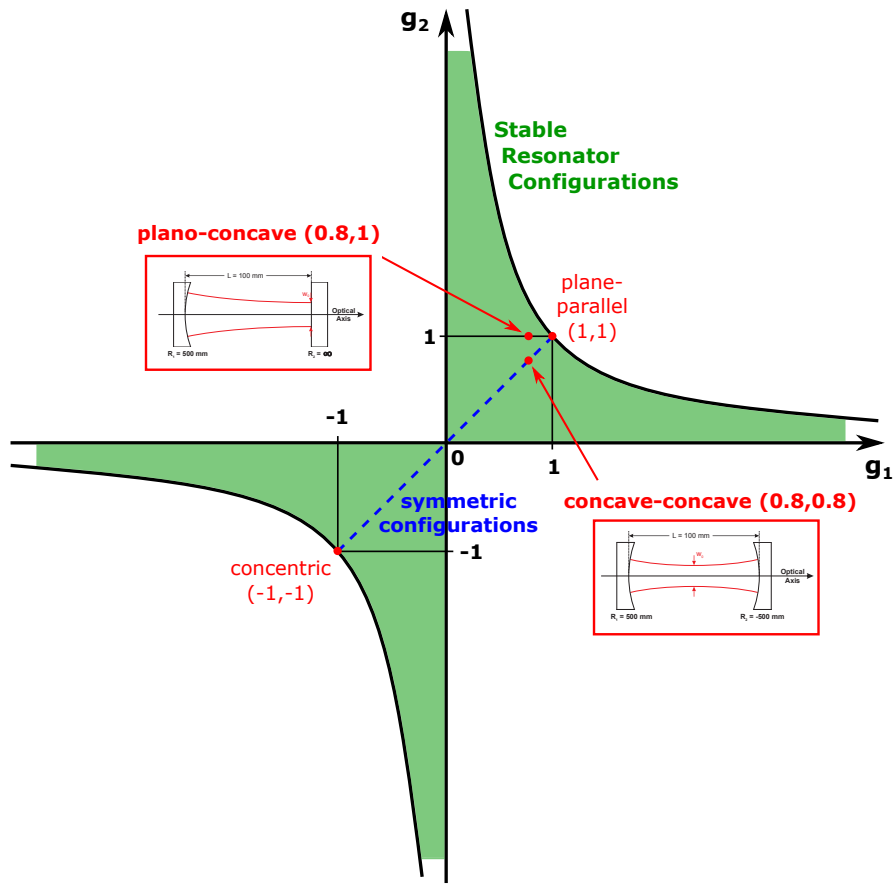
FIGURE C.1: *Stability diagram of spherical two-mirror resonators.* *The green area which is described by $0 \leq g_1 g_2 \leq 1$ represents all stable resonator configurations in terms of the two stability parameters $g_{\{1/2\}} = 1 \mp L/R_n$. The dashed blue line indicates all symmetric configurations built up of two similar mirrors. Additionally, the illustration shows the position of especially those two resonator configurations that are considered within this thesis (compare section 3.7).*

Next to this formal criterion, there is also an easy and illustrative graphical way to investigate the stability of a given resonator geometry which. This technique is visualized in figure C.2. Therefore, first two circles with each exhibiting half the radius of one of the cavity mirrors have to be drawn in such a way that they tangent the reflecting surface of the corresponding mirror. If these two circles overlap as it is the case in the figure, the cavity turns out to be stable. Additionally, this method provides information about the focal position: By connecting the circles' intersections by a straight line, the beam's focal position will conform to the crossing point of this line with the optical axis [67].

For the construction of a SFPC, it should be paid attention the fact that cavity stability is guaranteed for all tunable resonator lengths.

Free Spectral Range

By changing the wavelength of the light at a fixed mirror spacing or, respectively, by scanning the resonator length by at least one wavelength, characteristic equidistant peaks will be
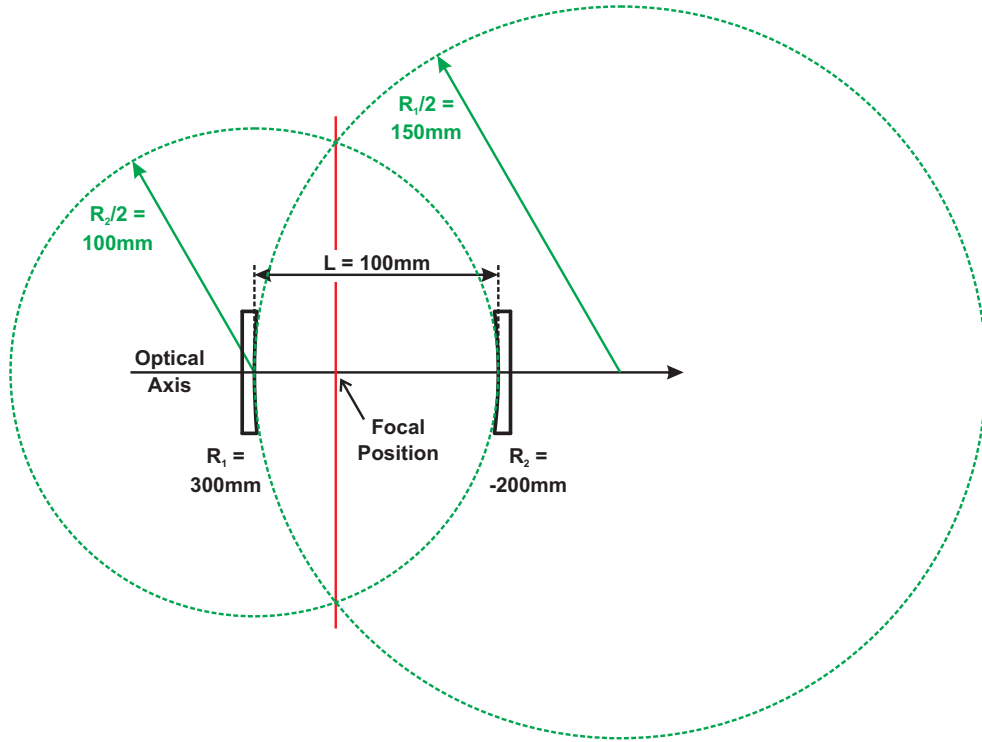
FIGURE C.2: *Graphical method for estimating resonator stability.* *A detailed explanation is given in the text. Values have been chosen arbitrarily.*

observed in the spectrum. They occur at wavelengths λ_q which satisfy the resonance condition 3.1 for longitudinal modes. The spacing between adjacent resonances is quantified by the so called free spectral range (FSR) which is typically expressed as the difference $\Delta\nu_{FSR}$ between successive resonance frequencies $\nu_q = c/(n_g \lambda_q)$ where n_g denotes the refractive index of the medium inside the cavity [67]. $\Delta\nu_{FSR}$ is then given by

$$\Delta\nu_{FSR} = \nu_{q+1} - \nu_q = \frac{c}{2 n_g L} \tag{3.3}$$

In the following discussion the cavity is assumed to be filled with air ($n_g = 1$) so that expression (3.3) reduces to $\Delta\nu_{FSR} = c/(2L)$. The denominator in equation (3.3) represents the optical path length for one round trip inside the cavity supposed the beam is perfectly coupled into the cavity along the optical axis.

However, representing a critical practical consideration it should be kept in mind, that slight misalignment in terms of nonzero angles of incidence or parallel offset of the injected beam with respect to the cavity's optical axis, can quite severely affect the optical path length. Additionally, misalignment will make it more difficult or even impossible to couple the light efficiently into the cavity.

Full Width at Half Maximum

Each resonance peak in the spectrum features a certain full-width at half-maximum (FWHM) $\Delta\nu_{FWHM}$ which solely depends on the mirrors' reflectivity according to

$$\Delta\nu_{FWHM} = \frac{c}{\pi L}\arcsin\left(\frac{1-|r|^2}{2|r|}\right) = \frac{c}{\pi L}\arcsin\left(\frac{1}{\sqrt{F}}\right) \tag{3.4}$$

The quantity F which has been introduced here and which is defined as

$$F = \left(\frac{2\,|r|}{1-|r|^2}\right)^2 \tag{3.5}$$

is called coefficient of finesse [67], [73]. Since in the case of resonators the reflectivity $|r|^2$ is typically only slightly smaller than one, F will become quite large which jusitifies to approximate $\arcsin(F^{-1/2})$ in expression (3.4) by $F^{-1/2}$.

Finesse

The most important quantity related to resonators in general is the ratio between the free spectral range and the FWHM which represents the distance between two resonances in units of their spectral width. The resulting quantity is referred to as the finesse $\mathcal{F}$ and is given by [30], [67]

$$\mathcal{F} = \frac{\Delta\nu_{FSR}}{\Delta\nu_{FWHM}} = \frac{\pi|r|}{1-|r|^2} \tag{3.6}$$

Hence, the finesse is a measure of the interferometer's ability to resolve the light's spectral features with the minimal resolution being defined by the Rayleigh criterion [49], [127].

Roughly speaking, this criterion states that two spectral signals with equal intensity can only be resolved if their summed intensity still shows a dip in the middle as illustrated in figure C.3. Based on this criterion, different light modes that are indicated by their wavelength, can only be resolved by means of a SFPC if the corresponding spectral lines are separated by at least one FWHM.
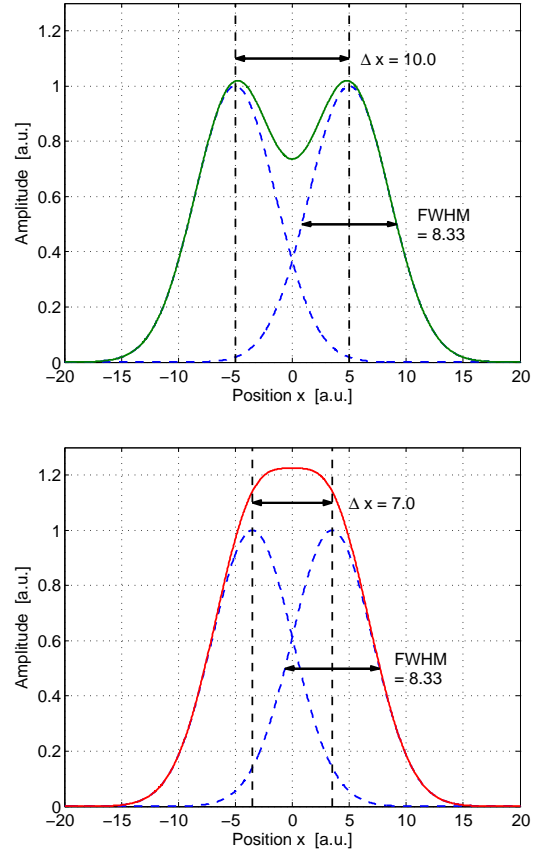
FIGURE C.3: *Illustration of the Rayleigh criterion. According to this criterion two arbitrary signals (dashed blue lines) can generally only be resolved if the minimum of the summed signal (continuous lines) is smaller than its maximum as shown on the left. Otherwise, the detail stays unresolved as illustrated on the right. Mathematically expressed, resolution is given if $(\Delta x \gtrsim 1.05 \times FWHM)$ [73]. The Rayleigh criterion applies to various purposes such as resolution of spectral lines or imaging systems.*

Appendix D

Polarization Maintaining Fibre Coupling

Polarization Maintaining Fibres

The technique of polarization maintaining fibre coupling is mainly based on the composition of corresponding polarization maintaining single-mode fibres: Whereas the property of single-mode transmission is simply achieved by means of total internal reflection which is established for sufficiently small core diameters combined with an appropriate refractive index of the cladding material.

Polarization maintenance on the other hand makes use of another property of the fibre's core material, namely birefringence. Typically, this feature is created by applying anisotropic stress to the core material during fabrication. For the type of fibre used here, the stress was induced by rods with a so called panda structure that are enclosed by the cladding. This is visualized in figure D.1. Without going too much into details[95], the most important consequence of the panda-type structure is the perpendicular orientation of the core's slow and fast axis both with respect to each other as well as to the propagation direction.

Due to this feature, thermal drifts which lead to elongations of the fibre will distort the transmission performance if the light is not perfectly aligned along either of the axis.
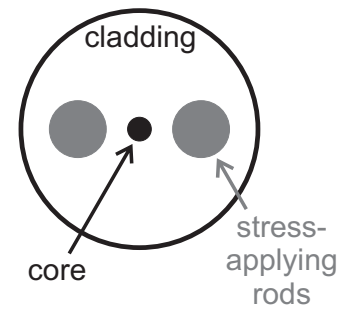
FIGURE D.1: *Schematic cross section of a panda-type single-mode fibre. By inserting two rods into the cladding anisotropic stress is applied to the core which results in birefringence.*

The Technique of Polarization Maintaining Fibre Coupling

This is why first of all the influence of thermal drifts should minimized by casing the fibre completely within a foamed tube. Then, polarization maintaining transmission is achieved by coupling the light into the fibre in such a way that its polarization is oriented along one of the fibre's axis.

This alignment is optimized according to the following procedure[96]

(a) First of all, the polarization of the light which is transmitted by the fibre is coarsely set by the orientation of the fibre in- and out-coupler. Fine-tuning can then be performed by means of a wave plate in front of and behind the fibre which both allow for continuous polarization rotation of transmitted light.

---

[95] For more information on different fibre types, their properties and way of fabrication as well as for an analysis of the performance of fibres with panda-type structure, refer to [128], [129] and [130].

[96] A much more elaborate and comprehensive explanation of this method including conceptual and theoretical explanations as well as systematic measurements can be found in [131].

Directly after leaving the laser source the beam is transmitted through a PBS which imposes horizontal polarization on the light. In order to minimize the influence of misalignment the polarization should, if possible, be coupled into the fibre without changing this orientation. Therefore, both the in-coupler and the wave plate in front of the fibre should be orientated like this.

(b) As explained in the context of setting up the dimple (refer to 4.1.3), behind the fibre the dimple light has to be vertically polarized when arriving at the cube. By taking into account the periscope's property to swap vertical and horizontal polarization, the out-coupler thus has to be oriented similar to the in-coupler, namely that the light leaving the fibre will stay horizontally polarized. Next, complete conservation of light polarization is achieved by fine-tuning of both wave plates in the following way:

(c) A test cube is placed behind the wave plate as a tool to separate between vertical and horizontal polarization of the light which leaves the fibre. Next, two photo diodes are used to detect both light paths and quantify the power comprised by each polarization component. However, for optimization of polarization maintaining transmission it is not sufficient to only detect the absolute power values and simply maximize or minimize the respective component. Instead, a much more elaborate method has to be applied:

(d) Generally, if the light is not coupled into the fibre exactly along either the slow or the fast axis, during transmission it will always be split up between both. This imperfection can now be utilized for optimizing polarization maintaining transmission: Since the two fibre axes possess different refractive indices n_s and n_f, they inherently produce a certain phase shift between both components that depends on the ratio between fibre length and wavelength. Thus, changing one of these two parameters will result in different phase shifts.

The phase shift becomes visible by a rotation of the output relative to the input polarization so that changes of the phase shift can be quantified by measuring the ratio[97] between transmitted and reflected light at the cube. In case of perfect polarization conservation the phase shift will stay constant since then the light is transferred only along one direction. Then, variation of the fibre length or wavelength does no longer affect the output polarization. Consequently, polarization maintaining transmission is optimized by eliminating changes of the phase shift with the help of the wave plates' orientations.

(e) Thus, for the purpose of optimization, phase shifts, which serve as a measure for the quality of polarization maintenance, have to be induced intentionally. In the case here, the output light polarization was periodically changed by tuning the laser frequency [98] by means of the laser scan control. [99] Corresponding phase shifts are then generated due to

---

[97] Of course, nominator and denominator should always be chosen so as to maximize their absolute ratio which enables to observe variations earlier.

[98] Alternatively, one can also continuously vary the fibre length for example by periodically heating and cooling the fibre.

[99] In this context, it should be noted that the *Feedback*-labelled potentiometer should be turned all the way up for the sake of stability. This will internally trigger an active intensity stabilization: Intensity drifts which are typically induced by frequency changes are then automatically compensated for by adjusting the laser current. Furthermore, the knob labelled with *Amplitude* should not be turned on completely in order to avoid possible mode jumps. Settings between 30 and 40 percent of the maximum value turned out to be adequate in the present setup. This corresponds to wavelength scans on the order of 0.003 nm. If necessary, the laser current offset can additionally be varied to eliminate mode hopping.

chromatic dispersion.

While scanning the frequency, the ratio between transmitted and reflected power at the cube has to be detected on the two photo diodes and displayed on the oscilloscope. Changes are flattened by successively changing the alignment of both wave plates, but especially the one in front of the in-coupler since this is the one that is responsible for correct in-coupling.

(f) Finally, long-term stability of the polarization maintaining light transmission could be confirmed by monitoring the detected ratio between cube-transmission and -reflection over a period of several hours. Fluctuations were observed to be smaller than 1%.

List of Figures

Bibliography

[1] E. Urban et al., "Observation of Rydberg blockade between two atoms", *Nature Physics*, vol. 5, no. 2, pp. 110–114, 2009.

[2] D. Tong et al., "Local Blockade of Rydberg Excitation in an Ultracold Gas", *Phys. Rev. Lett.*, vol. 93, p. 063 001, iss. 6, Aug. 2004. DOI: `10.1103/PhysRevLett.93.063001`. URL: `http://link.aps.org/doi/10.1103/PhysRevLett.93.063001`.

[3] Y. O. Dudin et al., "Strongly Interacting Rydberg Excitations of a Cold Atomic Gas", *Science*, vol. 336, no. 6083, pp. 887–889, 2012, ISSN: 0036-8075. DOI: `10.1126/science.1217901`. URL: `http://science.sciencemag.org/content/336/6083/887`.

[4] R. Heidemann et al., "Evidence for Coherent Collective Rydberg Excitation in the Strong Blockade Regime", *Phys. Rev. Lett.*, vol. 99, p. 163 601, iss. 16, Oct. 2007. DOI: `10.1103/PhysRevLett.99.163601`. URL: `http://link.aps.org/doi/10.1103/PhysRevLett.99.163601`.

[5] J. D. Pritchard et al., "Cooperative Atom-Light Interaction in a Blockaded Rydberg Ensemble", *Phys. Rev. Lett.*, vol. 105, p. 193 603, iss. 19, Nov. 2010. DOI: `10.1103/PhysRevLett.105.193603`. URL: `http://link.aps.org/doi/10.1103/PhysRevLett.105.193603`.

[6] O. Firstenberg et al., "Attractive photons in a quantum nonlinear medium", *Nature*, vol. 502, no. 7469, pp. 71–75, 2013.

[7] A. V. Gorshkov et al., "Photon-Photon Interactions via Rydberg Blockade", *Phys. Rev. Lett.*, vol. 107, p. 133 602, iss. 13, 2011. DOI: `10.1103/PhysRevLett.107.133602`. URL: `http://link.aps.org/doi/10.1103/PhysRevLett.107.133602`.

[8] D. Maxwell et al., "Storage and Control of Optical Photons Using Rydberg Polaritons", *Phys. Rev. Lett.*, vol. 110, p. 103 001, iss. 10, Mar. 2013. DOI: `10.1103/PhysRevLett.110.103001`. URL: `http://link.aps.org/doi/10.1103/PhysRevLett.110.103001`.

[9] W. Li et al., "Coherence in a cold-atom photon switch", *Phys. Rev. A*, vol. 92, p. 043 828, iss. 4, Oct. 2015. DOI: `10.1103/PhysRevA.92.043828`. URL: `http://link.aps.org/doi/10.1103/PhysRevA.92.043828`.

[10] M. K. E. L. Planck, "Zur theorie des gesetzes der energieverteilung im normalspectrum", *Verhandl. Dtsc. Phys. Ges.*, vol. 2, p. 237, 1900.

[11] A. Einstein, "Über einen die Erzeugung und Verwandlung des Lichtes betreffenden heuristischen Gesichtspunkt", *Annalen der Physik*, vol. 322, no. 6, pp. 132–148, 1905, ISSN: 1521-3889. DOI: `10.1002/andp.19053220607`. URL: `http://dx.doi.org/10.1002/andp.19053220607`.

[12] Nobel Media AB 2014, "Press Release: The 1997 Nobel Prize in Physics", `http://www.nobelprize.org/nobel_prizes/physics/laureates/1997/press.html`, Oct. 1997. (visited on 04/27/2016).

[13] Nobel Media AB 2014, "Press Release: The 2001 Nobel Prize in Physics", http://www.nobelprize.org/nobel_prizes/physics/laureates/2001/press.html, Oct. 2001. (visited on 04/27/2016).

[14] Nobel Media AB 2014, "Press Release: The 2005 Nobel Prize in Physics", http://www.nobelprize.org/nobel_prizes/physics/laureates/2005/press.html, Oct. 2005. (visited on 04/27/2016).

[15] Nobel Media AB 2014, "The 2012 Nobel Prize in Physics - Press Release", http://www.nobelprize.org/nobel_prizes/physics/laureates/2012/press.html, Oct. 2012. (visited on 04/27/2016).

[16] M. D. Lukin et al., "Dipole Blockade and Quantum Information Processing in Mesoscopic Atomic Ensembles", *Phys. Rev. Lett.*, vol. 87, p. 037 901, iss. 3, Jun. 2001. DOI: 10.1103/PhysRevLett.87.037901. URL: http://link.aps.org/doi/10.1103/PhysRevLett.87.037901.

[17] K. Singer et al., "Suppression of Excitation and Spectral Broadening Induced by Interactions in a Cold Gas of Rydberg Atoms", *Phys. Rev. Lett.*, vol. 93, p. 163 001, iss. 16, Oct. 2004. DOI: 10.1103/PhysRevLett.93.163001. URL: http://link.aps.org/doi/10.1103/PhysRevLett.93.163001.

[18] M. Fleischhauer et al., "Electromagnetically induced transparency: Optics in coherent media", *Rev. Mod. Phys.*, vol. 77, pp. 633–673, iss. 2, Jul. 2005. DOI: 10.1103/RevModPhys.77.633. URL: http://link.aps.org/doi/10.1103/RevModPhys.77.633.

[19] R. Löw et al., "An experimental and theoretical guide to strongly interacting Rydberg gases", *Journal of Physics B: Atomic, Molecular and Optical Physics*, vol. 45, no. 11, p. 113 001, 2012. URL: http://stacks.iop.org/0953-4075/45/i=11/a=113001.

[20] E. A. Goldschmidt et al., "Anomalous Broadening in Driven Dissipative Rydberg Systems", *Phys. Rev. Lett.*, vol. 116, p. 113 001, iss. 11, 2016. DOI: 10.1103/PhysRevLett.116.113001. URL: http://link.aps.org/doi/10.1103/PhysRevLett.116.113001.

[21] T. Wilk et al., "Entanglement of Two Individual Neutral Atoms Using Rydberg Blockade", *Phys. Rev. Lett.*, vol. 104, p. 010 502, iss. 1, Jan. 2010. DOI: 10.1103/PhysRevLett.104.010502. URL: http://link.aps.org/doi/10.1103/PhysRevLett.104.010502.

[22] D. Møller et al., "Quantum Gates and Multiparticle Entanglement by Rydberg Excitation Blockade and Adiabatic Passage", *Phys. Rev. Lett.*, vol. 100, p. 170 504, iss. 17, Apr. 2008. DOI: 10.1103/PhysRevLett.100.170504. URL: http://link.aps.org/doi/10.1103/PhysRevLett.100.170504.

[23] D. Jaksch et al., "Fast Quantum Gates for Neutral Atoms", *Phys. Rev. Lett.*, vol. 85, pp. 2208–2211, iss. 10, Sep. 2000. DOI: 10.1103/PhysRevLett.85.2208. URL: http://link.aps.org/doi/10.1103/PhysRevLett.85.2208.

[24] I. E. Protsenko et al., "Operation of a quantum phase gate using neutral atoms in microscopic dipole traps", *Phys. Rev. A*, vol. 65, p. 052 301, iss. 5, Apr. 2002. DOI: 10.1103/PhysRevA.65.052301. URL: http://link.aps.org/doi/10.1103/PhysRevA.65.052301.

[25] L. Isenhower et al., "Demonstration of a Neutral Atom Controlled-NOT Quantum Gate", *Phys. Rev. Lett.*, vol. 104, p. 010 503, iss. 1, Jan. 2010. DOI: 10.1103/PhysRevLett.104.010503. URL: http://link.aps.org/doi/10.1103/PhysRevLett.104.010503.

[26] M. Saffman et al., "Quantum information with Rydberg atoms", *Rev. Mod. Phys.*, vol. 82, pp. 2313–2363, iss. 3, 2010. DOI: `10.1103/RevModPhys.82.2313`. URL: `http://link.aps.org/doi/10.1103/RevModPhys.82.2313`.

[27] C. J. Foot, *Atomic Physics*. Oxford University Press, 2005.

[28] R. Grimm et al., "Optical dipole traps for neutral atoms", *arXiv preprint physics/9902072*, 1999.

[29] D. Meschede, *Optik, Licht und Laser*, ser. Teubner Studienbücher Physik. Vieweg+Teubner Verlag, 2015, ISBN: 9783663109549.

[30] B. Saleh et al., *Fundamentals of Photonics*, ser. Wiley Series in Pure and Applied Optics. Wiley, 2007, ISBN: 9780471358329.

[31] F. Pampaloni et al., "Gaussian, hermite-gaussian, and laguerre-gaussian beams: A primer", *arXiv preprint physics/0410021*, 2004.

[32] S. J. M. Kuppens et al., "Loading an optical dipole trap", *Phys. Rev. A*, vol. 62, p. 013 406, iss. 1, Jun. 2000. DOI: `10.1103/PhysRevA.62.013406`. URL: `http://link.aps.org/doi/10.1103/PhysRevA.62.013406`.

[33] D. Cho, "Analogous Zeeman effect from the tensor polarizability in alkali atoms", *J. Korean Phys.Soc.*, vol. 30, p. 373, 1996. DOI: `10.3938/jkps.30.373`.

[34] D. A. Steck, "Rubidium 87 D Line Data", `http://steck.us/alkalidata/rubidium87numbers.pdf`, Sep. 2001. (visited on 03/28/2016).

[35] H. M. Gorniaczyk, "'A Crossed Optical Dipole Trap,'" Diplomarbeit, Universität Stuttgart, 2011.

[36] A. Harsono, "'Dipole trapping and manipulation of ultra-cold atoms,'" PhD thesis, University of Oxford, 2006.

[37] L. Weller et al., "Absolute absorption and dispersion of a rubidium vapour in the hyperfine Paschen–Back regime", *Journal of Physics B: Atomic, Molecular and Optical Physics*, vol. 45, no. 21, p. 215 005, 2012. URL: `http://stacks.iop.org/0953-4075/45/i=21/a=215005`.

[38] A. Banerjee et al., "Precise fine-structure and hyperfine-structure measurements in Rb", *arXiv preprint physics/0209019*, 2002.

[39] J. Schmidt, "'Generation of non-classical light using ultra-cold Rydberg ensembles,'" Master's Thesis, Universität Stuttgart, 2014.

[40] OCLARO, "Preliminary Data Sheet, 830nm single mode diode laser", `https://www.thorlabs.com/thorcat/QTN/L830P200-MFGSpec.pdf`, Aug. 2013. (visited on 03/10/2016).

[41] M. Ligare, "Classical thermodynamics of particles in harmonic traps", *American Journal of Physics*, vol. 78, no. 8, pp. 815–819, 2010. DOI: `http://dx.doi.org/10.1119/1.3417868`. URL: `http://scitation.aip.org/content/aapt/journal/ajp/78/8/10.1119/1.3417868`.

[42] G. Reinaudi et al., "Strong saturation absorption imaging of dense clouds of ultracold atoms", *Opt. Lett.*, vol. 32, no. 21, pp. 3143–3145, Nov. 2007. DOI: `10.1364/OL.32.003143`. URL: `http://ol.osa.org/abstract.cfm?URI=ol-32-21-3143`.

[43] L. M. Bennie et al., "A versatile high resolution objective for imaging quantum gases", *Opt. Express*, vol. 21, no. 7, pp. 9011–9016, Apr. 2013. DOI: 10.1364/OE.21.009011. URL: http://www.opticsexpress.org/abstract.cfm?URI=oe-21-7-9011.

[44] E. A. Salim et al., "High resolution imaging and optical control of Bose-Einstein condensates in an atom chip magnetic trap", *Applied Physics Letters*, vol. 102, no. 8, 084104, 2013. DOI: http://dx.doi.org/10.1063/1.4793522. URL: http://scitation.aip.org/content/aip/journal/apl/102/8/10.1063/1.4793522.

[45] K. E. Wilson et al., "*In situ* imaging of vortices in Bose-Einstein condensates", *Phys. Rev. A*, vol. 91, p. 023 621, iss. 2, Feb. 2015. DOI: 10.1103/PhysRevA.91.023621. URL: http://link.aps.org/doi/10.1103/PhysRevA.91.023621.

[46] A. Lipson et al., *Optical Physics*. Cambridge University Press, 2010, ISBN: 9781139492607.

[47] B. Masters, *Confocal Microscopy and Multiphoton Excitation Microscopy: The Genesis of Live Cell Imaging*, ser. SPIE Press monograph. SPIE Press, 2006, ISBN: 9780819461186.

[48] G. B. Airy, "On the Diffraction of an Object-glass with Circular Aperture", *Transactions of the Cambridge Philosophical Society*, vol. 5, pp. 283–291, 1835.

[49] F. Lord Rayleigh, "XXXI. Investigations in optics, with special reference to the spectroscope", *Philosophical Magazine Series 5*, vol. 8, no. 49, pp. 261–274, 1879. DOI: 10.1080/14786447908639684. URL: http://dx.doi.org/10.1080/14786447908639684.

[50] Optomark GmbH. (2014). "VCSEL", URL: http://www.optomark.eu/products/laser-components/vcsel.html (visited on 03/10/2016).

[51] E. Gehrig et al., *Spatio-Temporal Dynamics and Quantum Fluctuations in Semiconductor Lasers*, ser. Springer Tracts in Modern Physics. Springer Berlin Heidelberg, 2003, ISBN: 9783540007418.

[52] R. Michalzik, *VCSELs: Fundamentals, Technology and Applications of Vertical-Cavity Surface-Emitting Lasers*, ser. Springer Series in Optical Sciences. Springer Berlin Heidelberg, 2012, ISBN: 9783642249860.

[53] R. Michalzik et al., "'Vertical-Cavity Surface-Emitting Laser Devices,'" in, H. E. Li et al., Eds. Berlin, Heidelberg: Springer Berlin Heidelberg, 2003, ch. Operating Principles of VCSELs, pp. 53–98, ISBN: 978-3-662-05263-1. DOI: 10.1007/978-3-662-05263-1_3. URL: http://dx.doi.org/10.1007/978-3-662-05263-1_3.

[54] C. J. Chang-Hasnain et al., "Dynamic, polarization, and transverse mode characteristics of vertical cavity surface emitting lasers", *IEEE Journal of Quantum Electronics*, vol. 27, no. 6, pp. 1402–1409, Jun. 1991, ISSN: 0018-9197. DOI: 10.1109/3.89957.

[55] A. Valle et al., "Transverse Mode Switching and Locking in Vertical-Cavity Surface-Emitting Lasers Subject to Orthogonal Optical Injection", *IEEE Journal of Quantum Electronics*, vol. 43, no. 4, pp. 322–333, Apr. 2007, ISSN: 0018-9197. DOI: 10.1109/JQE.2007.893004.

[56] M. V. Berry, "Lateral and transverse shifts in reflected dipole radiation", *Proceedings of the Royal Society of London A: Mathematical, Physical and Engineering Sciences*, vol. 467, no. 2133, pp. 2500–2519, 2011, ISSN: 1364-5021. DOI: 10.1098/rspa.2011.0081. URL: http://rspa.royalsocietypublishing.org/content/467/2133/2500.

[57] M. Fukuda, *Optical Semiconductor Devices*, ser. A Wiley Interscience publication. Wiley, 1999, ISBN: 9780471149590.

[58] M. Ahmed et al., "Enhancing the modulation bandwidth of VCSELs to the millimeter-waveband using strong transverse slow-light feedback", *Opt. Express*, vol. 23, no. 12, pp. 15 365–15 371, Jun. 2015. DOI: 10.1364/OE.23.015365. URL: http://www.opticsexpress.org/abstract.cfm?URI=oe-23-12-15365.

[59] T. Shimada et al., "Lateral integration of vertical-cavity surface-emitting laser and slow light Bragg reflector waveguide devices", *Appl. Opt.*, vol. 53, no. 9, pp. 1766–1774, Mar. 2014. DOI: 10.1364/AO.53.001766. URL: http://ao.osa.org/abstract.cfm?URI=ao-53-9-1766.

[60] J. Jimenez, *Microprobe Characterization of Optoelectronic Materials*, ser. Optoelectronic properties of semiconductors and superlattices. Taylor & Francis, 2002, ISBN: 9781560329411.

[61] C. Webb et al., *Handbook of Laser Technology and Applications: Laser design and laser systems*, ser. Handbook of Laser Technology and Applications Bd. 2. Institute of Physics, 2004, ISBN: 9780750309639.

[62] M. Atef et al., *Optoelectronic Circuits in Nanometer CMOS Technology*, ser. Springer Series in Advanced Microelectronics. Springer International Publishing, 2016, ISBN: 9783319273389.

[63] Thorlabs, "PDA10A(-EC), Si Amplified Fixed Detector, User Guide", http://www.thorlabs.de/thorcat/13000/PDA10A-EC-Manual.pdf, Jun. 2015. (visited on 03/15/2016).

[64] A. N. Al-Omari et al., "Fabrication and performance of bottom-emitting flip-chip bonded 980 nm vertical-cavity lasers with copper- and indium-plated heat-sinks", *Semiconductor Science and Technology*, vol. 26, no. 12, p. 125 020, 2011. URL: http://stacks.iop.org/0268-1242/26/i=12/a=125020.

[65] A. Cutolo et al., "Transverse mode analysis of a laser beam by near- and far-field intensity measurements", *Appl. Opt.*, vol. 34, no. 34, pp. 7974–7978, Dec. 1995. DOI: 10.1364/AO.34.007974. URL: http://ao.osa.org/abstract.cfm?URI=ao-34-34-7974.

[66] C. M. Warnky et al., "Determining spatial modes of lasers with spatial coherence measurements", *Appl. Opt.*, vol. 39, no. 33, pp. 6109–6117, Nov. 2000. DOI: 10.1364/AO.39.006109. URL: http://ao.osa.org/abstract.cfm?URI=ao-39-33-6109.

[67] W. Silfvast, *Laser Fundamentals*. Cambridge University Press, 2004, ISBN: 9780521833455.

[68] G. Machavariani et al., "Improving the stability of longitudinal and transverse laser modes", *Optics Communications*, vol. 239, no. 1–3, pp. 147 –151, 2004, ISSN: 0030-4018. DOI: http://dx.doi.org/10.1016/j.optcom.2004.05.014. URL: http://www.sciencedirect.com/science/article/pii/S0030401804005097.

[69] National Instruments, "Stimulated Emission Devices LASERS", http://www.ni.com/white-paper/14878/en/pdf, Sep. 2013. (visited on 03/16/2016).

[70] T. A. Heumier et al., "Detecting mode hopping in semiconductor lasers by monitoring intensity noise", *IEEE Journal of Quantum Electronics*, vol. 29, no. 11, pp. 2756–2761, Nov. 1993, ISSN: 0018-9197. DOI: 10.1109/3.248933.

[71] M. Vaughan, *The Fabry-Perot Interferometer: History, Theory, Practice and Applications*, ser. Series in Optics and Optoelectronics. Taylor & Francis, 1989, ISBN: 9780852741382.

[72] APC International Ltd, *Piezoelectric Ceramics: Principles and Applications.* APC International, 2002, ISBN: 9780971874404.

[73] E. Hecht, *Optics.* Addison-Wesley, 2002, ISBN: 9780805385663.

[74] R. Wynands et al., "A compact tunable 60-dB Faraday optical isolator for the near infrared", *Review of Scientific Instruments*, vol. 63, no. 12, pp. 5586–5590, 1992. DOI: `http://dx.doi.org/10.1063/1.1143386`. URL: `http://scitation.aip.org/content/aip/journal/rsi/63/12/10.1063/1.1143386`.

[75] R. Dorf, *Sensors, Nanoscience, Biomedical Engineering, and Instruments: Sensors Nanoscience Biomedical Engineering*, ser. The Electrical Engineering Handbook. CRC Press, 2016, ISBN: 9781420003161.

[76] Laser 2000, "Optical Isolator Specifications", `http://www.laser2000.co.uk/ds/DS_00952.pdf`. (visited on 03/22/2016).

[77] J. Ohtsubo, *Semiconductor Lasers: Stability, Instability and Chaos*, ser. Springer Series in Optical Sciences. Springer Berlin Heidelberg, 2007, ISBN: 9783540726500.

[78] Y.-F. Hsiao et al., "Cold atomic media with ultrahigh optical depths", *Phys. Rev. A*, vol. 90, p. 055 401, iss. 5, Nov. 2014. DOI: `10.1103/PhysRevA.90.055401`. URL: `http://link.aps.org/doi/10.1103/PhysRevA.90.055401`.

[79] C. Braun, "'Implementation of a Raman Sideband Cooling for 87Rb,'" Bachelor Thesis, Universität Stuttgart, 2015.

[80] T. M. Brzozowski et al., "Time-of-flight measurement of the temperature of cold atoms for short trap-probe beam distances", *Journal of Optics B: Quantum and Semiclassical Optics*, vol. 4, no. 1, p. 62, 2002.

[81] H. Gorniaczyk et al., "Single-Photon Transistor Mediated by Interstate Rydberg Interactions", *Phys. Rev. Lett.*, vol. 113, p. 053 601, iss. 5, Jul. 2014. DOI: `10.1103/PhysRevLett.113.053601`. URL: `http://link.aps.org/doi/10.1103/PhysRevLett.113.053601`.

[82] T. Gallagher, *Rydberg Atoms*, ser. Cambridge Monographs on Atomic, Molecular and Chemical Physics. Cambridge University Press, 2005, ISBN: 9780521021661.

[83] Y. O. Dudin et al., "Emergence of Spatial Spin-Wave Correlations in a Cold Atomic Gas", *Phys. Rev. Lett.*, vol. 109, p. 133 602, iss. 13, Sep. 2012. DOI: `10.1103/PhysRevLett.109.133602`. URL: `http://link.aps.org/doi/10.1103/PhysRevLett.109.133602`.

[84] J. D. Pritchard, "'Cooperative Optical Non-linearity in a blockaded Rydberg Ensemble,'" PhD thesis, Durham University, 2011.

[85] H. Gorniaczyk et al., "Enhancement of single-photon transistor by Stark-tuned Förster resonances", *arXiv preprint arXiv:1511.09445*, 2015.

[86] F. Bariani et al., "Dephasing of Multiparticle Rydberg Excitations for Fast Entanglement Generation", *Phys. Rev. Lett.*, vol. 108, p. 030 501, iss. 3, Jan. 2012. DOI: `10.1103/PhysRevLett.108.030501`. URL: `http://link.aps.org/doi/10.1103/PhysRevLett.108.030501`.

[87] C. Ates et al., "Entropic enhancement of spatial correlations in a laser-driven Rydberg gas", *Phys. Rev. A*, vol. 86, p. 013 408, iss. 1, Jul. 2012. DOI: 10.1103/PhysRevA.86.013408. URL: http://link.aps.org/doi/10.1103/PhysRevA.86.013408.

[88] W. Dür et al., "Three qubits can be entangled in two inequivalent ways", *Phys. Rev. A*, vol. 62, p. 062 314, iss. 6, Nov. 2000. DOI: 10.1103/PhysRevA.62.062314. URL: http://link.aps.org/doi/10.1103/PhysRevA.62.062314.

[89] A. K. Mohapatra et al., "Coherent Optical Detection of Highly Excited Rydberg States Using Electromagnetically Induced Transparency", *Phys. Rev. Lett.*, vol. 98, p. 113 003, iss. 11, Mar. 2007. DOI: 10.1103/PhysRevLett.98.113003. URL: http://link.aps.org/doi/10.1103/PhysRevLett.98.113003.

[90] F. Bariani et al., "Retrieval of multiple spin waves from a weakly excited, metastable atomic ensemble", *Phys. Rev. A*, vol. 85, p. 033 811, iss. 3, Mar. 2012. DOI: 10.1103/PhysRevA.85.033811. URL: http://link.aps.org/doi/10.1103/PhysRevA.85.033811.

[91] T. Peyronel et al., "Quantum nonlinear optics with single photons enabled by strongly interacting atoms", *Nature*, vol. 488, no. 7409, pp. 57–60, 2012.

[92] P. Bienias et al., "Scattering resonances and bound states for strongly interacting Rydberg polaritons", *Phys. Rev. A*, vol. 90, p. 053 804, iss. 5, Nov. 2014. DOI: 10.1103/PhysRevA.90.053804. URL: http://link.aps.org/doi/10.1103/PhysRevA.90.053804.

[93] C. Tresp et al., "Dipolar Dephasing of Rydberg *D*-State Polaritons", *Phys. Rev. Lett.*, vol. 115, p. 083 602, iss. 8, Aug. 2015. DOI: 10.1103/PhysRevLett.115.083602. URL: http://link.aps.org/doi/10.1103/PhysRevLett.115.083602.

[94] A. Zavatta et al., "Subtracting photons from arbitrary light fields: experimental test of coherent state invariance by single-photon annihilation", *New Journal of Physics*, vol. 10, no. 12, p. 123 006, 2008. URL: http://stacks.iop.org/1367-2630/10/i=12/a=123006.

[95] V. Parigi et al., "Probing Quantum Commutation Rules by Addition and Subtraction of Single Photons to/from a Light Field", *Science*, vol. 317, no. 5846, pp. 1890–1893, 2007, ISSN: 0036-8075. DOI: 10.1126/science.1146204. URL: http://science.sciencemag.org/content/317/5846/1890.

[96] I. Shomroni et al., "All-optical routing of single photons by a one-atom switch controlled by a single photon", *Science*, vol. 345, no. 6199, pp. 903–906, 2014, ISSN: 0036-8075. DOI: 10.1126/science.1254699. URL: http://science.sciencemag.org/content/345/6199/903.

[97] J. Fiurá šek et al., "Conditional generation of arbitrary single-mode quantum states of light by repeated photon subtractions", *Phys. Rev. A*, vol. 72, p. 033 822, iss. 3, Sep. 2005. DOI: 10.1103/PhysRevA.72.033822. URL: http://link.aps.org/doi/10.1103/PhysRevA.72.033822.

[98] A. Ourjoumtsev et al., "Generating Optical Schrödinger Kittens for Quantum Information Processing", *Science*, vol. 312, no. 5770, pp. 83–86, 2006, ISSN: 0036-8075. DOI: 10.1126/science.1122858. URL: http://science.sciencemag.org/content/312/5770/83.

[99] A. Gilchrist et al., "Schrödinger cats and their power for quantum information processing", *Journal of Optics B: Quantum and Semiclassical Optics*, vol. 6, no. 8, S828, 2004.

[100] J. Honer et al., "Artificial Atoms Can Do More Than Atoms: Deterministic Single Photon Subtraction from Arbitrary Light Fields", *Phys. Rev. Lett.*, vol. 107, p. 093 601, iss. 9, Aug. 2011. DOI: `10.1103/PhysRevLett.107.093601`. URL: `http://link.aps.org/doi/10.1103/PhysRevLett.107.093601`.

[101] M. Bajcsy et al., "Quantum optics: Arithmetic with photons", *Nature Photonics*, vol. 10, no. 1, pp. 4–6, 2016.

[102] J. Calsamiglia et al., "Removal of a single photon by adaptive absorption", *Phys. Rev. A*, vol. 64, p. 043 814, iss. 4, Sep. 2001. DOI: `10.1103/PhysRevA.64.043814`. URL: `http://link.aps.org/doi/10.1103/PhysRevA.64.043814`.

[103] A. Ourjoumtsev et al., "Increasing Entanglement between Gaussian States by Coherent Photon Subtraction", *Phys. Rev. Lett.*, vol. 98, p. 030 502, iss. 3, Jan. 2007. DOI: `10.1103/PhysRevLett.98.030502`. URL: `http://link.aps.org/doi/10.1103/PhysRevLett.98.030502`.

[104] J. S. Neergaard-Nielsen et al., "Generation of a Superposition of Odd Photon Number States for Quantum Information Networks", *Phys. Rev. Lett.*, vol. 97, p. 083 604, iss. 8, Aug. 2006. DOI: `10.1103/PhysRevLett.97.083604`. URL: `http://link.aps.org/doi/10.1103/PhysRevLett.97.083604`.

[105] S. Rosenblum et al., "Extraction of a single photon from an optical pulse", *Nature Photonics*, vol. 10, no. 1, pp. 19–22, 2016.

[106] M. Scully et al., *Quantum Optics*. Cambridge University Press, 1997, ISBN: 9780521435956.

[107] R. H. Brown et al., "A test of a new type of stellar interferometer on Sirius", *Nature*, vol. 178, no. 4541, pp. 1046–1048, 1956.

[108] R. Loudon, *The Quantum Theory of Light*. OUP Oxford, 2000, ISBN: 9780191589782.

[109] M. Scholz, *New Light Sources for Quantum Information Processing – Single Photons from Single Quantum Dots and Cavity-Enhanced Parametric Down-Conversion*. Isd, 2009, ISBN: 9783832522209.

[110] J. L. Wiza, "Microchannel plate detectors", *Nuclear Instruments and Methods*, vol. 162, no. 1, pp. 587 –601, 1979, ISSN: 0029-554X. DOI: `http://dx.doi.org/10.1016/0029-554X(79)90734-1`. URL: `http://www.sciencedirect.com/science/article/pii/0029554X79907341`.

[111] A. Gaj et al., "From molecular spectra to a density shift in dense Rydberg gases", *Nature communications*, vol. 5, 2014.

[112] L. N. Brillouin, "Diffusion de la lumiére et des rayons X par un corps transparent homogéne", *Annales de Physique*, pp. 88–122, iss. 17, 1922.

[113] R. Hunsperger, *Integrated Optics: Theory and Technology*, ser. Advanced texts in physics. Springer, 2002, ISBN: 9783540433415.

[114] O. Svelto, *Principles of Lasers*. Springer US, 2010, ISBN: 9781441913029.

[115] Crystal Technology, "AOMO 3080-194",
http://www.eqphotonics.de/cms/cms/upload/datasheets/3080-194_97-02814-
01_Rev_B.pdf. (visited on 01/06/2016).

[116] B. Fröhlich, "'Strong Dipolar Effects in a Chromium Bose-Einstein Condensate,'"
Diplomarbeit, Universität Stuttgart, 2007.

[117] D. Hecht, "Multifrequency Acoustooptic Diffraction", *Sonics and Ultrasonics, IEEE Transactions on*, vol. 24, no. 1, pp. 7–18, Jan. 1977, ISSN: 0018-9537. DOI: 10.1109/T-SU.1977.30905.

[118] B. Fröhlich et al., "Two-frequency acousto-optic modulator driver to improve the beam pointing stability during intensity ramps", *Review of Scientific Instruments*, vol. 78, no. 4, 043101, 2007. DOI: http://dx.doi.org/10.1063/1.2720725. URL: http://scitation.aip.org/content/aip/journal/rsi/78/4/10.1063/1.2720725.

[119] Mini-Circuits, "Coaxial Directional Coupler ZDC-10-1+, ZDC-10-1",
http://www.minicircuits.com/pdfs/ZDC-10-1.pdf. (visited on 01/04/2016).

[120] ISOMET, "Application Note, AN1106 Maximizing AO Diffraction efficiency",
http://www.isomet.com/App-Manual_pdf/Maximizing%20DE.pdf, Nov. 2006. (visited on 01/07/2016).

[121] Mini-Circuits, "Coaxial High Isolation Switch ZASWA-2-50DR+",
http://www.minicircuits.com/pdfs/ZASWA-2-50DR+.pdf. (visited on 01/07/2016).

[122] VISHAY, "DG417, DG418, DG419, Precision CMOS Analog Switches",
http://www.vishay.com/docs/70051/dg417.pdf, Jul. 2010. (visited on 01/07/2016).

[123] P. Horowitz et al., *The Art of Electronics*, ser. Cambridge low price editions. Cambridge University Press, 1989, ISBN: 9780521498463.

[124] H. Jackson et al., *Introduction to Electric Circuits*. Oxford University Press, 2015, ISBN: 9780199020485.

[125] Y. Papananos, *Radio-Frequency Microelectronic Circuits for Telecommunication Applications*. Springer US, 2013, ISBN: 9781475730173.

[126] M. Young, *Optics and Lasers: An Engineering Physics Approach*, ser. Springer Series in Optical Sciences. Springer Berlin Heidelberg, 2013, ISBN: 9783662158166.

[127] M. Born et al., *Principles of Optics: Electromagnetic Theory of Propagation, Interference and Diffraction of Light*. Cambridge University Press, 2000, ISBN: 9780521784498.

[128] T. Li, *Optical Fiber Communications: Fiber Fabrication*. Elsevier Science, 2012, ISBN: 9780323153478.

[129] V. Ter-Mikirtychev, *Fundamentals of Fiber Lasers and Fiber Amplifiers*, ser. Springer Series in Optical Sciences. Springer International Publishing, 2013, ISBN: 9783319023380.

[130] T. Hosaka et al., "Stress-applied polarization-maintaining optical fibers. Design and fabrication", *Electronics and Communications in Japan (Part II: Electronics)*, vol. 68, no. 3, pp. 37–47, 1985, ISSN: 1520-6432. DOI: 10.1002/ecjb.4420680305. URL: http://dx.doi.org/10.1002/ecjb.4420680305.

[131] T. T. Aalto et al., "Method for the rotational alignment of polarization-maintaining optical fibers and waveguides", *Optical Engineering*, vol. 42, no. 10, pp. 2861–2867, 2003. DOI: 10.1117/1.1600730. URL: http://dx.doi.org/10.1117/1.1600730.

Acknowledgements

Danksagung